ADVANCING ULTRA-HIGH FIELD MAGNETIC RESONANCE MICROSCOPY

By

Benjamin Michael Hardy

Dissertation

Submitted to the Faculty of the

Graduate School of Vanderbilt University

in partial fulfillment of the requirements

for the degree of

DOCTOR OF PHILOSOPHY

in

Physics

August 11th, 2023

Nashville, Tennessee

Approved:

John C. Gore, Ph.D.

Adam W. Anderson, Ph.D.

William A. Grissom, Ph.D.

Junzhong Xu, Ph.D.

Todd A. Peterson, Ph.D.

To Bailey, with all my love.
To my family, thank you for believing in me.

ACKNOWLEDGMENTS

I am immensely thankful to so many in my life for helping me reach this point. The entire graduate school experience has been much more than an intellectual journey for me. I have grown into someone entirely different than the person I was in the fall of 2017.

First I would like to thank God. I believe the complexity and beauty of the world around us requites a loving and scientific God. He designed electricity and magnetism and left it here for us to discover, much like he leaves a lot of things here for us to figure out. A Proverb comes to mind: "It is the glory of God to conceal a matter, But the glory of kings is to search out a matter." -Proverbs 25:2

I would like to acknowledge my lovely wife Bailey. She is the light of my life and a constant inspiration to me. Her encouragement has brought me through many days of considering quitting. I wouldn't have made it this far if she wasn't by my side. My parents for raising me and encouraging my curiosity and creativity. They brought me up in a home filled with imagination, hope, and gratitude no matter our circumstances. My siblings, Danielle and Liam for putting up with my nonsensical musings and always picking up where we left off, even if its been months.

The mentorship I've received at Vanderbilt has been nothing short but incredible. Dr. Adam Anderson's door has always been open to me. There have been many times, I've walked up to his office unscheduled and he's always made time for my thoughts, questions, and concerns. I'm so grateful that he accepted me as his student back in 2019 without asking anything of my credentials. No doubt I would not be here today had he not accepted me as his student. Some day I wish to have my own office filled with as much zen as Adam's.

With the million + 1 things on his plate, Dr. Gore has always been only an email away. It is clear that he values his students and prioritizes them with his time and funds. I'm honored to say that I've spent time under his tutelage and scientific rigor. It's something else to listen to the rapid-fire brainstorm of ideas and concepts when he is inspired in a research setting.

Dr. Junzhong Xu and Dr. Todd Peterson probably have the most perspective on my growth as a researcher. I'm grateful for the early semesters spent in their labs. They allowed me to get my feet wet and have continued to support my research when needed.

Dr. William Grissom has always been encouraging and enthusiastic about my work. His comments have encouraged me probably more than he knows. Also, we're both from Michigan, so we have a strange but strong mutual understanding of midwestern culture that transcends social norms.

Dr. Xinqiang Yan for being a wonderful and caring advisor for RF projects. His creativity and ability to encourage students is 2nd to none. The number of students I've seen excel under his leadership is astounding. Dr. Jonathan Martin for truly running this race with me, late nights playing chess, and understanding my research qualms. Thanks for rooting me on. Dr. Tom Manuel for sitting next to me through most of graduate school and putting up with my antics. Dr. Charlotte Sappo for teaching me how to make my first RF coil. Rana Banik for his hard work and always welcoming attitude. I'm always happy to see your smile in the office.

I should mention Dr. Mark Does. Even though he's from Canada, he's passionate about seeing his students succeed and grow in the process.

The cryochamber would not have happened without Gary Drake. Gary is a wizard in the machine shop and is simultaneously smart and personable, which is a breathe of fresh air in academics. Dr. Dan Colvin for his consistent help and correspondence at the 15.2T. Dr. Yue Zhu was a post-doc during some of my time here. He taught me what it means to be peer-mentor and how to share knowledge. His time at Vanderbilt was invaluable and pushed me forward. Drs. Feng Wang, Fatemeh Adelnia, Ming-Zhi Zhang, Xiaofeng Fan, and Ming Jiang assistance with the muring kidney studies were instrumental for the completion of this work.

In terms of funding, I am gracious for the financial support of my projects via the Chan-Zuckerberg Initiative (CZI) for Deep Tissue Imaging and the National Institutes of Health grants R21 EB024311 and R01 NS095291.

TABLE OF CONTENTS

LIST OF TABLES

LIST OF FIGURES

CHAPTER 1

Introduction to magnetic resonance

Before embarking through the dissertation's contributions to magnetic resonance microscopy (MRM), chapter 1 will describe some of foundations of magnetic resonance. The concepts presented are meant to familiarize and aid the reader in interpretation of the dissertation's results. Commensurate review of MRM such as Paul Callaghan's *Principles of Nuclear Magnetic Resonance Microscopy* should be consulted for thorough review of the topic and greatly aided in development of the subsequent chapters. In chapter 2, a thorough description of relevant previous work will situate the dissertation's complementary contributions to the field. After the relevant background, the specific aims of the dissertation will be described. Chapters 3-5 will deliberate on the aims and describe the experimental and theoretical methods used to achieve them. Finally, chapter 6 will comment on the conclusions, potential improvements, and ideas for future MR microscopists.

1.1 Imaging with magnetic resonance

The concepts presented here are by no means complete and are only meant to give the reader proper context to interpret the dissertation's contributions to the field.

1.1.1 The Larmor equation and linewidths

A simple explanation describing why MRI is possible starts with the Larmor equation [3]:

$$\omega_0 = \gamma B_0 \tag{1.1}$$

where ω_0 is the Larmor frequency, γ is the gyromagnetic ratio of the nucleus, and B_0 the applied magnetic field. For ^1H nuclei, $\gamma = 2\pi$ 42.58 MHz/T. Two observations should be noted: 1) For 1-15 Tesla, ^1H imaging, the precession frequency is 42-647 MHz or radio

frequencies (RF) with well established protocols and devices to achieve resonance. The precession of isochromats, or groups of nuclei, allows transfer of information from the molecular level to interpretable signals effectively bridging two worlds. 2) By deliberately modifying the magnetic field across space, the frequency of precession becomes spatially dependent. By applying a magnetic field gradient $B_0(x)$, a ^1H ridden space is discretized across a frequency distribution. This is the basis for frequency encoding further described in ch. 3. Similarly, each isochromat has a corresponding net phase which may be encoded. The following derivations follow the approach taken by Farrar and Becker [4]. Deriving the Larmor equation follows from simple identities in quantum mechanics. Along with ^3H, ^{13}C, ^{19}F, and ^{31}P, ^1H nuclei have a non-zero magnetic dipole moment μ with spin quantum number $I = 1/2$. From elementary quantum mechanics, a nucleus of quantum spin number I has $2I+1$ of energy levels quantized with differences in energy [5] given by

$$\Delta E = \mu B_0 / I \tag{1.2}$$

where μ is the nuclear magnetic moment given by

$$\mu = \gamma \mathbf{p} = \gamma \hbar I \tag{1.3}$$

where $\mathbf{p}$ is the angular momentum and $\hbar$ is Planck's constant over 2π. The Bohr model dictates the frequency needed to transition between energy states:

$$h f_0 = \Delta E \tag{1.4}$$

Substituting equations 1.2 and 1.3 into equation 1.4 yields

$$f_0 = \frac{\gamma B_0}{2\pi} \tag{1.5}$$

or the Larmor equation. Nuclear spin aside, MR may be completely described using

classical and statistical mechanics [6]. Confusion arises when discussing the spin-states of singular ^1H nuclei. Single nuclei are more appropriately described by quantum mechanics as existing in a super-position of the $2I+1$ energy states. However, standard MR techniques typically deal with ensembles of nuclei, or isochromats, subjected to a strong B_0. Thus the net magnetization (**M**) is described classically using the 'compass in a dryer' analogy. The net magnetization is determined by a Boltzmann distribution of the two energy states with equilibrium slightly favoring alignment with the external field. After perturbation of the net-magnetization with an orthogonal resonant RF pulse, the system will return to equilibrium in the longitudinal direction in time on the order of T_1. The time it takes for the spins to return to equilibrium with the surroundings is then called the spin-lattice relaxation. Continuing Farrar and Becker's approach [4], a minimum line width defined by the frequencies at the full-width of half max (FWHM) can then be determined using the Heisenberg uncertainty principle in terms of energy and time, $\Delta E \Delta t \gtrsim h$. Substituting T_1 and eqn. 1.4 yields

$$h f_{1/2}\, T_1 \gtrsim h \; and \; f_{0,1/2} \gtrsim 1/T_1 \tag{1.6}$$

where $f_{0,1/2}$ represents the frequencies at FWHM intensity. Lines are further broadened by other processes some of which will be thoroughly elaborated in chapter 3. T_1 relaxation describes the time the spins take to return to equilibrium with their surroundings, whereas T_2 relaxation describes how phased spins in the transverse plane lose their coherence. Bloch's equations [7] describe relaxation after application of an orthogonal resonant RF pulse. The resonant RF pulse's associated magnetic field is referred to as B_1. For a full description of excitation and relaxation, introductory MRI textbooks [8] should be consulted or better yet, Bloch's original publication *Nuclear Induction*.

M may be tipped into the transverse plane using a resonant B_1 pulse due to the torque or change in **p**, the angular momentum, of the **M** vector, similar to the effects observed in a gyroscope, hence the root word 'gryo-' in 'gyromagnetic' [9]. The resulting trajectories of

the $\mathbf{M}$ vector are simplified if the frame of reference is rotating with the precession of the ensemble of spins. $\mathbf{M}_{xy}$ denotes the magnetization vector in the transverse plane. As $\mathbf{M}_{xy}$ grows, appreciable voltages induce an electromotive force (EMF) in RF coils (see section 1.2) perpendicular to the static field. Phase sensitive detection or demodulation transforms the signals to the rotating frame of reference [10]. In an ideal magnetic field, the signal in the transverse plane decays exponentially and can be written in its complex form as

$$\mathbf{M}_{xy} = \mathbf{M}_0 e^{-t/T_2} e^{-i\Delta\omega t} \tag{1.7}$$

where $\mathbf{M}_0$ denotes the spin density of the excited region, $\Delta\omega = \omega_{ref} - \omega_0$ and ω_{ref} is the reference frequency of the phase sensitive detection. For an example when $\omega_{ref} \neq \omega_0$, see figure 1.1. Typically, the B_0 field is imperfect due to non-ideal hardware and susceptibility differences in the sample. Therefore the signal decays with a varying time constant T_2^*. Including the variations in B_0, the new time constant may be written as

$$1/T_2^* = 1/T_2 + \gamma\Delta B_0 \tag{1.8}$$

1.1.2 The Fourier transform, k-space, and magnetic field gradients

Observing equation 1.1, deliberately manipulating the magnetic field results in frequency differences across the sample. Some earlier [11] and more recent [12] work considered dynamic B_0 fields instead of static fields in a technique now called field-cycling. Assuming static B_0, the spatial distributions of spins may be mapped onto a frequency space. The algorithmic key that allows a remapping of the spatially encoded data lies within the Fourier transform. Relating the time evolution of a signal $s(t)$ to its corresponding frequency dependent form may be done with the Fourier transform. In its continuous form it's written as

$$S(\omega) = \int_{-\infty}^{\infty} s(t) e^{-i\omega t} dt \tag{1.9}$$

where $i = \sqrt{-1}$. Since acquisition occurs at discrete and finite time points, mathematically the signal is transformed using the discrete Fourier transform (DFT). In practice, the DFT is applied when literature mentions the transform. Thorough review of efficiently applying the algorithm can be found elsewhere [13] and is beyond the scope of the current chapter.

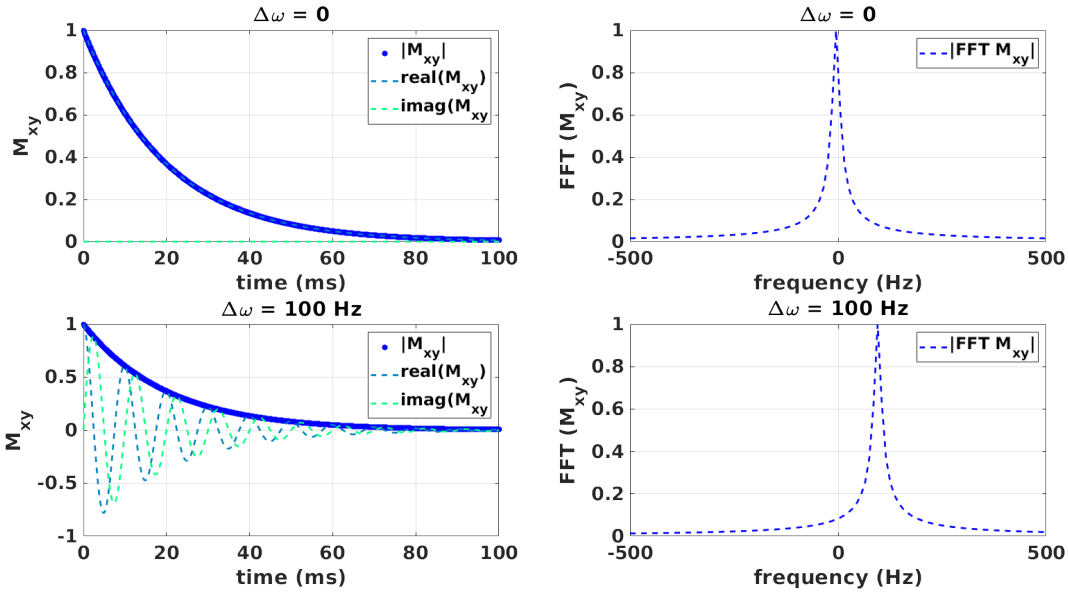

Figure 1.1: On resonance (top left), the signal is simply a mono-exponential decay with zero 'imaginary' component since the signal is in phase. After Fourier transforming, the result is a Lorentzian centered at 0 Hz. Off-resonance, the signals oscillate over time, and the imaginary component is non-zero (bottom left). After Fourier transforming, the Lorentzian is centered at the offset frequency, in this case 100 Hz.

Taking the real part of the decaying signal in equation 1.7, setting $\omega_{ref} = \omega_0$, and taking the inverse fourier transform yields a Lorentzian function. The Lorentzian has a FWHM or linewidth of

$$\lambda = \frac{1}{\pi T_2^*} \tag{1.10}$$

Thus an updated minimum linewidth is given for the MR experiment considering relaxation in the transverse plane, and non-ideal B_0 due to the sample and hardware. Further treatment of linewidth broadening effects in small voxels will be considered in chapter 3.

1.1.3 Spatial encoding

Up to this point, we have considered singular lines across frequency space corresponding to 1-D time signals. To encode signals originating across a heterogeneous sample, a magnetic field gradient is applied shifting the local Larmor frequency

$$\omega(x) = \gamma(B_0 + G(x)) \tag{1.11}$$

where G(x) is a 1D magnetic field gradient. Combining equation 1.11 and 1.7 the signal in the transverse plane for a small portion of spatially distributed frequencies may be written as

$$d\mathbf{M}_{xy}(G,t) = \mathbf{M}_0(x)e^{-t/T_2}e^{i\omega(x)t}dx \tag{1.12}$$

with further simplification

$$d\mathbf{M}_{xy}(G,t) = \mathbf{M}_0(x)e^{-t/T_2}e^{i(\gamma(B_0+G(x)))t}dx \tag{1.13}$$

Now just as was previously mentioned, since the signal is mixed with a reference frequency $\omega_{ref} = \omega_0$ the signal is either DC or only a few Hz off-resonance. This effectively nulls the γB_0 term in the exponent. Mathematically, this is intuitive as Euler's formula, $e^{i\omega}$ is cyclical in nature. Finally, integrating over the 1D space

$$\mathbf{M}_{xy}(t) = \int \mathbf{M}_0(x)e^{-t/T_2}e^{i\gamma G(x)t}dx \tag{1.14}$$

Now the equation bears a striking resemblance to equation 1.9. Mansfield made this more salient [14, 15] by introducing the k or reciprocal space vector

$$\mathbf{k} = \frac{\gamma}{2\pi}\int_0^t G\,dt \tag{1.15}$$

Often the gradient is held constant through time or modelled as a step function so that

k simplifies to $\gamma Gt/2\pi$. Now the magnetic field gradient, applied for specific time intervals and strengths, allows a stepping through the reciprocal k-space.

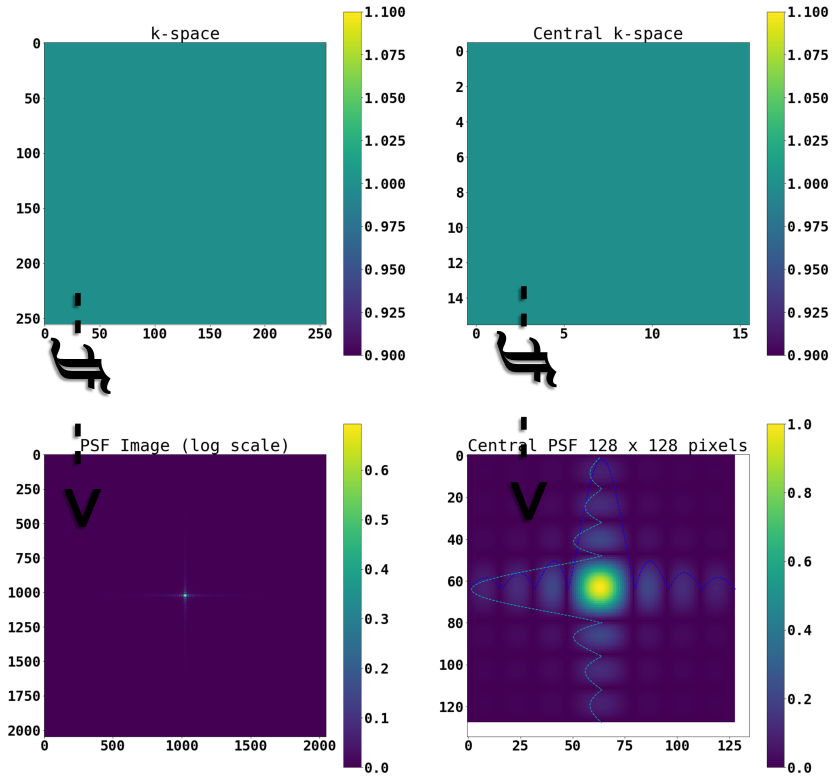

Figure 1.2: Neglecting spin density, a uniform cartesian k-space trajectory with unit amplitude is plotted across cartesian k_x and k_y (top). After Fourier transforming across both dimensions, the resulting spatial domain signal is the PSF in the spatial domain (bottom).

The 1D representation in equation 1.14 may easily be generalized for a 3D field gradient using vector notation **G(r)** where **r** is the spherical coordinate representation of cartesian (x,y,z). Following [16] and ignoring T_2^* relaxation for convenience, the **k**-space formalism may be written for 3D spatial encoding as

$$\mathbf{M}_{xy}(\mathbf{k}) = \iiint \mathbf{M}_0(\mathbf{r}) e^{i2\pi \mathbf{kr}} d\mathbf{r} \tag{1.16}$$

$$\mathbf{M}_0(\mathbf{r}) = \iiint \mathbf{M}_{xy}(\mathbf{k}) e^{-i2\pi \mathbf{kr}} d\mathbf{k} \tag{1.17}$$

where $\mathbf{M}_{xy}(\mathbf{k})$ represents the signal acquired by the RF coil at each **k**-space point, and

$\mathbf{M}_0(\mathbf{r})$ represents the spin-density of pixels across space. In the ideal case, $\mathbf{M}_{xy}(\mathbf{k})$ and $\mathbf{M}_0(\mathbf{r})$ are mutually conjugate. In practice, their mutual conjugacy is violated by the measurement itself, noise, imperfect gradient response, discretization of the Fourier transform, and other factors. For example, the number of **k**-space points acquired is finite due to limited gradient strength and acquisition times. This ultimately discretizes the Fourier transform. A simple demonstration of discrete **k**-space points is given in figure 1.2 (top) adapted from Hargreaves. The map consists of a grid of unit amplitude **k**-space points. After Fourier transforming the grid and taking its absolute value, an estimation of the sampling function's point-spread-function (PSF) is given in figure 1.2 (bottom). Discrete and finite sampling of the **k**-space points results in a non-zero linewidth across space. In an infinite sampling of **k**-space the width of the PSF would be infinitesimally small. This means that the features smaller than this width in image space ($\mathbf{M}_0(\mathbf{r})$) will not be observable. More discussion on the PSF criteria for resolvable features is discussed in section 2.3.2. The influence of diffusion and relaxation on the estimation of $\mathbf{M}_0(\mathbf{r})$ is further investigated with transfer function analysis in chapter 3. For further elaboration on encoding schemes not included in chapter 3 such as projection reconstruction see [17] and [16]. There are other means of encoding **k**-space besides using gradients [18, 19]. Chapter 3 compares conventional forms of spatial encoding with gradients mainly phase and frequency encoding which are arguably the most common methods of spatial encoding for MR imaging of humans and MRM.

1.2 RF coils

The dissertation pays special attention to RF coils, therefore a brief introduction to the types of RF coils used in the dissertation is justified.

1.2.1 Wavelength effects

There are many forms of RF coils from single [20] to multi-channel arrays [21, 22, 23]. Typically, MRM utilizes single channel systems. This is mainly because the relative size

of the wavelength is large in comparison to the sample. The RF wavelength (λ_{RF}) is given by the following equation

$$\lambda_{RF} = \frac{c}{f_0\sqrt{\varepsilon_r}} \tag{1.18}$$

where c is the speed of light in vacuum and ε_r the relative permittivity of the medium. ε_r decreases with the frequency and at 650 MHz, $\lambda_{RF}/4$ in brain tissue is 16 mm. Therefore assuming an adequately designed coil, the B_1 fields are homogeneous for MRM. This is not to say that multi-channel RF coils wouldn't be useful for MR microscopy in terms of accelerated acquisitions [24]. For human imaging the wavelength is comparable to the human head. Therefore special measures must be taken to homogenize the RF field (see appendix A). For microscopy, the field of view (FOV) rarely exceeds a few centimeters [25] therefore single channel systems are appropriate.

1.2.2 The principle of reciprocity

The most thorough treatment of relating the sample signal to the induced electro-motive force (EMF) in an MR RF coil would be Hoult's publications [26, 27, 28, 29]. Using Lorentz's principle of reciprocity, Hoult convincingly shows the physical basis for SNR in MR. The principle of reciprocity explains why the sensitivity of a loop or solenoid increases as the coil diameter shrinks (see figure 1.3). Referring to figure 1 in [30], the induced EMF from a magnetic dipole near the loop (A) is more than that of the same dipole farther away (B). Similarly, as a coil shrinks, the distance between it and the respective voxel decreases and the sensitivity goes up. This speaks nothing of the noise originating in the system which is more thoroughly considered later in ch. 4.

It has been reported that when the skin depth is comparable to the coil wire diameter, SNR begins to trend with $d^{-1/2}$ [31]. The noise originating from the sample depends on the frequency and size of the coil [25]. For a solenoid resonating at 650 MHz noise from the coil hardware dominates the noise from the sample. This is demonstrated in figure 1.4,

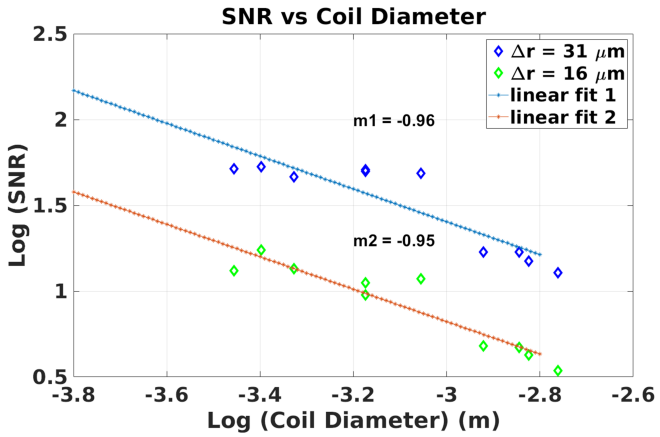

Figure 1.3: A log-log plot demonstrating increased sensitivity of shrinking coil sizes. It is well-known that SNR is inversely proportional to the coil diameter. This relationship was verified by varying the diameters of solenoids and imaging a $CuSO_4$ phantom at 650 MHz. The plots are two different measurements at varying resolution.

where a changing sample diameter has no effect on the SNR of the images. There are other noise sources in MR, for a complete list see [32]. Further treatment of the topic occurs in chapter 4.

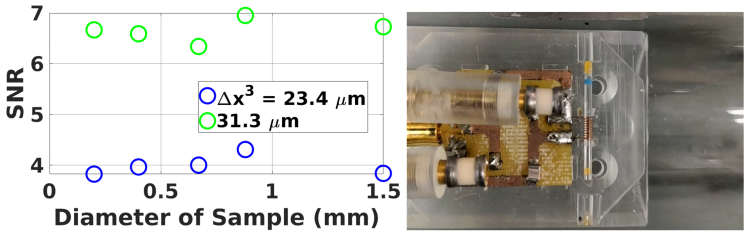

Figure 1.4: For a microcoil 1.5 mm in diameter resonating at 650 MHz, most of the noise originates from the circuit. To verify this, capillaries of varying diameter were placed within the same coil to determine if SNR would be influenced by changes in the sample volume.

1.2.3 Solenoids

The solenoid is perhaps the most intuitive form of an RF coil. Using Ampere's law (who coined the term 'solenoid') and the right hand rule, the magnetic field may be visualized as near uniform in the center of the geometry. A solenoid is also self-resonant as its inter-turn capacitance is non-negligible when the spacing between turns is small [33] creating an

equivalent parallel LC circuit. One drawback of a solenoid wound tightly around a sample are susceptibility differences between the air (or whatever medium), conductor, sample, and if applicable sample holder. Artefacts emerge from large susceptibility differences in the form of B_0 inhomogenieties [16]. The sample's average magnetic field B_0^s is offset by the diamagnetic susceptibility of the material and can be written as

$$B_0^s = (1 + \chi_m)B_0 \tag{1.19}$$

where χ_m is the diamagnetic susceptibility of the medium. Maxwell's equations require the field lines to be continuous on the boundaries of materials therefore the B_0 is offset near the edges of materials. An example of these artefacts can be seen in figure 1.5. The silver solenoid has a larger χ_m therefore the artefacts are more pronounced [34]. Methods of mitigating this include decreasing $\Delta\chi$ between the conductor and the medium[35].

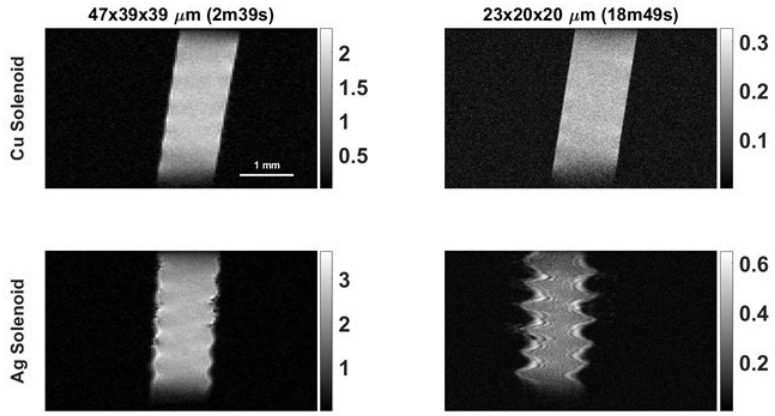

Figure 1.5: Images of a capillary filled with $CuSO_4$ are shown for varying resolutions. The Ag solenoid has a noticeable increase in SNR however the susceptibility artefacts on the edge of the capillary are more pronounced with increasing resolution as the bandwidth per pixel decreases.

1.2.4 Surface loops

The surface loop is a singular or multi-turn loop fixed in a relatively thin 2D plane. There are many forms of surface loops in MR including microstrip [36] and self-resonant designs

[37, 38]. The advantage of the surface loop lies in its simplicity. With fewer turns, resistance of the conductor is minimized in comparison to many turn solenoids. The field originating from a surface loop can also be tailored to the sample by increasing or decreasing the power. The general rule of thumb is to place the surface loop a distance $d/2$ away from the sample for optimized homogeniety. The well-known formula giving the RF B_1 field strength at a depth z within a sphere [39] is given by

$$B_1 = \frac{\mu_0 \, d^2 \, I_c}{2(d^2 + z^2)^{3/2}} \tag{1.20}$$

where μ_0 is the permeability of free space, I_c the current through the loop, and z the depth into the sample. Full wave finite difference time domain simulations were used to validate equation 1.20 at 650 MHz (see figures 1.6 and 1.7). The decreased sensitivity further from the loop, as predicted by the principle of reciprocity is the main disadvantage of the surface loop. This tends to limit the imaging FOV to regions near the coil.

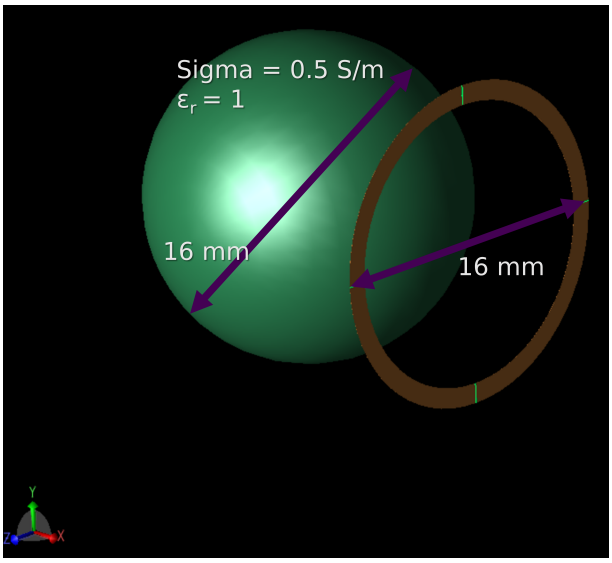

Figure 1.6: A 16 mm surface loop resonating at 650 MHz was simulated with full-wave finite difference time domain (FDTD) method software to validate surface loop equations usually applied to much lower frequencies.

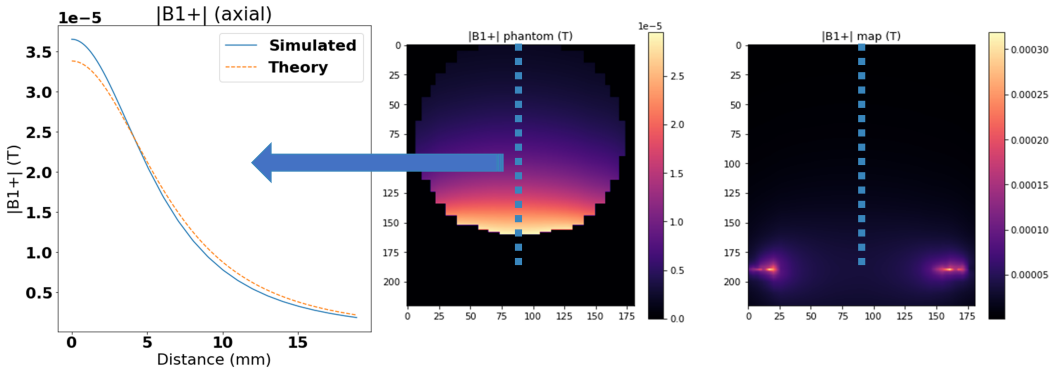

Figure 1.7: Equation 1.20 was validated for a 16 mm diameter surface loop resonating at 650 MHz near a spherical sample with $\sigma = 0.5\ S/m$ and $\varepsilon_r = 1$.

CHAPTER 2

Introduction to magnetic resonance microscopy

2.1 Background

In the earliest publications of MR imaging, Nobel laureate Sir Peter Mansfield, mentions the discrete nature of spins distributed across molecules and MR's potential ability to achieve "microscopy in ... cell membranes and filamentary or fibrous structures" [14, 15]. His prophecy was fulfilled, and today MRM is an ideal modality for imaging biophysical systems for a few reasons; 1) samples may remain intact or living allowing for normal processes and functions during dynamic imaging and 2) MRM provides a rich resource of contrast mechanisms sensitive to molecules and structure including but not limited to chemical shift, spin relaxation, quantitative magnetization transfer, and diffusion [16]. The disadvantage of MRM is the intrinsic loss of signal as the resolution is increased [40]. Since 1973, advancements in the field of MRI have overcome significant signal deficits in human imaging with increased field strength, improved hardware, parallel transmission, hyperpolarization, deep learning, and advanced reconstruction. Many of these improvements have yet to be applied to MRM. Hedges, a student of Lauterbur, imaged snails at 35 μm in-plane only publishing his results in his dissertation in 1984 [41]. Single cell image was reported by Aguayo, Blackband, and coworkers in 1986 [42]. Around the same time, while much research was focused on 'scaling-up' Nuclear Magnetic Resonance (NMR) for human imaging, Eccles and Callaghan were some of the first to image plant stems in a small solenoid to achieve in-plane resolution of 25 μm at 1.5T with 200 G/cm gradients [43]. Later in 1991, Callaghan would author the seminal work *Principles of Nuclear Magnetic Resonance Microscopy* [44]. Other notable and thorough consideration of μm level imaging by Cho and coworkers stressed implications of diffusion on total signal and questioned the theoretical limits of MRM for cell imaging [45]. It was also noted early on

that resolution is limited by line broadening due to the susceptibility differences at interfaces of the cell [46]. Discussion surrounding the degradation of resolution from diffusion and line broadening effects was discussed utilizing transfer function analysis [47]. Fulfilling his own prophecy 20 years later in 1994, Mansfield and coworkers used a microscope slide and inductively coupled surface coil to image onion cells at 5 μm in-plane resolution [48]. In 1995, Blackband, Mansfield, and coworkers collaborated and differentiated cell nucleus from cytoplasm in neurons of adult sea hares *Aplysia californica* and mentioned the implications of the variation of relaxation times in intra- and extra-cellular spaces [49].

With respect to hardware, microcoils have been widely used for small samples as $SNR \propto d^{-1}$ [50] with the most common being the micro solenoid. Minard and Wind developed a thorough process of optimizing solenoid microcoil dimensions, homogeneity, and winding parameters given sample properties and desired pulse sequence (gradient or spin echo) [1, 2]. Although solenoids are most common due to their ease of production, other coils have been developed and used for specific applications [51, 52].

Coil noise is caused by random thermal fluctuations in the conductor so low temperature circuits offer higher SNR. Hoult and Richards were the first to point out the possibility of super cooling the RF electronics for decreased noise from the circuit [30]. It was not until the late 80s that cryogenic technology translated to medical MRI [53] and high resolution spectroscopic NMR [54]. The main obstacle in cryogenic RF electronics is insulating the sample from the extreme temperatures while maintaining an adequate geometric fill factor [55, 56, 57]. Another similar but less common method of limiting the RF coil's contribution to the noise is to use high temperature superconductor (HTS) materials [58]. However, HTS materials are expensive, sensitive to conductive samples, and not well-characterized with respect to their non-linear electrical responses to varying magnetic fields [59].

The highest nominal resolution obtained on phantoms composed of glass microspheres is around 2.8 μm and utilized a field strength of 9.4T, 150 μm super cooled solenoid and a 72 hour acquisition time [60]. A 3 μm isotropic resolution acquisition of glass fibers

was accomplished in 58 hours using a planar micro coil of 20 μm operating at 18.8T [61]. Polymer beads were imaged at a resolution of 3.7 x 3.3 x 3.3 μm^3 in 30 hours with a 70 μm solenoid operating at 9T [62]. Recent work at 22.3T resolved plant root cells at an isotropic resolution of 7 μm^3 with a 1.5 mm solenoid in 34 hours [63]. Myofibers and myonuclei were resolved at 6 μm^3 isotropic with commercially available 200 μm and 500 μm micro planar coils in 30 hours [64]. It is clear MRM possesses the means to achieve structural and functional images of biophysical systems at resolutions < 10 μm.

2.2 Objectives

Magnetization dephasing, and thus attenuated SNR, occurs when spins diffuse within a magnetic field gradient. The line broadening effects of diffusion can be understood as a convolution in the spatial domain of the gradient dependent diffusive attenuation envelope with the signal spectrum. Careful experimental demonstration of diffusion's effects of line broadening and signal attenuation at resolutions below 10 μm will quantify what conditions readout gradients should be replaced by 3D phase encoded sequences. To minimize hardware noise, cryogenically cooled electronics will enhance SNR. Experimental demonstration of coil and sample noise in the predicted coil noise dominated regime ($d < 1$ cm at 650 MHz) will quantify the limits to SNR improvement with hardware and sample preparation. With optimized acquisitions and hardware, excised tissue will be imaged below 10 μm isotropic resolution with MRM.

2.3 Relevant background: limitations of imaging with MRM

A brief introduction to the previous work outlining the primary hindrances to achieving MRM.

2.3.1 Time considerations

Most MRM images acquired with voxel lengths < 10 μm take tens of hours to achieve acceptable SNR [63, 64]. This can be understood with the following equation formulated

by Mansfield and Morris [65], where the scan time needed for a finite volume (Δx^3) is

$$t_{vol} = (SNR)^2 d^2 \frac{T_1}{T_2} \frac{2.8 \times 10^{-15}}{f_0^{7/2}} \left(\frac{1}{\Delta x} \right)^6 \tag{2.1}$$

where SNR describes the intrinsic signal-to-noise ratio contributions from the spin density of the sample, hardware sensitivity and noise, f_0 is the Larmor frequency, and Δx is the dimension of the voxel where Δx^3 is the volume of the signal origin. Equation 2.1, plotted in figure 2.1, demonstrates the severe time requirements below 5 μm of isotropic resolution with $T_1/T_2 = 6$. Smaller coil radii defer the drastic increase in time requirements for increased resolution at fixed SNR. Equation 2.1 does not include the line broadening effects of molecular diffusion.

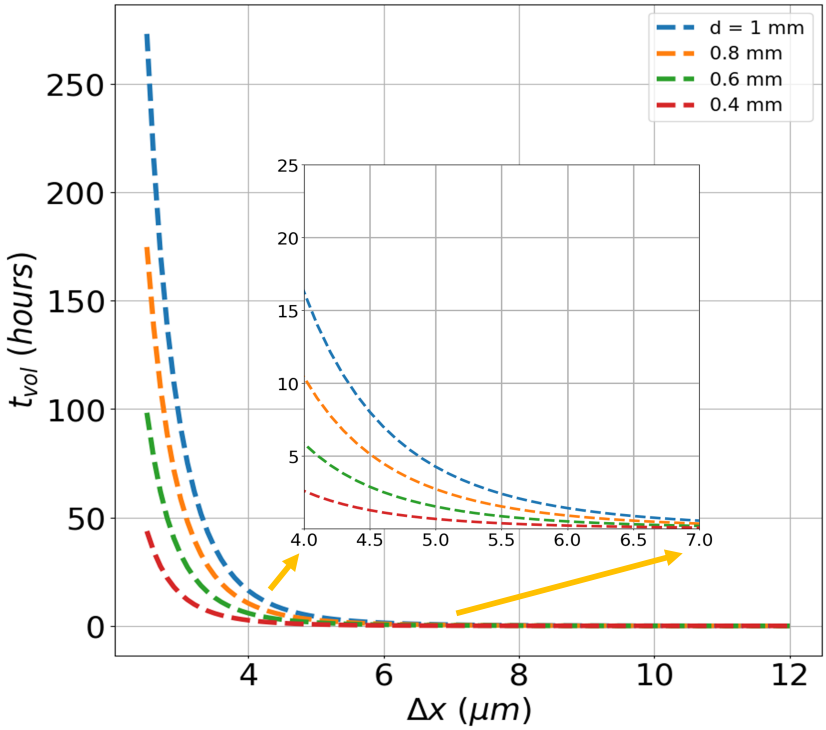

Figure 2.1: With $T_1/T_2 = 6$, SNR = 10, and a $f_0 = 650\,MHz$, the time requirements for a 3D isotropic resolution beyond 3 μm quickly approach hundreds of hours. By using smaller coils, sensitivity increases and the wall of drastic time requirements is deferred. The model assumes ideal scanning conditions and does not include signal loss due to diffusion.

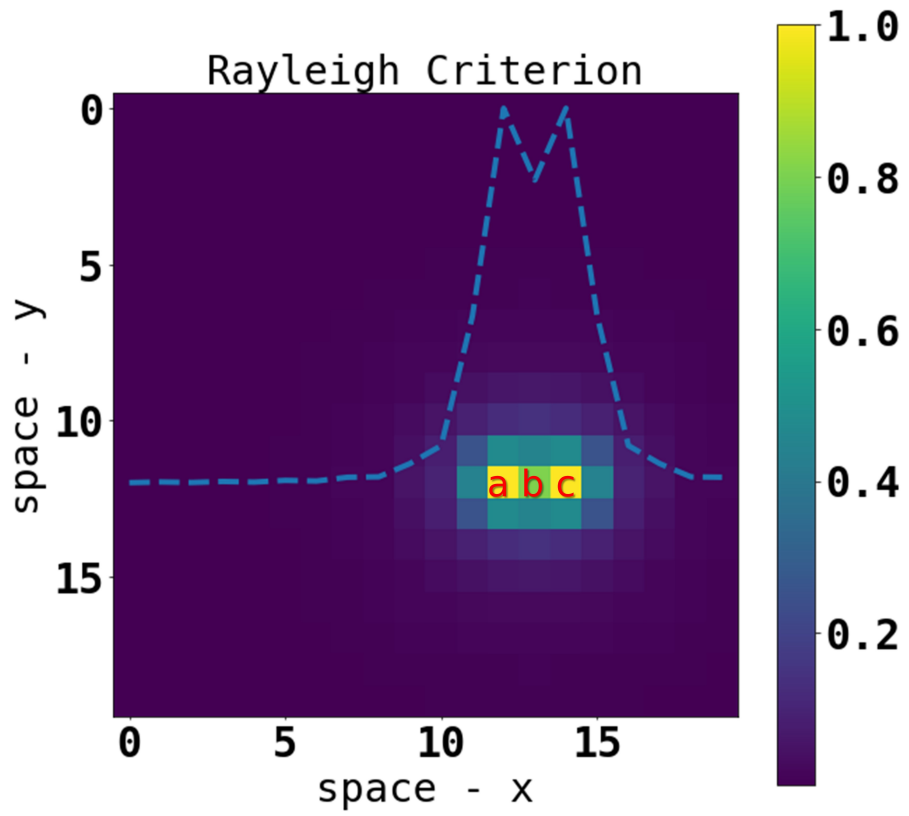

Figure 2.2: Two normalized pixels a and c are considered minimally resolved when the contrast ratio between them is 0.81. The image shown is the point spread function of a filtered MR experiment convoluted with two delta functions with centers 2 pixels apart. To achieve the Rayleigh criterion, the point spread function, determined by parameters of the acquisition and the filtering method, must be optimized.

2.3.2 Resolution considerations

Nominal resolution in MRM is simply the FOV divided by the number of frequency or phase encoded steps in the respected dimension. Achieved resolution depends on a number of factors including the T_2 and T_2^* of the sample, SNR, and more (see equation 2.2). To further help visualize what is meant by resolution and resolvable detail, figure 2.2 shows two pixels, a and c, whose centers are 2 pixels apart. Pixel a and c are considered resolved when they meet the Rayleigh criterion. Named after Lord Rayleigh himself [66], the Rayleigh criterion states that the contrast ratio (b/a) between the two pixels must be 0.81. Following the work of Callaghan [16, 67], achieved spatial resolution at the Rayleigh criterion, with an optimal receiver bandwidth determined by T_2, and for a 2D Fourier transformed image is

$$\Delta x_{opt} = 16 d^{1/2} F^{1/4} \sigma^{1/4} SNR^{1/2} \Delta z^{-1/2} f_0^{-7/8} N_{acc}^{-1/4} N_x^{-1/4} T_2^{-1/4} d^{1/2} \tag{2.2}$$

where F is the spectrometer noise factor, σ is the coil skin effect factor, Δz is the slice thickness, N_{acc} is the number of accumulated scans, and N_x is the number of encoding points. Equation 2.2 does not account for further broadening of the true resolution due to the signal attenuation of diffusion (see figure 2.3).

2.3.3 SNR considerations

There are many models for SNR especially considering the many different types of resonating coil geometries. Starting with the hardware and sample, Hoult and Richards derivation [30] based on the principle of reciprocity for a solenoid is

$$SNR_{solenoid} = \frac{\mu_0 V_s N_{spins} \gamma \hbar^2 I(I+1)}{12.32 k_b T_s d} \frac{1}{F k_b T_c \zeta \Delta f}^{1/2} \frac{\omega_0^{7/4}}{[\mu \mu_0 \rho(T_c)]^{1/4}} \tag{2.3}$$

where μ_0 is the permeability of free space, V_s is the volume of the sample, N_{spins} the number of spins per unit volume, γ is the gyromagnetic ratio, $\hbar$ is Planck's constant over

2π, I is the angular momentum quantum number (1/2 for hydrogen in the 'spin-up' state), k_b is Boltzmann's constant, T_s is the temperature of the sample, d is the diameter of the coil, T_c is the temperature of the coil, ζ is a corrective term for the "proximity effect", Δf is the receiver bandwidth, ω_0 is the Larmor frequency in radians, μ is the permeability of the wire, and $\rho(T_c)$ is the temperature dependent resistivity of the coil. It is important to note that the temperature of the coil affects the noise in the experiment in the resistivity term, total coil resistance, and temperature. The sample characteristics are important when resistance is not dominated by the coil, especially considering the volume, temperature of the sample, and B_1 homogeneity when the Biot-Savart approximation does not hold.

2.3.4 Tradeoffs between time, resolution, signal, and diffusion

The SNR of a 3D sequence with 1 frequency and 2 phase encoding gradients can be written as

$$SNR_{3Dseq} = \alpha_{seq} A(D, G, T_{read}) SNR_{solenoid} \Delta x \Delta y \Delta z \sqrt{N_{acc} N_y N_z T_{read}} \tag{2.4}$$

where α_{seq} is the SNR factor due to the sequence choice (gradient vs spin echo), A is the attenuation due to diffusion (see ch. 3), $\Delta x,\ \Delta y,\ \Delta z$ are the voxel sizes in each respected dimension, $N_y,\ N_z$ are the number of samples in each dimension, and T_{read} is the length of the read gradient acquisition ($T_{read} = N_x/\Delta f$). The trade-offs between resolution, signal, and time determine the ultimate outcome of an imaging experiment. An experimental setup may lack the signal at a given resolution and time constraint, however signal may be reclaimed by shrinking the coil albeit by minimizing the FOV (see equation 2.3).

Although several seminal works have detailed the limiting factors of achieving μm-level resolution [16, 50, 45, 68, 69], experimental demonstration of these limitations is sparse [62, 70]. Often MRM images tend to be taken with pulse sequences fast low angle shot (FLASH) and Fast Spin Echo (FSE) due to their resilience towards susceptibility artifacts and ease of acquisition and reconstruction. Certain work boasts nominal resolutions

below 5 μm but say nothing of the sample's intrinsic diffusion which may extend the true resolution beyond the nominal resolution. To demonstrate this, Andrew Webb's work [71] is referred to and the expected diffusion attenuation of a few apparent diffusion coefficient (ADC) values in the spatial domain are plotted in figure 2.3A.

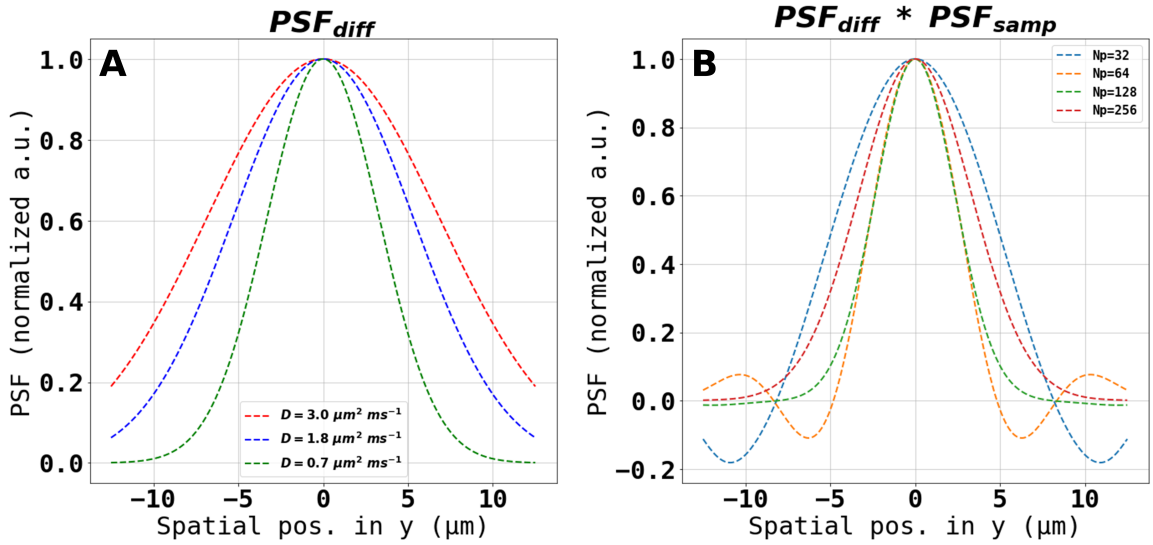

Figure 2.3: PSF_{diff} represents the PSF of diffusion contributions. $PSF_{diff} * PSF_{samp}$ represents the convolution of the discrete sampling function's PSF with the diffusion contributions. By increasing the apparent diffusion coefficient (A) the full-width at half max (FWHM) or the point spread function of the attenuation curve broadens. Furthermore, convolution of the sampling and diffusion point spread function (B) shows the importance of choosing the optimal number of sampling points in phase encoded directions. In this case, the optimal number of sampling points is between 64 and 128 sampling points.

The achieved resolution of an experiment can also be described with the full width at half max (FWHM) of the point spread function of the experiment. In figure 2.3A, as the apparent diffusion coefficient is increased, the FWHM of the point spread function increases. Figure 2.3B demonstrates the sampling function convoluted with the diffusion attenuation to give the total point spread function. The diffusion of the sample (fixed at 1.8 $\mu m^2\ ms^{-1}$ in fig. 2.3B) along with the number of samples influences the final FWHM and thus resolution. In this way, resolution degradation due to diffusion can be understood simply as a convolution of the sampling function with the diffusive time envelope. This line broadening due to diffusion has not been quantified experimentally and thus is a goal

of aim 1.

2.4 Aim 1: Quantify the limits of resolution and SNR due to diffusion attenuation

As resolution increases, diffusion's limiting effects on signal and resolution become more important since the size of the voxel is close to the root mean square displacement of the molecule. To better understand this we refer to Callaghan's work [16, 72]. T_2 optimal resolution can be derived (see eq. 2.2) and diffusion can be included to theoretically determine the final limiting resolution of an experiment (see fig. 2.4). According to Callaghan the final optimal resolution of a frequency encoded sequence is

$$\Delta x = 1.34[\Delta x_{diff} \Delta x^2_{T_2,\ opt}]^{1/3} \tag{2.5}$$

where Δx_{diff} is the 1D root mean square distance diffused in time t by a molecule undergoing Brownian motion with a self-diffusion coefficient D ($\Delta x_{diff} = (2Dt)^{1/2}$).

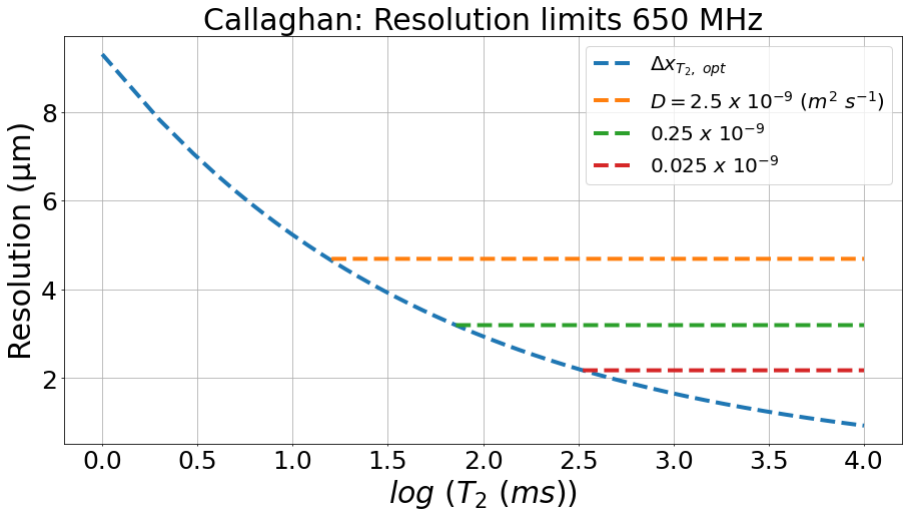

Figure 2.4: Adapted from Paul Callaghan's Principles of NMR Microscopy and modified for 650 MHz. The horizontal lines represent the Δx in equation 2.5. $\Delta x_{diff} \propto T_2^{1/2}$ and $\Delta x_{T_2,\ opt} \propto T_2^{-1/4}$ meaning the limiting attainable resolution is not a function of T_2. The orange ADC line ($D = 2.5\ x\ 10^{-9}\ m^2\ s^{-1}$) represents diffusion of free water.

It has also been proposed that the signal attenuation due to diffusion may be circumvented by pure phase encoding [71]. Without a readout gradient, the receiver bandwidth

may be minimized which would otherwise contribute to spatial broadening. However, phase encoding in the 3rd dimension, say z, results in a acquisition that is N_z times longer than the frequency encoding alternative. Although this may prevent signal loss from diffusion, it is possible that using the increased time for signal averaging of the frequency encoding variant would compensate for the loss of signal. Thus, it is not well understood when 3D phase encoding is required or outright more advantageous when high resolution is the main objective.

Goals of aim 1 include the following. Validate the predictions of diffusive signal attenuation and resolution degradation at high resolution. Measure the achieved resolution with imaging techniques. Measure diffusion signal attenuation in the midst of a readout gradient. Determine the experimental conditions which warrant use of pure phase encoding over frequency encoding. Demonstrate appreciable advantages of phase encoding over frequency encoding in the form of achieved resolution or imaging time efficiency.

2.5 Aim 2: Enhance SNR via a cryogenic tune and match circuit

Aim 2 will predict and experimentally demonstrate *SNR* enhancement due to cooling of the RF circuitry.

Most high resolution MRM imaging is performed with either micro solenoids [63] (see figure 2.5) or planar microstrip coils [64]. It has been reported for a copper surface loop of room temperature and operating at 650 MHz the resistance of the coil begins to dominate at diameters less than 1 cm [32]. For example, images using a cryogenic surface loop ($d \approx 2\ cm$) manufactured by Bruker (Billerica, MA) are plotted in figure 2.6. As the sample decreases in size, the quality factor of the resonance increases and the noise of the images decreases. This indicates the noise of the sample is non-negligible.

For very small samples, the dominant source of noise is the RF circuitry itself (see fig. 1.4). With the disadvantage of a decreased FOV, SNR can be reclaimed by shrinking the coil diameter. A 1.5 mm diameter solenoid outperformed the Bruker cryoprobe improving

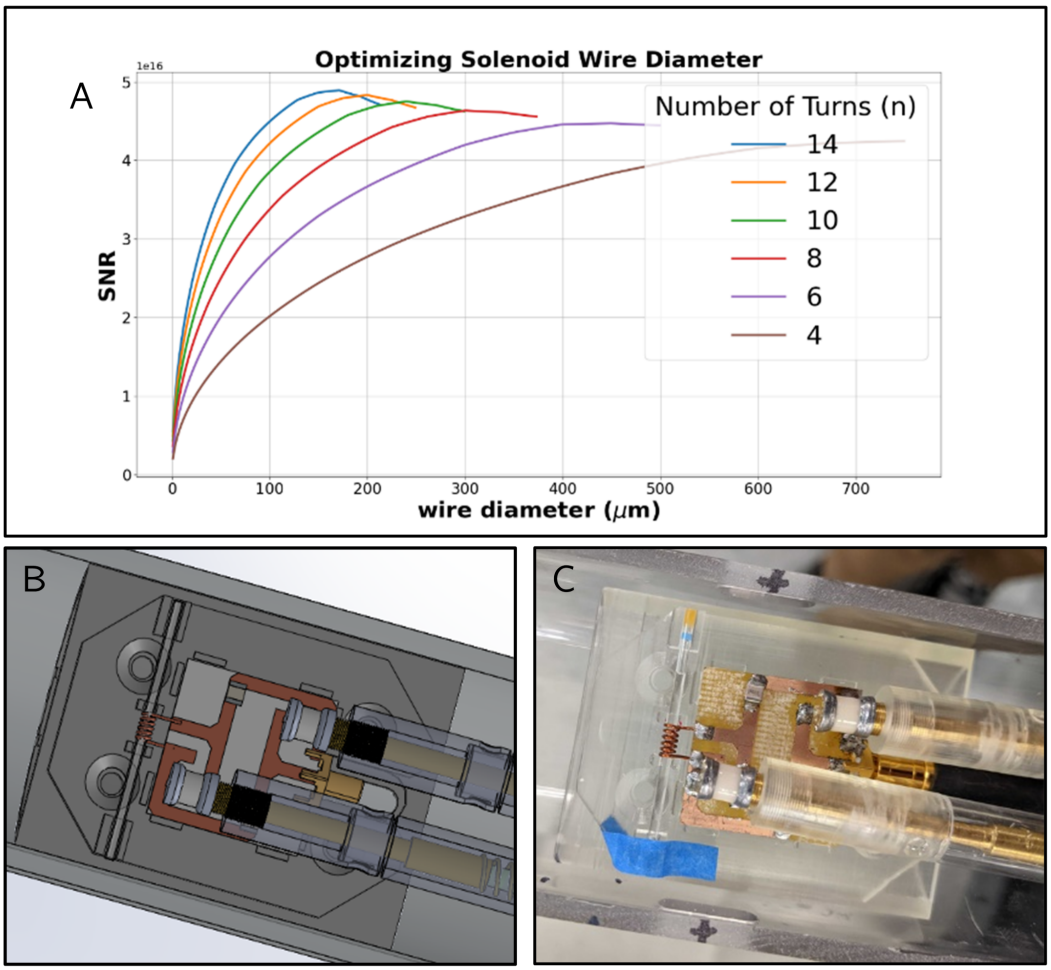

Figure 2.5: Micro solenoid winding parameters including wire diameter (A) were optimized considering the transmit field homogeneity, sample size, and resistance of the circuit [1, 2]. A stage for optimal placement of the sample and solenoid in the isocenter of the 15.2T magnet was designed (B and C). A simple circuit design was chosen to minimize resistance and common mode currents on the shield of the coaxial cable. A floating cable trap was also used to minimize any remaining common mode currents and ease the tune and match process.

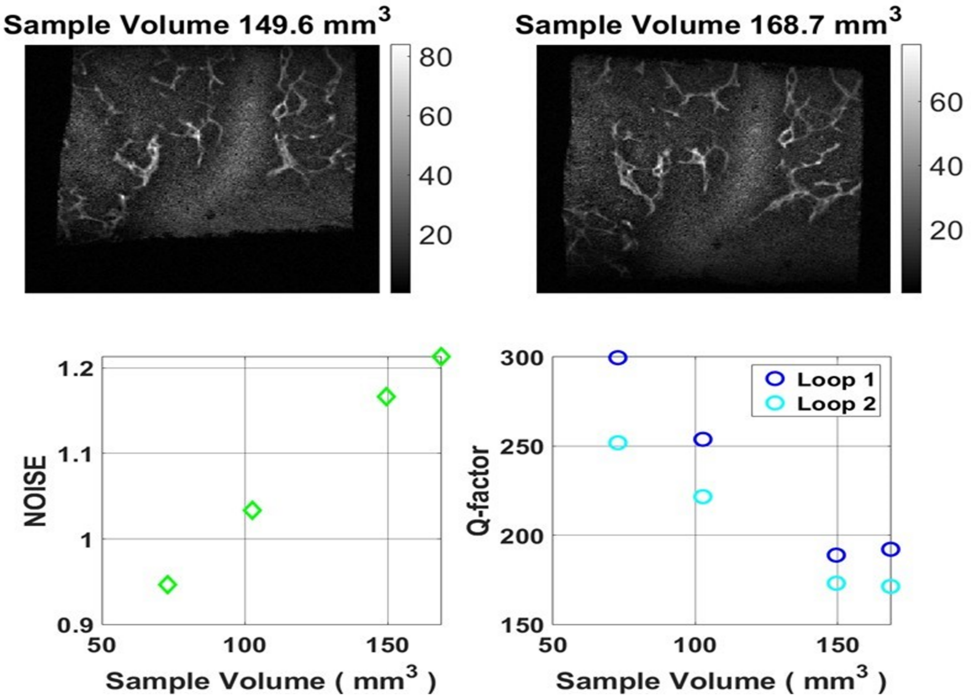

Figure 2.6: As more potato is removed, the Q-factor of the probe increases and the noise in the image decreases. This demonstrates that the noise contributions from the sample are significant for the cryogenically cooled cryoprobe.

SNR by a factor of 4 (see fig. 2.7).

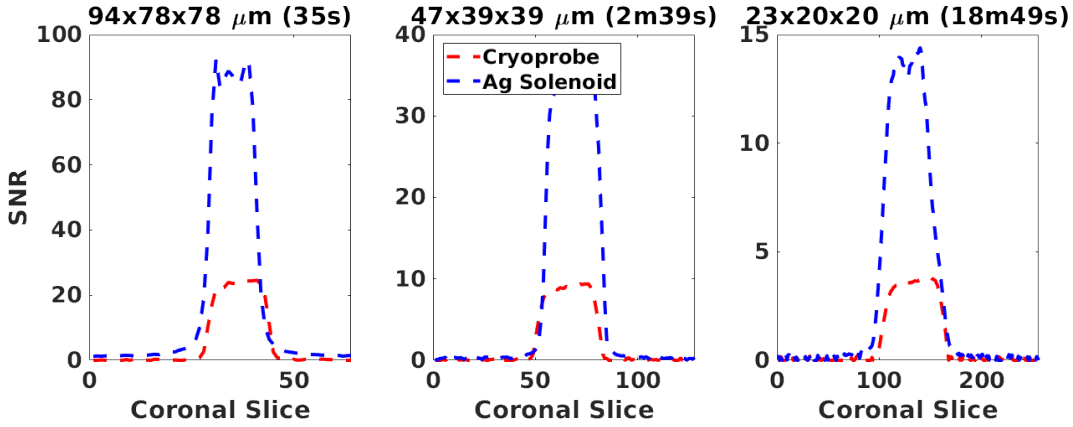

Figure 2.7: Images of a 6 mM/L CuSO4 solution within a 1.5 mm (outer diameter) capillary tube were taken for SNR comparisons between a silver wire solenoid and the cryoprobe. The solenoid had 6 mm length, 1.5 mm inner diameter, 0.4 mm wire diameter, and 6 turns. It has been well documented that $SNR \propto d^{-1}$, where d is the diameter of the coil. That is until the diameter of the wire is on the order of the skin depth for the given frequency. The increase in SNR from decreased coil diameter in the silver solenoid is ≈ 3.8 and near the expected value of 4.

The goals of aim 2 include the following: Enhance SNR via cooling of the tune and match circuitry. Show the sample noise is negligible for microcoils of < 1 cm. Finally, build a cryochamber for imaging at 15.2T with the RF circuitry at liquid nitrogen temperatures with the RF coil in ambient air and the sample above freezing.

2.6 Aim 3: Apply optimized acquisitions and hardware on excised tissue

The final aim of the dissertation involves combining all of the techniques presented for very high resolution structural and parametric imaging. An example deep tissue image of an excised mouse brain can be seen in figure 2.8.

Further applications of aim 3 include: 6 μm in-plane resolution images of green-onion roots. 100 μm^3 isotropic resolution diffusion tensor imaging of excised mouse cervix. Finally, 93 μm^3 isotropic resolution $R_{1\rho}$ dispersion curves were acquired to quantify fibrosis in the kidney.

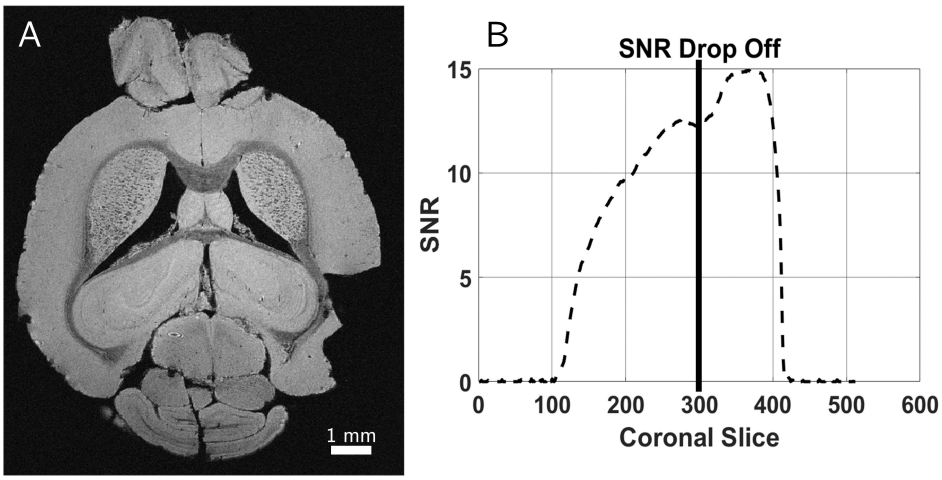

Figure 2.8: The 3D fast low-angle shot (FLASH) sequence parameters were optimized over an excised mouse brain (A). Using a cryogenically cooled quadrature-driven surface coil (Bruker, cryoprobe) a peak SNR of $\approx$ 15 (B) within 4.4 hours was achieved. The resolution was 20 x 19.5 x 19.5 μm^3. The scan was performed with parameters TE/TR = 12/30 ms, 15x10x10 mm field of view (FOV), 50 kHz receiver bandwidth, excitation flip angle of 25 degree, and averaged over 2 experiments. The SNR from the surface coil drops off as the sample is further from the transmit element (B). Given these results, the cryoprobe would achieve 10 μm isotropic resolution with a peak SNR of 5 in around 17.2 hours with a similar sample.

CHAPTER 3

Experimental demonstration of diffusion limitations on resolution and SNR in magnetic resonance microscopy

3.1 Abstract

MR microscopy is in principle capable of producing images at cellular resolution (< 10 μm), but various factors limit the quality achieved in practice. A recognized limit on the signal to noise ratio and spatial resolution is the dephasing of transverse magnetization caused by diffusion of spins in strong gradients. Such effects may be reduced by using phase encoding instead of frequency encoding read-out gradients. However, experimental demonstration of the quantitative benefits of phase encoding are lacking, and the exact conditions in which it is preferred are not clearly established. We quantify the conditions where phase encoding outperforms a readout gradient with emphasis on the detrimental effects of diffusion on SNR and resolution. A 15.2T Bruker MRI scanner, with 1 T/m gradients, and micro solenoid RF coils < 1 mm in diameter, were used to quantify diffusion effects on resolution and signal to noise ratio of frequency and phase encoded acquisitions. Frequency and phase encoding's spatial resolution and SNR per square root time were calculated and measured for images at the diffusion limited resolution. The point spread function was calculated and measured for phase and frequency encoding using additional constant time phase gradients with voxels 3-15 μm in dimension. The effect of diffusion during the readout gradient on SNR was experimentally demonstrated. The achieved resolutions of frequency and phase encoded acquisitions were measured via the point-spread-function and shown to be lower than the nominal resolution. SNR per square root time and actual resolution were calculated for a wide range of maximum gradient amplitudes, diffusion coefficients, and relaxation properties. The results provide a practical guide on how to choose between phase encoding and a conventional readout. Images of excised rat spinal cord at

10 μm x 10 μm in-plane resolution demonstrate phase encoding's benefits in the form of higher measured resolution and higher SNR than the same image acquired with a conventional readout. We provide guidelines to determine the extent to which phase encoding outperforms frequency encoding in SNR and resolution given a wide range of voxel sizes, sample, and hardware properties.

3.2 Background

The prospect of obtaining structural information at microscopic scale was mentioned in Lauterbur's revelation of the principle of MRI when he wrote "Zeugmatographic techniques should find many useful applications in studies of the internal structures, states, and compositions of microscopic objects" [73]. Mansfield and Grannell also stated that microscopic imaging of biophysical samples with magnetic resonance was possible [14]. Early studies by Hedges [41] identified the potential value and some challenges of MR microscopy. Ubiquitous in human and preclinical imaging, MRI provides deep 3D structural and functional tissue information with mm-scale resolution. MR images with voxel dimensions less than $\sim$100 μm are typically referred to as magnetic resonance microscopy (MRM). MRM offers the many forms of contrast intrinsic to MR and may resolve cells without compromising cell viability [74, 64, 75, 76]. In comparison, the poor penetration of light limits optical fluorescence microscopy to surface-level imaging and histology destroys the integrity of samples during processing. Thus, MRM is a prime candidate for in vivo, deep tissue imaging of intact cell systems.

With increased field strengths, strong gradients, cryogenically cooled RF coil arrays, and intelligent acquisition, reconstruction and post-processing, the practical limits of attainable resolution of MR acquisitions will continue to be challenged. Hedges acquired images on aquatic specimens with voxel volumes $\approx$ 0.15 nL with 35 μm in plane resolution [41], while Aguayo et al. imaged toad ova with 16 x 27 μm in-plane resolution in a 4 min acquisition at 9.5T [42]. Since then, the highest isotropic resolution claimed

with MRM is 2.7 μm with constant-time 3D phase encoded gradients, 9.4T field, 100 μm diameter microcoil, and a frozen 1:1 water glycerin paramagnetically doped sample in 52 hours [60]. Other notably high-resolution images include outlines of polymer beads with 3.7 x 3.3 x 3.3 μm resolution images at 9T, acquired with 3D phase encoded gradient amplitudes up to 6 T/m in $\approx$ 30 hours [62]. High resolution images are often achieved with small phantoms ($<$ 1 mm) or excised tissues as it allows for smaller FOVs, smaller higher sensitivity coils, temperature control of the sample, fixed positioning, and immersion of samples in signal enhancing solutions such as gadolinium.

Although phase encoding (PE) is claimed to be a superior acquisition scheme for MRM in terms of achievable resolution [71, 47, 77, 78, 79, 50], not all acquisitions beyond 10 μm in the literature have used this approach. Most images of biological samples have been acquired with either Fast Low Angle Shot (FLASH) or Rapid Acquisition with Refocused Echoes (RARE) sequences with conventional frequency encoding (FE) in 1 dimension. For example, mammalian neurons were imaged with a 200 μm surface coil, 3 T/m gradients, 14.1T, at 4.7 μm isotropic resolution with a FLASH sequence in $\approx$ 22 hours [75]. Single mammalian myofibers at 6 μm isotropic resolution, were imaged with FLASH and spin echo (SE) acquisitions with up to 25 T/m gradients, at 14.1T field strength, with a 200 μm surface coil in $\approx$ 30 hours [64]. More recently, plant root nodules were resolved with a 1.5 mm solenoid at 7 μm isotropic resolution, 22.3T, and up to 2.88 T/m gradients in $\approx$ 30 hours [63].

The intrinsic signal and resolution limits of MR have been extensively discussed and modeled previously [3,16,18–22] [41, 48, 26, 80, 17, 81, 82]. One of the primary limiting factors of MRM signal and resolution is diffusion. Callaghan and Eccles were two of the earliest to quantify the limits of MRM signal, resolution, and diffusion effects [72, 67, 83, 43, 84, 45, 70, 69]. Diffusion during the readout gradient was shown to broaden the linewidth and attenuate signal. McFarland quantified sampling, diffusion, and T_2 contributions to the measured resolution of phase and frequency encoding via the point-

spreadfunction (PSF) [47].

The discussion surrounding diffusive broadening led to the proposition of using PE in each dimension for MRM. Gravina et al [78] and Choi et al [77] demonstrated the theoretical advantage of constant time imaging's (3D PE but with 1 sample per repetition) use for imaging solids and its advantages over conventional readout acquisitions in terms of signal and resolution. Elaborating on PE's advantages, Webb simulated optimal phase encoding steps for varying gradient strengths and sample diffusion properties to provide recommendations for improved PE resolution [71]. Although Gravina and Cory discuss achievable resolution given diffusive broadening, they ignore diffusive attenuation in their SNR comparison. Choi and coworkers compare the calculated PSF of phase and readout encoded experiments. They mention there is a threshold where PE begins to outperform frequency encoding in terms of time requirements for constant SNR and resolution. However, they do not clarify the experimental conditions in which PE has narrower resolution or is more SNR efficient. Thus, the goal of this report is to demonstrate the conditions in which diffusion attenuates signal and degrades resolution in a conventional readout. We aim to provide guidelines to determine when PE outperforms readout-based acquisitions like FLASH or RARE. FLASH is chosen as the exemplar readout-based frequency encoded (FE) acquisition for comparison, although the results may be generalized for other readout acquisitions. The SNR per square root time and resolution of PE are compared to that of FE, given a wide range of maximum gradient strengths, relaxation, and diffusion properties of the sample. We measured the PSF for phase and frequency encoded acquisitions to confirm analytical models of broadening due to relaxation and diffusion. We experimentally demonstrate diffusive attenuation over shrinking voxel dimensions. The SNR per square root time of FE and PE sequences are compared, including the effects of diffusive attenuation with varying gradient strengths, T_2, and diffusion values. Finally, the benefits of PE in improved SNR and resolution are demonstrated with 10 μm in-plane images of excised rat spinal cord acquired at 15.2T with max 1 T/m gradients.

3.3 Theory

We aim to compare the imaging efficiency (SNR per square root time) in a FE versus a PE sequence assuming realistic sequence and sample parameters.

3.3.1 Imaging efficiency excluding diffusion and relaxation

The SNR per voxel a 3D acquisition may be written as

$$SNR/voxel \propto \Delta x \Delta y \Delta z \sqrt{N_{acc} N_x N_y N_z t_{acq}} \tag{3.1}$$

where $\Delta x \Delta y \Delta z$ are the voxel sizes in each dimension, N_{acc} is the number of accumulated signals averaged, N_x, N_y, N_z are the number of samples in each dimension, and t_{acq} is the signal sampling duration per k-space point. For a FE experiment, t_{acq} is the inverse of the receiver bandwidth, t_{acq} = 1/BW and equation 3.1 may be further simplified by including the duration of the readout gradient, $T_{read} = N_x/BW = N_x t_{acq}$ (fig. 3.1 left). The total time for a frequency encoded experiment is TT = TR $N_y N_z N_{acc}$ as every repetition time (TR) includes N_x samples. For a PE sequence, $t_{acq} = N_t/BW$ as after each excitation N_t samples of the FID may be sampled within the TR (fig. 3.1 right). Total time for the PE sequence is TT = TR $N_x N_y N_z N_{acc}$ as only 1 sample in k-space is acquired per TR. The SNR does not continue to increase with t_{acq} beyond a limiting value as the signal itself decays exponentially with a time constant of T_2^*. A more complete comparison includes relaxation effects (see 3.3.2).

The interplay between SNR, time, and resolution is already apparent in equation 3.1. With fixed field of view (FOV) and bandwidth, doubling the isotropic resolution of a 3D scan shrinks the voxel volume by a factor of 8 and the SNR drops by a factor of $8^{-1/2}$ as the number of samples is also doubled. Therefore, to maintain SNR with doubled resolution, the experiment must be averaged 8-fold, taking 32 (8-fold * 2 y samples * 2 z samples) or 64 times as long for frequency or phase encoding respectively. Considering the time differences in these acquisitions, it is useful to compare the SNR per square root of time or

the imaging efficiency defined as

$$\eta = \frac{SNR}{\sqrt{TT/T_1}} \tag{3.2}$$

where TT is the total time of the acquisition normalized by the spin-lattice relaxation of the sample T_1. Using the proportion in equation 3.1, setting $N_x t_{acq} = T_{read}$, and substituting the TT for a frequency and phase encoded acquisition, the ratio of imaging efficiency of FE to PE is

$$\frac{\eta^{FE}}{\eta^{PE}} = R^{FE/PE} \propto \sqrt{\frac{T_{read}}{t_{acq}}} \tag{3.3}$$

3.3.2 Imaging efficiency including T_2^* and steady state

To include the effects of sequence timing and relaxation of the sample on SNR we continue from equation (18) in Link et al [85]. The FE imaging efficiency depends on the echo time (TE), TR, and sample relaxation properties as

$$\eta^{FE} = SNR_0 \ \exp(-TE/T_2^*) \frac{1-\exp(-T_{read}/T_2^*)}{\sqrt{T_{read}/T_2^*}} \frac{(1-E_1)\ \sin(\arccos E_1)}{(1-E_1^2)\sqrt{T_R/T_1}} \tag{3.4}$$
$$where\ E_1 \ \equiv \ \exp(-T_R/T_1)$$

SNR_0 in equation 3.4 is scanner and sample dependent and is defined as S_0/N_0 where S_0 is the equilibrium magnetization measured immediately after a 90-degree pulse and N_0 a reference noise metric dependent on the bandwidth, hardware, and sample properties. T_2^* is the decay time of the signal due to T_2 and field inhomogeneities. Equation 3.4 includes the optimal Ernst angle for steady state acquisitions. For PE, η^{PE} is the same as equation 3.4, only T_{read} is replaced with t_{acq} [86]. The terms in equation 3.4 that include T_2^* have a maximum when t_{acq} or $T_{read} = 1.25T_2^*$ [87].

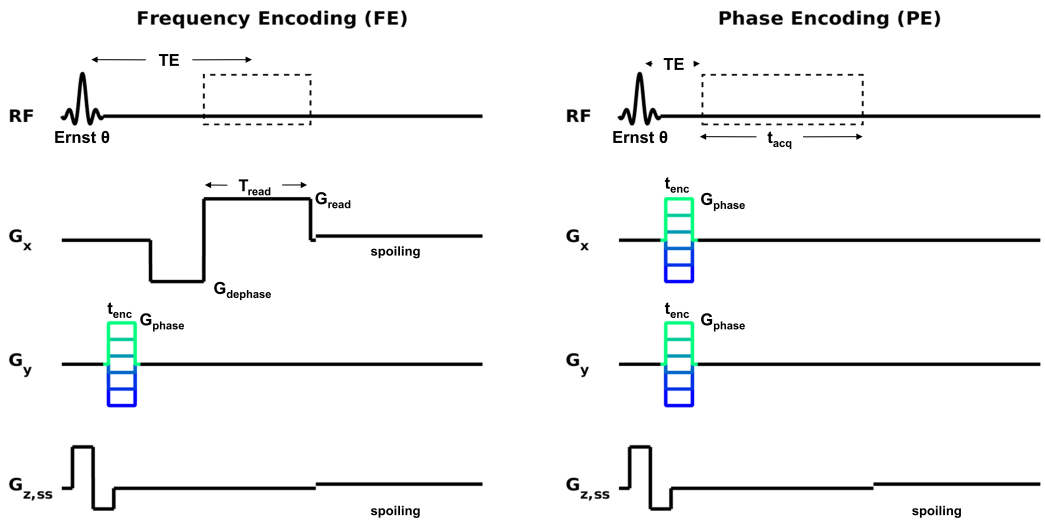

Figure 3.1: Pulse sequence diagrams indicating the key differences in the two acquisitions compared. A conventional readout gradient frequency encodes the first dimension. The phase encoded acquisition acquires data while the gradients are off after the phase encoding period, t_{enc}. Both sequences' RF pulses use the Ernst angle.

3.3.3 Diffusion's effects on signal

Diffusion in non-uniform magnetic fields causes spin dephasing which attenuates signal [88, 89]. During the frequency encoding readout gradient, the attenuation is

$$A_{FE}(D, G_{read}, T_{read}) = e^{-1/12\gamma^2 D G_{read}^2 T_{read}^3} \tag{3.5}$$

where D is the self-diffusion coefficient of spins in the sample (in the read direction), and G_{read} the strength of the readout gradient. Equation 3.5 assumes that $G_{dephase} = G_{read}$. The factor of $1/12$ will change depending on the precise shape in time of the dephase and readout gradients B. Similarly, the attenuation during phase encoding may be written as,

$$A_{PE}(D, G_{read}, t_{enc}) = e^{-1/3\gamma^2 D G_{phase}^2 t_{enc}^3} \tag{3.6}$$

The PE gradient waveform has a constant time and variable gradient strength for each repetition. The worst attenuation will be when G_{phase} is the maximum value, which is

determined by the largest k-space point.

3.3.4 Diffusion's effects on imaging efficiency

By combining equations 3.3 and 3.4-3.6, the ratio of FE to PE's imaging efficiency is altered by the influence of diffusion on signal but may be defined as,

$$R^{FE/PE} = \frac{\eta^{FE}}{\eta^{PE}} \frac{A_{FE}}{A_{PE}} \tag{3.7}$$

Substituting equation 3.4 for FE and PE into equation 3.7 and cancelling like-terms,

$$R^{FE/PE} = \sqrt{\frac{t_{acq}}{T_{read}}} \frac{\exp(-TE^{FE}/T_2^*)}{\exp(-TE^{PE}/T_2^*)} \frac{[1-\exp(-T_{read}/T_2^*)]}{[1-\exp(-t_{acq}/T_2^*)]} \frac{A_{FE}}{A_{PE}} \tag{3.8}$$

Figure 3.2 plots curves using equation 3.8 with varying gradient strengths and nominal resolution. The following sample and acquisition parameters are fixed in the plot: T_2^* = 10 ms, FOV = 2 mm, $G_{read} = G_{phase}$ = 0.1 - 10 T/m, BW = $\gamma FOV G_{read}/2\pi$ where γ is the gyromagnetic ratio, $t_{acq} = T_{read}$, where $T_{read} = N_x BW^{-1}$, and N_x is determined by the FOV and resolution, and $TE^{FE} = TE^{PE}$. At larger voxel sizes, R = 1. In smaller voxel sizes, attenuation of signal by diffusion in the readout gradient dominates and the advantages of PE become increasingly apparent in more time efficient acquisitions. The effects of longer read durations may be ameliorated by using higher gradient strengths to reduce signal losses in smaller voxels.

3.3.5 Diffusion's effects on resolution

Another important consideration for high-resolution MRM is the effect of diffusion on the spatial resolution actually achieved. As has been previously reported, PE suffers less line broadening and thus offers an intrinsically narrower PSF [71, 47, 79, 90, 91, 61]. To compare the differences between the PSF for phase and frequency encoding we use a numerical calculation and measurements of the PSF with an MR sequence. For clarity, nominal resolution refers to the resolution determined by the FOV and number of samples,

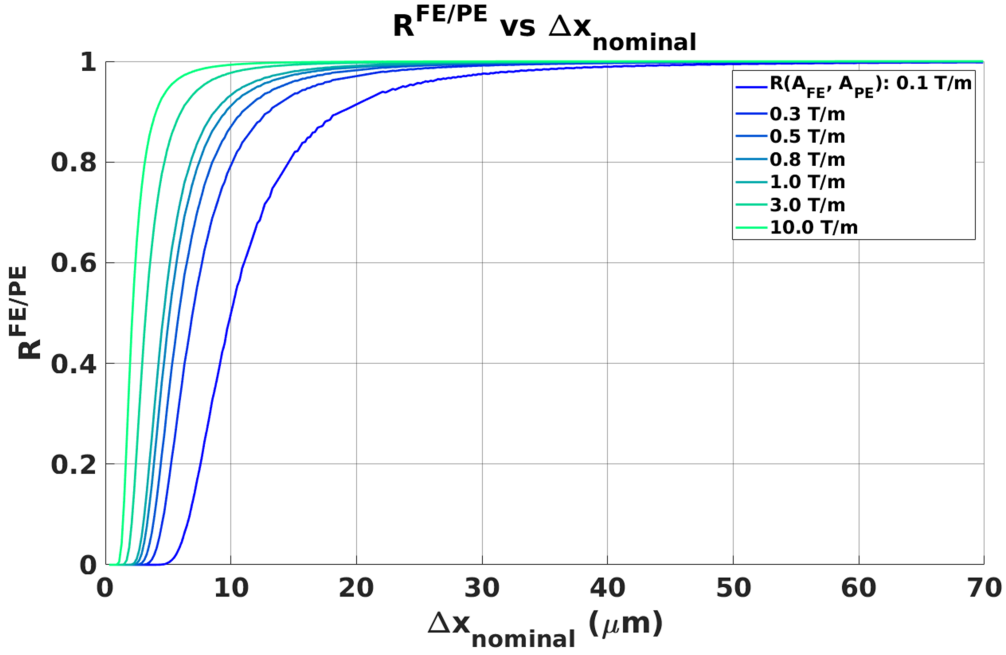

Figure 3.2: $R^{FE/PE}$ in a simulated sample and imaging scheme where $t_{acq} = T_{read}$, $T_2^* = 12$ *ms*, and diffusion is that of free water. For larger voxel sizes, R approaches 1. In smaller voxels, the readout gradient rapidly attenuates signal, and PE outperforms FE with more time efficient acquisitions.

such that $\Delta x_{nominal} = FOV/N_x$. Δx_{actual} refers to the resolution predicted by the transfer function analysis outlined below in 3.3.5.1. Finally, $\Delta x_{measured}$ is the resolution returned by the measurement method outlined in 3.3.5.2.

3.3.5.1 Analytical point spread function calculation

We follow closely McFarland and Webb's approach [71, 47]. The actual resolution for frequency encoding may be approximated as the FWHM of the PSF or

$$\begin{aligned} \Delta x^{FE}_{actual} &= FWHM[\mathscr{F}^{-1}(MTF_{sampling}MTF_{relaxation}MTF^{FE}_{diffusion})] \\ &= FWHM[PSF_{sampling} * PSF_{relaxation} * PSF^{FE}_{diffusion}] \\ &\quad where\ *\ denotes\ a\ convolution \end{aligned} \tag{3.9}$$

where MTF is the modulation transfer function and $\mathscr{F}^{-1}$ is the inverse Fourier transform. It should be noted that $PSF_{sampling}$ includes finite sampling and truncation of the MR signal resulting in the well-known sinc function [8]. For phase encoding, T_2^* decay does not contribute to the resolution degradation because the echo time is kept constant for all values of the phase encoding gradients. Thus, the actual resolution of phase encoding may be approximated as

$$\begin{aligned} \Delta x^{PE}_{actual} &= FWHM[\mathscr{F}^{-1}(MTF_{sampling}MTF^{PE}_{diffusion})] \\ &= FWHM[PSF_{sampling} * PSF^{PE}_{diffusion}] \end{aligned} \tag{3.10}$$

For both phase and frequency encoding $PSF_{sampling}$ is

$$PSF_{sampling} = \Delta k \frac{\sin(\pi N_x \Delta k x)}{\sin(\pi \Delta k x)} where\ \Delta k = 1/FOV \tag{3.11}$$

Considering relaxation during frequency encoding,

$$\begin{aligned} PSF_{relaxation} &= \mathscr{F}^{-1}[\exp(-t/T_2^*)] = \mathscr{F}^{-1}[\exp(^{-k}/_{\gamma G_{read} T_2^*})] \\ &= \frac{a}{\pi(a^2+x^2)}\ where\ a = {}^{1}/_{\gamma G_{read} T_2^*} \end{aligned} \tag{3.12}$$

where the resulting $PSF_{relaxation}$ is a Lorentzian like that mentioned in ch. 1. McFarland [47] shows that the diffusion contributions to the PSF in frequency encoding may be written as

$$PSF^{FE}_{diffusion} = \mathscr{F}^{-1}[MTF^{FE}_{diffusion}] = \mathscr{F}^{-1}[\exp(-k^3 D/3\gamma G_{read})]. \tag{3.13}$$

Webb [71] derived the PSF contributions from diffusion for phase encoding with variable gradients,

$$PSF^{PE}_{diffusion} = \exp(-3x^2/4Dt_{enc}) \tag{3.14}$$

For direct comparison of equations 3.13 and 3.14 see figure 3.14. In figure 3.3, the actual resolution is numerically calculated for phase and frequency encoding by using equations 3.9 - 3.14.

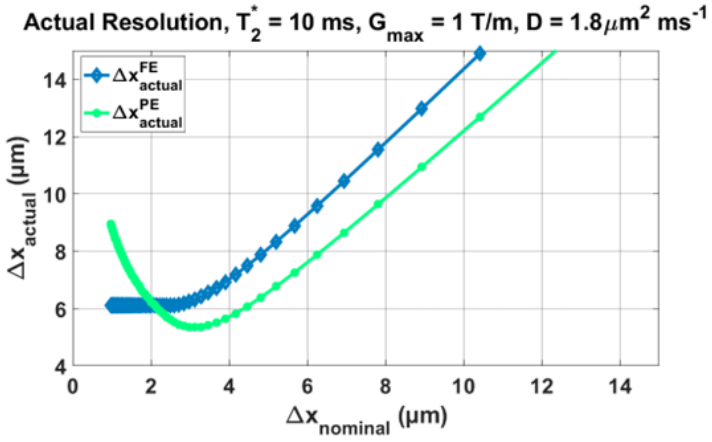

Figure 3.3: Equations 3.9 and 3.10 demonstrate the clear resolution benefit of phase encoding. Relaxation does not contribute to PE's PSF, and diffusion's effects are lessened thus phase encoding has a higher achievable resolution. With voxels smaller than 3 μm, and a fixed gradient, phase encoding's actual resolution begins to degrade due to t_{enc} increasing to accommodate the fixed gradient strength.

3.3.5.2 Measurement of point spread function with imaging

To experimentally measure the PSF, we use a constant time gradient sequence. Signals are acquired using extra phase encoding gradients in the respective dimension to be measured, followed by an inverse Fourier transform. This method was previously developed and demonstrated for EPI-based acquisitions by Robson et al and Zeng and Constable [92, 93]. A full k-space trajectory is traversed for each value k' of the additional phase encoding gradients. The k-space data are inverse Fourier transformed along each spatial dimension forming an image for each k'. This is followed by an inverse Fourier transform along the k' direction at each pixel. The resulting profile is the spin-density weighted point spread function. An example profile and image is provided in figure 3.4. The measured resolution may then be defined as

$$\Delta x_{measured} = FWHM(\mathscr{F}^{-1}[S(x,y,k')]), \tag{3.15}$$

where x and y denote the pixel spatial location, and S denotes sample image from each k' encoding. To measure the PSF precisely, k' space must be adequately sampled. Adequate sampling may be achieved by increasing the number of k' encoding points (N_{PSF}) or increasing k' by increasing the gradient ($\Delta k' = 1/FOV_{PSF}$). A compromise between imaging time and measurement accuracy was determined by setting $FOV_{PSF} = \frac{3}{4}FOV$ and $N_{PSF} = 2N_x$. see figure 3.11 for more information.

3.4 Methods

3.4.1 MRI equipment, hardware, and phantoms

All data were acquired with a Bruker (Billerica, MA) 15.2T Biospec imaging spectrometer equipped with 1 T/m maximum magnetic field gradients. The Avance III console used ParaVision 6.0.1. The bore is 6 cm in diameter within the gradients with 3rd order B_0 shims. For SNR and PSF measurements a small solenoid was used. The solenoid was a copper, 6 turn, 1.5 mm diameter coil with a wire diameter of 300 μm coated in polyurethane.

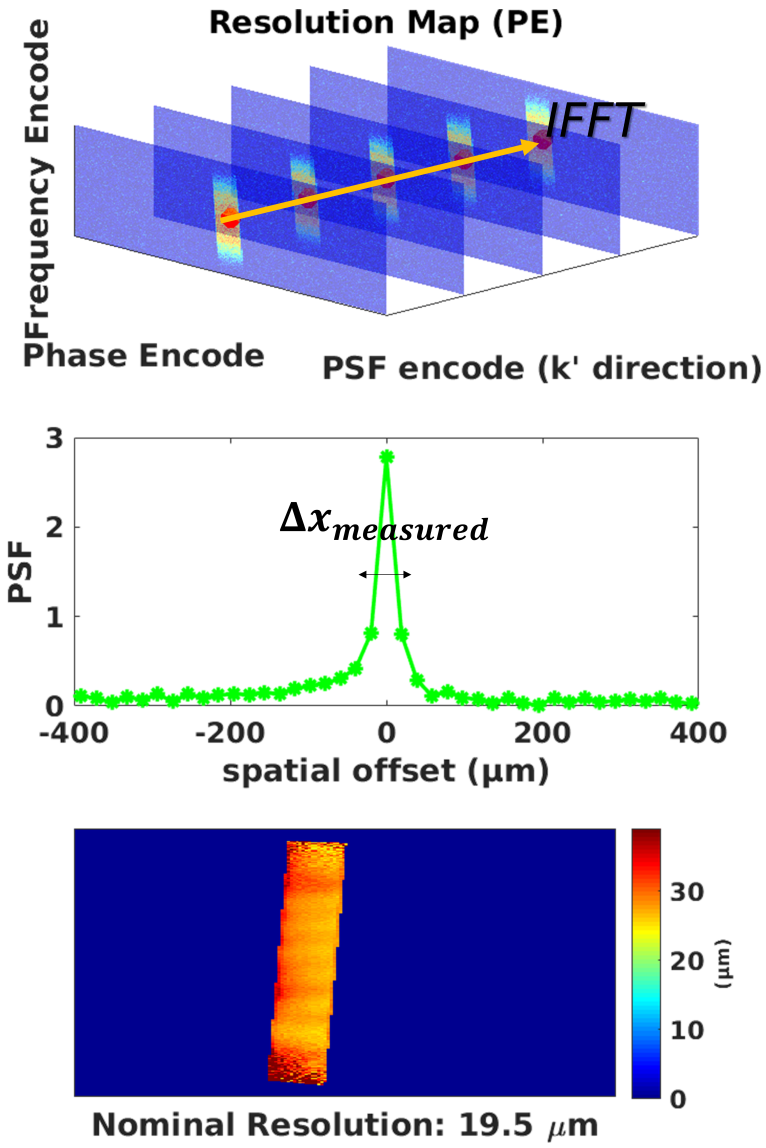

Figure 3.4: A resolution map is obtained by plotting the FWHM of the PSF for each pixel within the sample. The inverse Fourier transform is performed for each pixel along the k' direction to render the PSF. Then the FWHM of the PSF for each pixel is plotted back onto the masked sample, In this case, a $CuSO_4$ filled capillary.

The tune and match circuit consisted of 2 variable capacitors, and 2 fixed capacitors. A Bruker 20 mm cryoprobe was used to image excised tissue described in section 3.4.3.4. The phantom for resolution and SNR experiments was a 6 mM $CuSO_4$ solution in glass capillaries of varying sizes (Drummond Scientific Company, Broomall, PA). The capillaries were filled via the capillary effect and sealed using a wax pen.

3.4.2 SNR measurements

SNR was measured by selecting 2 regions of interest across magnitude images of the experimental sample. The mean signal region consisted of pixels within the sample and the noise region consisted of areas at the corners of the image with no sample present. The magnitude image values were plotted on a log-scale to ensure noise and sample regions were visually free from distortion or artifacts. Magnitude images were used so a correction was applied following the work of Henkelman [94, 95] in order to ensure low signal images did not overestimate SNR.

3.4.3 Experiments

To demonstrate the effects of diffusion at high resolution, several experiments and simulations were performed.

3.4.3.1 Demonstration of diffusion in a read-out gradient

To demonstrate attenuation due to diffusion during the readout gradient, images at varying resolution in the frequency encoding dimension were acquired. The resolution was varied by changing the number of readout points which lengthened T_{read}. TE was fixed for every image by using the minimum TE allowed for the highest resolution image. The following parameters were fixed for each nominal resolution: the bandwidth at 40 kHz, G_{read} = 0.47 T/m, N_{acc} = 9, FOV = 2 x 2 mm, TE/TR = 14.7/80 ms, Ernst angle of 47.9°, and slice thickness, Δz = 2 mm. The experiment used a 2D acquisition with relatively large slice thickness to avoid diffusion attenuation from the slice dimension [77] and ensure adequate

SNR from larger voxel sizes. Each scan took ≈ 23 seconds. The sample was a 0.4 mm inner diameter 0.9 mm outer diameter capillary tube filled with 6 mM $CuSO_4$ solution.

The SNR was fit to the following equation formulated from equations 3.1, 3.4, and 3.7:

$$SNR_{2D}^{FE} = SNR_0 \Delta x \Delta y \Delta z \sqrt{N_{acc} N_y} \exp(-TE/T_2^*) \frac{1-\exp(-T_{read}/T_2^*)}{\sqrt{T_{read}/T_2^*}} \frac{(1-E_1)\sin(\arccos(E_1))}{1-E_1^2} A_{FE}$$
$$where\ A_{FE} = \exp(-\varepsilon \gamma^2 D G_{read}^2 T_{read}^3) \tag{3.16}$$

In equation 3.16, TE is fixed, $T_{read} = T_s FOV_x/\Delta x$, and ε depends on the duration and amplitude of the dephase gradient (see appendix B), in this case $G_{read} \neq G_{dephase}$ so $\varepsilon \neq 1/12$. The data were fitted allowing SNR_0 and ε to vary. Given G_{read}, the bandwidth was calculated for FOV = 2 mm, using $BW = FOV \gamma G_{read}/2\pi$. A multi-gradient echo sequence was used to measure the T_2^* of the solution and on average was 12 ms. The T_1 was measured using a variable TR RARE sequence and was 200 ms. The ADC of the sample was measured with a diffusion weighted spin echo and was ≈ 1.8 $\mu m^2 ms^{-1}$. A similar experiment to the above was carried out following Cho et al [45] (see figure 3.13).

3.4.3.2 Demonstration of imaging efficiency loss due to diffusion

To demonstrate the steep drop off in the ratio of imaging efficiencies due to diffusion, ,the resolution was varied for the FE and PE from 15 to 10 μm. The resolution was varied by changing the number of readout points which lengthened T_{read}. The following parameters were fixed for each nominal resolution: the bandwidth at 40 kHz, G_{read} = 0.47 T/m, N_{acc} = 1, FOV = 2 x 2 mm, TE/TR = 7/20 ms, and slice thickness, Δz = 0.6 mm. Each FE acquisition was ≈ 2.6 s and the PPE scans ran from 5 to 8 min. The sample was a 0.4 mm inner diameter 0.9 mm outer diameter capillary tube filled with 6 mM $CuSO_4$ solution. The microcoil was a 6 turn 1.5 mm diameter coil with a wire diameter of 300 μm coated in polyurethane. G_{phase} was set to G_{read} by varying t_{enc} for each resolution. $G_{dephase}$ was set to G_{read} by varying the dephasing duration for each resolution. To ensure the sample

temperature change from rapid excitations did not significantly alter the ADC values, the same experiment was performed except with a temperature probe on the capillary. A coarse ADC map was also acquired using a diffusion weighted spin echo before and after the experiment to measure any changes in the ADC of the sample (see figure 3.10).

3.4.3.3 Measuring resolution broadening

To demonstrate broadening contributions of diffusion and T_2^* to the actual resolution of the experiment, the PSF was acquired at varying resolutions with the microcoil using theory outlined in 3.3.5.2. To measure the actual resolution in the frequency encoded dimension, the number of readout points was incrementally increased from 67 to 100, then 125 points with a FOV of 1 x 1 mm and N_y set to 32. There were 134, 200, and 250 N_{PSF} encoding points. For the phase dimension, the same FOV and N_{PSF} points were used and the PSF was acquired in the y direction, N_x was 32. For each acquisition, the following parameters were fixed: G_{read} = 0.56 T/m, bandwidth = 24 kHz, N_{acc} = 9, TE/TR = 16.4/80 ms, and the slice thickness was 1 mm.

3.4.3.4 Excised rat spinal cord images

To demonstrate a scenario in which PE is clearly advantageous in SNR and resolution, images of an excised rat spinal cord were acquired. The spinal cord was divided near the lower lumbar/upper sacral region. The tissue was prepared for imaging by first fixing in a 10% Phosphate buffered saline (PBS). It was then soaked overnight in 2 mM Gadolinium (Gd) and 0.1 mM sodium azide (NaN_3). By washing the sample of fixative before imaging, T_2 and thus SNR will increase [96]. To remove excess signal, the tissue was placed in Fomblin (Solvay Brussels, Belgium) and a microcentrifuge tube for imaging. Before each experiment, a multi-gradient echo sequence was used to measure the T_2^* of the spinal cord. The T_1 was measured using a variable TR RARE sequence. The ADC of the sample was measured in the readout direction with a diffusion weighted spin echo. Two experiments were performed. One set of images to compare FE to PE with all sequence parameters

the same, and one image to demonstrate PE's ability to resolve fine structure. For the first set of images, 30 and 10 μm in-plane resolution images were acquired. The sample was soaked in 10% PBS and 1 mM Gd overnight. The 30 μm resolution images had the following sequence parameters: FOV = 5 x 5 mm, 168 x 168 encoding matrix, 250 μm slice thickness, TE/TR = 8.17/75 ms, and an Ernst angle of 42.2°. N_{acc} = 168 for the FE image so that the total scan time for both images was 35 min. For the FE image, receiver BW was set to 15 kHz, resulting in the G_{read} = 0.07 T/m. This was to ensure the length of T_{read} was roughly the same as t_{acq} for the PE sequence. For the PE images, the receiver BW was 3.2 kHz with N_s = 39. The 10 μm images had the following parameters: FOV = 4 x 4 mm, 400 x 400 encoding matrix, 250 μm slice thickness, TE/TR = 9.01/100 ms, an Ernst angle of 47.9° for a total imaging time of 4h 26 min with N_{acc} = 400 for the FE image. The receiver BW was set to 34.7 kHz for 16 the FE image, resulting in the G_{read} = 0.2 T/m. For the PE images, the receiver BW was 3.2 kHz with N_s = 39. Because PE allows for shorter TE and TR values with respect to the FE sequence, a single image was acquired with PE to demonstrate fine details in the spinal cord. The sample was soaked overnight in a 10% PBS and 2 mM Gd solution. The sequence had the following parameters: FOV = 5 x 5 mm, 512 x 512 acquisition matrix, 9.8 x 9.8 μm resolution, 250 μm slice thickness, TE/TR = 2.5/30 ms, an Ernst angle of 44.2°, the BW of the receiver was 3.2 kHz, N_s = 64, with t_{acq} = 20 ms, and t_{enc} = 1.75 ms. G_{phase} was 0.69 T/m. The shortest TE available to the FE sequence for the same imaging parameters without exceeding the gradient duty cycle was 8.2 ms, resulting in SNR loss from T_2^* of around 25%.

3.4.3.5 Microscopy recommendations considering T_2^*, G_{max}, and diffusion

To provide recommendations for imaging in the diffusive regime at very high resolution, equations 3.8, 3.9, and 3.10 were used to calculate $R^{FE/PE}$, $\Delta x^{FE}_{actual}/\Delta x_{nominal}$, $\Delta x^{PE}_{actual}/\Delta x_{nominal}$ over varying diffusion, T_2^* and G_{max} values. The T_{read} was determined by 3 fixed G_{max} values 0.5, 1, and 2 T/m and a fixed FOV of 2 mm. T_2^* values were 1, 10, and 30 ms. Diffusion

values were 0.5, 1, 2, and 2.8 $\mu m^2 ms^{-1}$. The range of diffusion values is meant to span ADC values from room temperature (18 °C) to physiological temperatures (35 °C) [97]. It is assumed that TR and TE are fixed for the two acquisitions. To simulate the most realistic case, t_{acq} was set to the SNR ideal value of $1.25T_2^*$ [85, 87]. The was calculated for two conditions: 1) When the PE is twice as time efficient as FE and 2) when the encoding returns actual resolutions 1.5x the nominal. Broadening intrinsic to sampling and digitization is 1.21x the nominal resolution [71, 47], therefore 1.5x was chosen arbitrarily since it is more than the resolution broadening of sampling and digitization but less than a factor of 2.

3.5 Results

3.5.1 Diffusion during the read-out

The experimentally measured SNR is plotted in figure 3.5 as red dots. By simply shrinking the voxel size, the SNR is expected to go down since there is less signal in a smaller voxel (red diamonds). The predicted SNR due to smaller voxels does not adequately characterize the measured loss in SNR as the resolution is increased experimentally. However, once the attenuative term (equation 3.5) is added to the model, the fit (blue diamonds) follows the measured data (red dots). With the diffusion attenuation term, $R^2 = 0.99$ and without it, $R^2 = 0.73$. SNR_0 best fit was 4.4e13 and $\varepsilon = 0.038$. The diffusion coefficient of the sample was measured to be 1.8 $\mu m^2 ms^{-1}$ based on a diffusion weighted image prior to the experiment. The T_1 and T_2^* of the sample was $\approx$ 200 and 12 ms respectively.

3.5.2 Simulated G_{read} and T_{read} combinations

Using the fit in figure 3.5, it is useful to consider varying T_{read} and G_{read} combinations effects on SNR attenuation. For larger voxels, the well-known relationship of SNR $\propto BW^{-1/2}$ holds, although a more precise description of this relationship is that SNR $\propto$ the time that the receiver is on (T_{read} or t_{acq}) [98]. When diffusion attenuates signal, stronger gradients have an SNR advantage at higher resolution. Given a chosen resolution in the readout di-

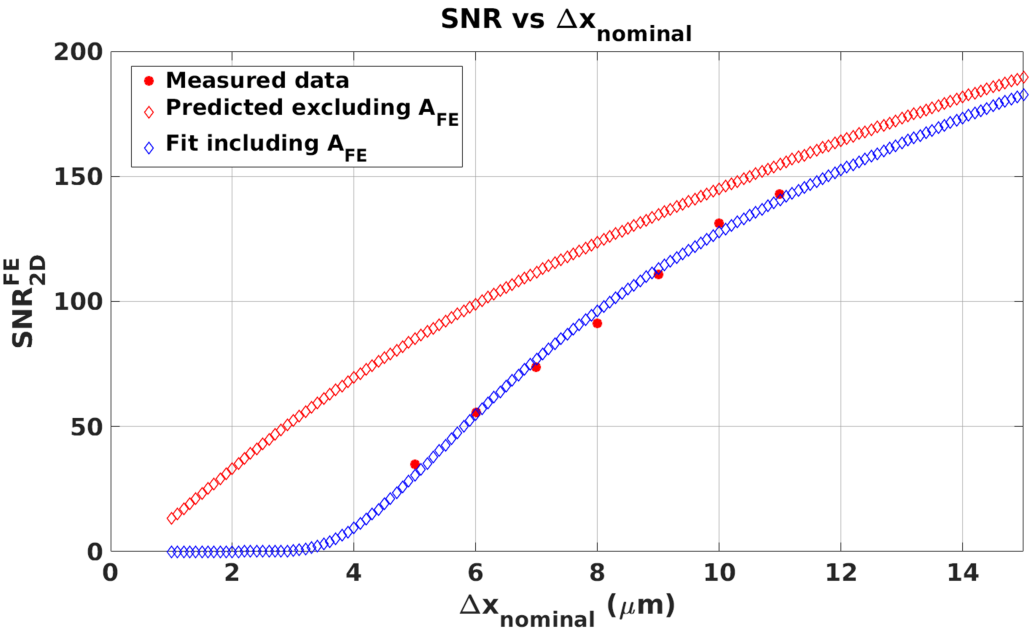

Figure 3.5: SNR of a FE acquisition was measured with increasing resolution in the readout dimension. Resolution was increased by fixing the FOV and increasing the number of samples acquired during the readout extending the duration of the readout gradient. The TE was fixed by using the minimum TE for the highest resolution scan. For comparison, the model was plotted with and without the diffusive attenuation term given the same initial SNR. At larger voxel sizes, the two models agree since the attenuation term is negligible for shorter read durations.

mension, there exists an optimal bandwidth and G_{read} combination. To demonstrate this for the $CuSO_4$ phantom, G_{read} and the bandwidth were varied with simulation while maintaining SNR_0 and ε from the fitted data in figure 3.5. The results of varying G_{read} are plotted in figure 3.6. Given G_{read}, the bandwidth was calculated for FOV = 2 mm, using BW = FOV$\gamma G_{read}/2\pi$. For voxels larger than 14 μm, the smallest BW has the largest SNR. For 9-13 μm, the 0.3 T/m gradient has the highest SNR. Between 6 and 9 μm, 0.5 T/m is optimal. Below 6 μm, the highest gradient has the highest SNR since T_{read} is the shortest.

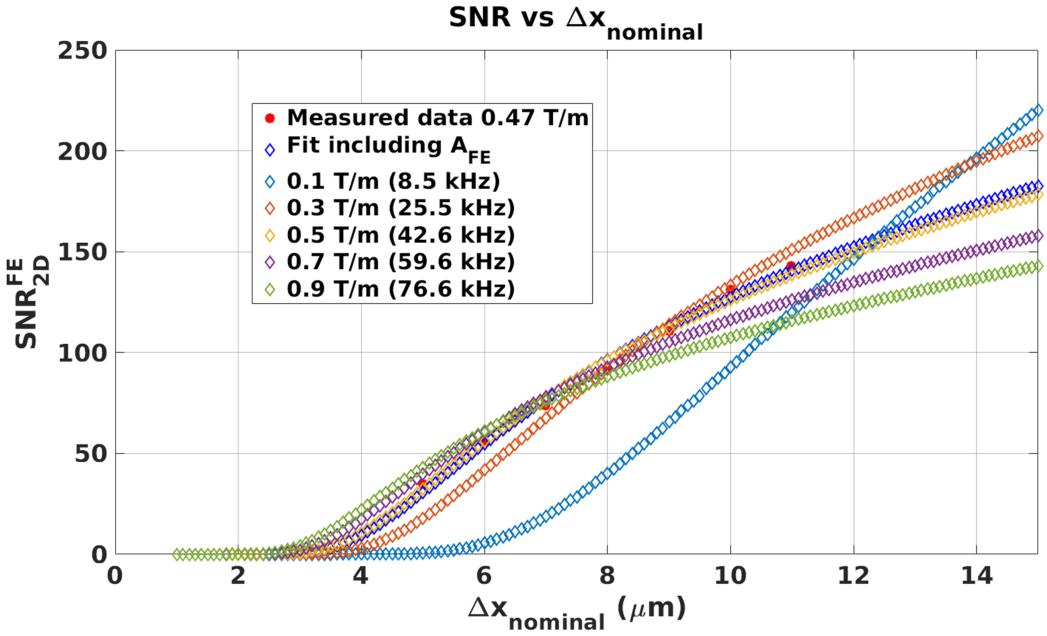

Figure 3.6: The simulated SNR for varying gradient strengths for very small voxels in a FE acquisition. For the smallest voxels, stronger gradients have higher SNR since the attenuation $\propto e^{G^2T^3}$ and longer readouts are penalized at high resolution. For larger voxels, the well know relationship of SNR $\propto BW^{-1/2}$ is apparent and weaker gradients produce higher SNR. Between the extremes care must be taken to choose optimal gradient strength.

3.5.3 Demonstration of imaging efficiency loss due to diffusion

From figure 3.2, it is expected that for gradients < 1 T/m, $R^{FE/PE}$ will begin falling below 1 when $\Delta x_{nominal}$ is 10-20 μm. This is shown in figure 3.7 to experimentally verify equation 3.8. The experimentally measured ratio (blue diamonds) is plotted followed by the calculated ratio (solid line) given by equation 3.8. The acquisition durations varied from 5 to 3.4

ms. The calculated ratio is plotted using equation 3.8 and by plugging in the experimental parameters. For the PE sequence, the receiver bandwidth was fixed to 3.2 kHz for every acquisition. This resulted in small differences in t_{acq} from T_{read} since $t_{acq} = N_s/BW$ and depends on a finite number of samples, thus the calculated and experimental data do not vary smoothly. The error bars are the standard deviation of the measurement. Expected changes in temperature and thus ADC [97] from the short TR sequence and 1 hour of scan time resulted in $< 0.7\%$ percent difference in the $R^{FE/PE}$ (see figure 3.10).

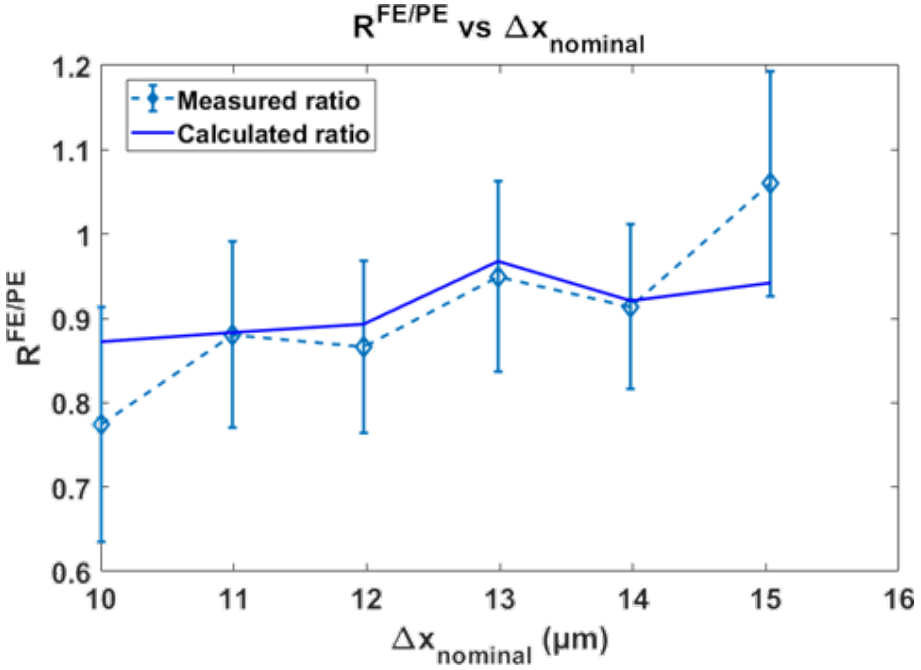

Figure 3.7: Experimental verification of equation 3.8. With a fixed readout gradient, diffusion begins to attenuate the SNR of a FE acquisition and PE becomes more efficient. For diffusion of free water, T_2^* = 12 ms, and $G_{read} = G_{phase}$ = 0.47 T/m, R < 0.9 when $\Delta x_{nominal} = 11\mu\ m$.

3.5.4 Experimentally measuring resolution

For the frequency encoding resolutions (blue histogram in fig. 3.8) the scan times were as follows: 51m, 1hr17m, 1hr36m, for 14.9, 10, and 8 μm respectively. The phase encoding resolutions (green histograms in fig. 3.8) had the following scan times: 1 h 48 m, 4 h, 6 h 15m for 14.9, 10, and 8 μm respectively. The phase encoding experiment took much

longer since changing N_x and N_{PSF} increased the time whereas for the frequency direction, only changing N_{PSF} increased the time requirements.

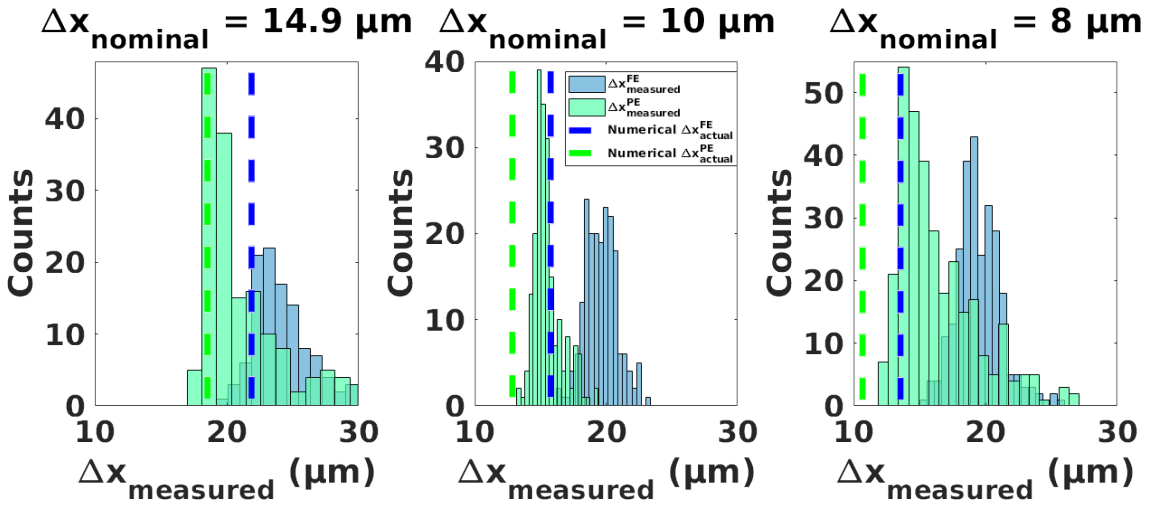

Figure 3.8: The numerical predictions of the actual resolution show agreement with the measured resolutions at larger voxel sizes 14.9 μm. However, as diffusion begins to degrade resolution, the additional phase encoding gradients from the measurement begin to contribute even more resolution broadening.

For $\Delta x_{nominal}$ = 14.9 μm, the mean of the $\Delta x_{measured}$ was 24.8 and 22.8 μm for FE and PE. The predicted Δx_{actual} was 21.1 and 18.5 μm for FE and PE respectively. For $\Delta x_{nominal}$ = 10 μm, the mean of the $\Delta x_{measured}$ was 19.6 and 15.5 μm for FE and PE. The predicted was 15.9 and 12.9 μm for FE and PE. For $\Delta x_{nominal}$ = 8 μm, the mean of the $\Delta x_{measured}$ was 19.5 and 16.4 μm for FE and PE. The predicted Δx_{actual} was 13.7 and 10.7 μm for FE and PE. The analytical predictions of the actual resolution (equations 3.9 and 3.10) are included in figure 3.8 as the blue and green dashed lines. For each nominal resolution, phase encoding returns a better measured resolution. There is good agreement in the analytical measurement for the 14.9 μm voxel sizes. However, as the resolution is increased the measurement is worse. This may be due to the analytical model not accounting for the measurement's extra phase encoding gradients which also contribute to resolution broadening.

3.5.5 Excised rat spinal cord images

Figure 3.9 shows the 30 and 10 μm in-plane FE and PE images (fig. 3.9 A-D) and the single PE image with shorter TE and TR (fig. 3.9 E). The 30 and 10 μm images had T_1 = 250 ms, T_2^* = 10 ms on average across the bulk sample. The white matter ADC was roughly 0.1 $\mu m^2\ ms^{-1}$ and the gray matter ADC was roughly 0.3 $\mu m^2\ ms^{-1}$ (see figure 3.12). The SNR was 20.2, 8.7, 24.8, and 9.4 for A-D. The images are unmasked, and the image limits were manually adjusted for view-ability. All images had 250 μm slice thickness. For the single PE image (fig. 3.9 E), the total imaging time was 2 h and 11 min and SNR = 8.5. The TR was 30 ms for E versus 100 ms for B and D resulting in a large difference in total scan time. The FE image required a much longer TR in order to avoid exceeding the duty cycle. In figure 3.9E, the T_2^* across the whole sample was $\approx$ 20 ms. The T_1 was measured to be $\sim$90 ms on average. The shorter T_1 is simply because the sample was soaked in 2 mM overnight and not 1 mM (A-D). The increased quality from D to E is most likely due to the increase in T_2^* in E and increased G_{phase} with 0.3 T/m versus 0.69 T/m. The image is masked and normalized to the range of signal in gray and white matter.

3.5.6 Microscopy recommendations considering T_2^*, G_{max}, and diffusion

To provide recommendation for imaging with optimal actual resolution and time efficiency, equations 3.8-3.10 were used to determine the nominal resolutions at which PE is a clear choice for an imaging experiment. The results are presented in Table 3.1. An example use of this table is as follows. If a tissue sample of interest has a diffusion value of 1 $\mu m^2 ms^{-1}$ and T_2^* of 10 ms and the MR scanner in use has a maximum gradient of 2 T/m, PE will be twice as time efficient as a FE acquisition at $\Delta x_{nominal}$ = 10 μm resolution. FE images with resolution higher than 10 μm will only suffer more time requirements and resolution broadening. Similarly, with D = 2 $\mu m^2 ms^{-1}$, T_2^* = 10 ms, and G_{max} = 0.5 T/m, frequency encoding will return $\Delta x_{nominal}$ = 10 μm images with 150% broadening, preventing resolution of details $<$ 15 μm. With no increased time requirements, PE will

only blur by 120%, resulting in images with 3 μm finer resolution.

			$\Delta x_{FE}/\Delta x_{nominal} = 1.5$	$\Delta x_{PE}/\Delta x_{nominal} = 1.5$	$R^{FE/PE} = 0.5$
$D\ (\mu m^2 ms^{-1})$	$T_2^*\ (ms)$	$G\ (T/m)$	$\Delta x_{nominal}(\mu m)$	$\Delta x_{nominal}(\mu m)$	$\Delta x_{nominal}(\mu m)$
0.5	1	0.5	33.5	3.0	6.4
		1	18.7	2.4	4.1
		2	10.5	1.9	2.9
0.5	10	0.5	7.5	3.0	3.8
		1	5.1	2.4	3.1
		2	3.6	1.9	10.1
0.5	30	0.5	5.6	3.0	13.2
		1	4.2	2.4	5.1
		2	3.2	1.9	n/a
1	1	0.5	35.2	3.8	7.2
		1	19.8	3.0	4.8
		2	11.4	2.4	3.4
1	10	0.5	8.8	3.8	4.8
		1	6.1	3.0	4.0
		2	4.4	2.4	9.8
1	30	0.5	6.8	3.8	12.6
		1	5.2	3.0	n/a
		2	4.0	2.4	n/a
2	1	0.5	36.0	4.8	8.3
		1	20.5	3.8	5.7
		2	12.2	3.0	4.1
2	10	0.5	10.3	4.8	6.2
		1	7.3	3.8	5.3
		2	5.4	3.0	9.2
2	30	0.5	8.4	4.8	10.2
		1	6.4	3.8	n/a
		2	4.9	3.0	n/a
2.8	1	0.5	39.1	5.4	8.9
		1	22.6	4.3	6.2
		2	12.6	3.4	4.5
2.8	10	0.5	11.0	5.4	7.1
		1	8.0	4.3	6.1
		2	6.0	3.4	8.3
2.8	30	0.5	9.3	5.4	n/a
		1	7.1	4.3	n/a
		2	5.5	3.4	n/a

Table 3.1: Diffusion, gradient strength, and T_2^* were varied to create a lookup table using equations 3.8-3.10. The resolution broadening due to frequency encoding is much more than phase encoding with the primary contribution being increased diffusion values. The $\Delta x_{nominal}$ for which $R^{FE/PE}$ = 0.5 is also given in the final column to demonstrate the $\Delta x_{nominal}$ for which PE is twice as time efficient as the FE sequence. Note that n/a indicates there is no value of $\Delta x_{nominal}$ for which $R^{FE/PE}$ = 0.5, meaning PE is more than twice as time efficient with the same sample and hardware properties.

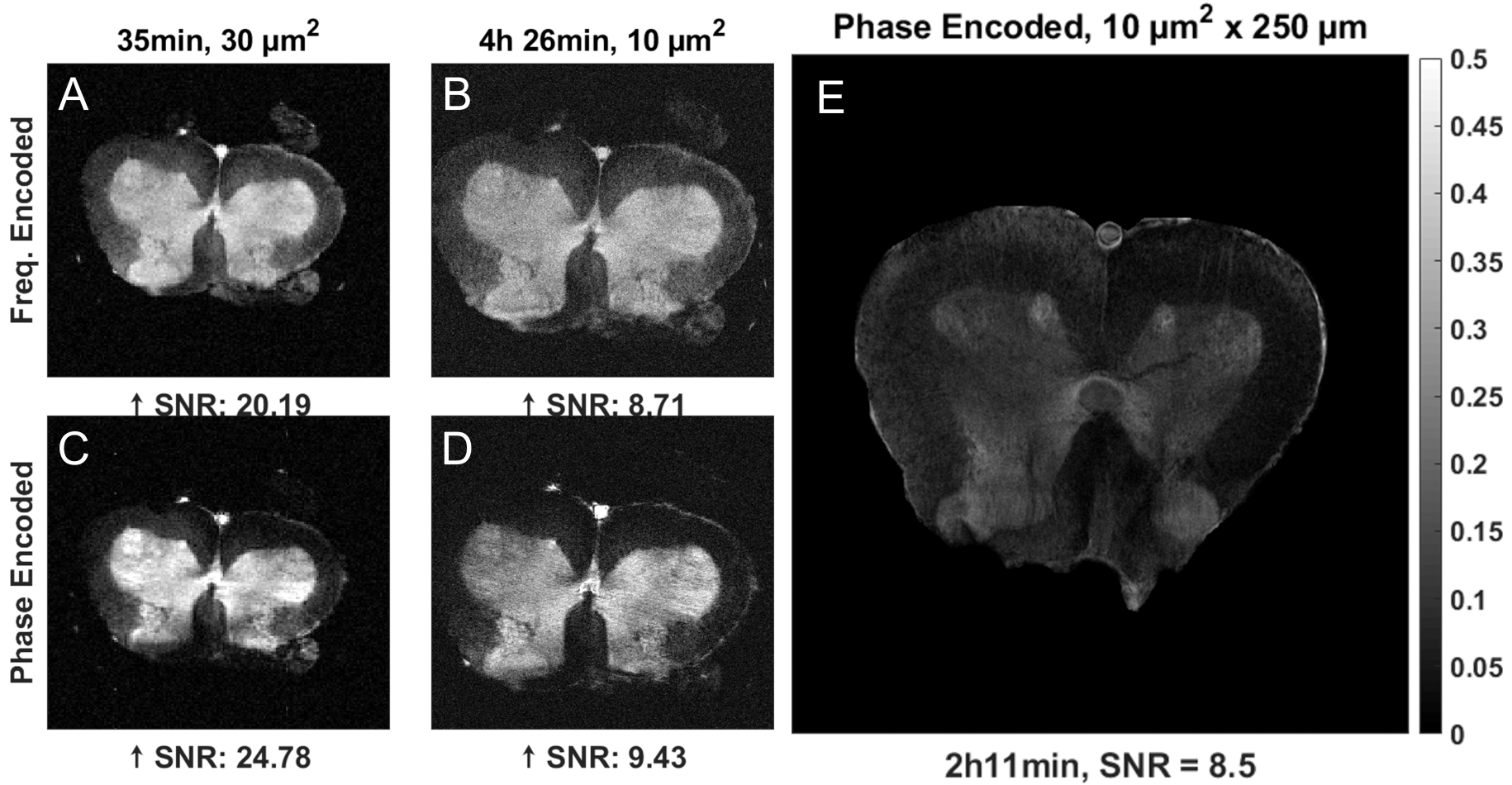

Figure 3.9: Upper sacral region of an excised rat spinal cord imaged with FE (A, B) and PE (C-E). Finer structures are apparent in the PE images at the expense of some contrast between the gray and white matter (A-D). Vasculature may be observed in the left ventral horn. In E, TE and TR are shortened and G_{phase} and T_2^* are increased. Vasculature can also be seen within the gray matter to the right and left of the central canal.

3.6 Discussion

The objective of this work is to give an MR microscopist tools to choose between PE and a conventional readout gradient. We lay out the hardware and sample properties in which the image quality and time efficiency of PE greatly exceeds that of a conventional readout sequence. Without diffusion present, the η^{FE} is generally equal to η^{PE}. However, as voxels shrink and the diffusion of the sample attenuates signal during the frequency encoding readout gradient, PE offers benefits in the form of actual resolution and time efficiency especially in voxels < 15 μm and gradients < 2 T/m. This is important for future MRM experiments that are limited by finite gradient strengths and require time efficient acquisitions with resolution beyond 15 μm. No work to date has included the SNR attenuation of diffusion in a side-by-side comparison of a readout and PE acquisition for MRM. Although Gravina and Cory discuss diffusion's effects in a SE, they do not include diffusion attenuation in their signal model and are primarily interested in imaging solids [78]. Choi and coworkers point out that constant time imaging may be more time efficient than SE in certain cases, however they do not generalize for PE or include variation of diffusion, T_2^*, and G_{max} values as is included here. The assumption that $t_{acq} = T_{read}$ in figure 3.2 is reasonable for certain imaging conditions. However, PE has highest SNR for $t_{acq} = 1.25T_2^*$ which is not necessarily a realistic T_{read} value given the T_2^*, limited gradient, and number of samples. A more realistic comparison was chosen for table 3.1, allowing for T_{read} to be determined by the maximum gradient strength available and to avoid further blurring. Figure 3.3 demonstrates the immediate advantage of PE in higher achievable resolution. However, the phase encoding resolution is dependent on the encoding time (or phase difference), broadening of resolution continues as t_{enc} is lengthened for higher resolutions [71]. For frequency encoding the resolution depends on frequency difference between voxels so broadening stops at the diffusive limit (≈ 6 μm in figure 3.3) [47]. Therefore, at $\Delta x_{nominal} < 2$ μm, phase encoding's Δx_{actual} exceeds that of frequency encoding. This may be avoided with higher gradient strengths. The map shown in figure 3.4 provides the spa-

tially dependent point spread function across the sample. With varying diffusivity and T_2^* across the sample's resolution map, the FWHM is thus a T_2^* and diffusion weighted contrast image. The large time commitment should be noted. The PSF contrast image or resolution map may be of use for certain applications that are focused on multi-parametric variation with resolution. Diffusion in the readout dimension has been derived and discussed in many previous publications [50, 72, 70, 99, 100]. The results in figures 3.4, 3.5, and 3.6 beg the question whether ADC values may be measured from a readout gradient by itself for instance by varying the $G_{read}/G_{dephase}$ ratio to vary the effective b-value. Although parsing out the attenuation's contributions from T_2^* may be cumbersome, the advantage of this would be much shorter TR's, higher SNR, and more efficient diffusion maps since FLASH is inherently more efficient than SE [85]. A purely phase encoded spin echo for diffusion measurements or T_2 quantitation is also possible if higher resolution is desired [101, 102, 103, 104]. In figure 3.6, the simulated readout gradient strengths may be used to calculate the bandwidth that optimizes SNR at a given resolution. Callaghan discusses this in [81, 67]; however the methods presented here allow for a quick and relatively simple method of calculating the bandwidth for optimal SNR considering diffusion. Given the target $\Delta x_{nominal}$, FOV, and sample properties, equation 3.16 may be used to find an optimal $T_{read}G_{read}$ combination or rather the diffusion optimal BW. However, a decrease in gradient strength for SNR may compromise the actual resolution of the image if the diffusive broadening exceeds the unavoidable contributions of sampling and relaxation. In figure 3.7, we demonstrate experimental verification that the imaging efficiency differences of FE and PE begin to become apparent at resolutions 10 – 15 μm especially with gradients $<$ 2 T/m. Often pure phase encoding is quoted to be less SNR time efficient than readout acquisitions [77, 78] which may lead some away from PE acquisitions. This may be true for single point imaging methods like constant time imaging, however when the sequence allows for longer acquisition times (i.e. $T_2^* > 1$ ms), PE is very comparable if not better than readout acquisitions especially at high resolution. Another added benefit is that

PE does not require a dephasing gradient thus the lower duty cycle allows TE and TR to be shortened. With longer T_2^* values, most of the sequence duration could be spent acquiring signal, since phase encoding is the only time requirement between excitation and acquisition. In figure 3.8, the measured PSF demonstrates clear agreement with phase encoding's resolution advantage. At 15 μm, the numerical PSF and measured PSF agree since most of the broadening is determined by the sampling function. However, as the resolution increases, the measured and analytical model differ. This is to be expected as the model doesn't include the extra phase encoding gradients that are used to measure the PSF as the diffusive broadening from these becomes more significant at higher resolution. The measured PSF however confirms that at high resolution, phase encoding provides finer resolution. In the 30 μm and 10 μm images (fig. 3.9 A-D) certain structures are more noticeable especially in the left ventral horn. There is however loss of contrast between the gray and white matter. The SNR of the FE image is expected to be slightly lower than the PE image due to attenuation of diffusion. The ADC values are more constricted (< 0.5 $\mu m^2 ms^{-1}$) and the gradients are ramped down to ensure T_{read} is roughly t_{acq} thus the SNRs are not significantly different between A and C and B and D respectively. According to table 3.1, FE would be half as time efficient at nominal resolutions below 4 μm. However, resolution benefits from PE are already clear at 30 μm. The actual resolution of the 30 μm images (fig 3.9 A,C) in the first dimension (up and down) is expected to be 45.9 and 35.9 for FE and PE respectively. The actual resolution of the 10 μm images (fig 3.9 B,D) in the first dimension is expected to be 16.9 and 12.1 μm for FE and PE respectively. For the single PE image, the actual resolution is expected to be 11.8 μm isotropic versus the 9.8 μm nominal resolution. This slight increase in achieved resolution is due to the higher G_{phase} of 0.69 T/m. The excised rat spinal cord image (fig. 3.9 E) is the highest reported inplane resolution and smallest voxel size to date with the closest image being 25 x 25 x 50 μm resolution with a gradient echo in 36 min with a ferroelectric ceramic resonator at 17T [105] . Limitations of this study include neglecting susceptibility considerations and

contrast differences between PE and FE. Although PE is often claimed to be more robust to susceptibility artefacts [78, 79, 101, 106]. Another limitation of PE is aliasing if the Nyquist condition is not met, requiring the sample to be fully encompassed in the FOV, although this could be avoided with FOV saturation methods. Furthermore, resolution higher than 20 μm is not often achieved in-vivo thus the study is inherently limited to small FOVs, high sensitivity coils, excised, and/or in vitro samples. The importance of this work may be demonstrated in equations 3.8, 3.9 and 3.10 as summarized in table 3.1. There are clear transition points when PE is preferred in terms of image efficiency and actual resolution. For instance, D = 2 $\mu m^2 ms^{-1}$, T_2^* = 10 ms, and G_{max} = 0.5 T/m, resolution degradation for frequency encoding reaches 150% at $\Delta x_{nominal}$ = 10.3 μm vs 4.8 μm for phase encoding. Given the above sample and hardware properties, imaging features < 15 μm is impossible in the FE dimension without the use of phase encoding in that dimension. The benefit of PE is two-fold, SNR is relatively unaffected by diffusion while providing finer resolution than FE. Low N_{acc} values have the added benefit of avoiding compounded systematic error which doesn't average out with increased accumulations [80].

3.7 Conclusion

In this work, we demonstrate the sequence, sample, and image properties which warrant switching from a FE to a PE acquisition. Diffusion during the readout gradient is experimentally demonstrated with shrinking voxel sizes. As has been previously shown in literature, the role of gradient strength in smaller voxels is demonstrated with simulated SNR and actual resolution. Conditions are laid out in which the imaging efficiency of PE greatly exceeds that of FE, an important guidepost for future high resolution MRM experiments. Theoretical resolution broadening in the readout and phase encoded dimensions is experimentally verified via measurement of the PSF. Finally, excised rat spinal cord images at 10 μm in-plane resolution demonstrate a practical scenario where PE exceeds FE's imaging efficiency and image quality at very high resolution.

3.8 Additional information

To investigate if the temperature changes in the sample with the combination of short TRs and microsolenoids, the same solution and capillary were run with the exact same sequence parameters (section 3.4.3.2). Only this time a temperature probe was inserted into the capillary to monitor the temperature of the solution. A coarse ADC map was acquired immediately before and after these sequences to measure change in ADC values. The results are in the following figure:

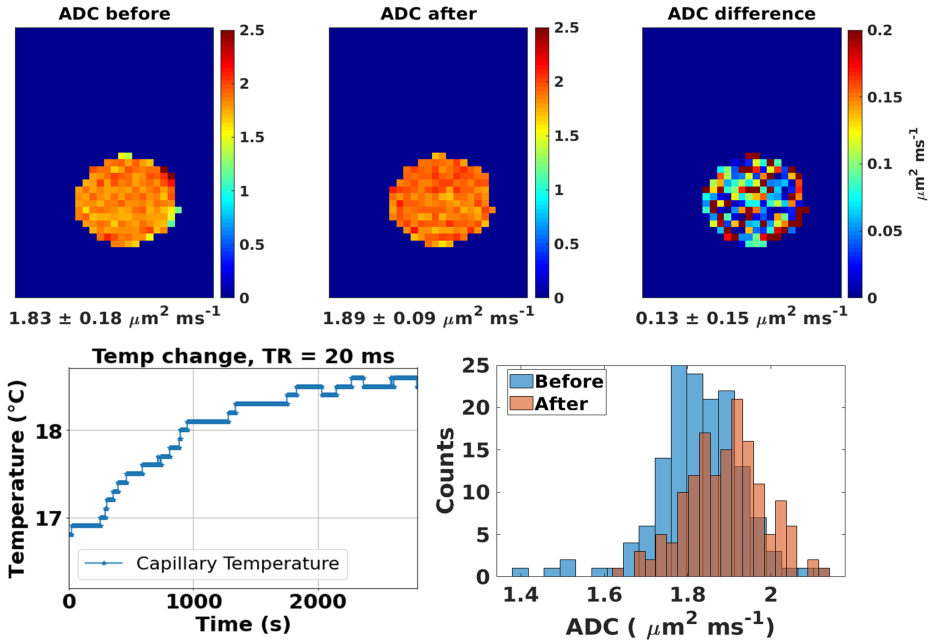

Figure 3.10: Using the exact experimental parameters in 3.4.3.2, temperature was monitored using probe taped to the capillary. Before and after the experiment, coarse ADC maps were acquired with a diffusion weighted spin echo. The final resolution was 27.8 x 26.1 μm in-plane with x 600 μm slice thickness. The temperature started at 16.8 °C and heated to 18.6 °C. For every measurement in figure 3.7, ADC was assumed to be 1.8 $\mu m^2 ms^{-1}$, considering the highest temperature of 18.6 °C, the expected ADC could be closer to 1.9 $\mu m^2 ms^{-1}$. Thus, the largest percent difference in the measured $R^{FE/PE}$ value from a change in the ADC would be 0.6%.

The changes in ADC from temperature agree with the literature [97]. To ensure the change in temperature and thus the ADC did not confound the results of figure 3.7, the "hottest" (18.6 °C) and "coldest" (16.8 °C) ADC values were plugged in to equation 3.8. The percent difference of the R values were all $< 0.7\%$ with the highest being for the

final scan of 10 μm with 0.64%. Since this was the sequence with the shortest TR and roughly an hour of scan time, it can be assumed the other sequences have negligible effect on diffusion.

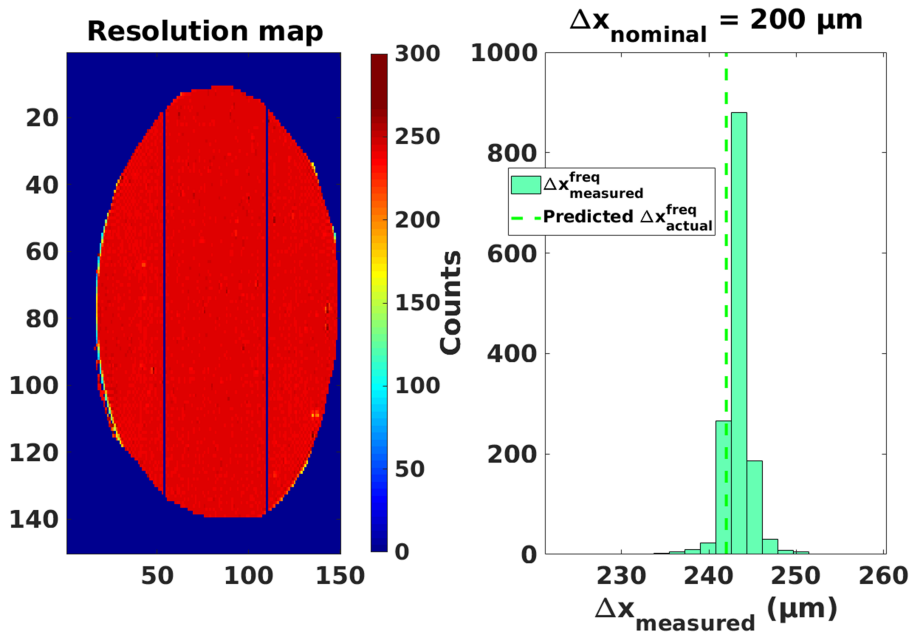

Figure 3.11: An agar phantom was imaged at varying resolutions in the phase and frequency directions. The FWHM of the PSF was measured with a custom FLASH sequence. When the ratio of N_{PSF} to N_x is > 2, the FWHM shows good agreement with the theoretically predicted values given by McFarland. It should be noted that the $FOV_{PSF} = 0.75$ FOV such that the sampling resolution in the PSF direction will always be 3/8 the resolution in the encoding direction when $N_{PSF}/N_x = 2$. Although the measurement will be more accurate with higher PSF sampling resolutions, N_{PSF}/N_x was set to 2 as a compromise of FWHM measurement accuracy and the total time needed to acquire the data.

To determine an optimal N_{PSF}/N_x ratio, a FLASH sequence's PSF with resolutions of 100 and 200 μm was measured with varying ratios N_{PSF}/N_x from 1 to 6 (see figure 3.11). With $FOV_{PSF} = 3/4FOV_x$ and a N_{PSF}/N_x ratio of 2, a 200 μm resolution scan's measured resolution was $\approx$ McFarland's FWHM prediction including sampling, relaxation, and diffusion.

Transverse ADC values of the vary from ≈ 0.1 $\mu m^2 ms^{-1}$ (white matter) to ≈ 0.3 $\mu m^2 ms^{-1}$ (gray matter) which is a little lower than previously reported work of 0.2 and 0.6 $\mu m^2 ms^{-1}$, however this may be due to the samples being prepped differently. In [107],

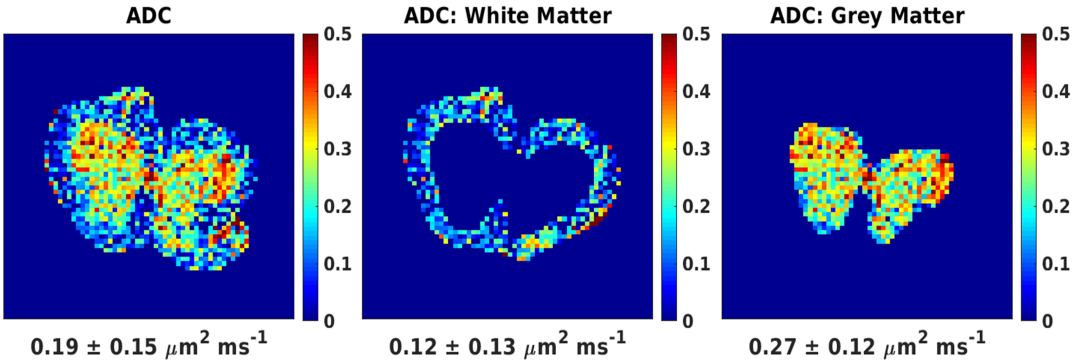

Figure 3.12: A diffusion weighted spin echo was used to generate a transverse ADC map in the frequency encoding dimension (top to bottom of image). The sequence had TE/TR = 13/100 ms, N_{acc} = 16, and a total scan time of 10 min 14 s. The resolution was 78.1 x 78.1 μm with .5 mm slice thickness. There was 1 b0 image and 5 b-values ranging from 100-500 s mm^{-2} with δ = 1.6 ms and Δ = 7.1 ms

samples were imaged in $CuSO_4$ whereas we imaged in Fomblin.

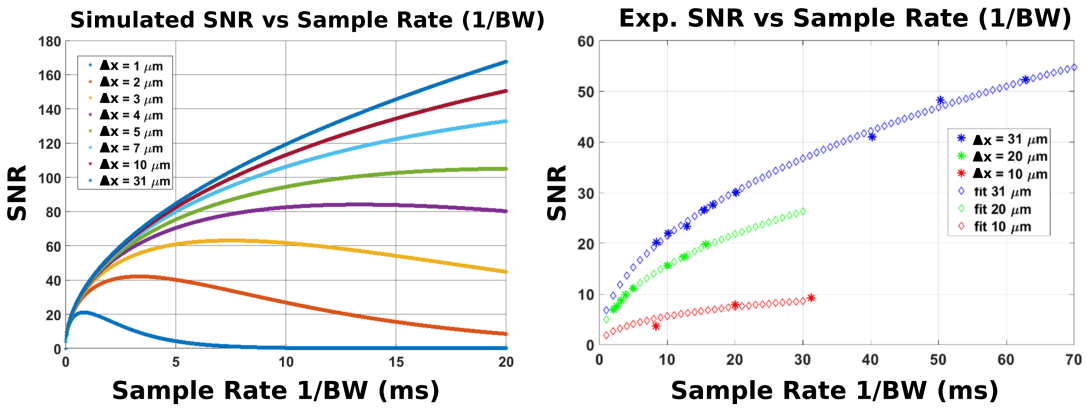

Figure 3.13: Diffusion attenuates SNR with longer and stronger gradients. However, SNR also depends on the total time the receiver is on thus for some smaller voxel lengths, there are optimal dwell times for acquisitions Here T_s = 1/BW. See for example the 1-4 μ m resolution in the plot on the left, where SNR peaks at certain dwell times. The plot on the right is the experimental measurement of this relationship. Notice how the change in SNR is not as drastic with longer dwell times as the voxel size is smaller. This is because diffusion is attenuating the signal.

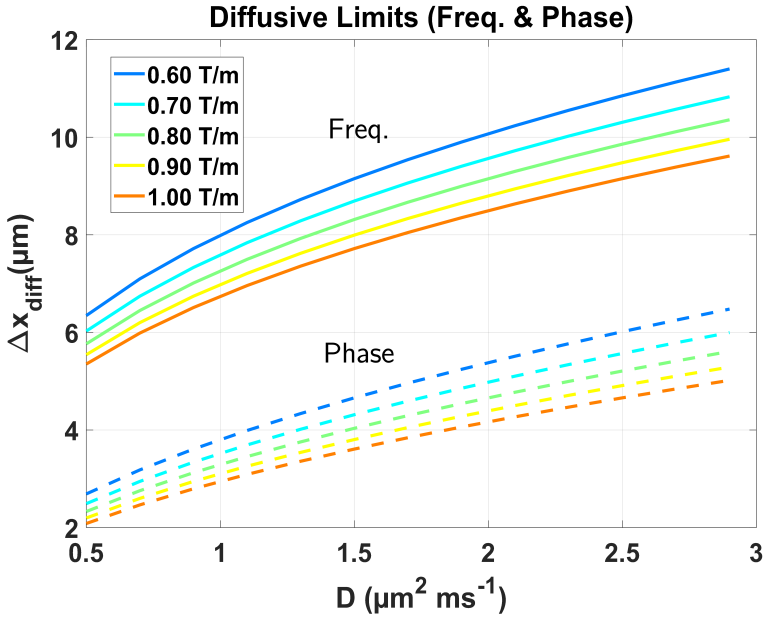

Figure 3.14: Equations 3.13 and 3.14 demonstrate the clear resolution benefit of phase encoding across many gradient strengths and diffusion values. Phase encoding may allow over 4 μm's worth of resolution considering diffusion alone. The actual resolution will be determined by combining the sampling, T_2^*, and diffusion contributions.

CHAPTER 4

A cryogenic tune and match circuit for MRM at 15.2T

4.1 Abstract

Achievable resolution in an MRM experiment is intrinsically limited by finite scan times and the decreased number of spins in smaller voxels. A common method of enhancing SNR is to cryogenically cool the RF coil. SNR gains are only realized when the relative noise of the RF hardware is significant in comparison to the noise produced by the sample. It is difficult to insulate the sample from the extreme temperatures of cryogenic probes and typically samples are desired to be above freezing to avoid signal loss from decreased T_2. We show experimentally it is possible to achieve SNR gains by directly cooling the tune and match circuitry while leaving the loop or solenoid in ambient air with the sample. A microcoil circuit consisting of two tuning capacitors, one fixed capacitor, and SMB coaxial cable was designed to resonate at 650 MHz for imaging on a Bruker 15.2 T scanner. Surface loops and solenoids of varying diameters were tested on the bench to determine the largest diameter coil that demonstrated significant SNR gains from cooling since sample noise increases with coil diameter. A liquid N_2 cryochamber was designed to cool the tune and match circuit, coaxial cable, and connectors while leaving the loop in ambient air. As the cryochamber was filled with liquid N_2, quality factors were measured on the bench while monitoring the coil's surface temperature. Imaging SNR improvements are demonstrated via cooling the tune and match circuit in the bore at 15.2T. For 650 MHz, we reiterate the coil diameters for which cooling with liquid N_2 improves SNR by including the resistance of necessary circuit components. A cryochamber was designed for testing the proof-of-concept. Loops and solenoids < 3 mm in diameter had significant improvement in quality factor on the bench. Resistance contributions of lumped elements such as variable capacitors and the coaxial cable are measured and reduced by cooling. Images are obtained

with a 2 turn, 3 mm diameter surface loop with the matching circuit at room temperature and then cooled with liquid nitrogen to demonstrate SNR improvement by a factor of 2. By cooling the tune and match circuit and leaving the surface loop in ambient air, SNR was improved by a factor of 2. The results are significant because it allows for more space to insulate the sample from extreme temperatures. A cryochamber was designed to cool the tune and match circuit within the bore. A unique Fomblin bath was designed to insulate the sample from extreme temperatures without introducing further noise from circulating water.

4.2 Background

Magnetic resonance microscopy (MRM) is potentially capable of resolving cellular features [63, 108, 74, 49, 75]. With its many contrast mechanisms and ability to probe structure deep within intact tissue, MR is an attractive imaging method for understanding biological systems such as the pharmacokinetic effects of cancer killing drugs on vasculature [109] or renal pathology [110]. As voxels shrink in size, the number of excitable spins quickly diminishes. Furthermore, diffusion attenuates signal and blurs the point spread function ultimately limiting the achievable resolution [111, 71, 47, 45]. Many methods have been promoted to overcome the SNR and resolution limitations of MRM. Increased sensitivity is often achieved by using smaller RF coils typically referred to as microcoils [31] as SNR is inversely proportional to the coil diameter. The smallest reported microcoils are usually surface loops or solenoids 100 - 500 μm in diameter. The highest resolution MRM images achieved are ≈ 3 μm [61, 62] with the highest being 2.7 μm isotropic where the sample and coil were cooled with liquid helium. Cooling circuitry and hardware is often necessary for many electronic applications and industries [112, 113]. Hoult is credited with directing the field of MR towards cooling RF coils [30] although the idea was certainly not original. Cooling hardware is common in multi-nuclear MR. By cooling the preamp and RF coil with liquid helium an SNR improvement of 9 was achieved for ^{13}C spectrum at 1T and

small liquid samples [114]. For larger loops and samples, and lower Larmor frequencies, SNR factors of improvement range from 1.5 – 3x [115, 22, 116, 57].

High-temperature superconductor (HTS) RF coils demonstrate promising increases in SNR however they suffer from non-linear B_0 dependencies, temperature sensitivity, and hysteretic behavior [59]. For cryogenically cooled and HTS coils, the relative noise contributions of the sample should be small or negligible to maximize the SNR gain from cooling. An example of this for a relatively large sample would be a recent study that cooled a 14 channel ^{13}C head coil. The design chose a surface loop size that optimized the tradeoff between B_1^+ sensitivity depth and SNR gain from cooling with liquid nitrogen (N_2) [117]. For larger heterogeneous samples, the estimation of sample noise is not trivial and usually is precisely calculated with time consuming simulations (see appendix C) or inferred from Q-factor differences [118, 22]. Whether surface loop or solenoid, the inductor is often cooled via immersion or contact with a cold head. Thus, when the sample is very close to the coil, as is often the case, a key challenge is insulating the sample from the extreme temperatures to avoid signal loss due to shortened T_2 relaxation in a frozen sample. There have been no reported cases of immersion cooling of only the coaxial cable and tune and match circuit while keeping the inductor in open air. Thus, we aim to leave the inductor in ambient air with the sample while cooling the tune and match circuit to liquid N_2 temperatures. The resistance contributions of the transmission line elements are investigated at varying temperatures. SNR gains are demonstrated by flooding the tune and match circuit in a custom-built double walled N_2 chamber. The chamber is designed such that the inductor and sample are in open air and only the tune and match components and coax are immersed in N_2. To the author's knowledge, this is the first use of a cryogenically cooled circuit while keeping the inductor of the RF coil outside of the cryogenic environment in ambient air.

4.3 Theory

4.3.1 Motivation for cooling

Most MRM images taken at $< 10\ \mu m$ resolution take tens of hours to achieve acceptable SNR [63, 64]. This can be understood with the following equation formulated by Mansfield and Morris [65, 43], where the scan time needed for a finite volume (Δx^3) is

$$t_{vol} = (SNR_0)^2 d^2 \frac{T_1}{T_2} \frac{2.8 \times 10^{-15}}{(f_0^{7/2}} (\frac{1}{\Delta x})^6 \tag{4.1}$$

where SNR_0 is the combination of hardware sensitivity and noise, d is the coil diameter, T_1 the spin-lattice relaxation, T_2 the spin-spin relaxation of the sample, f_0 is the Larmor frequency, and Δx is the dimension of the voxel where $(\Delta x)^3$ is the volume of the signal origin. The severe time requirements of voxels smaller than 5 μm isotropic are demonstrated in figure 4.1. Smaller coil radii defer the drastic increase in time requirements for increased resolution at fixed SNR. Eq. 4.1 does not include signal attenuation due to diffusion [111] (see ch. 3). A small SNR increase results in significant time advantages for MRM. For example, the time requirements for a 4 μm isotropic image are more than halved from 15 to 7 hours when SNR is improved by 1.5 via cooling (figure 4.1).

4.3.2 Resistance contributions

The noise in the MR experiment is given by the following equation

$$Noise_{MR} = \sqrt{4 k_b BW T_{total} R_{total}} \tag{4.2}$$

Where k_b is boltzmann's constant, T_{total} is the temperature of the system, BW is the bandwidth of the receiver, and R_{total} is the combined series resistances of the hardware and sample which may be written as

$$R_{total} = R_{sample} + R_{circuit} \tag{4.3}$$

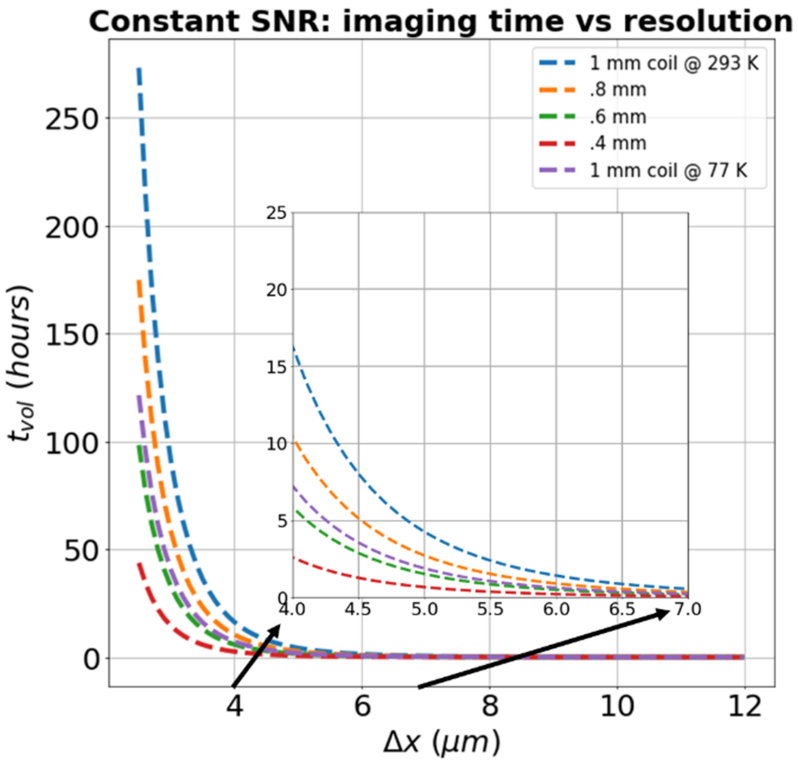

Figure 4.1: By cooling a 1 mm coil with a modest SNR improvement factor of 1.5, the time requirements for imaging at 4 μm isotropic drop from 16 to 7 hours.

The relative contributions of the sample and coil have been well characterized and studied [30, 98]. Darrasse and Ginefri have the most thorough discussion surrounding the relationship between frequency, sensitivity, coil size, and temperature [32]. SNR gain from cooling the hardware is most effective when the noise is dominated by the RF receiver chain with negligible contributions from the sample. This so-called coil noise dominated regime is described by Darrasse and Ginefri across frequencies, coil sizes, and temperatures. Their estimate of the coil and sample noise dominated regimes uses a surface loop and an infinite conductive sample. Although their description is salient it may leave the cryogenic RF coil designer with an underestimate of the noise contributions of the RF receiver chain. By including resistance contributions of a necessary variable capacitor with a generous Q of 1000 and a modest lead length of 5 mm the coil noise dominated region is pushed out towards increasing coil diameters (figure 4.2).

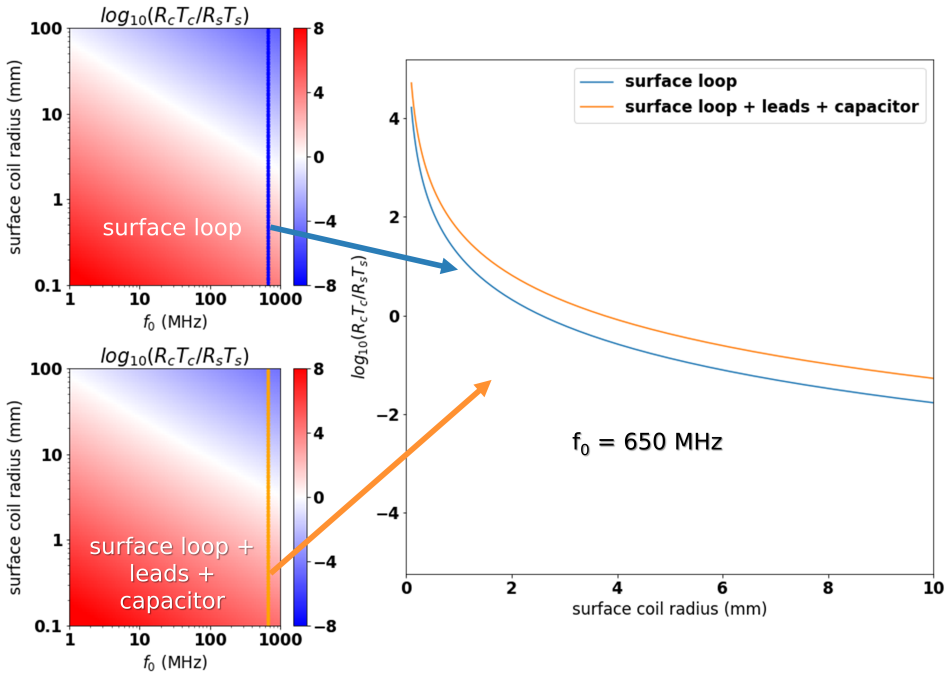

Figure 4.2: By considering series resistance contributions of the capacitor (Q=1000) and necessary leads to the inductive loop, larger coil sizes are included in the coil noise dominated region. The capacitor and lead losses are not trivial in the RF receiver chain for microcoils at 650 MHz.

The two main contributions of noise from the sample are magnetic and dielectric losses

where

$$R_{sample} = R_{magnetic} + R_{dielectric} \tag{4.4}$$

The most thorough work considering sample losses for a microcoil are the two publications by Minard and Wind [1, 2] which have the most specific and experimentally verified description of the dielectric losses from the sample. The following passages follow their work closely with some further simplification and extrapolation to higher frequencies.

4.3.2.1 Sample magnetic losses

In a conducting sample, magnetic losses incur due to induced eddy currents by the rotating magnetic field from the RF coil. For a homogeneous sample of cylindrical shape, these losses may be written as,

$$R_{magnetic} = \frac{\pi \omega_0^2 \mu_0^2 n^2 A^4 B \sigma}{128(d^2 + B^2)} \tag{4.5}$$

Where ω_0 is f_0 in radians, μ_0 is the magnetic permeability of free space, n is the number of turns, A is the sample radius, B is the sample length, and σ is the conductivity of the sample. For microcoils, magnetic losses in the sample contribute much less than the dielectric losses (figure 4.12).

4.3.2.2 Sample dielectric losses

Dielectric loss is typically characterized with the loss tangent or tan δ of a material and is frequently used by RF engineers when selecting materials such as circuit substrates. Since the electric field lines inevitably pass through the conductive sample, energy is dissipated in the form of conduction, dielectric relaxation, and dielectric resonance [119, 120]. Modelling the dielectric loss can be quite complicated without full-wave simulation thus Minard and Wind [2] approximate the resistance by modeling the coil and sample as equivalent circuit models. By combining Minard and Wind's equations 18-20 and 22-26 a more

simplified expression is obtained for the effective dielectric losses from the sample

$$R_{dielectric} = \frac{0.5\omega_0^3 L^2 C_{stray} \varepsilon'' f_d}{\varepsilon''(1-f_d)^2 + f_d^2(\varepsilon'-1)^2 + \varepsilon'^2(1-2f_d) + 2\varepsilon' f_d)} \tag{4.6}$$

Where L is the inductance of the coil, ε is the complex frequency dependent permittivity of the sample where $\varepsilon(\omega) = \varepsilon'$ - iε'', and f_d is the experimentally determined dielectric filling fraction of the coil. C_{stray} is the parasitic capacitance of the coil outlined by Medhurst [33], where

$$C_{stray} = d(0.1126\frac{l_{coil}}{d} + 0.08 + \frac{0.27}{\sqrt{l_{coil}/d}}) \times 10^{-10} \tag{4.7}$$

Where l_{coil} is the length of the solenoid or width of surface loop. We follow Minard and Wind's experimentally verified approach and set f_d = 0.948 since the coil sizes investigated here are similar. The frequency dependent complex permittivity of ionic samples is well-studied and may be calculated using the following equations.

$$\varepsilon(\omega)' = \varepsilon_\infty + \frac{\varepsilon(0) - \varepsilon_\infty}{1+\omega^2\tau^2} \; and \; \varepsilon(\omega)'' = \frac{\sigma}{\omega\varepsilon_0} + \frac{(\varepsilon(0) - \varepsilon_\infty)\omega\tau}{1+\omega^2\tau^2} \tag{4.8}$$

Where ε_∞ and ε_0 the permittivity at very high and low frequencies, τ is the dielectric relaxation time, and ε_0 is the permittivity of free space. For an ionic water solution at 25 °C with σ = 1 S/m, $\varepsilon(0)$ = 78.32, ε_∞ = 5.30, and τ = 8.27 $\times 10^{-12}$ [121].

4.3.2.3 Resistance contributions of the circuit

Capacitors, connectors, coaxial cable, the loop, and the small trace area for the tune and match circuit all contribute to the total resistance of the coil. Since hardware dominates the noise in a microcoil [22, 50], small changes in the circuit topology could result in significant changes in the SNR of the circuit. The total resistance of the coil may be expressed as a series of resistive elements where

$$R_{circuit} = R_{coax} + R_{connectors} + 2R_{cap} + R_{coil} \tag{4.9}$$

where R_{coax} is the resistance of the coaxial cable, $R_{connectors}$ the resistance from cable connectors and leads between elements, R_{cap} is the resistance of a variable capacitor multiplied by 2 for the tune and match capacitor, and R_{coil} the resistance of the resonating geometry such as a solenoid or surface loop. Most of these items have losses characterized by industry standard resonant line methods [122]. For the coaxial cable, textbooks, online calculators, and the product data sheets provide loss per unit length [123] and connectors have added resistance which can usually be found in their respective data sheet. When calculating resistance of the leads and coil, it is important to account for the resistive contribution of the skin effect. At higher frequencies, Faraday's law of induction induces the skin effect and the current effectively travels on the outermost part of traces or wires within the circuit. Since resistance is inversely proportional to the cross-sectional area of the conductor, the resistance increases as the skin depth decreases. The skin depth is given by the following equation:

$$\delta = \sqrt{\frac{\rho}{\pi \mu_0 \mu_r f_0}} \tag{4.10}$$

where ρ is the resistivity of the conductor (1.72×10^{-8} Ωm for Cu at 293 K) and μ_r is the relative permeability of the conductor ($\mu_r \approx 1$ for Cu). It is interesting to note that ρ is temperature dependent and could be lowered with temperature or a better conductor such as silver [124, 125]. Minard et al. and Hoult et al. use the skin effect to calculate the resistive contributions from wire for the leads and a solenoid [30, 2]. For a solenoid the resistance may be described with the following equation:

$$R_{solenoid} = \frac{l\xi}{d_{wire}} \sqrt{\frac{\mu_0 \mu_r \rho f_0}{\pi}} \tag{4.11}$$

where l is the total wire length (l = ndπ), d_{wire} is the wire diameter, and ξ is the resis-

tance enhancement factor to account for the added eddy currents from adjacent turns. The ξ factor is determined by the theoretical predictions of Butterworth [126] and was experimentally verified by Medhurst [33]. The ξ values may be found for varying d/l_{coil} and d_{wire}/s ratios in table 1 of Medhurst and Minard et al where s is the spacing between turns (s = l_{coil}/n). ξ may be calculated by interpolating across the table. For a surface loop the resistance is given by Darrasse and Ginefri,

$$R_{loop} = \frac{2d\xi n^2}{d_{wire}}\sqrt{\rho\mu_0\pi f_0} \tag{4.12}$$

For a capacitor the equivalent series resistance (ESR) may be related to the Q, operating frequency, and capacitance with the following equation:

$$R_{cap} = \frac{1}{2\pi f_0 Q_{cap} C} \tag{4.13}$$

where Q_{cap} is the quality factor of the capacitor and C is its capacitance. Most MR RF circuits utilize at least two variable capacitors for tuning to the Larmor frequency and matching the characteristic impedance (Z_0 = 50 Ω).

4.3.3 Relative contributions considering coil size and temperature

The calculated SNR gains may then be inferred [115] by combining equations 4.2-4.13 where

$$SNR_{gains} = \frac{SNR_{N_2}}{SNR_{RT}} \propto \frac{\sqrt{T_{sample,RT}R_{sample,RT} + T_{circuit,RT}R_{circuit,RT}}}{\sqrt{T_{sample,N_2}R_{sample,N_2} + T_{circuit,N_2}R_{circuit,N_2}}} \tag{4.14}$$

The SNR gains may be further related to the temperature and resistance of each circuit element in equation 4.9.

$$\frac{SNR_{N_2}}{SNR_{RT}} \propto \frac{\sqrt{T_{sample,RT}R_{sample,RT} + T_{cap,RT}R_{cap,RT} + T_{coax,RT}R_{coax,RT}\cdots}}{\sqrt{T_{sample,N_2}R_{sample,N_2} + T_{cap,N_2}R_{cap,N_2} + T_{cap,N_2}R_{cap,N_2}\cdots}} \tag{4.15}$$

Predictions for a solenoid and surface loop are plotted in figure 4.3 utilizing equations 4.2-4.15. SNR gains are plotted for both geometries with two scenarios: 1) cooling the full circuit (every element in eq. 4.9) to liquid nitrogen temperatures 77K and 2) partially cooling the resonant geometry while cooling the rest of the circuit to 77K.

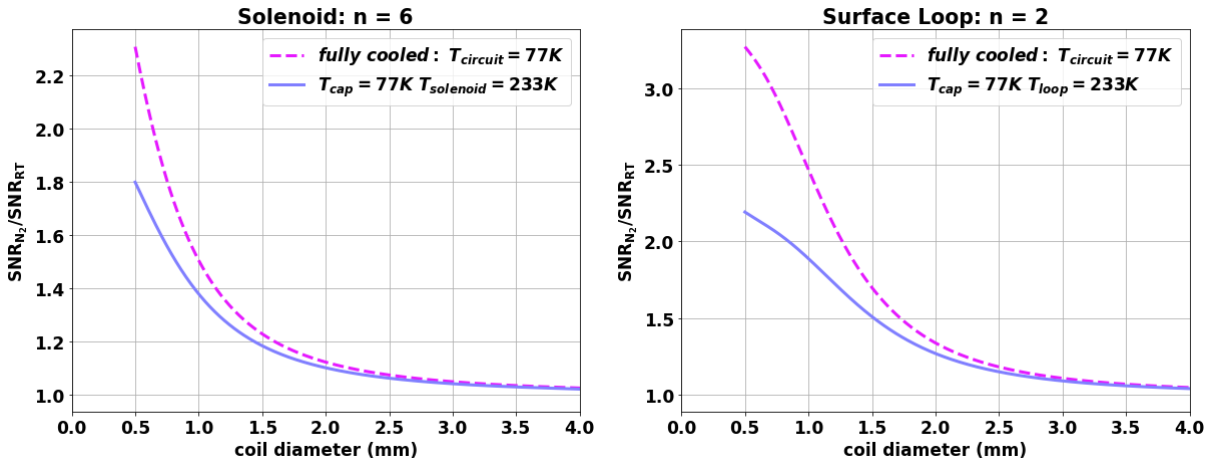

Figure 4.3: Predictions for two microcoil geometries. The dashed line represents SNR gains from cooling the entirety of the circuit to liquid nitrogen temperatures (77K). The solid line represents partially cooling the solenoid/loop to 233K and cooling the rest of the circuit to 77K. The model does not account for the capacitor change in Q with temperature.

In figure 4.3, the sample had a conductivity of 0.5 S/m and was scaled with the coil size where A = 0.8d and B = $5l_{coil}$. The surface loop had a fixed length. The solenoid length scaled with coil diameter where $l_{coil} = 1.2d$. The quality factor of the capacitor was set to 2000. All equations and figures from section 2 are available on github at https://github.com/benjhardy/Coil_vs_Sample_Noise_MRI including the coil class that summarizes Minard and Winds publications in a python class for ideal micro-solenoid design choices.

4.4 Methods

4.4.1 The magnet and equipment

All images were acquired with a Bruker (Billerica, MA) 15.2T Biospec imaging spectrometer equipped with max 1 T/m magnetic field gradients (Resonance Research Inc, Billerica,

MA). The Avance III console used ParaVision 6.0.1. The bore is 6 cm in diameter within the gradients with 3rd order B_0 shims. All Q measurements were performed with a Keysight (Santa Rosa, CA) ENA Network Analyzer E5080A. All temperature measurements were performed with an Amprobe (Everett, WA) TMD-56 multilogger thermometer and flat-pin, k-type, thermocouple probes. LCR measurements at 100 kHz were performed with an Agilent (Santa Clara, CA) 4263B LCR meter. Custom 3D prints were designed in SolidWorks (Waltham, MA) and printed with a FormLabs (Somerville, MA) Form 3 printer with tough resin 2000. The small surface loop and circuit trace was milled using an LPKF (Garbsen, Germany) Protomat S103 PCB router. The substrate of the surface loop was Rogers (Chandler, AZ) R3006. Solenoids were wound around Drummond (Broomall, PA) capillaries using copper wire. Air tubular trimmer capacitors were acquired from Passive Plus Incorporated (Huntington, New York) and had a capacitance range of 0.3-10 pF. Temperature of the Fomblin (Solvay, Brussels, Belgium) bath was maintained using a Fisherbrand (Waltham, MA) Isotemp Refrigerated/Heated Bath Circulator.

4.4.2 Liquid N_2 chamber

The following description is supplemented by figure 4.4. The structure may be broken down into the following 4 key components: the surface loop and tune and match circuit, the dual walled liquid N_2 chamber, the N_2 in/outlet where o-rings seal the tune rods, and the garolite housing and insulative materials.

4.4.2.1 Surface loop and tune and match circuit

Beginning at the front of the chamber, the surface loop is soldered onto leads protruding from the cryochamber. The solder and seal are further solidified with a layer of epoxy (figure 4.4B). The surface loop was inspired by the design used by Lee and coworkers to image mammalian myofibers [64]. The number of turns in the loop was limited to 2 within the 3 mm diameter. For a closer look at the surface loop design see figure 4.14. The loop was placed $\approx$ 1.5 mm away [127] from the sample with the PCB dielectric and

thin layer of glass between sample and loop. The cryochamber is a 3.19 cm OD, 2.54 cm ID garolite tube threaded on each end so that custom garolite caps are screwed in with a watertight seal. Each thread was wrapped tightly with 3-5 layers of Polytetrafluoroethylene (PTFE) tape and were fitted with low temperature o-rings. The threaded front cap of the cryochamber was hollowed out so that the small tune and match circuit could fit tightly inside. The width of the garolite wall between the surface loop and the circuit where N_2 flows freely was $\approx$ 3 mm. The tune and match circuit was as simple as possible to ensure it fit within the $<$ 2.54 cm diameter cap. The hollow slot was machined to $\approx$ 15 mm to fit the circuit snugly. The circuit consisted of a variable series matching capacitor, a variable parallel tuning capacitor, and a fixed series capacitor (figure 4.13) to ensure the circuit was as balanced as possible.

4.4.2.2 Dual-walled liquid N_2 chamber

The dual-walled chamber consisted of the 2.54 cm ID garolite tube surrounded by ultra-thin low temperature aerogel insulation. The insulation was then surrounded by the 2nd wall which consists of ultra-low temperature garolite tube with OD 5.08 cm and ID of 4.45 cm. The front of the dual walled chamber has a larger cap that threads into the outermost tube and surrounds the innermost tube with an opening for the surface loop leads (figure 4.4 B,C). The back of the dual walled chamber had another garolite cap that threaded into the outermost tube. The two front and back caps were necessary to maintain the position of the internal tube which was sitting on layer of aerogel insulation. The threaded external back cap also functioned as a fixed point for the o-ring compression mechanism (figure 4.4D).

4.4.2.3 N_2 input/exhaust and o-ring compression point

The internal cap threaded into the cryochamber had 5 holes; N_2 input tube, exhaust tube, 2 tune rods, and the coaxial cable. The N_2 input tube was threaded and sealed with PTFE tape. The coax and exhaust tube were sealed with an external layer of epoxy. A key challenge in the design was simultaneously allowing the tune rods to rotate while maintaining

a liquid N_2 tight seal. This was accomplished by using low temperature vacuum grease and low temperature o-rings. The o-rings were compressed by a custom garolite disk that pressed the o-rings around the tune rods and against the wall of the internal cap. The o-ring compression piece was tightened with screws into the external cap. To maintain the seal, the whole chamber was cooled down to liquid N_2 temperatures and the screws were re-tightened to ensure any shrinkage from lower temperatures was accounted for. N_2 input flowed directly from a 240L dewar with a 6.1 m vacuum jacket extension. The extension was sealed to a barb end using PTFE tape. A 10 cm plastic tube connected the barb to the N_2 input at the back panel of the cryochamber. The tube was clamped to the barb and N_2 input tube for a tight seal.

4.4.2.4 Garolite housing and insulating materials

Surrounding the external cap and o-ring compressor was another 5.08 cm OD low temperature garolite tube. The tube followed the input and exhaust tubes, coax, and tune rods as structural support and acted as another layer of insulation surrounding the input tube (figure 4.4E). A small amount of aerogel insulative material was placed inside the housing although most of its volume was ambient air. The remaining space between the housing and wall of the bore (6cm diameter bore) was filled with aerogel insulation, a small layer of heat shrink, and Kapton tape (figure 4.4F).

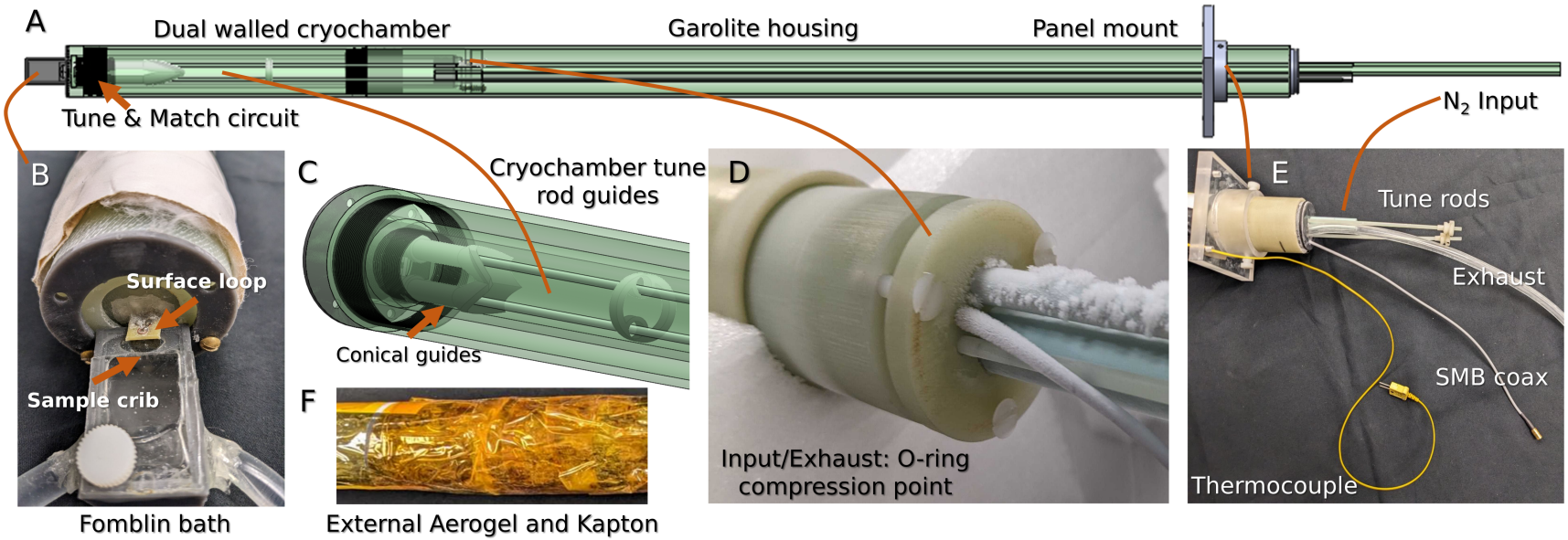

Figure 4.4: The cryochamber key components include the tune and match circuit and surface loop (A and B), the dual walled cryochamber (A and C), the input/exhaust and o-ring compression point (D), and the garolite housing and insulative material (A and F). The Fomblin bath is installed onto the front external cap via brass screws (B). Within the chamber conical guides were 3D printed to thread onto the variable capacitors (C). A floating guide was also placed within the chamber to ensure the rods contacted the conical guide (loop in C). The o-rings were compressed with a garolite disk mounted onto the back external cap (D). Tune rods, exhaust, SMB coax, and input line flowed through the housing past the magnet panel mount for easy access (E). The surface of the entire assembly was surrounded by Aerogel, heat shrink, and Kapton tape for insulation (F).

4.4.3 Sample crib and Fomblin bath

In some bench tests (see 4.5.1 and 4.5.2), the sample would freeze since the coil wires are indirectly cooled via thermal conduction. To maintain sample temperature above 0°C a sample insulation system was designed utilizing a small Fomblin bath (figure 4.5). Temperature controlled water circulated through a plastic tube embedded into the Fomblin bath. The setup exploits existing systems for temperature control in the bore while avoiding any artefacts from the flow of water near the FOV. The Fomblin is invisible to the MR experiment thus there is negligible added noise. The sample crib was designed within a small cage so that any air bubbles would be trapped on the outside of the FOV at the surface of the bath. The Fomblin bath was covered and sealed using a hot glue and thin microscope glass. The water was run at room temperature for testing within the bore.

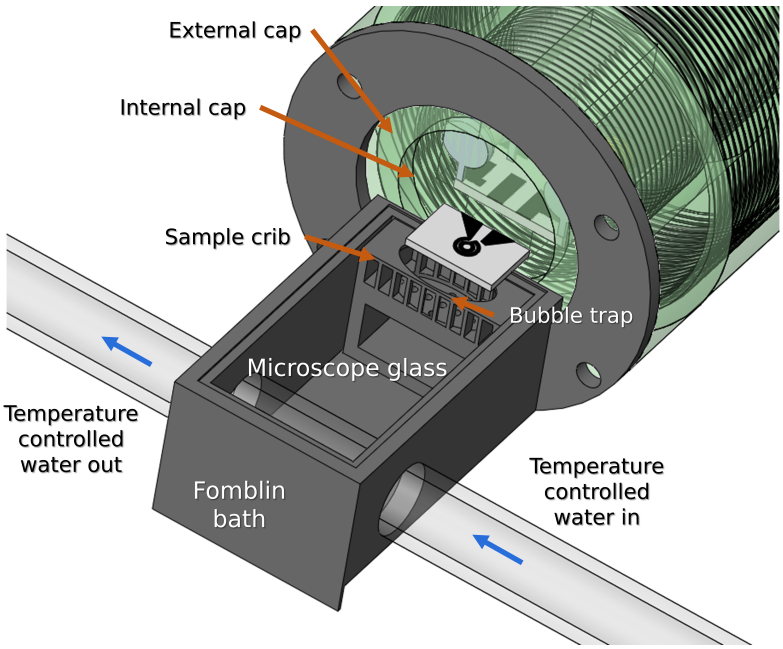

Figure 4.5: The Fomblin bath was designed to insulate the sample from extreme temperatures on the surface of the internal cap and the trace of the surface loop. Temperature controlled water flows through a plastic tube that heats the Fomblin and inevitably the sample via convection. The sample is suspended in a crib directly under the surface loop. The crib acts as a bubble trap if bubbles are kept on the opposite side of the sample. A small microscope glass slide was placed over sample crib to minimize the distance between the coil and sample.

4.4.4 Bench measurements

4.4.4.1 S_{11} quality factor measurement

After an Open-Short-Load (OSL) calibration on the network analyzer, the coil is tuned and matched to resonate at 650 MHz. The S_{11} curve is exported for processing with a python script where the peak and the -3 dB points to the left and right of the resonance are used to determine the bandwidth at half-power or the full-width-half-max (FWHM) on the linear scale. The quality factor of the resonating circuit is then calculated with the following equation:

$$Q(S_{11}) = \frac{2f_0}{(f_{right}(-3dB) - f_{left}(-3dB))} \tag{4.16}$$

where f_0 is the resonance frequency and $f_{right,left}(-3dB)$ are the frequencies to the right and left of resonance at -3 dB. The factor of 2 accounts for the signal's forward and backward traveling wave.

4.4.4.2 S_{21} shunted lumped element ESR measurement

Data sheets of the capacitors do not contain Q measurements at varying temperatures. A vector network analyzer (VNA) was used to assess the effect of temperature on the ESR of the tune and match circuit. The ESR measurement may be performed with some caveats. Mainly the measurement is only accurate at the capacitor's self-resonance and when it's below 1 GHz to avoid confounding influences of parasitic high frequency effects. Placing circuit elements as shunted circuits (i.e. parallel) at the ends of coaxial cables is the most accurate method of measuring ESR with a network analyzer [128]. Each element was placed in parallel with two BNC connectors after a full through open short match calibration (TOSM) and S_{21} was measured. The ESR at the self-resonance of the element may then be calculated using the following equation, derived from simple 2-port systems.

$$ESR(S_{21}) = \frac{Z_0}{2(\frac{1}{10^{S_{21}/20}} - 1)} \tag{4.17}$$

where Z_0 is the characteristic impedance of the transmission line which is 50 Ω. 3 variable capacitors, an open 87 cm length of RG174, and a fixed 200 pF capacitor were placed in parallel between the BNC connectors. The lumped element was then carefully placed over the N_2 bath. The S_{21} curve was acquired. The element was then lowered into the N_2 bath and the S_{21} measurement was acquired again.

4.4.4.3 LCR measurements of ESR at 100 kHz

Using an LCR meter, ESR measurements at 100kHz were done on the following circuit elements: 3 variable capacitors, the surface loop, a fixed 39 pF capacitor, shorted RG174 coaxial cable, and a shorted SMB to PCB connector. The measurement was done by carefully placing each element between the LCR probe ends. 10-15 ESR measurements were taken at room temperature. The element was then gently dipped into an N_2 bath, and 10-15 measurements of ESR were taken. Before measuring the subsequent elements, the probe was allowed to return to ambient temperatures.

4.4.5 Imaging experiments

To verify that bench tests translated to SNR improvements for MR imaging, a series of images were acquired as the cryochamber cooled down. The following is a description of the experimental setup and the corresponding results. The water circulator for the Fomblin bath was set to 22°C (slightly warmer than the scanner room, 18°C). A thermocouple was placed at the observed coldest point of the external insulation on the cryochamber. After tuning, matching, shimming ($\lambda = 85\ Hz$), and power calibration, sets of FLASH images were acquired at room temperature. The images were 128 x 128 pixels, averaged over 2 acquisitions with 4 slices and 10 repetitions making for a total of 40 images for each set. The FOV was set to 30 x 30 mm with 600-micron slice thickness. TE/TR = 2.6/50ms and

the total time for the set was 2 min 8s. This same set of 10 images x 4 slices was acquired as the cryochamber cooled down. To avoid damaging the water-cooled gradient coil, cooling of the surface of the cryochamber was limited to ≈ -25°C.

4.5 Results

4.5.1 Quality factor measurements on the bench without cryochamber

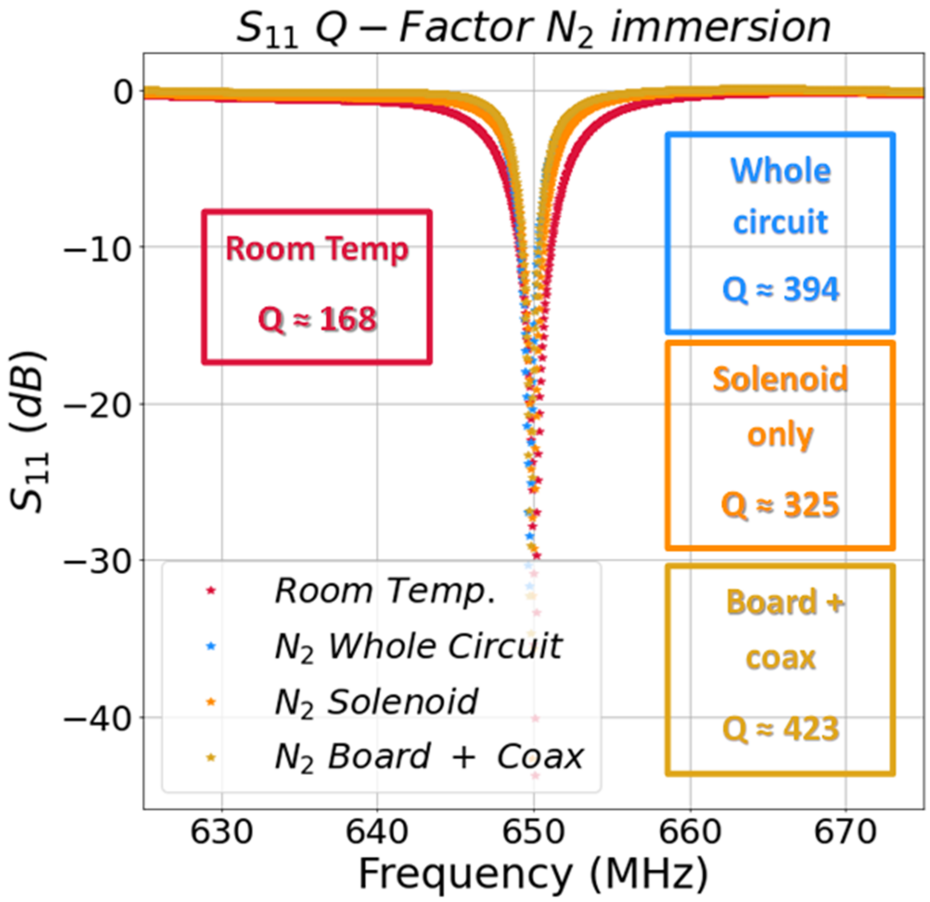

Figure 4.6: Using a 0.9 mm solenoid, immersing the circuit in liquid N_2 results in increased Q factors as characterized by the S_{11} on the bench. The Q-factor enhancement, 168 to 423, corresponds to an SNR increase by at least a factor of 1.6. Further gains from decreased temperatures of the coil may also be realized.

For Johnson noise or thermal noise from the circuit, R $\propto Q^{-1}$. A simple experiment was designed on the bench to investigate if immersing certain regions of the circuit and leaving others in ambient air would result in improved Q factors. Immersing the whole circuit

including the solenoid resulted in ΔQ corresponding to an SNR increase of 1.5. Immersing only the 0.9 mm solenoid resulted in ΔQ corresponding to an SNR increase of 1.4. By including 10 cm of the coaxial cable in the immersion, the Q factor increased the most and corresponded to an SNR increase of 1.6. The results of the test are in figure 4.6.

4.5.2 Quality factor measurements with cryochamber

Several Q-factor measurements were carried out with the cryochamber. The results are summarized in table 4.1. The initial circuit configuration (circuit 1 in table 4.1) consisted of 2 variable capacitors and 2 fixed capacitors. Later this design was modified to include only 1 fixed capacitor (circuit 2 in table 4.1). For a schematic of the two circuit configurations see the figure 4.13. Solenoids and surface loops ranging in size from 0.9-4 mm in diameter were investigated on the bench. The final design (surface loop v2 in table 4.1) demonstrated promising Q improvements corresponding to an SNR improvement of 1.26. The sizes investigated were informed by the calculations in section 2 and results of figure 4.3. The results in figure 4.3 agree with the experimental data presented here as a solenoid with a diameter of 4 mm demonstrated no improvements in Q when cooled. The final surface loop design was tested again this time while monitoring the temperature of the outside Kapton insulation of the coil. Once the Kapton reached 6 °C the Q was measured. The Q improved from 34 to 37.4 as the Kapton's initial temperature dropped from 22 to 6°C (final row in table 4.1).

An example Q-factor improvement is shown in figure 4.7 including the S_{11} curve after the solenoid has cooled down. As the cryochamber is cooled, the resonance shifts upwards $\approx$ 5 MHz. The circuit must be retuned and rematched back to resonance once cooled.

To correlate Q with the temperature of the 3 mm surface loop a thermocouple was placed on the epoxy covered loop while the chamber cooled down. The change in Q and expected increase in SNR is plotted in figure 4.8. The Q-factor increases from 52 at 22 °C to 83 once the coil reached -42 °C. For each point, the circuit is retuned and matched.

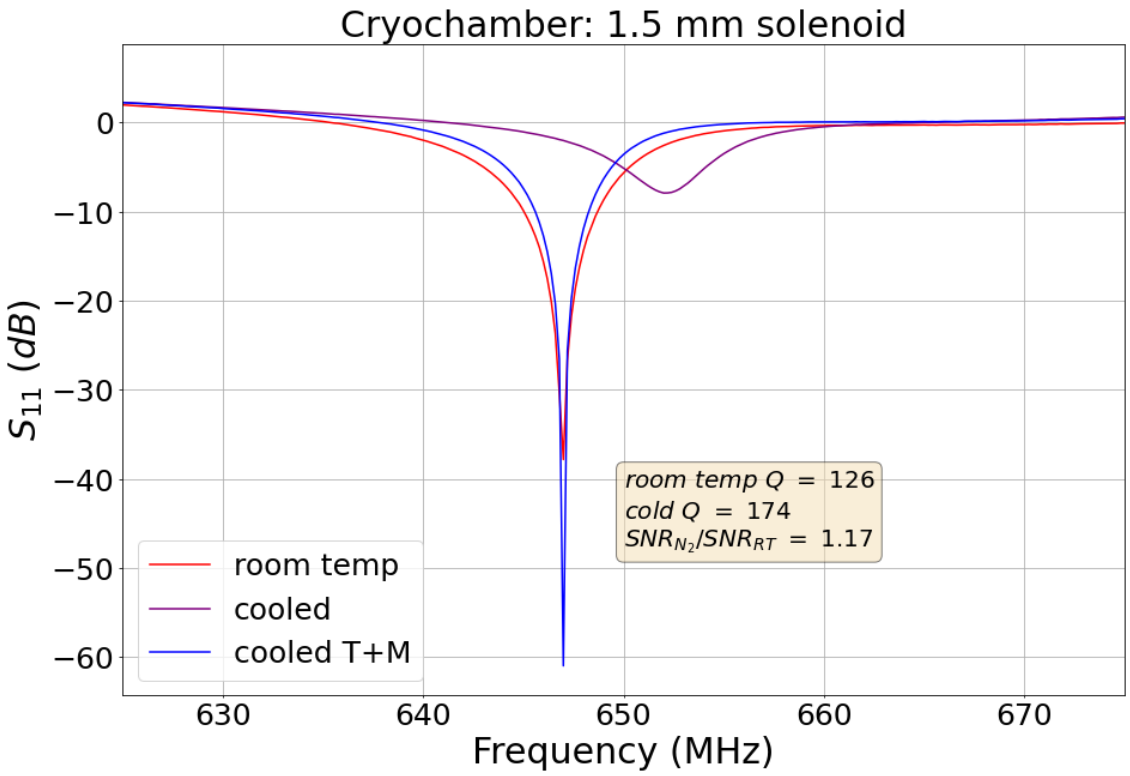

Figure 4.7: An example of the S_{11} curves before (room temp), during (cooled), and after retuning and matching (T+M). While the system cools the frequency is shifted upwards about 5 MHz. After retuning and matching, the quality factor is improved.

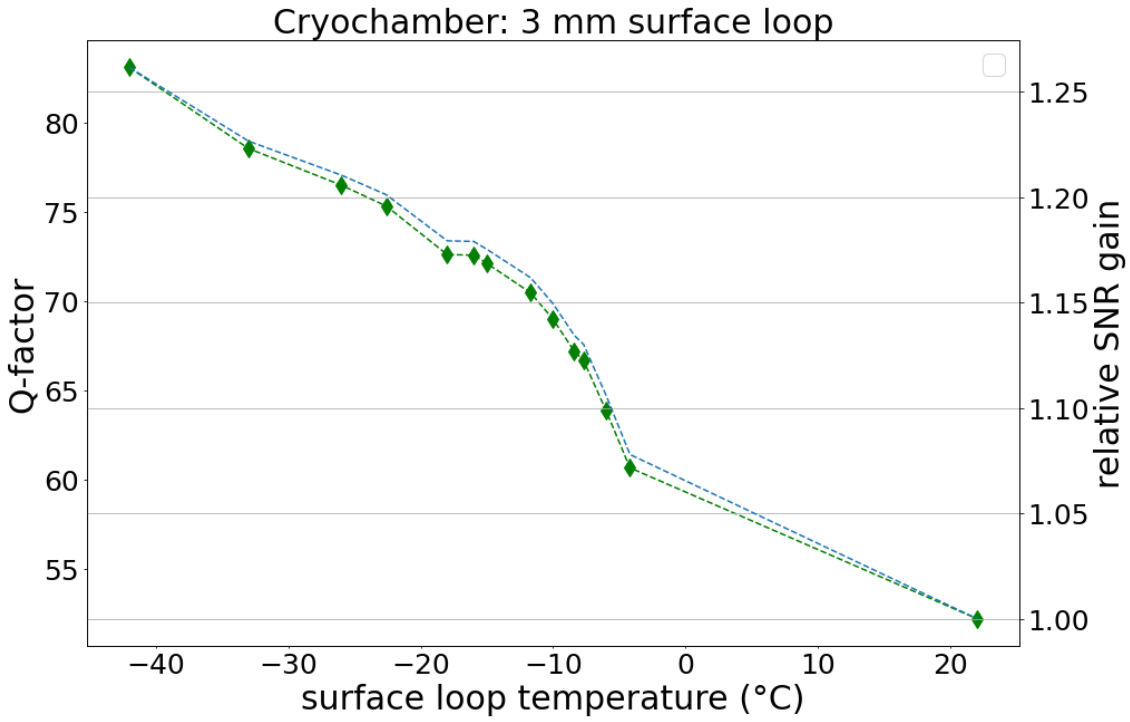

Figure 4.8: Quality factor measurements were acquired as the coil 2 turn 3 mm surface loop was cooled down. The temperature of the surface loop was measured using a thermocouple. As the surface loop cools, the Q-factor changes significantly with the peak SNR gain being 1.26.

The abrupt increase at -5°C to -20°C may be due to the phase changes of the gaseous N_2 condensing to liquid as the internal system cools down.

4.5.3 Imaging experiments

The 20 room temperature images had an average SNR of 26.06 and standard deviation of 0.32. The temperature on the cryochamber housing at these measurements was 17.4 °C. Once the housing dropped 10°C the flow of N_2 was interrupted and another set of 10 images was acquired. This set of 10 images had an average SNR of 30.88 and a standard deviation of 0.6. The SNR of each image slowly droops for each image since the N_2 is no longer flowing into the chamber (figure 4.9A). The same pattern can be seen in the next 4 sets of 10 images. The average and standard deviation of the SNR for the next 4 sets of images are as follows: 29.84 ± 0.48, 31.16 ± 0.9, 33.93 ± 0.24, and 32.22 ± 0.35. The time between the 6th and 7th set of images was much longer than the time between sets 2-6 (figure 4.9B). This was intentional to avoid damaging the water-cooled gradients by freezing the circulating water within the gradient. Thus, the flow of N_2 was slowed between the 6th and 7th set of images. As soon as the chamber reached -19°C the final set of 10 images was acquired with an average SNR of 46.64 ± 5.86. The final set of 10 images had the following SNR in order of acquisition: 41.09, 39.77, 40.47, 40.6, 44.62, 49.21, 53.03, 53.4, 51.9, 52.4.

In figure 4.10, a room temperature (17.4°C) image of the $CuSO_4$ phantom is compared with 5th image of the final set of 10 images acquired when the housing of the cryochamber reached -20 °C. The SNR increased by a factor of 1.7 for these images. The maximum increase of SNR was 53.28/25.9 or ≈ 2.06.

4.5.4 Effects of cooling on lumped elements

Figure 4.11 displays the S_{21} curves for room temperature and cooled lumped elements. The dip of each curve is the self-resonance of each element as inevitably they contain some inductance, capacitance, and resistance from their geometry. Each element's ESR

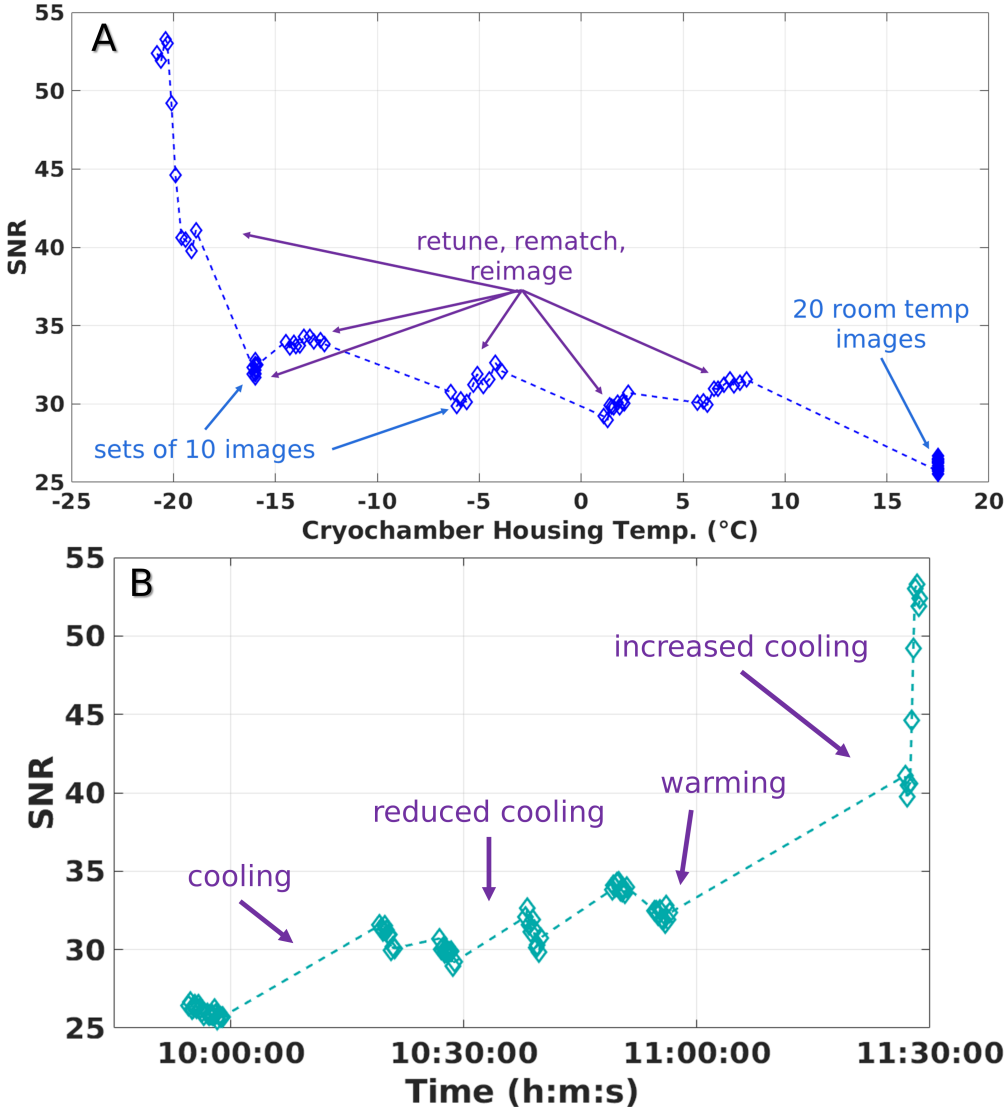

Figure 4.9: At room temperature, 20 images were acquired to establish a baseline SNR (A). While the cryochamber was cooled down inside the bore, sets of 10 images were acquired to determine any SNR increase from cooling. At each set of images, the N_2 was slowed or stopped altogether to ensure the tune and match were adequate (B). At -15 °C, the N_2 was stopped to ensure the chamber did not fall significantly below -20°C. The coil was cooled to image as close to the threshold of -20°C as possible, and the final set of 10 images was acquired as the housing reached dropped from -19 to -23°C.

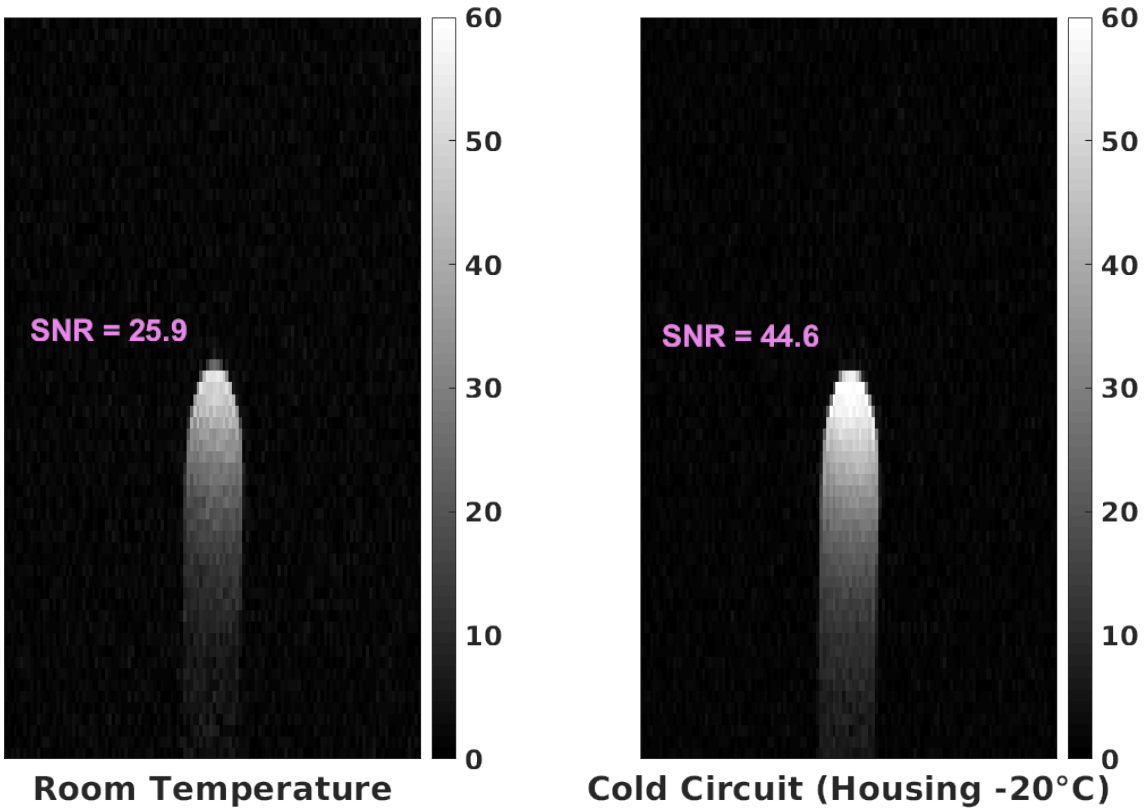

Figure 4.10: The highest room temperature SNR image (left) compared with the 5th image of the final set of images (right). The SNR_{gain} for the two images is 1.72.

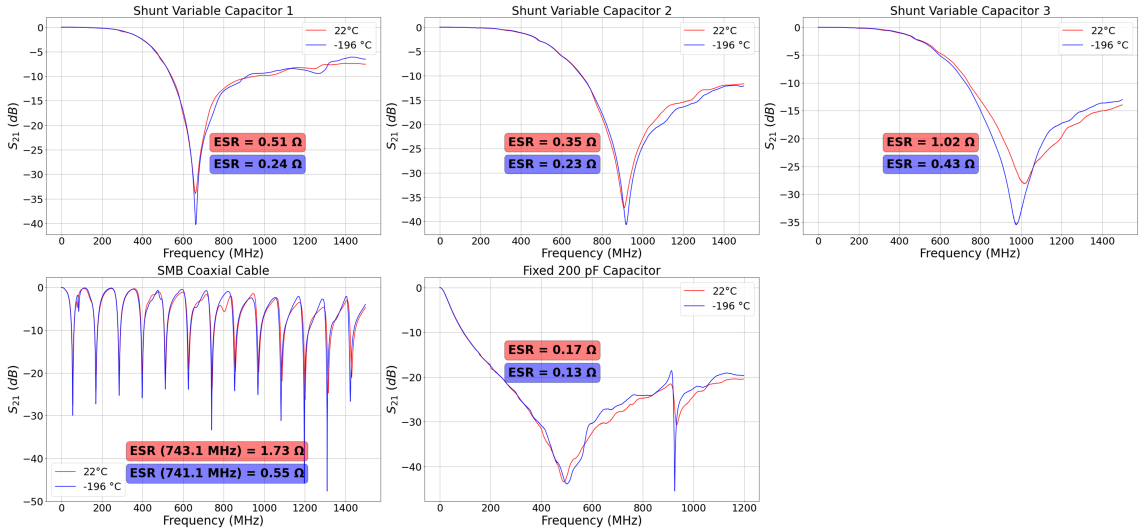

Figure 4.11: After a full TOSM calibration, five lumped elements were shunted across two coaxial cable connectors. The variable capacitors and coaxial cable saw the largest change in ESR due to cooling. This may be because of the small leads on the variable capacitor contributing to resistance. The periodic peaks for the RG174 coaxial cable correspond to the length of the cable and may be calculated with the frequency distance, the velocity of propagation in the coax, and its dielectric constant.

was measured at its self-resonance using equation 4.17. For the coaxial cable, the periodic resonances correspond to the length of the cable and the dielectric constant or velocity of propagation in the cable. For the coax, the ESR was measured at around 740 MHz which was the closest dip near 650 MHz. For the first variable capacitor, the S_{21} dropped from -34 to -40 dB corresponding to a decrease in ESR of 0.27 Ω. For the second variable capacitor, the S_{21} dropped from -37 to -41 dB corresponding to a decrease in ESR of 0.12 Ω. For the third variable capacitor, the S_{21} dropped from -28 to -35 dB, corresponding to a decrease in ESR of 0.59 Ω, although the self-resonance was near 1 GHz and was not a well-defined peak. For the RG174 coaxial cable, the S_{21} dropped from -24 to -33 dB corresponding to a decrease in ESR of 1.18 Ω. The >10,000 Q, fixed capacitor's S_{21} peak dropped from -44 to -45 dB corresponding to a much smaller decrease of 0.04 Ω. The results of the S_{21} and LCR measurements are summarized in table 4.2. Using equation 4.13, the variable capacitors ESR at room temperature correspond to the following quality factors: 48, 50, and 16. At -196 °C their quality factors increased to 102, 76 and 37.

4.6 Discussion

We demonstrate that by cooling the tune and match circuit and leaving the microcoil in ambient air it is possible to achieve improved SNR. This is significant because it allows more space to insulate the sample and may provoke new cryogenic coil designs utilizing the concept. In general, cooling allows the RF coil designer to trade sensitivity of smaller coils for larger FOVs of cooled coils or decreased scan times (figure 4.1). The mechanism of tuning and matching to f_0 and Z_0 has remained relatively unchanged since Marconi's first transmitter [129], thus we can reasonably treat tune and match circuits and RF coils as interdependent, with some exceptions [130, 131]. Since the noise contributions from the circuit are relatively large in comparison to the loop (figure 4.2), cooling the circuit lowers the total ESR. Other work has focused on cooling and reducing the noise contributions of the preamplifier [132] and commercial products such as the Bruker Cryoprobe have imple-

mented it [115]. Most work has focused on cooling the coil itself [57, 118, 133, 56, 91] and to the authors knowledge none have emphasized the possibility of leaving the loop in ambient air. The cryochamber is a proof-of-concept designed to demonstrate the improved SNR from cooling of the tune and match circuit (figure 4.4). Further improvements of the design could include controlled regulation of N_2, temperature monitoring of the sample, surface loop, and inner chamber, and control of temperature in the chamber via a proportional-integral-derivative (PID) device (see appendix D). Temperature stability of the probe is lacking thus prohibiting scan times that exceed a few minutes, a crucial requirement for MR microscopy [60]. The overall design could also be condensed into a smaller chamber to allow more room for insulation between the cryochamber and the inner walls of the bore. Further improvements of the surface loop geometry (see figure 4.14) could be achieved with more sophisticated production techniques including laser milling, thin film deposition, or photolithography of the trace [134]. Although silver has a lower resistivity than copper at room temperature, at 77 K, copper's resistivity is lower [125]. Thus, copper was chosen as the conductor for the trace. As materials with low thermal conductivity and high electrical conductivity become more commonplace and well-understood, RF coils could reap significant SNR benefits as has been demonstrated [135, 136, 137, 138]. The Fomblin bath is a unique way of controlling the sample temperature while avoiding noise from the flow of water near the FOV (figure 4.5). Often excised samples are suspended in Fomblin or fluorinert [105] to avoid increased FOVs and added noise from undesired signal. Another method of isolating the sample from extreme temperatures not investigated here is inductively coupling the loop into another passive device that resonates at 650 MHz. This would add further distance of the sample ($\approx$ a coil diameter) from the extreme temperatures. The cooling of the circuit shifts the frequency higher thus requiring a retune and rematch (fig 4.6 and 4.7). The shift upwards is most likely from a decrease in resistance and capacitance in the system. The decrease in capacitance could be due to the dielectric constant decreasing rapidly as the materials in the circuit go through phase changes [139]. The frequency

shift is evidence that the impedance of the circuit is changing. The drastic phase change of N_2 gas to liquid may also explain the abrupt SNR changes in figure 4.8 and 4.9. In figure 4.8, when the surface loop temperature passes 0°C, the internal chamber could be filling with liquid N_2. In figure 4.9 during the final set of 10 images, the SNR quickly improves from 40 to 53. The 30-minute gap between the last two data sets in figure 4.9B was purely out of caution. We did not want to exceed -25 °C and risk freezing the circulating water within the 6 cm gradient coil. During the 30-minute gap, the transfer line had inevitably heated to above freezing (visible condensation) although the cryochamber remained below -11 °C. To approach -20 °C, the dewar was reopened and N_2 slowly re-cooled the transfer line. The re-cooling took $\approx$ 15 minutes. The final images were acquired as the chamber cooled from -19 to -23 °C yielding the final image in figure 4.10. In figure 4.11, the S_{21} measurement is intended to show that cooling decreases the circuit components ESR. The exact values may not be accurate. For example, at 500 MHz the 200-pF fixed capacitor is reported by the vendor to have an ESR of 0.05 Ω. This is 3x less than the ESR reported in figure 4.11. However, the measurement is not intended to provide exact values of the ESR, it is only intended to show the temperature decreases the ESR of the components. The exact ESR values would need to be measured with more precise and standardized resonant line methods [122]. The difference in predicted SNR_{gain} in figure 4.3 ($\approx$ 1.5) vs the measured SNR_{gain} in figure 4.10 ($\approx$ 2) could be due to a few reasons. In the calculated plots, the coaxial cable was not included since the data sheets do not include the loss of the cables as a function of temperature. Similarly, the Q of the capacitors was fixed at 2000 for room temperature and the cooled circuit. This is inaccurate as the ESR of the variable capacitors and thus Q is inevitably temperature dependent (see figure 4.11).

4.7 Conclusion

By cooling the tune and match circuit and leaving the surface loop in ambient air, SNR was improved by a factor of 2. The results are significant because it allows for more space

to insulate the sample from the extreme temperatures. A cryochamber was designed to cool the tune and match circuit within the bore without damaging the gradient system. A unique Fomblin bath was designed to insulate the sample from extreme temperatures without introducing further noise from circulating water.

4.8 Additional information

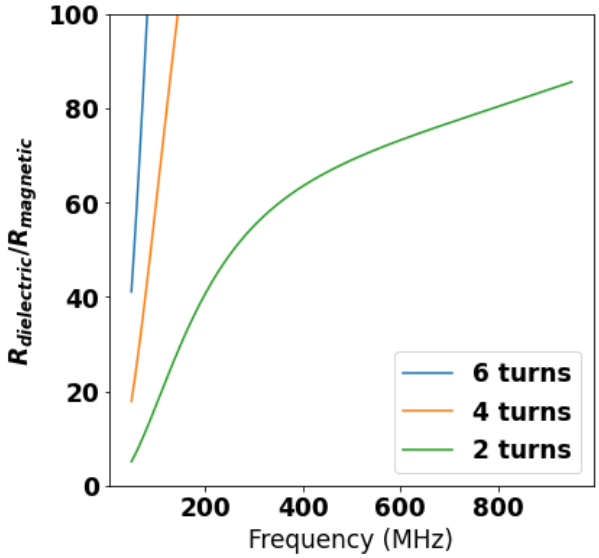

Figure 4.12: For a solenoid, the dielectric losses dominate the magnetic losses. As the number of turns increases, the number of electric field lines passing through the sample increase, drastically increasing the losses.

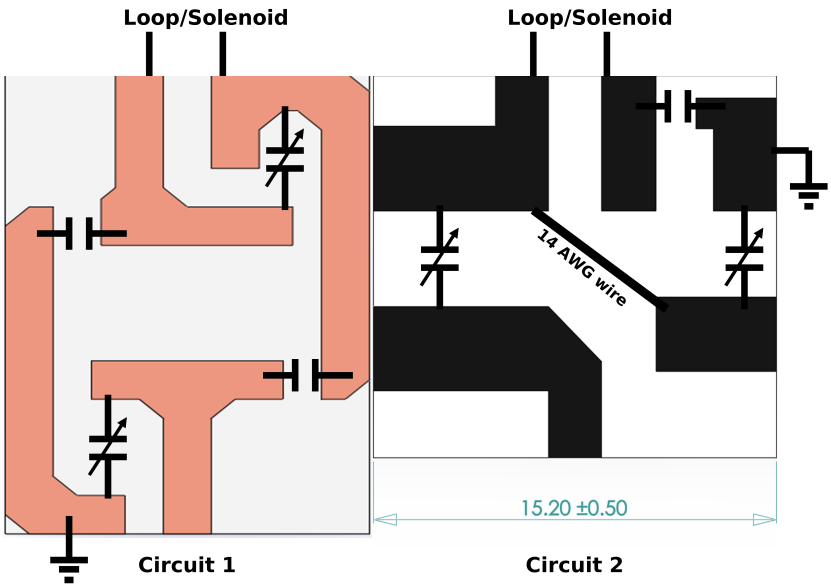

Figure 4.13: The two circuit schematics used in the cryochamber. The circuits shared the same width of 15.2 mm. The ground plane of circuit 2 was the 2nd side of a double sided PCB board.

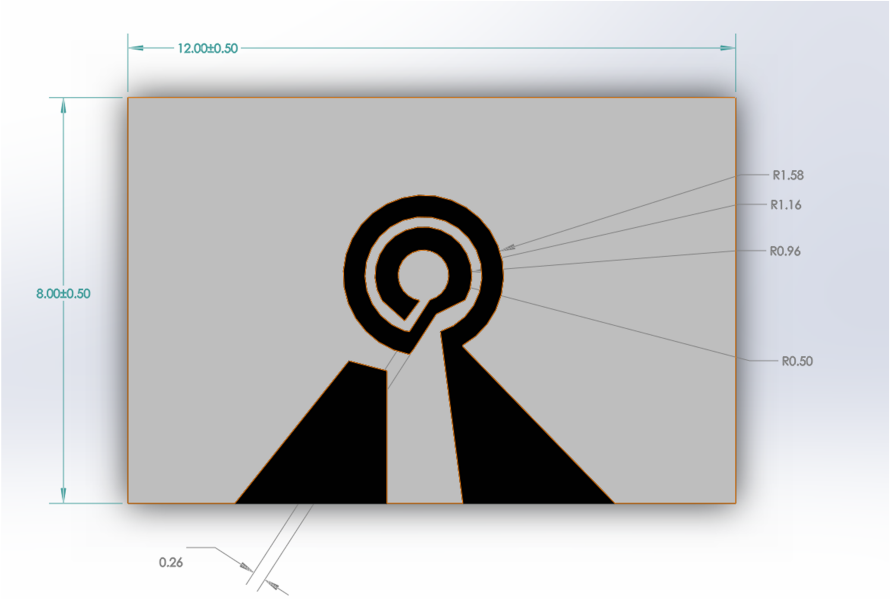

Figure 4.14: The 2 turn, 3mm surface loop with corresponding dimensions in mm.

Circuit	Geometry	Q (22 °C)	Q (cooled)	SNR_{N_2}/SNR_{RT}
1 (no-chamber)	solenoid(n=6,d=0.9mm)	168	423	1.59
1 (cryochamber)	solenoid(n=10,d=1.5 mm)	116	145	1.12
1 (cryochamber)	solenoid(n=10,d=1.5 mm)	126	173	1.17
1 (cryochamber)	s. loop v0 (n=1,d=3mm)	42	48	1.07
1 (cryochamber)	s. loop v0 (n=1,d=3mm)	28	37	1.15
1 (cryochamber)	solenoid (n=4,d=4mm)	59	59	1.00
2 (cryochamber)	s. loop v1 (n=2,d=3mm)	52	83	1.26
2 (cryochamber)	s. loop v1 (n=2,d=3mm)	34	37.4*	1.05
			*indicates partial cooling	

Table 4.1: Several Quality factor measurements were performed on the bench with and without the cryochamber. The initial test (Circuit 1, no-chamber) simply involved immersing the circuit into a N_2 bath. The highest increase in Q was the 2 turn, 3 mm surface loop with $\Delta Q = 31$ and an expected SNR improvement factor of 1.26.

Lumped Elements	100 kHz (22 °C)	100 kHz (-196 °C)	f_{res} (22 °C)	f_{res} (-196 °C)
surface loop (mΩ)	52	44	$\sim$	$\sim$
0.3-10 pF variable cap 1 (Ω)	718	474	0.51	0.24
variable cap 2 (Ω)	731	430	0.35	0.23
variable cap 3 (Ω)	638	495	1.02	0.43
39 pF fixed cap (Ω)	271	137	$\sim$	$\sim$
shorted SMB connector (mΩ)	161	136	$\sim$	$\sim$
shorted SMB coax (mΩ)	217	174	(open) 1.73 Ω	(open) 0.55 Ω

Table 4.2: LCR meter measurements at 100 kHz were obtained at room and liquid N_2 temperatures for select elements of the circuitry in the cryochamber. S_{21} of self-resonating elements (f_{res}) are also included. $\sim$ indicates that the element did not resonate when shunted across the two-port setup described in 4.4.4.2

CHAPTER 5

Deep tissue imaging and applications of MRM for fibrotic kidney disease

The following chapter contains high-resolution highlights of the methods described in chapters 3 and 4. The first 3 subsections under 5.1 demonstrate impressive imaging results. Section 5.2 summarizes a clinical application of high-resolution imaging in characterizing kidney fibrosis with high-resolution parametric mapping of $T_{1\rho}$ and its dispersion curve across spin-lock frequencies.

5.1 Deep tissue imaging

5.1.1 Single cell imaging of green onion root

To further demonstrate concepts described in chapter 3, a green onion root was imaged within a micro solenoid 1.5 mm in diameter. Other work has demonstrated the use of MRM in imaging of plants and larger plant cells and how it might be useful in characterizing plant-based diseases[63, 50]. The experiment is meant to demonstrate a scenario in which PE is clearly advantageous in SNR and resolution. This is mainly possible since the diffusion of the green onion was close to that of water. The T_2^* of the sample on average was $\approx$ 20 ms. In the readout direction, D = 1.3 $\mu m^2 ms^{-1}$ on average for the largest ring region in figure 5.1. The more constricted center of the root had D $\approx$ 0.9 $\mu m^2 ms^{-1}$. The T1 was measured on average $\approx$ 800 ms. G_{read} = 0.56 T/m, $T_2^* \leq$ 20 ms, D = 1.3 $\mu m^2 ms^{-1}$ and T_{read}/t_{acq} $\approx$ 1. The following parameters were fixed for the two acquisitions: FOV = 1.5 x 1.5 mm, 256 x 256 acquisition matrix, TE/TR = 8.74/175 ms, and an Ernst angle of 36.5°. For the FLASH sequence, the BW = 36 kHz, G_{read} = 0.56 T/m, T_{read} of 7.4 ms and N_{acc} = 256. For the PE sequence the BW of the receiver was 3.2 kHz, N_s = 30, with t_{acq} = 9.38 ms, and t_{enc} = 8 ms. G_{phase} was 0.25 T/m. The total time for both acquisitions was 3 hr 11 min 8s with measured SNR of 3.5 and 22.3 respectively. The η for the FLASH and PE acquisitions was 0.001 and 0.006 respectively. For the image in figure 5.1, the SNR of the PPE sequence is

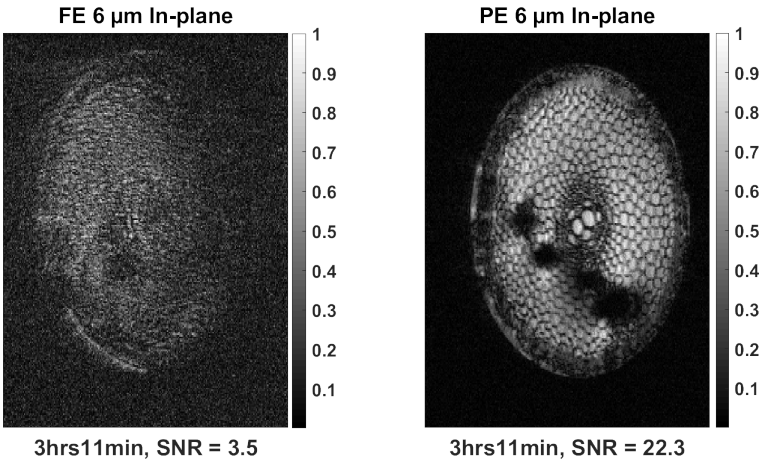

Figure 5.1: For D = 1.3 $\mu m^2 ms^{-1}$ and G_{max} of 0.6 T/m, $\Delta x_{nominal}$ = 6 μm, the $\eta^{PE} > \eta^{FE}$. The BW of the receiver for the PE sequence was 3.2 kHz. The BW of the FLASH acquisition was 36 kHz and could have been lowered for higher SNR but at the cost of a coarser achieved resolution.

6.4 times that of the FLASH sequence. Therefore, 41 averaged accumulated scans would be needed to achieve similar SNR taking $\approx$ 130.4 hours in total.

5.1.2 Diffusion tensor imaging of a mouse cervix

Another promising application of the approaches laid out in the previous chapters include diffusion tensor imaging (DTI) of muscle fibers in the mouse cervix. The well-established theory outlining DTI is beyond the scope of this chapter and the reader is referred to the abundance of literature describing the topic [140, 141]. With respect to the cervix, during gestation, the cervix begins structural changes in preparation for birth. This process is called cervical remodeling [142, 143]. There is a lack of understanding regarding the necessary muscular changes occurring within the cervix for a healthy birth. Recently, DTI tractography was used in humans to model the muscle fibers directionality along the gestation period [144, 145]. The muscle studies performed primarily had FOVs centered on the cervix and largely ignored the tracts leading to the uterine horns. By using a cryogenically cooled surface loop (Cryoprobe, Bruker), preliminary 100 x 100 x 133 μm^3 resolution DTI images were acquired with 6 diffusion weighting directions. The example fractional

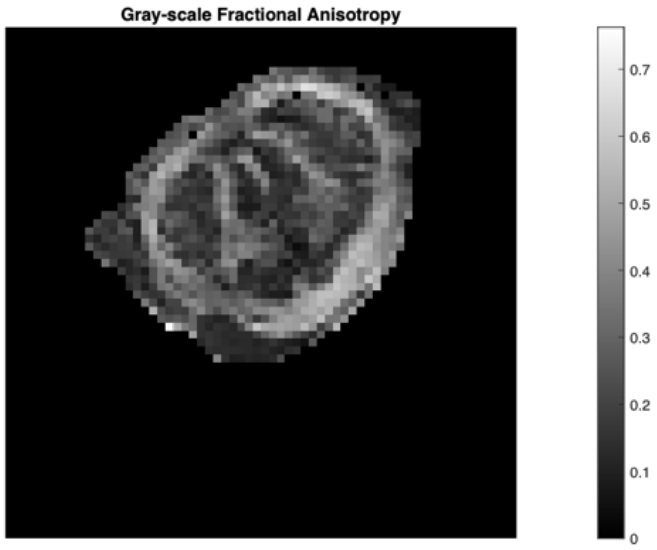

Figure 5.2: The fractional anisotropy map shows a high degree of anisotropy around the periphery of the cervical wall.

anisotropy and fiber directionality maps are shown for a select slice through the cervix. Without the sensitivity of ultrahigh field and the Cryoprobe or custom microcoils, the DTI data of the mouse cervix would be near impossible to achieve. The Rapid Imaging with Refocused Echoes (RARE) DTI image was acquired with the following sequence parameters. RARE factor = 4, Center Echo TE was 17.5, TR = 400 ms, FOV = 6.4 x 6.4 x 6.4 mm, with a 40 kHz BW. The total Scan time was 1 hr 11 m 40s. See figures 5.2 and 5.3.

5.2 Characterizing fibrosis with $T_{1\rho}$

5.2.1 Motivation

Chronic kidney disease (CKD) is a progressive, irreversible, and untreatable condition leading to total loss of kidney function. Although CKD is relatively slow in its progression most CKD patients develop cardiovascular diseases that ultimately lead to death [146]. The gold-standard of CKD diagnosis is calculating the glomerular filtration rate (GFR) from blood tests or albumin levels from urinalysis. In the last 20 years, CKD has grown to affect more

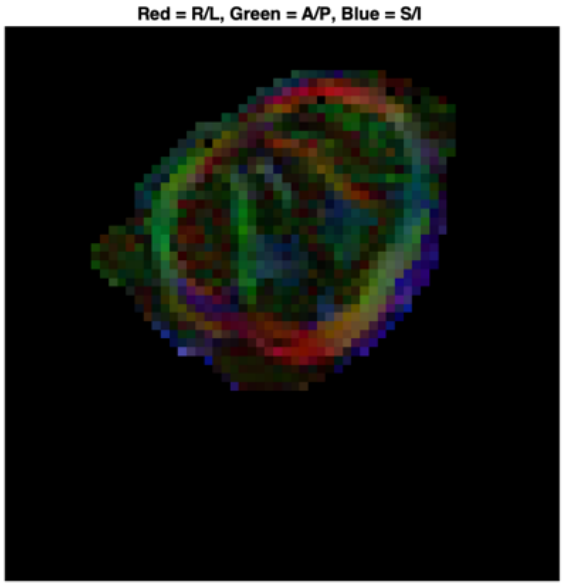

Figure 5.3: Red indicates right or left, green indicates up or down, and blue indicates in and out of the image plane. Clear fiber paths are observed around the cervical wall and the external blue pixels indicate muscles run along the outside wall of the cervix (through image plane).

than 10% of the global population partly because of increased rates of other risk factors including obesity and type 2 diabetes [147, 148, 149]. In CKD and cardiovascular diseases [150], fibrosis is a common indicator of disease progression and finality especially in end-stage renal failure [151]. Fibrosis is defined as a compounding excess of the extracellular matrix (ECM) that may become pathological or self-sustaining. Fibrosis is a complex byproduct of cellular responses to chronic inflammation. The epithelial growth factor receptor (EGFR) activates in the reparation process of damaged tubules. Although EGFR is a positive response for acute kidney injury, chronic activation leads to interstitial fibrosis [152]. In short, inflammatory cells, like lymphocytes release transforming growth factor beta 1, which stimulate fibroblasts causing the secretion of collagen and other byproducts in the ECM, slowly disrupting normal nephron function [146]. Since GFR and albuminuria are sensitive to hydration levels and often patients with CKD are asymptomatic in the early

stages, there exists a need for non-invasive kidney functional assessment and diagnostic tools [148]. Recently, many forms of MR contrast have been employed on kidney disease models in an effort to provide an earlier diagnosis [150, 153, 154, 155]. $R_{1\rho}$ ($1/T_{1\rho}$) or the longitudinal relaxation rate in the rotating frame has been used as a complementary contrast agent for characterizing several tissues and disease models. A few example applications include monitoring irregular cartilage development in children [156], micro-vessel sensitive functional MRI [157], uptake of 3-O-methyl-D-glucose in brain tumors [158], and $T_{1\rho}$ correlation with age and sodium levels in muscle [159]. It is only recently that $R_{1\rho}$ has been suggested to aid in diagnosing and assessing the severity of kidney related diseases [150, 160, 117]. Previous $R_{1\rho}$ kidney imaging studies achieved 250 x 250 x 1 mm^3 resolution maps on in-vivo wild-type and fibrotic kidneys [160, 117]. The relatively low-resolution maps were averaged over varying anatomical regions of the kidney and showed $R_{1\rho}$ and it's dispersion parameters decreased in fibrotic regions. The results averaged regions of interest including the cortex (C) and outer stripe of the medulla (OSOM). It is hypothesized that collagen deposition in ECM within the OSOM could be the cause of the change in dispersion parameters. Higher resolution MRM with microcoils could potentially resolve, vasculature, glomeruli, collagen deposits, and differentiate the cortex from the outer stripe of the outer medulla (OSOM). Furthermore, higher resolution parametric mapping of $R_{1\rho}$ could distinguish the exact locations of fibrosis negating the need for invasive biopsy.

5.2.2 Methods

5.2.2.1 Introduction to $T_{1\rho}$

The first demonstration of $T_{1\rho}$ was by Redfield for solid state NMR where he demonstrated what he called "rotary saturation" [161]. After exciting the equilibrium magnetization of precessing spins into the transverse plane, the decay of the phased signal follows a mono-exponential with time constant T_2^* (see 1). Redfield determined that Bloch's initial predic-

tions [7] for T_2^* do not hold when the transverse magnetization is under the influence of a strong, continuous RF field. During application of a strong RF pulse ($\approx \mu T$) in transverse plane, some of the spins begin to precess about the effective magnetization with a new rotating frequency determined by the strength of the pulse and the gyromagnetic ratio $\omega_{sl} = \gamma B_{sl}$. Thus, the transverse relaxation takes longer than T_2^* to decay since some spins were "locked" into the transverse plane with the strong RF pulse. $T_{1\rho}$ is also called the spin-lattice relaxation in the rotating frame or analogous to T1 in the rotating reference frame. In the same way that T1 decreases with B_0, $T_{1\rho}$ decreases with the strength of the B_{sl} locking pulse [162]. The spin-lock frequencies (FSL = $\gamma B_{sl}/2\pi$) typically range from 10s to a few thousand Hz. These frequencies correspond to macro-molecular processes such as motion, diffusion, and chemical exchange [163, 164]. $T_{1\rho}$ is sensitive to these frequencies making it a complementary contrast to tissue T1 and T2 relaxation. Ideal $T_{1\rho}$ imaging depends on uniform magnetic fields across the sample. Invariably RF fields from coils produce spatially varying B_1 fields especially at the edges of the sample and coil sensitivity profile (see eqn. 1.19). The static B_0 field is inevitably perturbed by intrinsic non-uniformity (a few ppm) of susceptibility interfaces within the sample. B_0 and B_1 spatial inhomogeneity vary the effective field ultimately introducing banding like artefacts as these regions experience varying levels of spin-lock relaxation. Methods to address the artefacts include variations on the spin-lock preparation pulses [165, 166]. In this study, the spin-lock preparation pulse consisted of a 90_{x+}, B_{sl} pulse of duration TSL, and then a 90_{x-}. This is known as the conventional spin-lock preparation sequence.

5.2.2.2 Analysis

In a $T_{1\rho}$ weighted acquisition, the signal decays mono-exponentially with the duration the spin-lock pulse of strength B_{sl} and time constant of $T_{1\rho}$. The signal may be fit to the following equation:

$$S_1 = S_0 e^{-TSL/T_{1\rho}} \tag{5.1}$$

where S_1 is the observed signal and S_0 the initial signal at TSL = 0. The corresponding flip angle Θ of the spin-lock pulse is given in radians by $2\pi TSLFSL$. A Dispersion curve may be obtained by fitting T_{1rho} over several spin-lock frequencies. The simplest model not accounting for diffusion was determined by Chopra [167] as

$$R_{1\rho} = \frac{R_{2fit} + \frac{R_{1\rho}^{\infty}\omega_{sl}^2}{S_\rho^2}}{1 + \frac{\omega_{sl}^2}{S_\rho^2}} \tag{5.2}$$

Where R_{2fit} is the $R_{1\rho}$ value at FSL = 0 and may be different than R2, $R_{1\rho}$inf is the rate at very high frequencies which converges on T1, and S_ρ is determined by the proton exchange rate and the $\Delta\omega_{cs}$ or the chemical shift from the static field's Larmor frequency. S_ρ in it's long form is given by [168]

$$S_\rho^2 = \frac{R_{1b}+k}{R_{2b}+k}((R_{2b}+k)^2 + \Delta\omega_{cs}^2) \tag{5.3}$$

where R_{1b} and R_{2b} are the relaxation rates of the bound sites and k is the exchange rate from the bound to free water pools. Chopra pointed out that when $k >> R_{1b}$ and $k > R_{2b}$ equation 5.3 simplifies to $S_\rho^2 \approx k^2 + \Delta\omega_{cs}^2$. The inflection point of the dispersive curve may be determined by taking the 2nd partial derivative of equation 5.2 and setting to zero which yields the inflection point as $\omega_{infl} = \sqrt{S_\rho^2/3}$.

5.2.2.3 Gelatin phantom experiments

Recent studies correlated increased $T_{1\rho}$ (decreased $R_{1\rho}$) with increased degraded collagen deposits in cartilage suffering osteoarthritis [169]. Gelatin (pork skin type A) was purchased from Sigma-Aldrich (St. Louis, MO) to prepare phantoms with various concentrations. 20% stock gelatin solution was first made with 20g of gelatin dissolved in PBS at 65°C for a final volume of 100ml. Samples of lower concentrations were then diluted from the 20% stock using pre-warmed PBS. After thorough mixing, these samples were centrifuged at 1000g for 5 minutes to remove any trapped bubbles and then sealed. All

concentrations of gelatin (>1%) settle as a gel form at room temperature.

5.2.2.4 Excised kidney samples

Tubulointerstitial fibrosis model is induced by overexpression of the epidermal growth factor receptor (EGFR). A homozygous transgenic model (Tg/Tg) was developed to chronically induce a EGFR ligand, human heparin-binding EGF-like growth factor (hHB-EGF) in mice to create persistent tubule interstitial fibrosis within the kidney [170]. Kidneys from $hHB-EGF^{Tg/Tg}$ mice are hereafter referred to as fibrotic. The mice were around 12 weeks old when sacrificed. After perfusion, kidneys were excised from wild-type and fibrotic mice and placed within PBS fixative. 24 hours before imaging, the kidneys were washed in a PBS, 1mM Gd, and 0.1 mM NaN_3 mixture for increased T2 and decreased T1 [96]. Hereafter, wild-type kidneys are referred to as healthy or WT.

5.2.2.5 MR hardware, imaging, and general relaxation parameters

All excised kidney images were acquired with a 15.2T Bruker MRI scanner, with 1 T/m gradients, and a 4-turn micro solenoid RF coil 4 mm in diameter and 1.2 mm wire gauge. The dimensions, wire gauge, and number of turns were optimized for the sample size using previously published work [1, 2].

The gelatin phantoms were collected with a 39 mm quadrature driven birdcage coil. The $T_{1\rho}$ weighted RARE images of gelatin phantoms were acquired with the following sequence parameters: TR/TE = 1000/10 ms, rare factor = 8, $TE_{effective}$ = 40 ms, 128 x 128 pixels, 20 x 20 mm FOV, 1 mm slice thickness, and total scan time of 2 min 24s for 9 TSL times. The $T_{1\rho}$ specific imaging parameters were as follows: TSL was set to 0.1, 10, 50, 80, 110, 140, 170, and 200 ms. For each TSL, FSL was also varied and was set to 443.5, 887.1, 1214.6, 1801.6, 1983.5, and 3136.2 Hz. T2 maps were acquired with MSME and T1 maps were acquired with a variable TR RARE sequence. The gelatin phantoms all had an average T2 of 200 ms and T1 of. The 3-dimensional $T_{1\rho}$ weighted RARE images of excised kidneys were acquired with the following sequence parameters: TR/TE = 570/6.7

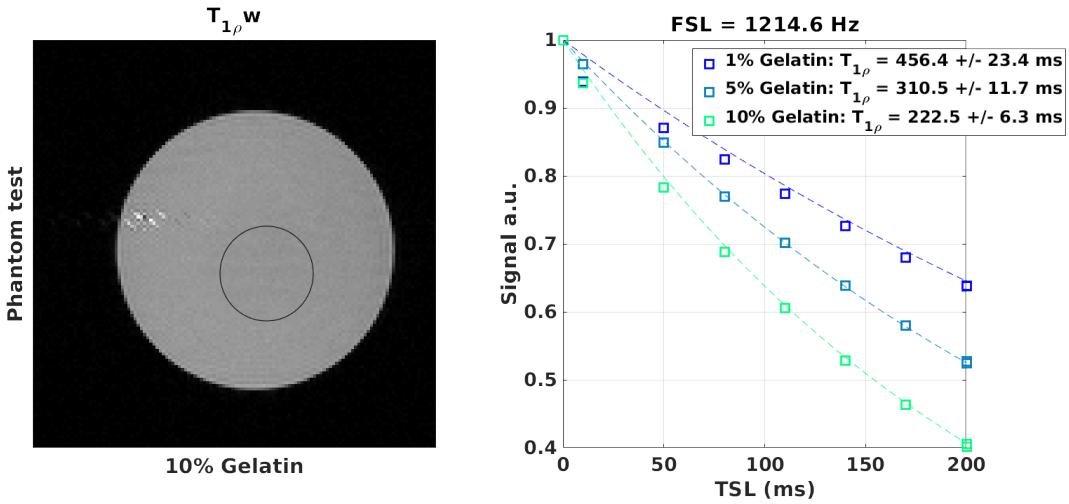

Figure 5.4: Gelatin, a degraded form of collagen, exhibits dispersive behavior. It consists of a large number of glycine and proline molecules which both have hydroxyl exchange sites. The T2 of the samples was roughly 200 ms for 1-10% concentrations. $T_{1\rho}$ is sensitive to varying concentrations of Gelatin.

ms, rare factor = 4, $TE_{effective}$ = 13.4 ms, 128 x 76 x 76 pixels, 12 x 7 x 7 mm FOV and a total scan time of 1hr 8 min and 35s for 5 TSL times. The $T_{1\rho}$ specific imaging parameters were as follows: TSL was set to 0.01, 10, 30, 60, and 90 ms. For each TSL, FSL was also varied and was set to 400.47, 598.74, 800.94, 999.99, 1498.42, and 2004.70 Hz. For each scan with the microcoil, the linewidth of the shimmed volume as defined by the FWHM of the Lorentzian was 75-85 Hz. The final resolution of the $R_{1\rho}$ maps was 93.8 x 92.1 x 92.1 micrometers, roughly 78.6 times smaller voxel sizes than previously reported $R_{1\rho}$ maps [160, 117].

5.2.3 Results

5.2.3.1 Gelatin $T_{1\rho}$ mapping

Figure 5.4 shows the $T_{1\rho}$ fits for the average signal in the ROI (blue circle) at FSL = 1214.6 Hz. The signal is normalized to the initial TSL. For FSL = 1214.6 Hz, the $T_{1\rho}$ decreases as Col increases. The 1% Col fit had a $T_{1\rho}$ value of 456.8 +/- 24.1 ms. The 5% Col fit had a $T_{1\rho}$ value of 311.2 +/- 11.5 ms. The 10% Col fit had a $T_{1\rho}$ value of 222.5 +/- 6.4 ms.

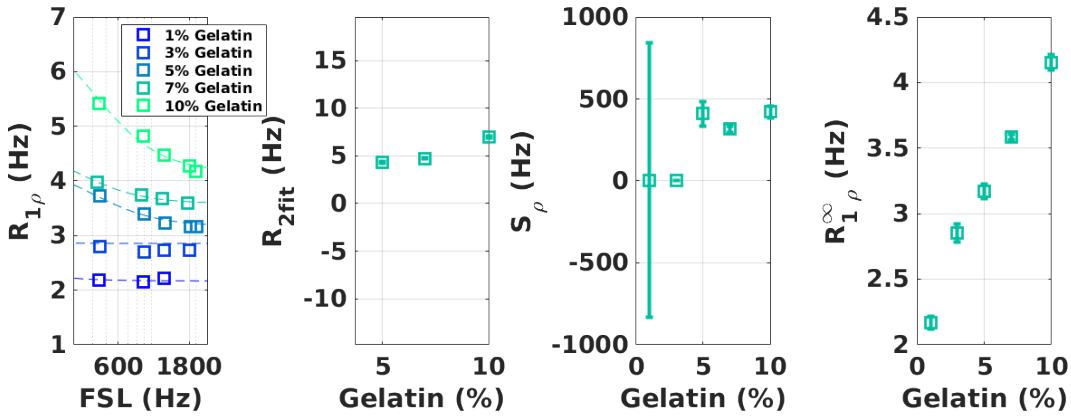

Figure 5.5: The Gelatin samples dispersion fits across FSL = 400 to 2400 Hz. The base solution was PBS, which isn't dispersive. The 1% and 3% Gelatin solutions were not dispersive thus the fits for $R_{1\rho}$ derived parameters were poor.

5.2.3.2 Gelatin $R_{1\rho}$ dispersion

Figure 5.5 shows the dispersion data points and their respective fits to equation 2 along with $R_{1\rho}$ derived parameters over varying concentration. For the 1% Col phantom, the R_{2fit}, S_ρ, and $R^\infty_{1\rho}$ were 249.1, 4.3, and and 2.2 Hz respectively. The expected standard deviation of the fitted values was 96000, 838.6, and 0.1 Hz. For the 3% Col phantom, the R_{2fit}, S_ρ, and $R^\infty_{1\rho}$ were 105, 2.1, and 2.9 Hz. The expected standard deviation of the fitted values was 0.4, 0.9, and 0.1 Hz.

For the 5% Col phantom, the R_{2fit}, S_ρ, and $R^\infty_{1\rho}$ were 4.3, 408.9, and 3.2 Hz. The expected standard deviation of the fitted values was 0.1, 75.4, and 0.1 Hz. For the 7% Col phantom, the R_{2fit}, S_ρ, and $R^\infty_{1\rho}$ were 4.7, 316, and 3.6 Hz. The expected standard deviation of the fitted values was 0.02, 19.2, and 0.02 Hz. For the 10% Col phantom, the R_{2fit}, S_ρ, and $R^\infty_{1\rho}$ were 7, 420.4, and 4.2 Hz. The expected standard deviation of the fitted values was 0.1, 34.2, and 0.1 Hz.

5.2.3.3 Excised kidney $T_{1\rho}$ maps

In figure 5.6, example segmentation (left) and $T_{1\rho}$ fits from the corresponding segmentation are demonstrated. The renal pelvis (RP), inner medulla and papilla (P), inner stripe of outer medulla (ISOM), outer stripe of outer medulla (OSOM), and the cortex (C) were

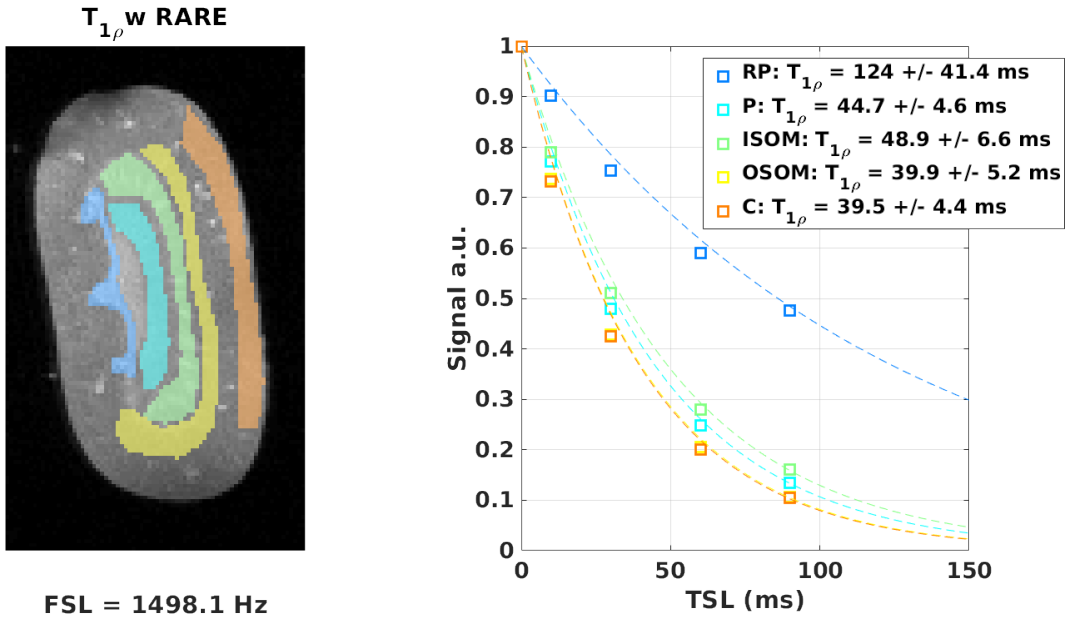

Figure 5.6: Regional differences in the fibrotic kidney are somewhat apparent from a single FSL $T_{1\rho}$ fit. The mean values are taken over each TSL and region highlighted in the image on the left. Final result of the fit is plotted on the right.

segmented. Fits were performed over the average of these segmented regions (right). The results of the fit for $T_{1\rho}$ for an FSL of 400.4 Hz were as follows : RP was 120.4 +/- 40.8 ms, P was 43.9 +/- 4.8 ms, ISOM was 46.9 +/- 7.1 ms, OSOM was 39.3 +/- 5.6 ms, and C was 38.7 +/- 4.8 ms.

5.2.3.4 Excised kidney dispersion curves

In figure 5.7, the same segmentation masks in figure 5.6 were applied to calculate the dispersion parameters of varying regions across the fibrotic kidney. For the inner medulla and papilla (P), the fitted R_{2fit}, S_ρ, and $R_{1\rho}^{\infty}$ values were 23.7, 295.7, and 22.3 Hz respectively. The expected standard deviation of the fitted values was 2.9, 451.4, and 0.1 Hz. For the ISOM, the fitted R_{2fit}, S_ρ, and $R_{1\rho}^{\infty}$ values were 21.6, 883.8, 20.1 Hz respectively. The expected standard deviation of the fitted values was 0.2, 208.4, and 0.2 Hz. For the OSOM, the fitted R_{2fit}, S_ρ, and $R_{1\rho}^{\infty}$ values were 25.6, 814.6, 24.9 Hz respectively. Their expected standard deviation was 0.2, 320.5, and 0.1 Hz. For the cortex (C), the fitted R_{2fit}, S_ρ, and

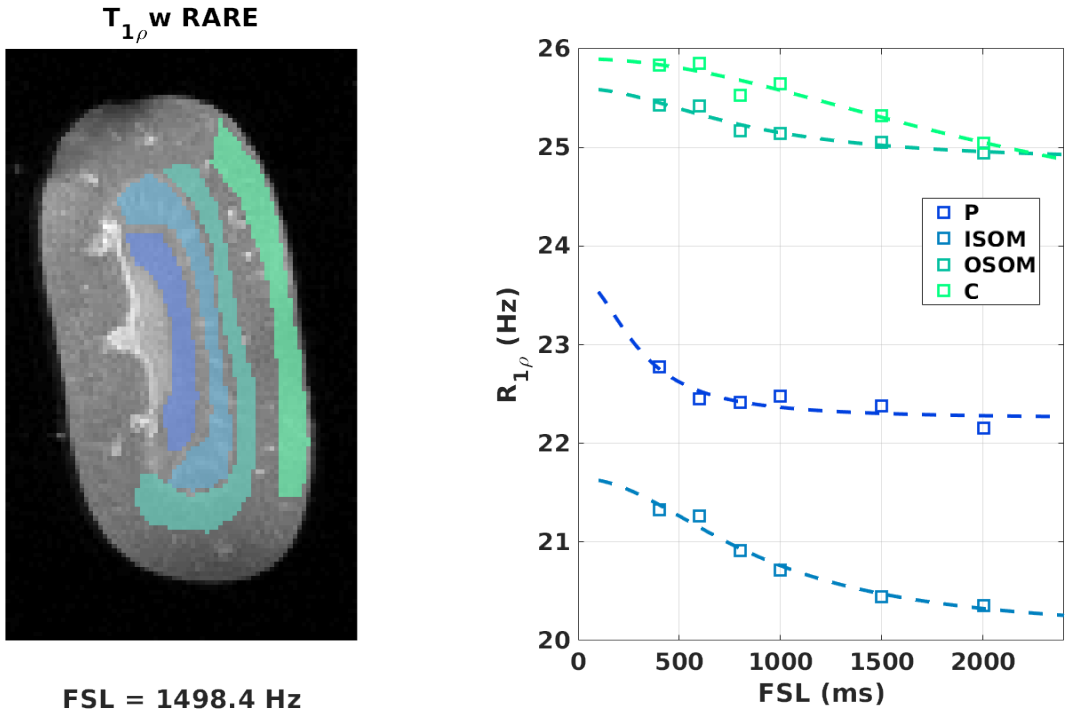

Figure 5.7: Across the kidney, dispersion curves of the mean values of the ROIs (left) demonstrate more appreciable tissue differences in the form of $R_{1\rho}$ derived parameters: R_{2fit}, S_ρ, and $R^\infty_{1\rho}$.

$R^\infty_{1\rho}$ values were 25.9, 2222.5, and 24.0 Hz respectively. The expected standard deviation of the fitted values was 0.1, 1579.2, and 0.2 Hz.

In figure 5.8, $R_{1\rho}$ maps of the fibrotic and healthy kidney along with the dispersion parameters in the OSOM of the kidney were plotted. The manually drawn masks are overlayed top the $R_{1\rho}$ maps for FSL of 962.6 Hz. The average of these masks are plotted in the center of figure 5.8. For the healthy OSOM region, the R_{2fit}, S_ρ, and $R^\infty_{1\rho}$ were 30.7, 1940, and 26.4 Hz. The expected standard deviation of the fitted values was 0.2, 788, and 1.8 Hz. For the fibrotic OSOM region, the R_{2fit}, S_ρ, and $R^\infty_{1\rho}$ were 26.1, 830.8, and 25.5 Hz. The expected standard deviation of the fitted values was 0.2, 536, and 25.5 Hz.

5.2.3.5 Difference of T_2^* and $T_{1\rho}$ images

At low FSL, the $T_{1\rho}$ weighted images have relaxation rates closer to T2. T_2^* weighted images show loss due to susceptibility influences on the effective field whereas these ef-

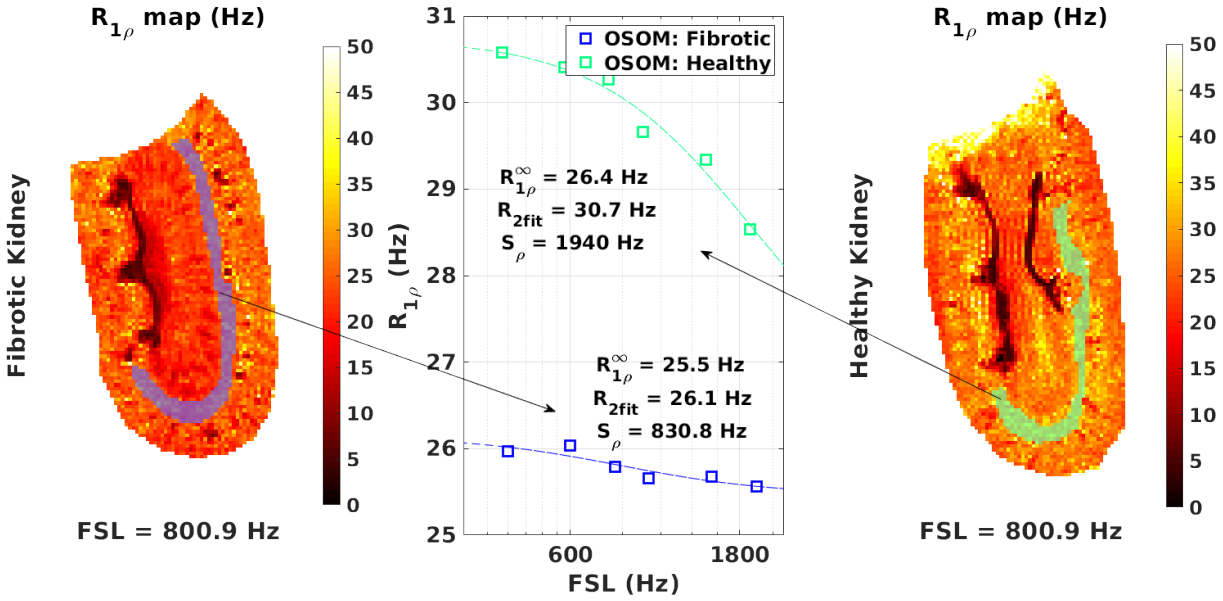

Figure 5.8: The fibrotic and healthy kidney were compared in $R_{1\rho}$ dispersion parameters specifically in the OSOM region were tubulointerstitial fibrosis is known to proliferate. The blue ROI is drawn on the fibrotic kidney (left) and plotted as blue squares with its corresponding fit (center). The green ROI is drawn on the WT kidney (right) and plotted as the green squares with its corresponding fit (center). Clear differences in the dispersion curve are noticeable as the fibrotic kidney has decreased $R_{1\rho}$ derived parameters.

fects are refocused in a T2 weighted spin echo experiment. The difference between the two images would correspond to the susceptibility interfaces within the sample or more specifically the vasculature of the kidney. An example image is plotted in figure 5.9.

5.2.3.6 Validation with histology

To confirm the presence of fibrosis in the kidney, histology needs to be performed. An example image of histology of the WT and fibrotic model kidneys ($hHB-EGF^{Tg/Tg}$) is seen in figure 5.10. This is not the fibrotic or healthy kidney shown in figure 5.8 but serves as an example of what the OSOM of the kidney in figure 5.8 looks like on a microscopic level. In the fibrotic model, the ECM is visibly larger (blue regions). For more detailed information on the methods of histology used to obtain the image see [160].

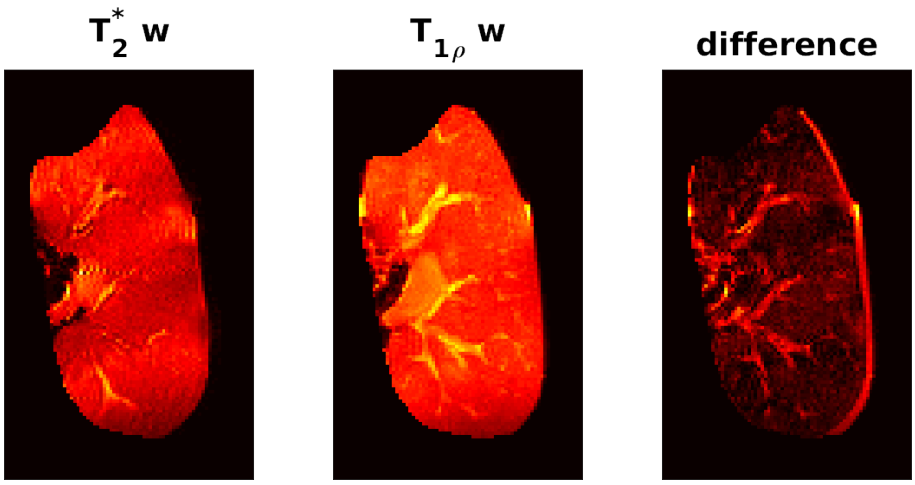

Figure 5.9: The absolute difference between high resolution T_2^* and $T_{1\rho}$ weighted images was taken in attempt to visualize vessels. The result is similar to a susceptibility weighted image.

5.2.4 Discussion

The gelatin phantoms demonstrate that gelatin is dispersive at higher concentrations. This is most likely because The 1% gelatin sample has a very high uncertainty at low FSL. Non-conventional spin lock preparation sequences are needed to precisely determine the S_ρ values. Conventional spin-lock is known to induce artifacts at FSL $<$ 400 Hz. It is interesting that $R_{1\rho}$ increases with the gelatin percentage. This result differs from other internal unpublished work and a recent cartilage study [171]. However, there are many forms of collagen and the chemical properties of ordered collagen like that of cartilage or that in the kidney may differ strongly from degraded forms such as gelatin [172]. Gelatin can be classified into two types, A and B, based on the manufacturing process. Type A gelatin, compared to type B gelatin, is more like native collagen in the body terms of amino acid components and size ($\approx$ 60 KDa) [173]. The internal study previously mentioned utilized collagen peptides which are extracted through strong corrosive hydrolysis or extreme high temperature and pressure. They consist of much smaller peptides with low molecular weight, ranging from 3 to 6 KDa, along with other ingredients [174]. Many supplement types of collagen peptides also contain additional additives to enhance their nutritional ap-

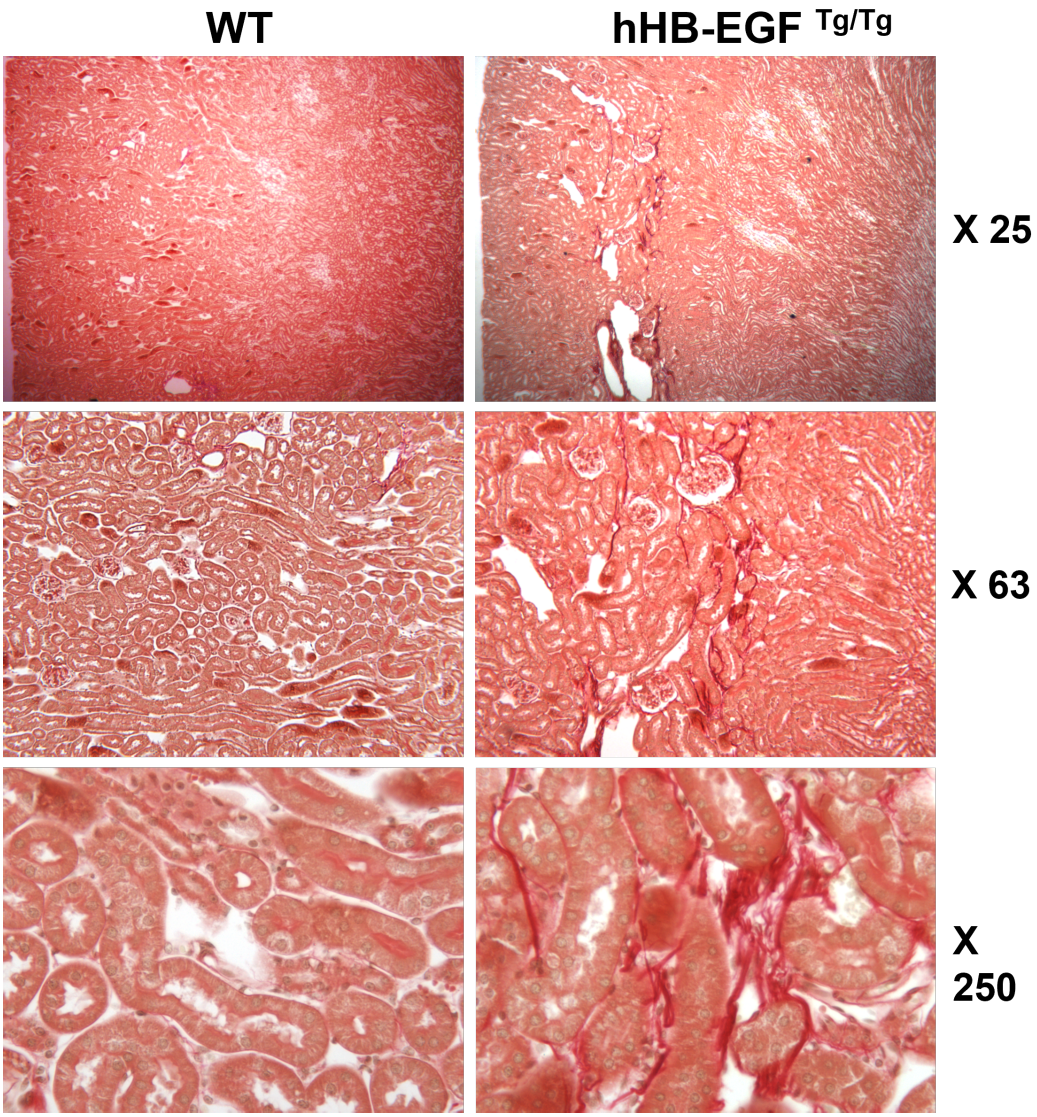

Figure 5.10: Histology image demonstrating increased ECM content in the OSOM of the fibrotic kidney model ($hHB-EGF^{Tg/Tg}$) in comparison to the healthy kidney (WT).

peal. In comparison, native collagen exists as a triple helix with a molecular weight of approximately 300 KDa total or 100 KDa for each chain. The extraction process of collagen peptides not only affects the size of the peptides but also their physicochemical and biological properties [174]. Pure collagen must be adapted via hydrolysis or high temperatures in order for it to become soluble. This may influence its final composition and thus its exchange parameters. The cause of decreased dispersion in fibrotic kidneys is not well understood and may require more detailed and controlled chemical studies for replication of the effect in the lab.

Pixel by pixel fitting performs reasonably well in the inner and outer medulla of the kidney (see figure 5.8). However, pixels in the cortex can be very noisy (see figure 5.11). Thus, it is very difficult to create maps of the dispersion parameters since only some of the points result in adequate fits. This could be improved with more advanced forms of spin-lock preparation pulses, however high-resolution images may still suffer from the problem. For example, with 100 μm^3 voxel sizes, it is possible that the voxel could consist entirely of a non-dispersive material such as PBS or air. It is often reported that partial volume averaging could detrimentally blur parametric results [47], however in certain cases partial volume averaging of larger voxels may aid in providing more uniform parametric mapping, especially when the identity of substances in small voxels is not well-known. The same complications may influence averaged regions of tissue as well. Pixel-by-pixel fitting with very high resolution across a region could include many forms of tissue material with widely varying parameters. When averaging across every fit, the result could represent meaningless information since the variation across pixels is so large. Figure 5.11 demonstrates the biological variation of the $R_{1\rho}$ fits in the cortex vs the ISOM. The ISOM has lower mean squared error (MSE) thus indicating the tissue is more homogeneous and fits the dispersion curve well.

Limitations of this work include the limited number of kidney samples. For a more convincing trend, several more fibrotic and wildtype kidney samples would need to be

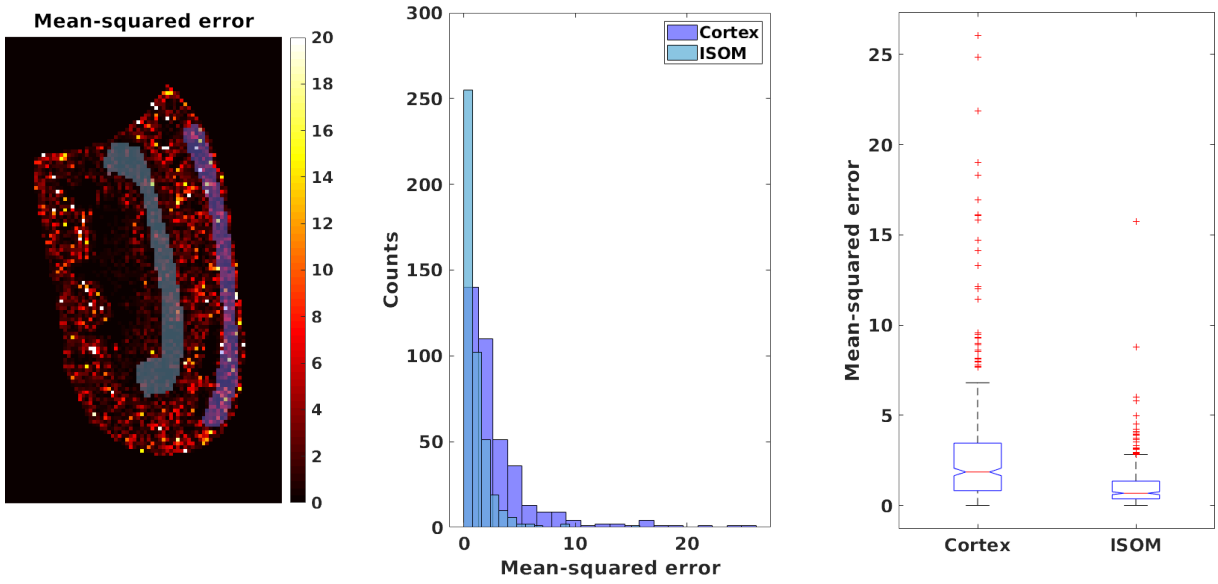

Figure 5.11: In the $R_{1\rho}$ maps, the ISOM and and inner medulla seem to have more defined structure (see figure 5.8) whereas in the OSOM and cortex the image seems noisier. To confirm the noise in the cortex corresponds to biological variation of the tisse, the mean-squared-error (MSE) of equation 5.2's fit was plotted onto the kidney image. The cortex fit's have higher MSE on average than the ISOM implying the variation is biological in nature. plots include the MSE map (left), histograms of the MSE in each ROI (center), and boxplots of the MSE (right).

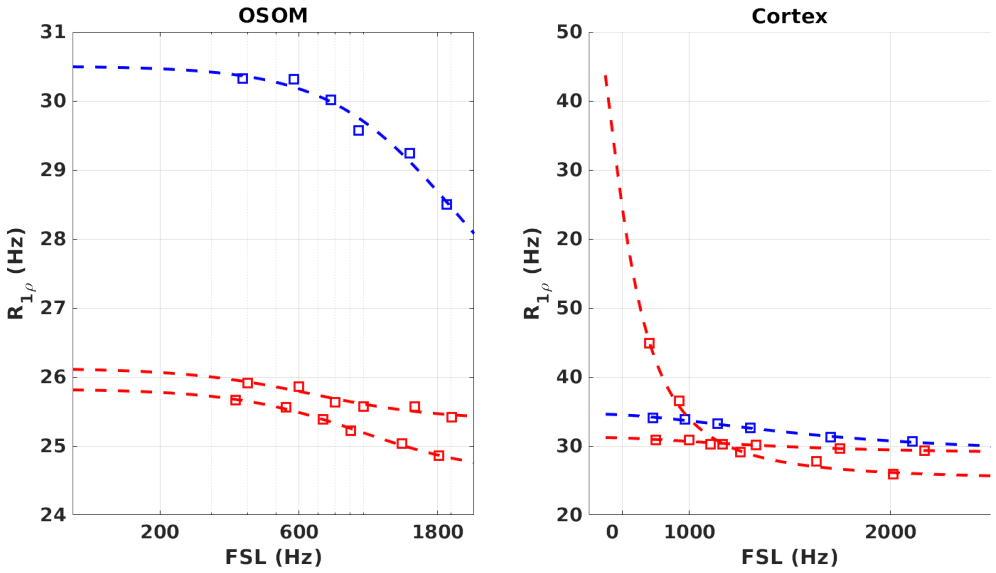

Figure 5.12: 2 fibrotic and 1 WT kidney were imaged. Mean dispersion curves are plotted from 400-2400 Hz for the OSOM and the Cortex (C) region of the kidneys. The OSOM has decreased $R_{1\rho}$ derived parameters in the fibrotic model in comparison to the healthy counterpart.

acquired. Two fibrotic and one healthy kidney were imaged with the protocol (see fig. 5.12). Another limitation involves the variation of T1 and T2 of the samples due differences in water content. In theory the changes in dispersion should indicate fibrosis regardless of the relaxation rates, but a more controlled study would have obvious added benefits. The samples were refrigerated in fixative for roughly 3 years. More recently excised samples could be acquired to ensure that T1 and T2 are normalized or somewhat similar upon initial scans.

5.2.5 Conclusion

93.8 x 92.1 x 92.1 μm $T_{1\rho}$ parametric maps show promising results for demonstrating changes in dispersion in a fibrotic kidney model.

CHAPTER 6

Conclusions and Future Work

6.1 Chasing smaller voxels

In chapter 3, the limitations of diffusion are emphasized with respect to conventional encoding gradients. The exact voxel sizes are given for the case in which phase encoding is more time efficient than frequency encoding. Diffusion is demonstrated to attenuate signal within the readout gradient in very small voxels. The achieved resolution is measured with imaging of the PSF. Examples of phase encoding achieving more in signal and resolution are given in chapters 3 and 5. Only Ernst angle imaging was used. For further refocusing of T_2^* losses, an inversion pulse or purely phase encoded spin echo sequence should also be considered. Furthermore, measuring diffusion in voxels smaller than 10 μm should be possible given a spin-echo pulse sequence that is purely phase encoded. Another possible way of measuring diffusion in very small voxels involves a few assumptions but deserves attention. Typically, diffusion weighting (DW) is achieved with large gradients surrounding a 180 inversion pulse. In small voxels with a single readout line, typical diffusion gradients may not be required. One potential way of going about this would involve a high-resolution FLASH image performed with two different readout gradient lengths. Both images signals will decay with T_2^*, but their diffusion attenuation should vary slightly (see B). Relaxation parameters should not change when the readout is adjusted and by fitting the attenuation for each readout length, the ADC value in that direction could be more precisely calculated with multiple lines. The question remains as to whether or not the non-ideal gradient amplifier response to quick changes adds uncertainty to the gradient waveforms that is enough to confound the exact b-value. If the waveforms can be precisely monitored through time (usually they can), this could be done. The primary advantage of this technique is that the time efficiency of the FLASH sequence could be utilized with short TRs to achieve ADC

maps in reasonable time with shorter TEs than SE diffusion imaging. Of course if it would take multiple FLASH images to achieve accurate estimation of the ADC, the time benefit may be lost. This method of determining the ADC may also achieve greater resolution than DW-SEI since gradients will have less on time alleviating the gradient duty cycle. With respect to the measurement of resolution, imaging of the PSF at this scale has never been done before. This is most likely because imaging of the PSF takes a very long time. An 8 μm resolution map took 8 hours. This was achieved in part because of increased sensitivity of 0.9 mm solenoids FOVs $<$ 1 mm. The PSF at high-resolution is nonetheless interesting because it provides a unique window into the linewidths of very small regions. If temperature and diffusion controlled phantoms were designed to correlate these linewidths with increased or decreased ADC values, it may be possible to infer more information. The PSF linewidths are also influenced by susceptibility interfaces in the voxels themselves. Precise estimation of the FWHM requires points further out in k-space meaning more time or gradient strength to achieve precise FWHM estimations. The additional phase encoding gradients add their own broadening as shown in figure 3.8. A better approach to measuring resolution without confounding the measurement would include setting the the extra gradients to the same attenuation no matter the k' point by adjusting $t_e nc$ and the gradient strength accordingly. This would effectively fix the added broadening of the additional gradients to a known value. Limitations of the work in chapter 3 include non-thorough treatment of contrast and susceptibility limitations. Further undersampled and non-cartesian acquisition strategies should be considered. A question remains as to what happens to the PSF and achieved resolution in undersampled or spiral k-space encoding. Although MRI k-space can be treated as a sparse domain, there may be loss of information in terms of achieved resolution with undersampled acquisitions. To the author's knowledge, this is an open question. The work presented in chapter 3 shows the importance of considering microscopy as a different imaging regime. Typical images in the literature largely rely on tried and true pulse sequences, FLASH and RARE. There needs to be a clever re-

consideration for efficient acquisitions that designed for the diffusive regime. Sequences such as single-point ramped imaging with T1-enhancement (SPRITE) [104, 103, 102] and Diffusion Enhancement of SIgnal and REsolution (DESIRE) [175, 176, 20], although considered unconventional, should be more thoroughly considered for the microscopy regime especially as hardware continues to improve.

There is promising direction for ultra-high field high-resolution imaging. Albeit signal is still the limiting factor, combining advanced pulse sequences, cryogenic hardware, and very strong gradients imaging of 0.5-3 μm should be possible.

6.2 Cryochamber material and hardware improvements

In chapter 4, arguments and experimental demonstration conclude that appreciable resistance from necessary circuitry may be diminished with temperature. Other cryogenically cooled coils may have experienced SNR gains from cooled circuitry, this is the first demonstration that the tune and match circuit may be cooled for SNR gains. The design of the fomblin bath may be useful to other MR microscopists in need of temperature controlled samples without added noise from water or other circulating solutions. The designs may prompt further innovation of novel tools for microscopy and sample preparation. The study also emphasizes how important choosing high-quality electronics and circuit designs may influence the final SNR of imaging experiments for microscopy. It is a shame that often the most rudimentary hardware in MR is the RF receiver chain. The RF components also happen to be the the easiest components to access for the imaging scientist. No doubt there are many ways that noise of the RF receiver chain could be further diminished for UHF. Some vendors have switched to placing the preamplifier and Analog-to-digital converter as close to the RF coil as possible [114]. Fiber optic cables could then send the signal to the console. MR microscopists would greatly benefit moving forward if they were to adopt this immediately. As field strengths increase, further high-frequency losses due to the skin effect may make coaxial cables impractical. Minimizing the RF receiver chain is one of

the most efficient way to improve MR microsopy at the present moment. The cryochamber design is only the 2nd iteration of the original design. Further modifications would include and active vaccuum and a smaller space for the N_2 along with more room for insulation. In certain benchtop experiments, condensation on the surface of the loop influenced the resonance frequency. This could be avoided by sealing or embedding the copper loop in a dielectric material. The dielectric could also be used to shape the field pattern [177]. The surface of the cryochamber reached -25 °C. Some gradients are not water-cooled. Members of the gradient manufacturing company (Resonance Research Inc.) mentioned it would be possible to add anti-freeze (Ethylene glycol) to the water cooled system. A 50-50 ratio of water to ethylene glycol would allow temperatures of -37 °C in the gradient coil. The problem may not have been too serious assuming the water is constantly flowing heat back into the system. Nevertheless, the extreme temperatures on the surface of the cryoprobe could be mitigated with more insulative material. With respect to sample preparation, for larger samples whose noise contribution is significant, anti-freeze soaked samples would be interesting as long as the sample's relaxation parameters are not heavily influenced. This would allow excised tissue to be imaged with temperatures below 0°C increasing the SNR.

In the design of the cryochamber it became clear that a material with low thermal conduction, and electrical conductivity like that of copper would greatly benefit the design. For the solenoid, the coil would drop below <-100 °C simply because the leads were connected to the inner N_2 chamber. If a material were able to conduct electrical signal, but hinder thermal conduction [136], it would allow use of a solenoid without freezing the sample. Other designs similar to this were tried with minimal success. A series of low ESR ceramic capacitors were soldered to the end of the leads to put more distance between the solenoid and the N_2 chamber. With a 2 capacitors between the solenoid and the chamber, the solution within the capillary still froze. Adding circuitry begs the question whether the coil would perform better at room temperature without the added components. Similar to this vein of thought, inductively coupling a cold solenoid into a room temperature passive

solenoid was not thoroughly investigated. In theory this should work, but the geometric tuning would be difficult to engineer as the loops are so small and any small deviation from perfect coupling between the two elements would negate any gains from cooling. Future designs could utilize an array of coil elements (see C) and perform parallel transmission for microscopy. Since the loops would inevitably be smaller, geometric decoupling seems cumbersome and circuit based decoupling schemes would be better suited for the array [178, 22]. Furthermore, temperature control using the PID controlled designed in appendix D would greatly benefit the system.

6.3 Microscopic parametric imaging

The use cases of MRM for excised tissue are abundant as demonstrated by the green onion root and the mouse cervix. The unique contrast methods allow probing of structure and function while keeping the tissue intact. The in-plane resolution of the green-onion root images is impressive for the limited gradient strength available (1 T/m). To put this in perspective, the 3 μm^3 resolution images obtained by [62] required a 50 T/m triaxial gradient system and a $< 100\mu m$ OD micro solenoid at 9T. Without phase encoding, the relatively high diffusion of the sample would attenuate the signal degrading the resolution and SNR in the midst of the long readout. The mouse cervix images demonstrate a unique collaborative effort to further understanding of a healthy functioning reproductive system in the mouse. With conventional MR techniques, the muscle fibers, $\approx 50\mu mindiameter$ [179] would not be resolved. The high-field strength, high-sensitivity microcoils, and cryogenically cooled surface loop allow adequate SNR for tractography in reasonable time frames. Tractography with $75\mu m^3$ isotropic resolution was acquired with 30 diffusion weighted directions and b0 images of SNR > 20 utilizing dsi.studio. See https://dsi-studio.labsolver.org/citation.html and [180],[181], and [182] for details of software. In chapter 5.2 93.8 x 92.1 x 92.1 μm $T_{1\rho}$, and $R_{1\rho}$ parametric maps were acquired with optimized acquisition and a micro-solenoid. These are the highest $T_{1\rho}$ parametric maps of excised kidneys and to the author's knowledge

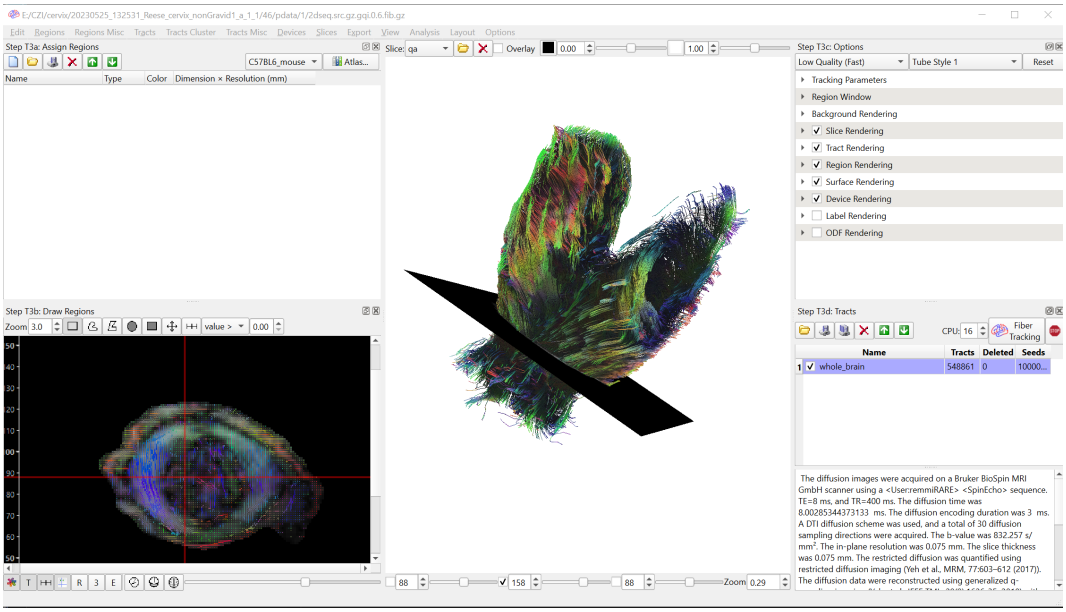

Figure 6.1: The diffusion images were acquired on a Bruker scanner using a RARE-SE sequence. TE = 8 ms, and TR = 400 ms. The diffusion time was 8 ms. The diffusion encoding duration was 3 ms. A DTI diffusion scheme was used, and a total of 30 diffusion sampling directions were acquired. The b-value was 832.257 s/mm^2. The in-plane resolution was 0.075 mm. The slice thickness was 0.075 mm. The restricted diffusion was quantified using restricted diffusion imaging. The diffusion data were reconstructed using generalized q-sampling imaging with a diffusion sampling length ratio of 0.6.

any excised tissue in general. The results demonstrate that MRM is useful for validation of disease presence in the kidney. If resolution is further improved, MRM at high-fields may offer an attractive complementary imaging technique to histological validation [183]. The results also confirm previous findings [160] that the OSOM is demonstrating the change in dispersion and that the cortex region dispersion changes are negligible (see figure 5.12). The conventional spin-lock pulse sequence is not often applied at 15.2T. The results confirm that further $R_{1\rho}$ imaging at 15.2T should be pursued. More advanced spin-lock composite pulses should be applied at 15.2T to allow for lower and higher FSLs.

High-resolution parametric imaging of tissue is touted as a promising alternative to histology. This may be true for diffusion imaging [184], however for parametric fitting like that described in section 5.2 it is not so clear that high-resolution parametric fitting will provide more information. This is clearly demonstrated in figure 5.11. The variation of tissue in the cortex on a voxel-wise basis will only increase as the voxels shrink. It is clear that some of the $\approx 100\mu m^3$ volume voxels are not dispersive. For example, some of these voxels could be purely PBS or another non-dispersive material. This becomes even more complicated considering the number of tissues types the pixel may represent. The evidence of variation in the fits in figure 5.11 demonstrates that the variation is biological in nature. Anatomically, this is intuitive as the cortex includes vessels, nephrons, and glomeruli and is more heterogeneous than the medulla. Further work investigating the limits of parametric mapping in heterogeneous tissue should be pursued.

Appendix A

Bench to bore ramifications of inter-subject head differences on RF shimming and SAR at 7T

A.1 Abstract

This study shows how inter-subject variation over a dataset of 72 head models results in specific absorption rate (SAR) and B_1^+ field homogeneity differences using common shim scenarios. MR-CT datasets were used to segment 71 head models into 10 tissue compartments. These head models were affixed to the shoulders and neck of the virtual family Duke model and placed within an 8 channel transmit surface-loop array to simulate the electromagnetic fields of a 7T imaging experiment. Radio frequency (RF) shimming using the Gerchberg-Saxton algorithm and Circularly Polarized shim weights over the entire brain and select slices of each model was simulated. Various SAR metrics and B_1^+ maps were calculated to demonstrate the contribution of head variation to transmit inhomogeneity and SAR variability. With varying head geometries the loading for each transmit loop changes as evidenced by changes in S-parameters. The varying shim conditions and head geometries are shown to affect excitation uniformity, spatial distributions of local SAR, and SAR averaging over different pulse sequences. The Gerchberg-Saxton RF shimming algorithm outperforms circularly polarized shimming for all head models. Peak local SAR within the coil most often occurs nearest the coil on the periphery of the body. Shim conditions vary the spatial distribution of SAR. The work gives further support to the need for fast and more subject specific SAR calculations to maintain safety. Local SAR_{10g} is shown to vary spatially given shim conditions, subject geometry and composition, and position within the coil.

A.2 Background

Ultrahigh field (UHF) MRI provides greater spin polarization [185] and SNR with a cost of higher RF power absorption and more inhomogeneous excitation [186]. Along with shorter wavelengths and higher conductivity, intersubject differences contribute profoundly to transmit inhomogeneity and increased specific absorption rates (SAR) at UHF [187]. Parallel transmission (pTx) and RF shimming are a few ways to lessen inhomogeneity and control SAR. Methods like universal pulses [188], dense transmission arrays [189], and dielectric padding [177], all attempt to improve the versatility and feasibility of $>$ 3T imaging of each patient. Understanding the contribution of intersubject variability to electric and magnetic (EM) field inhomogeneity and therefore B1 and SAR variation is an important step towards creating universal or patient tailored hardware and pulse design. The magnetic field inhomogeneity results in flip angle non-uniformity whereas the electric field inhomogeneity results in spatially varying local SAR. The current standard for accommodating intersubject variation in local SAR is the use of a vendor dependent safety margin [190, 191, 192] which depends on specific models and patient positioning. The safety margin may not account for patients that differ from standard models and potentially overcompensates for tissue heating, thereby limiting pulse sequence performance. Many studies have focused on predicting the appropriate safety margin from values spanning 1.5 to 5 or designing entirely different safety concepts [191, 192, 193, 194, 195]. Recently, studies have focused on predicting or monitoring local SAR while the patient is on the table [196, 197]. Meliado and coworkers used a large data set of prostate electromagnetic field maps to design a Convolutional Neural Network (CNN) capable of predicting local SAR with B_1^+ maps as the input [192]. Without a model for prediction, local SAR calculations are on the order of 10s of minutes and require the electric field data to assemble Q-matrices for individual SAR calculations or use the virtual observation point algorithm [198]. To address this, Milshteyn and coworkers designed a workflow to quickly segment subjects in the scanner and solve for electric field maps using a fast E&M solver to calculate local

SAR within an average of 8 min [196]. The subjects were segmented into 5 tissue classes with tissue below the shoulders approximated as a uniform rectangular block to allow the electric field to dissipate through the body rather than loop near an abrupt truncation [197]. Accounting for SAR in the scanner is difficult since many factors influence the final electric field distribution in the body including the RF coil, the circuit model, coil-coil coupling, the RF shield, patient position, patient composition, and the channels pulse weights. Beginning with the RF coil, ideal current distributions and coil placement have been investigated in depth by Lattanzi, Deniz, and coworkers [199, 200, 201]. Simulating accurate RF coil models complete with decoupling circuits and multiple radiating elements can take 10s of hours to converge. Fast optimization of the S-matrix, usually separate from the simulation space, are typically achieved with state of the art co-simulation methods introduced by Kozlov and Turner [202] and improved on by variants thereof [203, 204, 205]. Coil-coil coupling also influences the shape of the EM field [206] and should be considered in final RF coil safety assessments [203]. With respect to the patient, Kopanoglu and coworkers showed that with one head (Ella of the Virtual Family), slight variations in positioning within a surface loop array can result in up to 5-fold local SAR increases [193, 207]. These studies show the need for further investigation of SAR variation due to the relationship between patient-coil coupling. Publications focusing on patient variability say little regarding the essential metric used for benchtop coil design, the scattering parameters. Simulations have the luxury of assuming perfectly tuned and matched circuits, however this might not be the case on the bench or in the bore [203]. Non-ideal tuning and matching conditions due to patient variability are well known in RF coil design [130]. Solutions for this have included real-time circuit control, however these methods are expensive and have a large footprint in the scanner [208, 209]. Thus, this work attempts to include the field variations accompanying more realistic matching of surface loops in an array including coupling between elements. With respect to patient modeling, multi-tissue compartment, highresolution models most accurately describe the human body. However, SAR and B_1^+ field measurements may only

require a limited resolution [210] (1–3 mm for 7T) and limited number of compartments. Simplified models with only 4 clusters of gray matter, fat, cortical bone, and CSF have been shown to vary $< 12\%$ from more detailed 47-compartment models [190]. B1 fields are typically generated across parts of or the whole of the virtual population [211] to design pTx arrays. On this front, de Greef and coworkers simulated strip-line coil elements around 6 models of the virtual population and reported the worst-case SAR scenarios [212]. Work focusing on what makes RF coil elements robust to large patient populations is lacking. It is possible to simulate hardware across multiple head models with little loss of accuracy in SAR estimation. Although the individual models of the virtual population include over 300 tissue compartments and 0.5 mm isotropic resolution [213], the database is composed of 11 models and may not represent a more general population. It is thus important to understand the extent to which EM fields can vary in as many subjects as possible to identify characteristics that make coils appropriate for an entire population. Hence, the goal of this study is to show transmission, SAR, and coil efficiency variability across 72 unique, anatomically accurate head models in an 8-channel surface loop transmission coil array to provide an order of magnitude larger database of EM fields for comparison. It is clearly shown that the S-matrix, typically used to quantify the efficiency of a coil's tune, match, and decoupling circuits, vary with coil placement and subject head geometry. This is often ignored in assessments of SAR variability. Local SAR values are shown to depend on subject geometry and are more variable than global SAR. A comparison of local SAR values in the head, over a range of tissue compartments is made to correlate SAR with specific anatomical features.

A.3 Materials and methods

A.3.1 Coil design and simulation

An 8-channel (8ch.) surface loop design was chosen since it is one of the most common designs for parallel transmission methods at 7T. The coils are wrapped in an approximately

elliptical shape with a major axis of 26 cm from anterior to posterior and a minor axis of 25 cm from the patient's left to right centered around the brain. Each loop is 16.3 × 9.2 cm with a 5 mm trace width (Fig. A.1). The resonance was tuned with eleven distributed capacitors. The matching circuit consisted of 1 series inductor, 1 series and 1 parallel capacitor [214]. To achieve decoupling between neighboring coil elements, 2 capacitors made up the capacitive decoupling circuit [215] and connected neighboring elements near the center of each coil (Supplementary Fig. A.11). Each of the 8 coils within the array were tuned, matched, and decoupled from neighboring elements while loaded with the median-sized patient with respect to volume (Fig. A.1b). The coil was left at this circuit configuration for all other subjects, to mimic an in-scanner coil. A copper sheet of 3 mm thickness was used as an RF shield, surrounding the coil at a diameter of 30 cm and length of 30 cm with no slotting. FDTD simulations were performed with commercially available XFdtd software (Remcom Inc., State College, Pennsylvania). The meshing of the coil and each head model was 1 mm isotropic with adaptive meshing around circuit elements and the coil to ensure the circuits' inclusion in the mesh. The domain of the FDTD mesh ended in 7 perfectly matched layers. The time-step based convergence criterion of each simulation was set to - 40 dB, equivalent to the fields changing $<0.01\%$ at the last time step. Each port simulation was accelerated with 4 Maxwell architecture GPUs (NVIDIA, Santa Clara, CA). On average, each port took $\approx$ 50 min to converge. The total run time for the simulations was $\approx$ 20 days.

A.3.2 Scattering parameters

A key metric to indicate a well-tuned, matched, and decoupled transmit element is the scattering matrix. S_{mn}, where m and n indicate the mth and nth coil elements, corresponding to the entries of the scattering matrix and can be calculated with the equation

$$S_{mn} = 20\log_{10}\left|\frac{V_m^-}{V_n^+}\right|(dB) \tag{A.1}$$

where V_m^- and V_n^+ are the m^{th} and n^{th} port's reflected and incident voltage amplitude, respectively. For each transmit element, S_{mn} was quantified for each head. Each element's S_{mn} value was optimized for the median sized subject (with respect to volume) in the pool. The surface loop design distributes the capacitance across 11 capacitors in series to increase the individual capacitance of each. This ensures relatively uniform current distribution along the conductor as the copper traces are separated by a capacitor every $1/20^{th}$ of a wavelength. To determine optimal lumped element values for the tuned, matched, and decoupled array, a co-simulation approach was used [202]. Lumped element values were determined after running 12 lumped elements for each coil as 50 Ω ports and plugging the 96 × 96 scattering matrix into the Agilent/Keysight ADS 11 (Keysight, Santa Rosa, CA) circuit simulator. Initial values of optimal capacitor values were determined from previous experience. The S-matrix goals were $S_{nn} <$ - 30 dB, $S_{mn} <$ - 20 dB. An exception was made for S18 being $<$ - 15 dB, since it was assumed coils near the face would suffer from more variation in loading (Fig. A.1b). The final lumped element values can be found in supplementary Table A.1. Each capacitor was modeled with an equivalent series resistance taken from vendor datasheets and was roughly 0.05 Ω.

A.3.3 Head models

Seventy-one head models were segmented from T1-weighted MRI and computed tomography (CT) data. The subjects were deep brain stimulation (DBS) patients. To simulate heads without stimulation electrodes, the segmented labels of the electrode implants were replaced with their nearest neighbor tissue groups. The skull structure was calculated from the CT data, which for each patient included axial images from the top of the head down to approximately the roof of the mouth. For this reason, bone structures (mostly jaw and spinal vertebrae) below the CT data volume were replaced with air. The size of this region varies from patient to patient. MR data were used to segment soft tissue in this region, the shape of the mouth and neck is retained. Following the work of Wolf et al., a shoulder

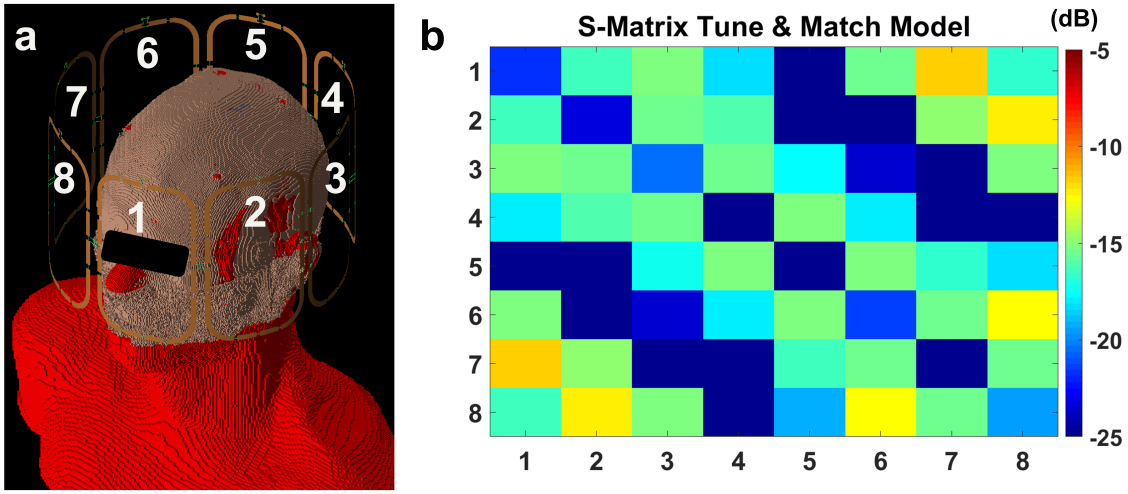

Figure A.1: The capacitively decoupled array can be seen in 1a surrounding the median sized subject. The red portion of the body model is the Duke neck and shoulder region composed of muscle. The two capacitors between coil elements make up the capacitive decoupling circuit. Each loop has 11 tuning capacitors with 4 fixed at 20 pF (see supplementary fig. A.11). The matching circuit is a series inductor, series capacitor, and parallel capacitor. The S-matrix for the same decoupled model is plotted in 1b. The worst decoupling was S_{17} with - 11.6 dB. The worst input reflection was S_{88} with - 19.7 dB. All other input reflections were $<$ - 20 dB.

and neck region composed entirely of one tissue (muscle) was taken from the virtual population Duke model in order to avoid SAR inaccuracies due to a truncated head. Muscle was chosen as the shoulder and neck tissue due to its similar properties to other tissues [216, 217, 121]. This shoulder and neck region was fixed for each head model so that any transmission or SAR variability subject to subject would originate from the differences in the head itself. It has already been shown that a simplification of the shoulder region's resolution and tissue compartments has only a small effect on SAR estimates in brain imaging [216]. The head models were segmented into 9 compartments including gray matter, white matter, CSF, cortical bone, fat, skin, eye, thalamus, and air. These tissues were chosen as they follow the work of de Buck et al. in determining the most important tissue labels via k-means clustering [190] which include gray matter, fat, cortical bone, CSF, and air. The head library was segmented but not registered to an atlas to maintain as much subject variability as possible. Since the Duke model's shoulder and neck region may be different in size or scale to each head in the database, the head model is moved up or down the neck of the Duke model until a reasonable difference between the top slice of the neck and bottom slice of the head appears. A linear interpolation was then applied radially to smooth out the discontinuity between the two slices. The purpose of including this neck and shoulder region is to maintain as close to an anatomically correct body model as possible while still maintaining the subject differences in the head region only. Each head was placed within the coil with the top of the coil level with the top of the head. The mesh of each coil and subject was exported to ensure the coil and model did not overlap in any voxels. Each head was also visually inspected within the simulation software to ensure the coil did not overlap with the patient.

A.3.4 RF-shimming

Three shim methods were applied to the electric and magnetic field sensitivity maps. Two shims, a traditional 45-degree phase offset between each coil (i.e., circularly polarized if

the coil is unloaded) is referred to as CP_{ul} and a shim where the sum of the phases from each coil is zero at the center voxel of the region of interest (i.e., circularly polarized when the coil is loaded) is referred to CP_l. A non-linear magnitude least squares iterative phase updating algorithm known as the Gerchberg-Saxton algorithm is referred to as GS [24]. These shim conditions were selected because they are incrementally complex. CP_{ul} fixes the amplitude and phase, independent of the subject, whereas CP_l's amplitude is fixed but phase is subject dependent, and the GS algorithm's phase and amplitude are both subject dependent. Each shim was applied and analyzed over two target fields of view, the entire brain (denoted as Brain Volume) and a 4 mm thick transverse slice (denoted as Slice) in the center of the coil excluding non-brain tissue.

A.3.5 Transmit and SAR metrics

Using the superposition principle, the B_1^+ and electric field for a given complex shim weight can be defined as

$$B_1^+(r) = \sum_{n=1}^{N} w_n b_n(r) \; and \; E(r) = \sum_{n=1}^{N} w_n e_n(r) \tag{A.2}$$

where r denotes the spatial location and n the coil number (out of N transmit elements). The field maps $b_n(r)$ and $e_n(r)$ represent the complex field of the nth transmit element with unit RF power and all other transmit elements zeroed. The $b_n(r)$ is also known as the sensitivity profile of the nth transmit element. The Coefficient of Variation (CoV) over a select region of interest (ROI) was defined as

$$CoV(||B_1^+||) = 100\frac{std(||B_1^+(ROI)||)}{mean(||B_1^+(ROI)||)}(\%) \tag{A.3}$$

where $||x||$ is the magnitude of the complex field x and std. denotes the standard deviation. Following the work of Deniz et al. [218], a transmit efficiency metric denoted as η was calculated and has the units of $\mu T^2 W^{-1}$. SAR metrics were also calculated. The SAR

in each voxel is defined as

$$SAR = \frac{\sigma ||E||^2}{2\rho} \tag{A.4}$$

where σ is the conductivity and ρ the tissue density of the voxel. By averaging SAR over global and local volumes, Global SAR (SAR_{global}), whole head SAR (SAR_{head}), and local SAR can be calculated. SAR_{global} averaged over the entire subject including the Duke shoulder portion whereas SAR_{head} truncated the shoulder region below the midpoint of the C5-C6 vertebrae in the Duke model. Local SAR_{10g} was calculated using the SAR Average tool [219] which uses a spherical masking technique around each voxel of interest to define 10-gram regions. SAR for an arbitrary pulse sequence (SAR_{seq}) was also calculated following the work of Collins et al. [220]. Defining a hard pulse's flip angle as

$$\alpha_{flip} = \gamma \tau ||B_1^+|| \tag{A.5}$$

where γ is the gyromagnetic ratio, and τ is the pulse duration. A hard pulse with a field strength of 1 μT and 6 ms duration corresponds to a 90° flip angle. SAR for an arbitrary pulse of flip angle α and duration τ can be defined using the SAR given by a 90-degree hard pulse of 1 ms duration as

$$SAR_{\tau/\alpha} = f(\frac{1\ ms}{\tau})^2 (\frac{\alpha}{90\,\mathrm{deg}})^2 SAR_{1ms/90\,\mathrm{deg}} \tag{A.6}$$

where f depends on the pulse shape (f = 1 for a hard pulse). The SAR levels of a sequence can then be defined through time as a sum of each pulse's SAR times its pulse length divided by the total imaging time described mathematically as

$$SAR_{seq} = [\sum_{p=1} P \tau_p SAR_{\tau_p/\alpha_p}](TT)^{-1} \tag{A.7}$$

where p indexes the pulses, τ_p is the pth pulse's duration, and TT is the total time of

acquisition. This can be used to estimate SAR limits imposed by the FDA for continuous imaging during a 6-min period.

A.3.6 Pulse sequences

To demonstrate how Average SAR depends on patient, sequence, number and type of pulses, Eq. A.7 was evaluated using each subject's unique SAR_{head} with the CP_{ul} shim weights. Two sequences, a 3D Gradient Echo (3D GRE) and 3D Fast Spin Echo (3D FSE), were considered for comparison, employing commonly used imaging parameters. Each sequence had a 250 × 200 × 200 mm field of view and a total scan time of 6 min. Every pulse is assumed to be a hard pulse and is based on each individual's SAR_{head} calculated for a 2 ms 90-degree hard pulse (Eq. A.6). The 3D GRE sequence had TR/TE = 24 ms/ 10 ms, and a 2 ms excitation pulse with a flip angle of roughly 10○. After 14,884 RF pulses within the 6-min sequence, the nominal resolution was 1.64 × 1.64 × 1.64 mm (Fig. A.5a). The 3D FSE's sequence had an echo train length (ETL) of 40, TR/TE = 11,500 ms/ 13 ms, 90-degree excitation pulse with 2 ms duration, and 180○ refocusing pulse with 4 ms duration. After 12,874 RF pulses within the 6-min scan, the nominal resolution was 1.8 × 1.8 × 1.8 mm (Fig. A.5b). All pulses were assumed to be 180-degree for refocusing, and 90-degrees for excitation except the GRE excitation pulse which was calculated as the Ernst angle given an average T1 across the head. Given a fixed scan time of 6 min for each FSE and GRE, the SAR_{seq} (Eq. A.7) was calculated for every subject and variable number of pulses.

A.4 Results

A.4.1 Scattering parameters

The median-sized subject that the coil was tuned, matched, and decoupled for is denoted as T&M. The S_{nn} values for the T&M subject for coils 1–8 were - 21.8, - 23.4, - 20.5, - 27.2, - 27.3, - 21.5, - 25.9, and - 19.7 dB respectively. For the worst tune, match, and decoupled subject (denoted Worst T&M), calculated as the lowest percent power transmitted summed

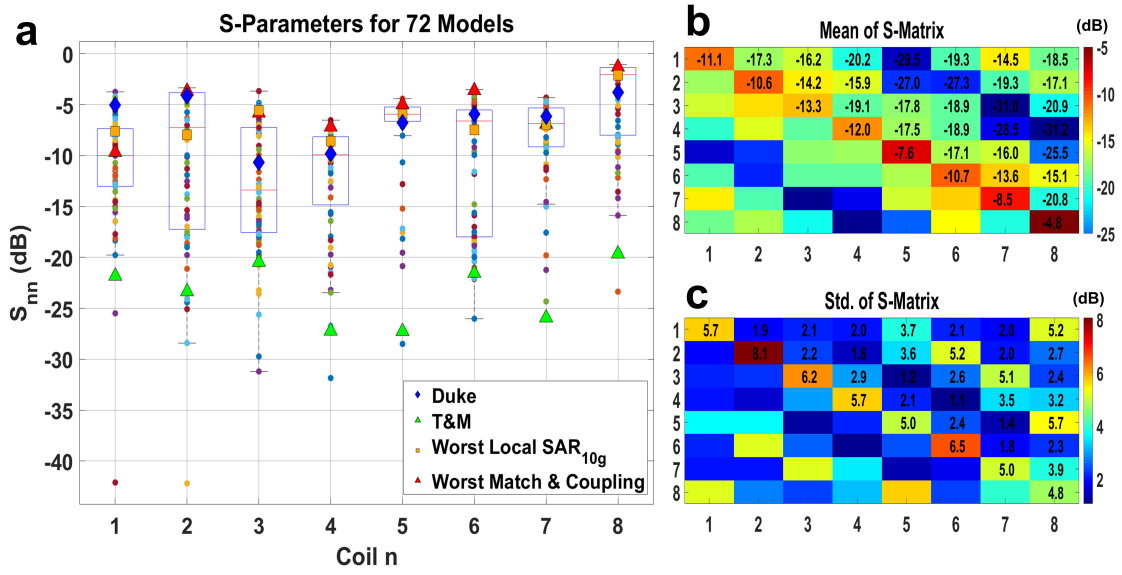

Figure A.2: S_{nn} was calculated to measure the response of each channel to variations in the loading of the head model in a. The Duke model is included in the dataset as the 72nd head model. Each patient is color coded as a circle except for the legend entries. The range of the S_{nn} values demonstrates subject to subject variability purely based on the impedance of the load from varying tissue composition and positioning. In b and c it is clear the diagonal of the S-matrix suffers from changing loading conditions more than the off-diagonal entries.

over all 8 coils, the S_{nn} values were - 9.7, - 3.7, - 5.8, - 7.2, - 5.0, - 3.6, - 6.9, and - 1.3 dB respectively (Fig. A.2a). The mean and standard deviation of each S-matrix coordinate was computed over all 72 models (Fig. A.2b, c). The worst mean input reflection was coil 8 with S_{88} = - 4.8 dB. The worst mean of the off-diagonal coupling coefficients was S67 = - 13.5 dB. The worst standard deviation on the diagonal was coil 2 with 8.1 dB.

A.4.2 RF-shim performance

With respect to slice-wise shimming (Fig. A.3), the GS shim weights achieved the best solution for field homogeneity with an average field homogeneity of 14.2% across the 72 models. This is to be expected as the solution has more degrees of freedom than the simple phase assignments of CP_{ul} and CP_l. Two subjects with coil 8 achieving an S_{nn} value $>$ - 1.2

dB, each reflecting >75% of the incident power, indicate the utility of the GS algorithm by achieving a $\approx 10\%$ CoV($||B_1^+||$) in the slice with coil 8 nulled in each respective case. With these same two patients, CP_{ul} and CP_l achieve >20% with comparable peak Local SAR_{10g}. GS also had a lower average SAR_{head} with 0.22 Wkg^{-1} vs the CP_{ul} and CP_l cases 0.26 and 0.24 Wkg^{-1}, respectively. Local SAR_{10g} on average was lowest for CP_{ul} with 3.3 versus 3.79 and 5.3 Wkg^{-1} for the GS and CP_l cases. The 10 Wkg^{-1} IEC limit [221] was violated by 3, 0, and 4 subjects for GS, CP_{ul}, and CP_l respectively. CP_l has a CoV($||B_1^+||$) spanning a range of 56%, wherease GS and CP_{ul} have ranges 14 and 19.7% indicating that for slice-based shimming of an axial slice near the center of the coil, traditional circularly polarized shimming is an excellent first order approach to achieve higher transmit efficiency with lower SAR_{head} and Local SAR_{10g}.

When RF shimming over the entire brain volume (Fig. A.4), the GS algorithm outperforms in transmit homogeneity at the cost of higher SAR_{head} and Local SAR_{10g}. GS's average CoV($||B_1^+||$) across the population is 28.2% whereas the CP_{ul} has 37.5%. The 51-tissue compartment Duke model is shown as the gold diamond in Fig. A.3 and Fig. A.4 and was plotted as a reference model for each metric.

A.4.3 Global SAR variability

Applying eqs. A.6 and A.7, Average SAR values over a 6-min sequence can be estimated across the population. The SAR_{seq} will depend on the number of pulses, flip angles, pulse lengths, and pulse types. These can vary for a given sequence and certain subjects may reach tissue heating limits before others. Fig. A.5 shows the results of applying eq. A.6 to 3D FSE and 3D GRE. Each line in Fig. A.5 represents a subject from the 72 models. The x-axis in each plot represents the number of hard RF pulses, which increases with the number of TRs. Each point on the line represents some number of pulses within a 6-min scan. The final number of pulses represents the $\approx 2 \times 2 \times 2$ mm 3D resolution. Higher flip angle pulse sequences like the FSE sequence are at risk of exceeding the 3.2 Wkg^{-1} limit

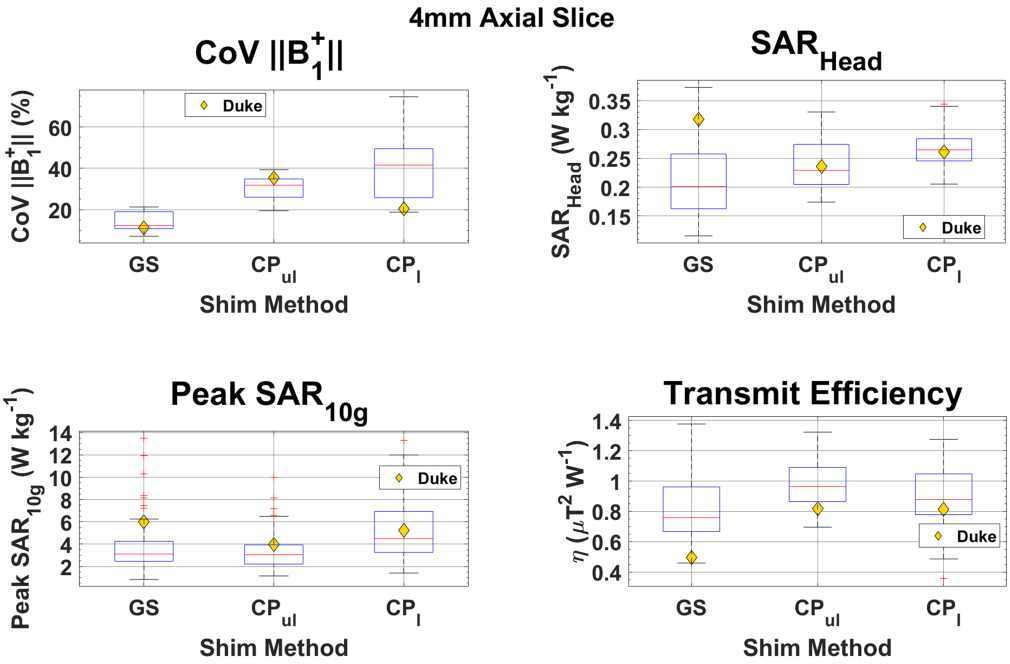

Figure A.3: Three RF shimming methods were applied to the pTx array's field maps across all 72 head models. The field of excitation consisted of a 4 mm axial slice in the center of the RF coil. The non-linear GS algorithm outperformed each CP shim condition (unloaded and loaded circularly polarized) in field homogeneity, the algorithm was run without regard for SAR limits. The GS algorithm had the lowest mean SAR_{head} compared to the CP shims. Local SAR_{10g} increased for 46 of the 72 models when GS shims were applied versus the traditionally circularly polarized weights. 3 subjects exceeded the 10 Wkg^{-1} IEC limit with the GS shims compared to 0 and 4 subjects for the CP cases. Transmit efficiency for the GS algorithm was lower on average. 51 of the 72 subjects had lower transmit efficiency with the GS shim versus traditionally circularly polarized CP_{ul} condition.

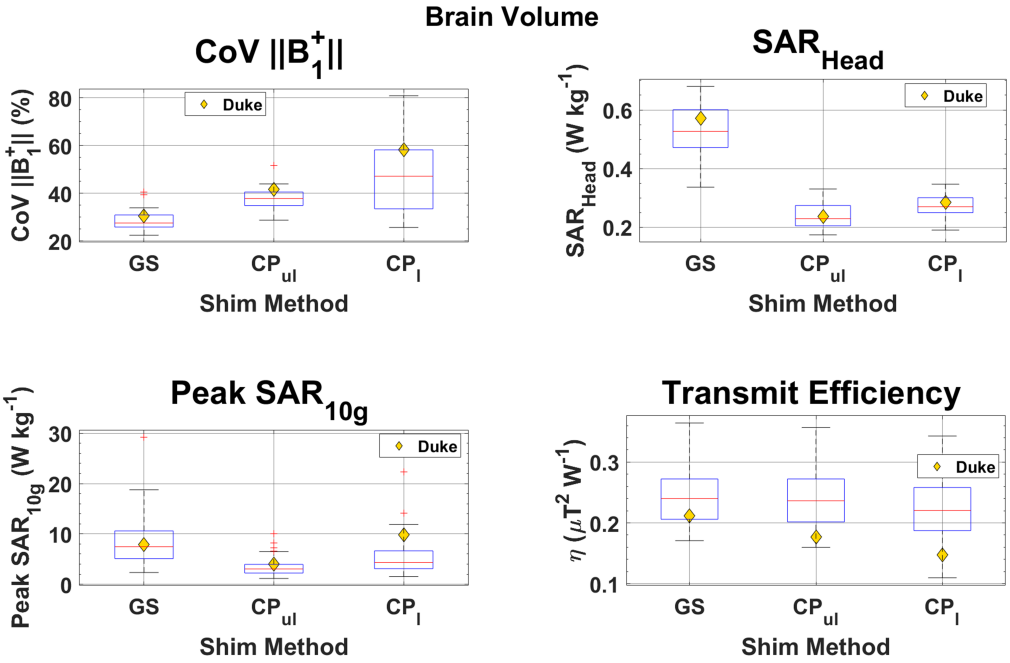

Figure A.4: On the brain volume, GS achieves more optimal transmit fields but suffers higher local and global SAR due to the size of the FOV. More elaborate shimming algorithms may be needed for optimal homogeneity across the entire brain volume.

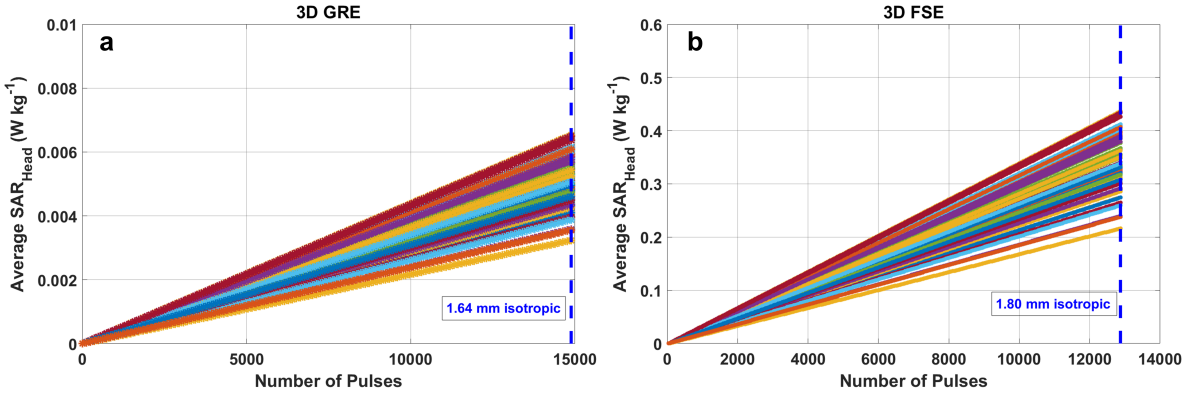

Figure A.5: Two conventional MRI sequences are played out with a fixed scan time of 6 min. Each line represents a specific subjects SAR_{seq} value over the number of pulses within a 6-min scan. The 3D GRE sequence has a much lower SAR_{seq} since the flip angles are small and pulse durations short (5a). The 3D FSE sequence used 90- and 180-degree excitation and refocusing pules, therefore the SAR_{seq} is higher (b). The pulses are assumed to be block pulses where f = 1 in eq. A.6. If more elaborate pulses are used, such as SLR or HS pulses, f becomes >1.

for SAR_{head} especially when longer excitation and more elaborate RF pulses like Shinnar-Le Roux (SLR) or Hyperbolic Secant (HS) shapes are used. These results could also be applied to SAR_{global}, but the SAR per pulse is lower since the global average includes the shoulder region with potentially lower RMS electric field values

A.4.4 Local SAR_{10g} variability

Local SAR_{10g} has been reported to be the limiting safety metric in many studies [222, 223, 224], thus this study focuses most on local SAR_{10g} spatial and tissue variability. Fig. A.6 shows the relationship between peak spatial SAR_{10g} and the nearest coil to this point's position. Nearest-coil distance is defined as the Euclidean distance between the local SAR_{10g}

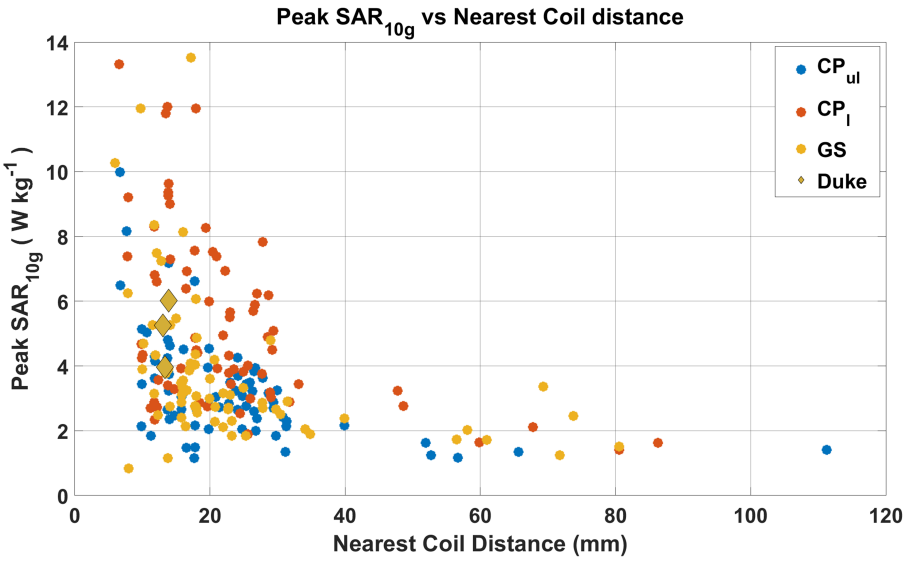

Figure A.6: The peak local SAR plotted against the minimum distance from the local SAR_{10g} point and the nearest point on the 8ch. coil. The nearest coil distance is defined as the Euclidean distance between the hotspot and the nearest coil labelled voxel in the cartesian simulation space. Tissue within 20 mm of a coil's trace have a higher risk of exceeding SAR constraints.

hotspot (maximum), and the nearest voxel labelled as the RF coil. Most of the higher value hot spots occur within 20 mm of the coil. Transmission coils may need to be kept farther than 20 mm from the subject.

In Fig. A.7, the coil can be seen with the Duke model as a reference along with all 216 peak SAR_{10g} spatial locations (72 models * 3 shim scenarios). Most of the peaks are at the points of the head that are closest to the coil at the front or back of the head, save some points within the head. Also, notable are the peak SAR_{10g} locations near the capacitive decoupling circuits between the coils at the back of the head or coil numbers 3, 4, 5 and 6.

Fig. A.8 demonstrates agreement with previous work [222] that skin is most likely to be the highest in local SAR, given different shim scenarios with this specific coil. In Fig. A.9, the highest one thousand local SAR_{10g} values are identified by tissue class and plotted for every model and slice shim scenario. The results indicate there may be changes in tissue

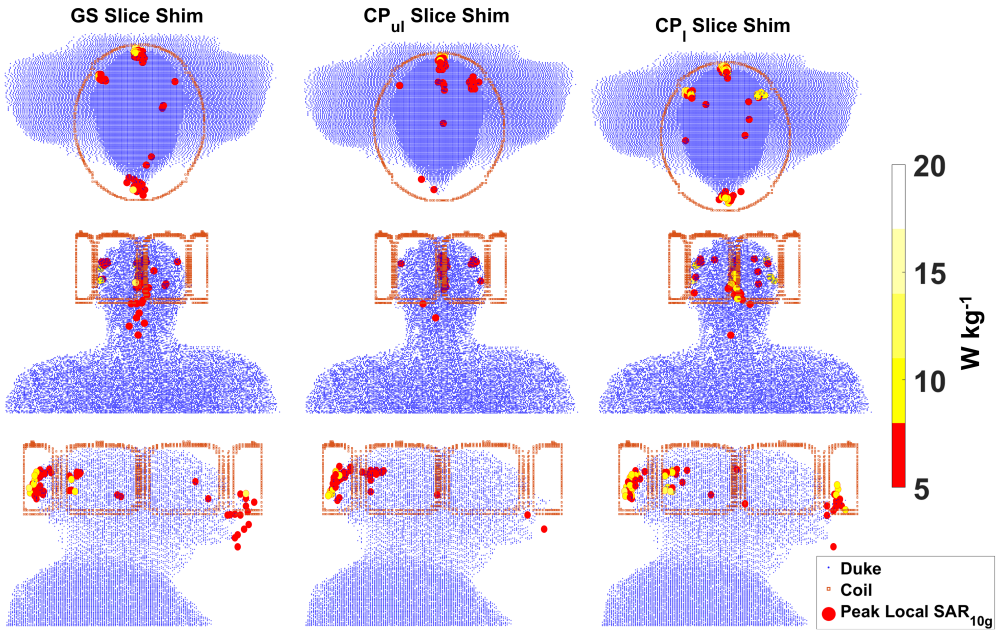

Figure A.7: With the Duke model as a reference, peak spatial local SAR_{10g} points for each head subject are plotted for each shim condition. Most of the points occur nearest the RF coil decoupling circuits at the anterior and posterior of the head. The coil is also included as a reference. The copper RF shield is not included in the plot. Special care must be taken in coil design to ensure extremities of the face such as the nose and ears are not exposed to higher local SAR.

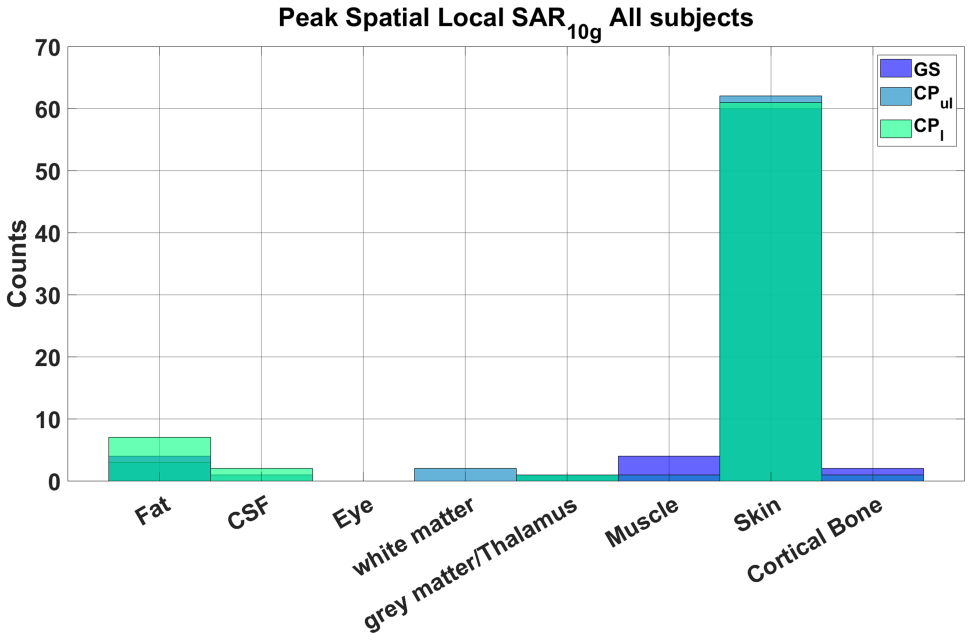

Figure A.8: For each shim condition, most of the peak spatial local SAR_{10g} points occur in the skin tissue compartment. It is therefore important in model segmentation to represent the skin accurately as these tissues are more likely to experience higher local SAR values.

heating distribution due to different shim algorithms. The spatial distributions of local SAR due to varying the shim methods is shown in Fig. A.10 and demonstrates clearly that shim conditions can influence the distribution of local SAR. The tune and match (T&M), Duke, and Worst Case SAR_{10g} are plotted over all 3 shimming conditions for the center slice. The Duke model demonstrates that higher local SAR values tend to congregate on the periphery of the head. Supplementary Fig. A.12 provides insight into peak local SAR_{10g} correlation with overall coil performance metrics. The 8ch. total power was calculated by taking the average of each coils percent power transmission calculated from the S_{nn} values.

A.5 Discussion

In this study, a decoupled pTx array's (Fig. A.1) electric and magnetic fields were simulated using 72 head models to demonstrate RF shim and SAR variations due to intersubject variability. The S-parameters for each coil demonstrate the loading variation due to each

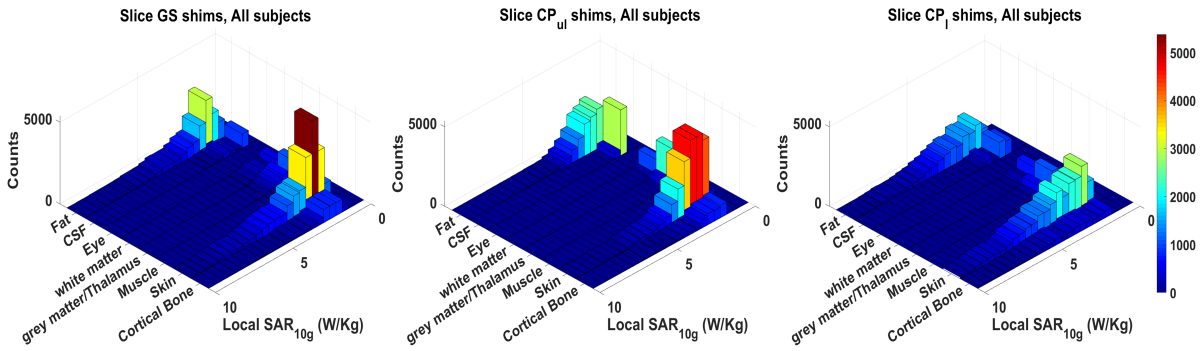

Figure A.9: For each subject and shim condition, the hottest 1000 voxels' tissue and local SAR_{10g} values were recorded. Across tissue distributions, the skin tissue voxels are the hottest SAR_{10g} voxels for each shim condition.

subject's tissue composition and position within the coil (Fig. A.2). Notably, the diagonal of the S-matrix changed the most due to varying loading conditions (Fig. A.2c). The capacitive decoupling circuits were more robust to changes in the load than the matching circuit. The work demonstrates the effect of designing surface loops with only 1 loading condition in mind. RF coils robust to varying loading conditions or self-matched coils [130] will ensure ideal power transfer no matter the subject. Simulation work focusing on uniform models and optimum distance for efficiency has already been done [200] but the human head is far from uniform and population heterogeneity may lead to very different scattering parameters. Arrays should consider as many human models as possible as has been done with gradient coils [82, 225]. Hybridized approaches for coil design including transmit homogeneity or SAR variation across many models could make RF coils more universal. Similar to this idea, Li and coworkers implemented a hybrid circuit and B_1^+ spatial field cost function optimizing the circuit using co-simulation while accounting for the magnetic field homogeneity across 4 models [226]. Hybridizing the cosimulation method to include other domains such as SAR variation and intersubject differences will further improve UHF coil design. It is unknown whether other decoupling strategies, such overlap or self-decoupled transmit arrays will be as robust to changes in the load as the capacitive decoupling circuits used here.

With respect to hardware, open questions remain considering the dependence of other coil designs such as dipole and loop-dipole combinations on intersubject differences [199, 227]. Recently, dipole based transceivers have been rising in popularity due to their simplicity and comparable SNR, transmit efficiency, and SAR management capabilities [228, 229]. In light of this, the first images of the human brain at 10.5T were acquired safely with fractionated and bumped dipole elements [229]. Further work considering the interaction between other coil designs and intersubject differences would benefit UHF safety at large. Finally, the RF shield is known to affect SNR at UHF [230] and its interaction between subjects and SAR variation was not investigated here. Optimizing the transmit field over

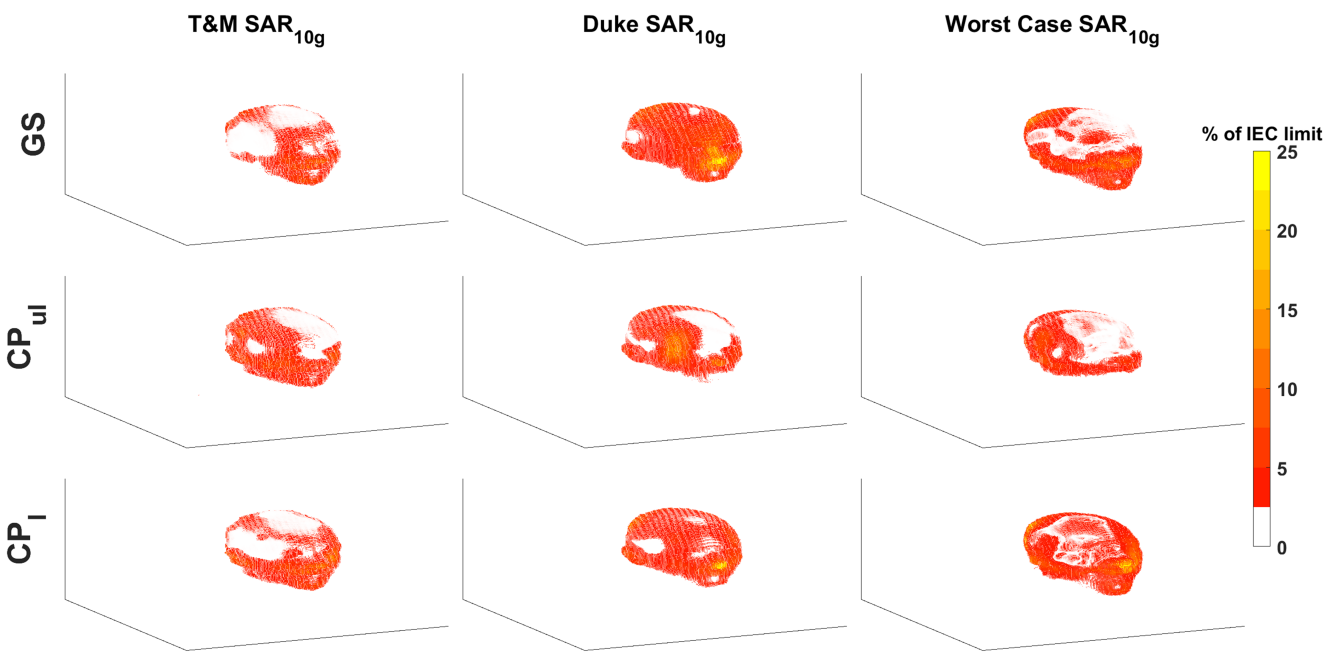

Figure A.10: Three specific subjects' local SAR_{10g} spatial distributions are plotted with respect to the 10 Wkg^{-1} IEC limit. The T&M case is the head model with tuned, matched, and decoupled circuit configurations for every coil. The Duke model is the most anatomically accurate model with 51 tissue compartments

the 4 mm axial slice, the utility of the GS algorithm is demonstrated across many subjects (Fig. A.3). The optimization's cost function was only regularized by the weights of each shim squared which is proportional to the power delivered to each coil port. GS had the lowest CoV($||B_1^+||$) with only 3 models that violated the Local SAR_{10g} 10 Wkg^{-1} limit. This is a concrete example of RF shimming outperforming conventional CP in transmit homogeneity, with comparable global and local SAR over a population. GS initialization phase was that of the CP_l shim weights and greater optimization may be reached if the phase was initialized to the CP_{ul} state. Nevertheless, for whole brain RF shimming (Fig. A.4), the CP_{ul} performance is impressive given the size of the ROI and demonstrates the strength and utility of traditional CP shimming for 8ch. systems. Future RF shimming work over multiple head models could use other regularization terms including explicit SAR measurements [24, 231]. With CP shim weights and a given pulse sequence, disparity of SAR over the head increases as the number of pulses within a 6-min window increases (Fig. **??**). This implies that in pulse-heavy sequences, certain patients will exceed the 3.2 Wkg^{-1} average SAR within a 6-min window before others. However, the slope of the line is close to constant while average SAR metrics can be monitored on the table by pickup coils [232] or equivalent circuit models [233] . There is little to no correlation between transmit efficiency with the reflected power at the port (Supplementary Fig. A.12). This is simply due to the electric and magnetic fields being proportional to the square root of the port power. Variation due to the models may be more important or impactful to transmit metrics than the port's power efficiency within a certain range of S_{nn} values since a subject with 68.7% total power efficiency has lower CoV($||B_1^+||$) than the T&M model with 99% total power when the two slices have mean target field in the FOV of 0.98 and 0.99 μT respectively. In most cases transmit efficiency may represent the limiting factor of peak spatial Local SAR_{10g} (Supplementary Fig. A.12). Transmit efficiency is calculated with the same Q-matrix given to local SAR algorithms without the time consuming 10 g averaging techniques (order of minutes). If Q-matrices become available within the bore, flagging

lower transmit efficiency coil and subject combinations at risk for exceeding local SAR may aid in SAR management. It is also clear that ideal repositioning of the patient may eliminate SAR risk altogether [193]. The tendency of local SAR to be concentrated at the edges of the sample and decrease nearly exponentially with distance from the coil has been discussed in the case of uniform spheres [200]. Given regions most susceptible to higher local SAR_{10g} an optimal distance for transmit only coils may exist. The range of S_{nn} values over 72 models raise questions concerning T/R coils near the head (e.g., how to balance SAR with SNR) and decoupling performance given varying head geometries. It also indicates special attention should be paid to the face region of each subject, to ensure array designs are robust to differing head geometries and nose sizes. Not included in this work is the effect of intersubject differences on temperature changes in the head. The Pennes bioheat equation requires SAR, specific heat capacity of tissue, tissue density, blood perfusion rate, and tissue thermal conductivity [186]. Common body models use fixed estimates of these parameters however they may vary between patients. Including these variables in the head models would affect SAR and temperature estimations. For example, Wang et al. showed as temperature rates exceeded 39$\circ$ C with SAR above 9 W/Kg, the perfusion rates also increased, thus removing heat from surrounding regions at greater rates [234].

A.6 Conclusion

In this work, the change in resistive load from differing patients' composition and position in the coil is shown to be significant enough to affect an array's S-matrix elements when tuning over a single head model. When designing an RF array, multiple loading conditions should be included to maintain acceptable S-matrix values across a population. For slice shimming, it is shown over a population that non-linear optimization schemes such as the Gerchberg-Saxton algorithm provide better transmit homogeneity with comparable global and local SAR. It is shown that average SAR in a window of time is dependent on the number of pulses and the subject, possibly limiting pulse-heavy sequences. RF coil

designs with traces <2 cm away from the subject are at a greater risk of violating local SAR constraints. Similarly, it is also confirmed that local SAR hotspots most often occur on the periphery of the subjects, with skin representing the most and highest-value local SAR hotspots.

A.7 Additional information

Coil #	I_m (nH)	C_p (pF)	C_m (pF)	C_f (pF)	C_t (pF)	C_mid (pF)	C_d (pF)
1	28.52	33.23	15.00	20.00	18.98	3.27	3.11
2	28.52	27.83	15.00	20.00	17.60	2.56	3.99
3	28.52	29.31	15.00	20.00	15.14	3.19	9.47
4	28.52	21.45	15.00	20.00	18.49	3.30	5.78
5	28.52	20.27	15.00	20.00	32.62	2.50	3.39
6	28.52	22.94	15.00	20.00	20.52	2.50	3.19
7	28.52	20.23	15.00	20.00	23.24	2.51	6.15
8	28.52	30.63	15.00	20.00	31.75	2.51	2.74

Table A.1: Lumped element values to accompany figure A.11.

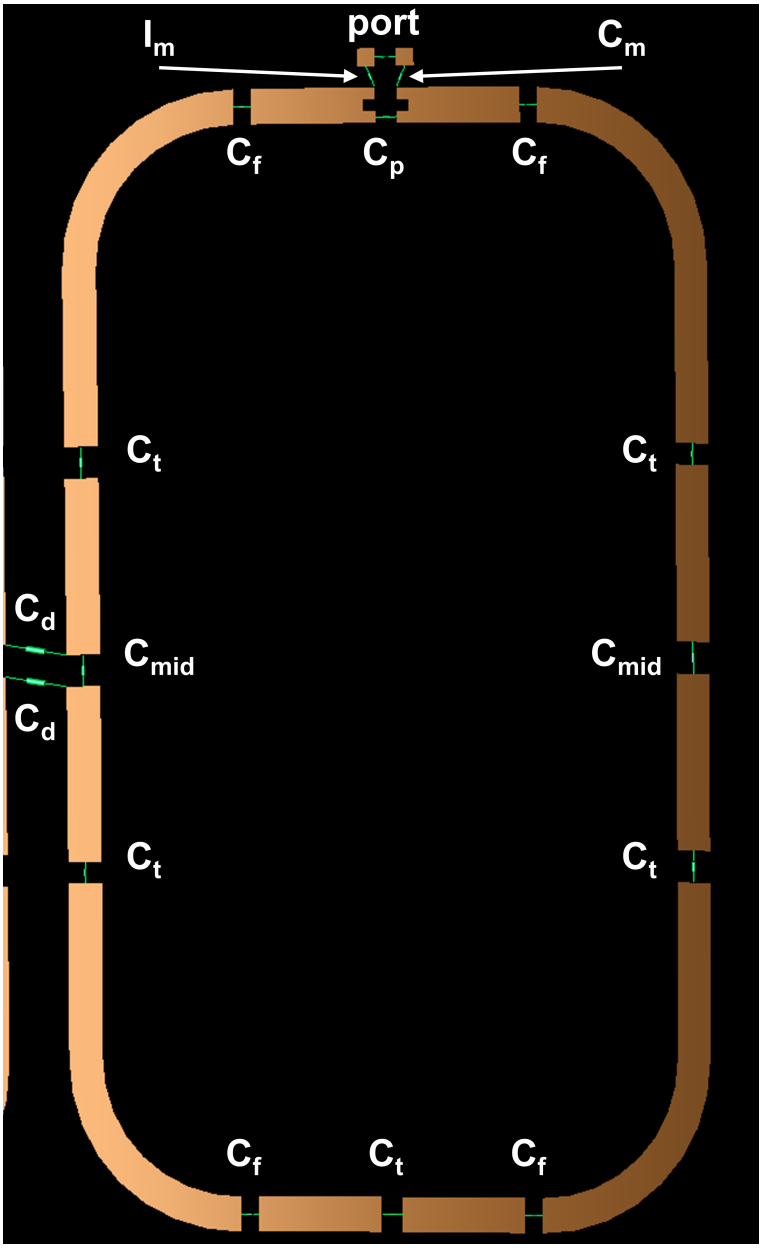

Figure A.11: A single loop-coil with each circuit element labelled. Supplementary table A.1 lists the optimized lumped element values. To simplify the co-simulation approach the Cf and Cm capacitors were not run as 50-ohm ports but were fixed to 20 pF and 15 pF respectively.

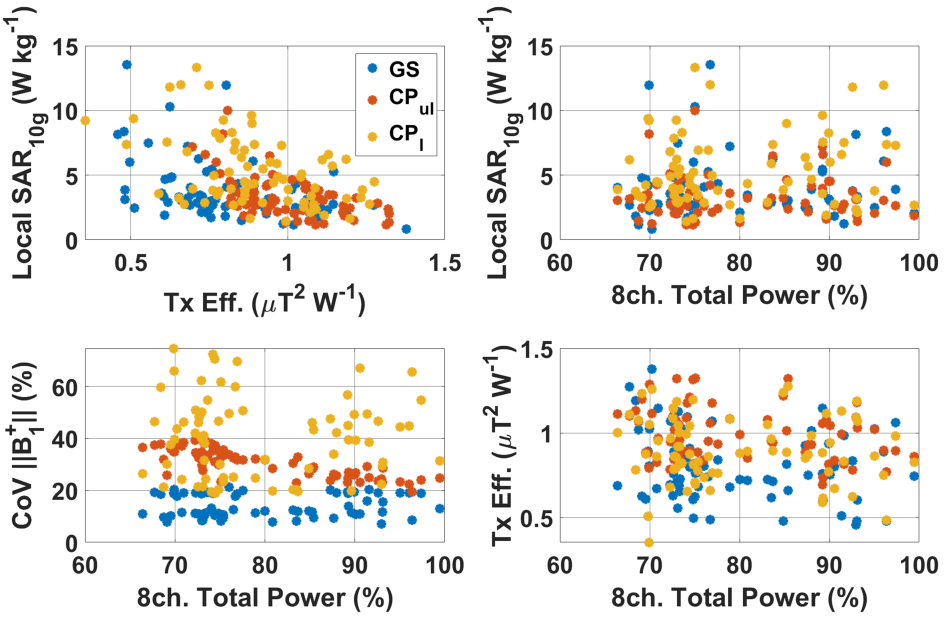

Figure A.12: Local SAR_{10g} is inversely proportional to lower transmit efficiency in most cases (top left). Converting the S-parameters of every coil to percent power and averaging over all 8 channels, total power with respect to the coil's ports is plotted on the x-axis. The CoV($||B_1^+||$) is uncorrelated with the total power transmission in this range of $\approx$ 70 - 100% power transmission. The electric and magnetic field magnitudes increase with the square root of the power transmitted at the ports, therefore the transmit efficiency, which is proportional to the square of the magnetic field the electric field stays flat across total power.

Appendix B

Diffusion attenuation calculation for arbitrary readout waveforms

B.1 Overview

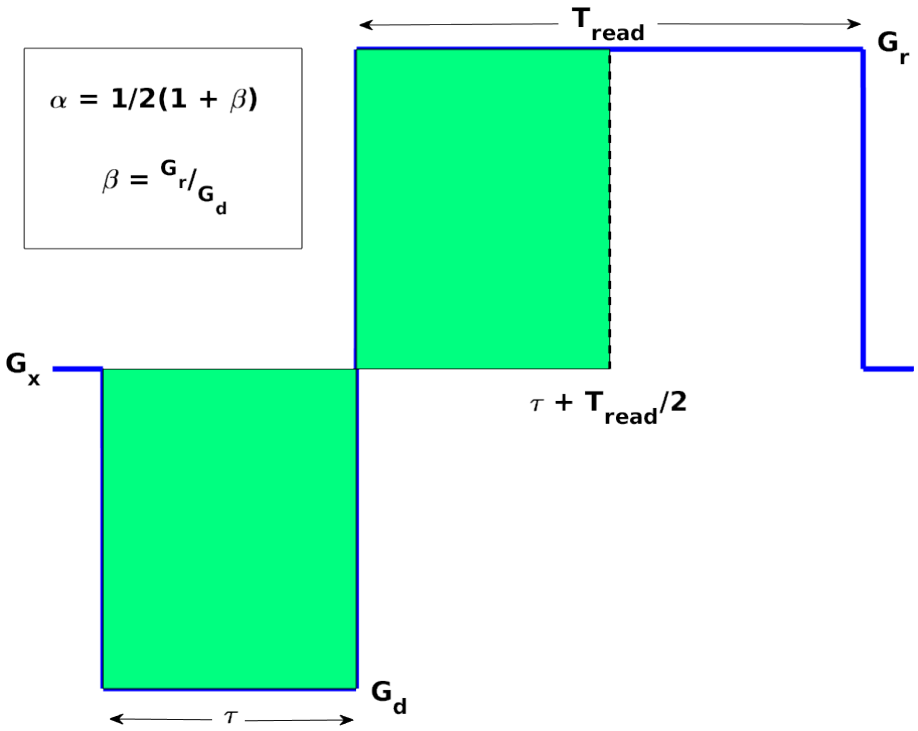

Figure B.1: Gradient waveform for a gradient echo. The area under the dephase gradient is equal to ½ of the area under G_r for conventional gradient echoes. TE is defined as the time between the center of the RF pulse and the center of T_{read}.

For simplification, G_{read} is referred to as G_r and $G_{dephase}$ is referred to as G_d. For readout gradients with varying G_r/G_d ratios, the integral describing the attenuation due to diffusion may be written as

$$A = \exp\left[-\gamma^2 D \int_0^t \left(\int_0^{t'} G(t'')dt''\right)^2 dt'\right] \tag{B.1}$$

which is the solution to the Bloch-Torrey equation [89]. The gradient waveforms (figure B.1) may be described as

$$\int_0^{t'} G(t'')\,dt'' = G_d t \;for\; t < \tau$$
$$\int_0^{t'} G(t'')\,dt'' = -G_d\tau + G_r(t-\tau) \;for\; t > \tau \tag{B.2}$$

Substituting into the attenuation term and integrating until the center of the echo

$$A = \exp\left[-\gamma^2 D\left[\int_0^{\tau} G_d^2 t^2 dt + \int_{\tau}^{\tau+T_r/2} (-G_d\tau + G_r(t-\tau))^2\,dt\right]\right] \tag{B.3}$$

Referring to figure B.1, $G_r T_{read}/2 = G_d\tau$, therefore $\tau = G_r T_{read}/2G_d$. We can define some simplifying parameters to relate the term in the exponent to the readout gradient and duration. Defining

$$\beta = \frac{G_r}{Gd}\; and\; \alpha = \frac{\beta+1}{2} \tag{B.4}$$

The echo time may be written in terms of T_{read}

$$\tau + T_{read}/2 = \frac{G_r T_{read}}{2G_d} + \frac{T_{read}}{2} = T_{read}(G_r/2G_d + 1/2) = T_{read}\alpha \tag{B.5}$$

Performing the integrals in equation B.3, substituting in equations B.4, B.4, and $\tau = G_r T_{read}/2G_d$ results in the exponent term in equation B.1,

$$\begin{aligned} &-\gamma^2 D G_r^2 T_{read}^3\left[\alpha/3(\alpha^2 - 3\alpha/2 + 3/4) + \alpha\beta(-\alpha/2 + \beta/4 + 1/2) + -\beta/24(\beta^2 + 3\beta + 2)\right] \\ &= -\gamma^2 D G_r^2 T_{read}^3 \varepsilon \end{aligned} \tag{B.6}$$

Simplifying further,

$$\begin{aligned} \varepsilon &= \alpha/3(\alpha^2 - 3\alpha/2 + 3/4) + \alpha\beta(-\alpha/2 + \beta/4 + 1/2) + -\beta/24(\beta^2 + 3\beta + 2) \\ &= \frac{\beta+1}{24} \end{aligned} \tag{B.7}$$

At $\beta = 1$, $\varepsilon = 1/12$, and at $\beta = 2$, $\varepsilon = 1/8$.

Appendix C

Simulation and design of 1x4 self-decoupled array

C.1 Overview

Following the work of Yan et. al [235], 2 cm radius self-decoupled coil geometries on an 8x1 modular array were simulated (see figure C.1) to determine if the self-decoupled mechanism would suit an 8x1 array of 2 cm radius loops. Table C.1 shows the select scattering parameters simulation vs benchtop results. Note the coupling of coil 2, where S_{12} and S32 are around -25 dB and well within the acceptable -15 dB rule of thumb for transmit element decoupling. Translating the array to the bench, self-decoupled coils were created with minor differences from the simulation. Mainly the bench circuit differed in that there is 1 tunable inductor along each arm of each loop (see figure C.2) whereas the loops in simulation have 3 inductors along the arm. A phantom matching the simulation sample's conductivity and permittivity was created to analyze the modular array's decoupling circuit. The worst coupling occurred between coil 2 and coil 3 at around S_{32} at roughly -10 dB. This may be due to the relatively short (roughly 5 mm) distance between the coils and the phantom. The constructed 4x1 array is a proof of concept for a stacked array of 4-8 self-decoupled loops along the z-direction. Decoupling between neighboring columns will need to be considered.

Bench (dB)			XF (dB)		
-32	-15	-25	$\leq$ -30	-21	-32
$\sim$	-23	-10	$\sim$	$\leq$ -30	-21
$\sim$	$\sim$	-30	$\sim$	$\sim$	$\leq$ -30

Table C.1: Benchtop vector network analyzer vs XFdtd simulated S-parameters.

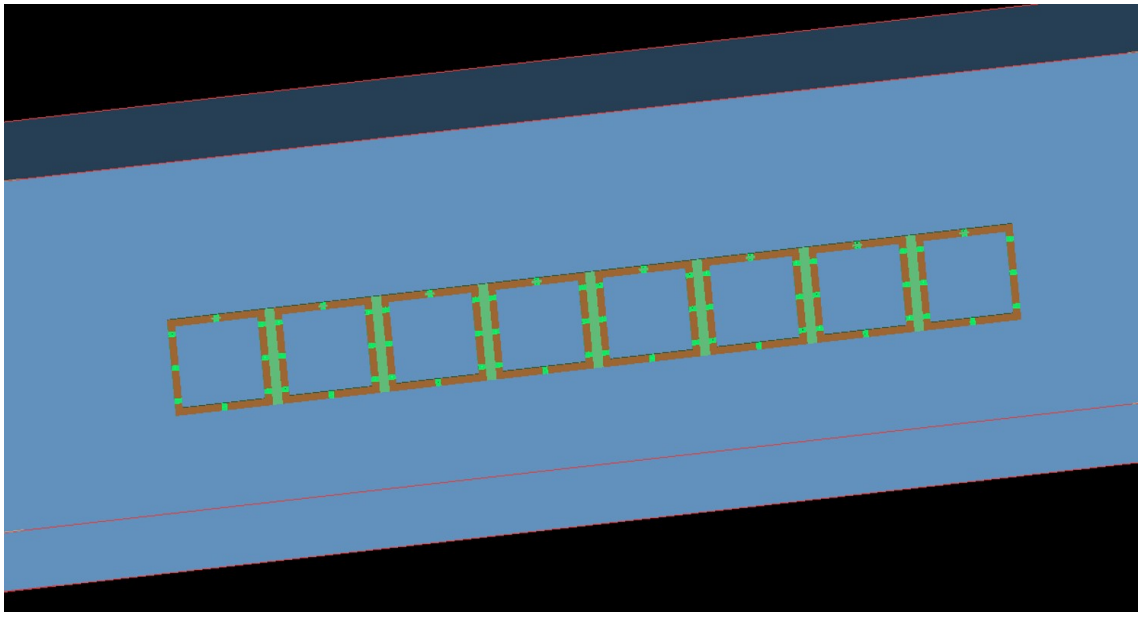

Figure C.1: The 1x4 surface loop array within XF-space.

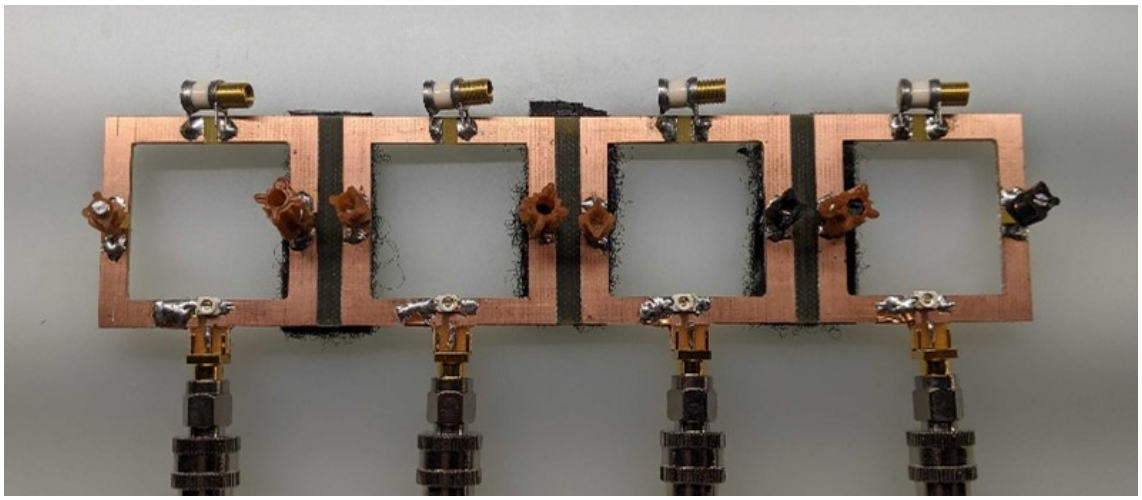

Figure C.2: The 1x4 surface loop array on the bench.

Appendix D

A proportional–integral–derivative (PID) controller for temperature control

D.1 Overview

Several regions of the cryochamber described in chapter 4 would benefit from variable temperature control. A common method of achieving this in engineering is a proportional–integral–derivative (PID) controller. A PID controller is a feedback loop that estimates the response of a system based on simple mathematical calculations performed on continuously updated data. The simplest form of a PID controller may be described using the following equation [236]:

$$y(t) = K_p e(t) + K_i \int_0^t e(t)\, dt + K_d \frac{d}{dt}\, e(t) \tag{D.1}$$

where $e(t)$ is the error or difference of the function from the target value and $K_{p,i,d}$ are tunable parameters to control the response of the system. There are more advanced forms of PID controllers [237] but this form and careful tuning of the parameters are well-suited for temperature control.

D.2 Process

A PID controller was designed for temperature control. The setup consisted of a heater, a 5V relay switch, thermocouple, and a programmable Raspberry Pi (Raspberry Pi Foundation, Cambridge, England). A python script utilizing an open-source PID module was run to control the on/off switch of the heater. The thermocouple temperature data was read on a laptop and transferred via scp to the raspberry pi for PID calculations. The flowchart of this process can be seen in figure D.1 The scripts and transfer protocol are available at https://github.com/benjhardy/Coil_vs_Sample_Noise_MRI.

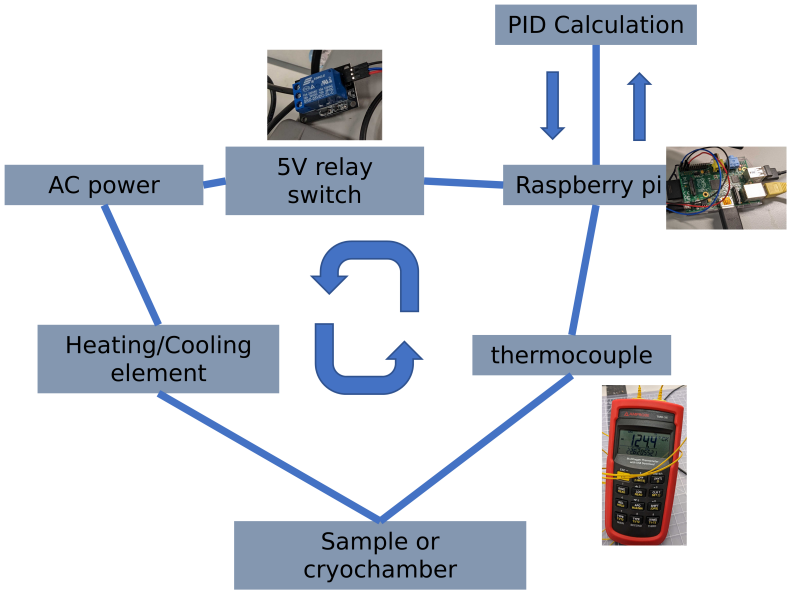

Figure D.1: Flowchart indicating update scheme for the PID temperature controller.

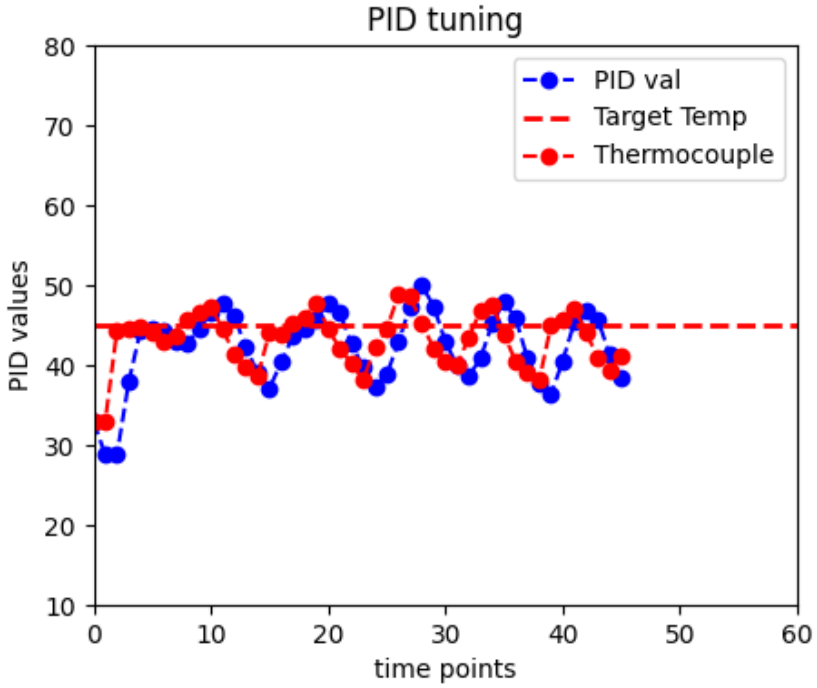

Figure D.2: With a target temperature 45°C, the PID controller was able to reach the target +/- 8°C with minimal tuning adjustments. Finer control could be achieved with more involved tuning. The PID shows excellent agreement with its predictions following the thermocouple's temperature closely. The time points were roughly every second.

D.3 Code

D.3.1 Transfer protocol

```
#!/bin/bash
# permanetly add IP-ADDRESS to ssh's known hosts for easy file transfer
# i.e. no password entry required
#ssh-keygen -t rsa
#ssh-copy-id -i rpi.pub USERNAME@IP-ADDRESS
# loop it to continuously send new temperature data written out
# by the Amprobe TMD-56 thermometer
x=1
while [ $x -le 5 ]
do
    # find the newest file in the record folder
    # (run this .sh script in the record folder of TMD-56)
    # write endline to small file
    echo $(tail -1 $(ls -t | grep *REG*) | awk ' { print $4 } ') > ...
    tempToTransfer
    # output new temperature in cmd
    cat tempToTransfer

    # transfer small file to RASPBERRY PI
    scp tempToTransfer USERNAME@IP-ADDRESS:/home/USERNAME/piHeater

    # arbitrary sleep time of 0.5 seconds
    sleep 0.5
done
```

D.3.2 Python PID update and display

```
# imports
from simple_pid import PID # open-source module
import numpy as np
import RPi.GPIO as GPIO
import time
import matplotlib.pyplot as plt
#import numpy as np
GPIO.setmode(GPIO.BOARD)
GPIO.setup(7,GPIO.OUT)

class controlled_system:
        """Reads temp from the TMD series, turns on the relay if needed."""

def update(onOff,sv):

    # if 1 turn on relay, might want to return previous state
    if onOff < 0:
        GPIO.output(7,True)
        print('Turn on relay onOff, sv{}'.format((onOff,sv)))
    else:
        GPIO.output(7,False)
        print('Turn off relay onOff, sv{}'.format((onOff,sv)))
    #GPIO.cleanup()
```

```
    # reads temp from transferred data
    f = open('tempToTransfer',"r")
    v = float(f.readline())
    f.close()
    # read temp
    print('updated temp: {}'.format(v))
    return v

# Set PID parameters
pid = PID(1,.1,.05,setpoint=1)
pid.sample_time = 0.01 # in seconds update
pid.setpoint = 45 # celsius value to achieve

# Tune Kp,Ki,Kd
pid.tunings = (-1.35,0,6)

# declare class
v = controlled_system.update(23.0,pid.setpoint)

# init arrays for plotting
vals = np.array(v)
tempVals = np.array(v)

# update plot params
plt.ion()
t = 0
tv = np.array([t])

figure, ax = plt.subplots(figsize=(5,4))
line1, = ax.plot(t, vals,'--bo',label='PID val')
line2, = ax.plot(np.linspace(0,60,60),pid.setpoint*np.ones((60,)), ...
'--r', linewidth=2,label='Target Temp')
line3, = ax.plot(t,tempVals,'--ro',label='Thermocouple')

plt.title('PID tuning')
plt.xlabel('time points')
plt.ylabel('PID values')
plt.xlim([0,60])
plt.ylim([10,80])
plt.legend()

# update figure continuously to track PID and temperature
while True:
        # compute new output from the PID according to
    #the systems current value
        onOff = pid(v)
        print('pid result: {}'.format(onOff))

        # feed the pid output to system and get the current value
        v = controlled_system.update(onOff,pid.setpoint)

        t += 1
        tv = np.append(tv,t)
        vals = np.append(vals,onOff+pid.setpoint)
        tempVals = np.append(tempVals,v)
```

```
            # updating data values
            line1.set_xdata(tv)
            line1.set_ydata(vals)
            line3.set_xdata(tv)
            line3.set_ydata(tempVals)

            # drawing updated values
            figure.canvas.draw()

            # This will run the GUI event
            # loop until all UI events
            # currently waiting have been processed
            figure.canvas.flush_events()

            time.sleep(0.01)

GPIO.cleanup()
```

References

[1] Kevin R. Minard and Robert A. Wind. Solenoidal microcoil design. part i: Optimizing rf homogeneity and coil dimensions. *Concepts in Magnetic Resonance*, 13(2):128–142, 2001.

[2] Kevin R. Minard and Robert A. Wind. Solenoidal microcoil design?part ii: Optimizing winding parameters for maximum signal-to-noise performance. *Concepts in Magnetic Resonance*, 13(3):190–210, 2001.

[3] J. Larmor. Lxiii. on the theory of the magnetic influence on spectra; and on the radiation from moving ions. *The London, Edinburgh, and Dublin Philosophical Magazine and Journal of Science*, 44, 1897.

[4] Thomas C. Farrar and Becker Edwin D. *Pulse and Fourier Transform NMR: Introduction to Theory and Methods*. Academic Press, 1971.

[5] Edwin D. Becker. *High resolution NMR Theory and Chemical Applications Third Edition*, volume 3. Academic Press San Diego London Boston, New York, 2000.

[6] Lars G. Hanson. Is quantum mechanics necessary for understanding magnetic resonance? *Concepts in Magnetic Resonance Part A*, 32A:329–340, 9 2008.

[7] F. Bloch. Nuclear induction. *Phys. Rev.*, 70:460–474, Oct 1946.

[8] Robert W. Brown, Yu Chung N. Cheng, E. Mark Haacke, Michael R. Thompson, and Ramesh Venkatesan. *Magnetic Resonance Imaging: Physical Principles and Sequence Design: Second Edition*, volume 9780471720850. 2014.

[9] Kwang W. Oh and Chong H. Ahn. Magnetic actuation. *Comprehensive Microsystems*, 2:39–68, 1 2008.

[10] E. R. Mcveigh, M. J. Bronskill, and R. M. Henkelman. Phase and sensitivity of receiver coils in magnetic resonance imaging. *Medical physics*, 13:806, 1986.

[11] S. H. Koenig, K. Hallenga, and M. Shporer. Protein-water interaction studied by solvent 1h, 2h, and 17o magnetic relaxation. *Proceedings of the National Academy of Sciences*, 72:2667–2671, 7 1975.

[12] Lionel M. Broche, P. James Ross, Gareth R. Davies, Mary Joan MacLeod, and David J. Lurie. A whole-body fast field-cycling scanner for clinical molecular imaging studies. *Scientific Reports 2019 9:1*, 9:1–11, 7 2019.

[13] M. Frigo and S. G. Johnson. The fastest fourier transform in the west. Technical report, USA, 1997.

[14] P. Mansfield and P. K. Grannell. Nmr 'diffraction' in solids? *Journal of Physics C: Solid State Physics*, 6(22):L422, 11 1973.

[15] P. Mansfield and P. K. Grannell. "diffraction" and microscopy in solids and liquids by nmr. *Physical Review B*, 12(9):3618, 11 1975.

[16] Paul T. Callaghan. *Principles of Nuclear Magnetic Resonance Microscopy*. Clarendon Press, Oxford, 1991.

[17] Luisa Ciobanu, Andrew G. Webb, and Charles H. Pennington. Magnetic resonance imaging of biological cells. *Progress in Nuclear Magnetic Resonance Spectroscopy*, 42(3-4):69–93, aug 2003.

[18] Jonathan B. Martin, Sai Abitha Srinivas, Christopher E. Vaughn, Heng Sun, Mark A. Griswold, and William A. Grissom. Selective excitation localized by the Bloch-Siegert shift and a [Formula: see text] gradient. *Magnetic resonance in medicine*, apr 2022.

[19] William A. Grissom, Mohammad Mehdi Khalighi, Laura I. Sacolick, Brian K. Rutt, and Mika W. Vogel. Small-tip-angle spokes pulse design using interleaved greedy and local optimization methods. *Magnetic Resonance in Medicine*, 2012.

[20] Markus Weiger, Yi Zeng, and Michael Fey. A closer look into DESIRE for NMR microscopy. *Journal of magnetic resonance (San Diego, Calif. : 1997)*, 190(1):95–104, jan 2008.

[21] Gregor Adriany, Pierre Francois Van De Moortele, Florian Wiesinger, Steen Moeller, John P. Strupp, Peter Andersen, Carl Snyder, Xiaoliang Zhang, Wei Chen, Klaas P. Pruessmann, Peter Boesiger, Tommy Vaughan, and Kamil Uğurbil. Transmit and receive transmission line arrays for 7 tesla parallel imaging. *Magnetic Resonance in Medicine*, 53(2):434–445, 2005.

[22] Benjamin M. Hardy, Yue Zhu, Mark D. Does, Adam W. Anderson, and John C. Gore. Noise Considerations for a Microsolenoid at 15.2T Designed for MR Microscopy. In *Proceedings of the International Society of Magnetic Resonance in Medicine 30*, page 1543, London, England, 2022.

[23] Charlotte R. Sappo, Gabriela L. Gallego, William A. Grissom, and Xinqiang Yan. On the design and manufacturing of miniaturized microstripline power splitters for driving multicoil transmit arrays with arbitrary ratios at 7 t. *NMR in Biomedicine*, 35:e4793, 11 2022.

[24] K Setsompop, L L Wald, V Alagappan, B A Gagoski, and E Adalsteinsson. Magnitude Least Squares Optimization for Parallel Radio Frequency Excitation Design Demonstrated at 7 Tesla With Eight Channels. *Magnetic Resonance in Medicine*, 59:908–915, 2008.

[25] F. David Doty, George Entzminger, Jatin Kulkarni, Kranti Pamarthy, and John P. Staab. Radio frequency coil technology for small-animal mri. *NMR in Biomedicine*, 20(3):304–325, 5 2007.

[26] D. I. Hoult and Paul C. Lauterbur. The sensitivity of the zeugmatographic experiment involving human samples. *Journal of Magnetic Resonance (1969)*, 34(2):425–433, may 1979.

[27] David I. Hoult and D. Phil. Sensitivity and power deposition in a high-field imaging experiment. *Journal of Magnetic Resonance Imaging*, 12(1):46–67, 2000.

[28] D. I. Hoult. The principle of reciprocity in signal strength calculations - A mathematical guide. *Concepts in Magnetic Resonance*, 2000.

[29] D. I. Hoult. The principle of reciprocity, 2011.

[30] D.I. Hoult and R.E. Richards. The signal-to-noise ratio of the nuclear magnetic resonance experiment. *Journal of Magnetic Resonance (1969)*, 24(1):71–85, 10 1976.

[31] H. Douglas Morris, Peter G. Gorkov, Andrew B. Harris, Jeffery Tsao, Kevin Moser, John G. Georgiadis, Andrew G. Webb, and Paul C. Lauterbur. Micro-samples, Micro-coils, Micro-magnets: Where will all this smallness end? In *5th International Conference on Magnetic Resonance Microscopy*, page 5 (L16), Heidelberg, Germany, 1999.

[32] L. Darrasse and J. C. Ginefri. Perspectives with cryogenic rf probes in biomedical mri. *Biochimie*, 85(9):915–937, 9 2003.

[33] R. G. Medhurst. Resistance and self-capacitance of single-layer solenoids. *Wireless Engineer*, March:35–92, 1947.

[34] R. Dupree and C. J. Ford. Magnetic Susceptibility of the Noble Metals around Their Melting Points. *Physical Review B*, 8(4):1780, aug 1973.

[35] Ravi Kc, Yashas N. Gowda, Danijel Djukovic, Ian D. Henry, Gregory H.J. Park, and Daniel Raftery. Susceptibility-matched plugs for microcoil nmr probes. *Journal of Magnetic Resonance*, 205(1):63–68, 7 2010.

[36] Xiaoliang Zhang, Kamil Ugurbil, and Wei Chen. Microstrip rf surface coil design for extremely high-field mri and spectroscopy. *Magnetic resonance in medicine*, 46:443–450, 2001.

[37] R. D. Black, T. A. Early, and G. A. Johnson. Performance of a High-Temperature Superconducting Resonator for High-Field Imaging. *Journal of Magnetic Resonance, Series A*, 113(1):74–80, mar 1995.

[38] R. D. Black, T. A. Early, P. B. Roemer, O. M. Mueller, A. Mogro-Campero, L. G. Turner, and G. A. Johnson. A high-temperature superconducting receiver for nuclear magnetic resonance microscopy. *Science*, 259:793–795, 1993.

[39] C-N. (Ching-nien) Chen and D. I. Hoult. *Biomedical magnetic resonance technology*. Adam Hilger, Bristol, 1989.

[40] L Ciobanu and C. H. Pennington. 3d micron-scale mri of single biological cells. *Solid state nuclear magnetic resonance*, 25(1-3):138–141, 2004.

[41] Lewis Kyle Hedges. *Microscopic Nuclear Magnetic Resonance Imaging (NMR)*. PhD thesis, State University of New York at Stony Brook, 1984.

[42] James B. Aguayo, Stephen J. Blackband, Joseph Schoeniger, Mark A. Mattingly, and Markus Hintermann. Nuclear magnetic resonance imaging of a single cell. *Nature*, 322(6075), 1986.

[43] C. D. Eccles and P. T. Callaghan. High-resolution imaging. the nmr microscope. *Journal of Magnetic Resonance (1969)*, 68(2):393–398, 6 1986.

[44] Bernhard Blümich. Book review p. t. callaghan. principles of nuclear magnetic resonance microscopy. oxford university press, oxford, 1993, 492 pp, £25. isbn 0 198 53997 5. *Magnetic Resonance in Chemistry*, 33(4):322–322, 4 1995.

[45] Z. H. Cho, C. B. Ahn, S. C. Juh, H. K. Lee, R. E. Jacobs, S. Lee, J. H. Yi, and J. M. Jo. Nuclear magnetic resonance microscopy with 4-mum resolution: Theoretical study and experimental results. *Medical Physics*, 15(6):815–824, 11 1988.

[46] R.W. Bowtell, G.D. Brown, P.M. Glover, M. McJury, and Peter Mansfield. Resolution of cellular structures by nmr microscopy at 11.7 t. *Philosophical Transactions of the Royal Society of London. Series A: Physical and Engineering Sciences*, 333(1632):457–467, 12 1990.

[47] E. W. McFarland. Time-independent point-spread function for nmr microscopy. *Magnetic Resonance Imaging*, 10(2):269–278, 1 1992.

[48] P. M. Glover, R. W. Bowtell, G. D. Brown, and Peter Mansfield. A microscope slide probe for high resolution imaging at 11.7 tesla. *Magnetic resonance in medicine*, 31(4):423–428, 1994.

[49] Richard W. Bowtell, Andrew Peters, Jonathan C. Sharp, Peter Mansfield, Edward W. Hsu, Nanci Aiken, Anthony Horsman, and Stephen J. Blackband. Nmr microscopy of single neurons using spin echo and line narrowed 2dft imaging. *Magnetic Resonance in Medicine*, 33(6):790–794, 6 1995.

[50] Paul Glover and Peter Mansfield. Limits to magnetic resonance microscopy. *Reports on Progress in Physics*, 65(10):1489, 8 2002.

[51] A. G. Webb. Radiofrequency microcoils for magnetic resonance imaging and spectroscopy. *Journal of Magnetic Resonance*, 229:55–66, 4 2013.

[52] Marios Masouridis, Tim B. Dyrby, and Vitaliy Zhurbenko. Design and implementation of solenoid and alderman-grant coils for magnetic resonance microscopy at 7t. *14th European Conference on Antennas and Propagation, EuCAP 2020*, 3 2020.

[53] A. S. Hall, B. Barnard, P. McArthur, D. J. Gilderdale, I. R. Young, and G. M. Bydder. Investigation of a whole-body receiver coil operating at liquid nitrogen temperatures. *Magnetic Resonance in Medicine*, 7(2):230–235, 6 1988.

[54] Peter Styles, Nick F. Soffe, and Christopher A. Scott. An improved cryogenically cooled probe for high-resolution nmr. *Journal of Magnetic Resonance (1969)*, 84(2):376–378, 9 1989.

[55] E. W. McFarland and A. Mortara. Three-dimensional nmr microscopy: improving snr with temperature and microcoils. *Magnetic resonance imaging*, 10(2):279–288, 1992.

[56] A. C. Wright, H. K. Song, D. M. Elliott, and F. W. Wehrli. Use of a joule–thomson micro-refrigerator to cool a radio-frequency coil for magnetic resonance microscopy. *Review of Scientific Instruments*, 76(1):014301, 12 2004.

[57] Chiwan Koo, Richard F. Godley, Jaewon Park, Mary P. McDougall, Steven M. Wright, and Arum Han. A magnetic resonance (mr) microscopy system using a microfluidically cryo-cooled planar coil. *Lab on a chip*, 11(13):2197–2203, 7 2011.

[58] R. D. Black, P. B. Roemer, A. Mogro-Campero, L. G. Turner, and K. W. Rohling. High temperature superconducting resonator for use in nuclear magnetic resonance microscopy. *Applied Physics Letters*, 62(7):771, 6 1998.

[59] Aimé Labbé, Gilles Authelet, Bertrand Baudouy, Cornelis J. van der Beek, Javier Briatico, Luc Darrasse, and Marie Poirier-Quinot. Recent advances and challenges in the development of radiofrequency hts coil for mri. *Frontiers in Physics*, 9:386, 7 2021.

[60] Hsueh Ying Chen and Robert Tycko. Low-temperature magnetic resonance imaging with 2.8 mum isotropic resolution. *Journal of magnetic resonance (San Diego, Calif. : 1997)*, 287:47–55, 2 2018.

[61] Markus Weiger, Daniel Schmidig, Schimun Denoth, Charles Massin, Franck Vincent, Michael Schenkel, and Michael Fey. Nmr microscopy with isotropic resolution of 3.0 mum using dedicated hardware and optimized methods. *Concepts in Magnetic Resonance Part B: Magnetic Resonance Engineering*, 33B(2):84–93, 4 2008.

[62] L. Ciobanu, D. A. Seeber, and C. H. Pennington. 3d mr microscopy with resolution 3.7 by 3.3 by 3.3 micron. *Journal of magnetic resonance (San Diego, Calif. : 1997)*, 158(1-2):178–182, 2002.

[63] Remco van Schadewijk, Julia R. Krug, Defeng Shen, Karthick B.S. Sankar Gupta, Frank J. Vergeldt, Ton Bisseling, Andrew G. Webb, Henk Van As, Aldrik H. Velders, Huub J.M. de Groot, and A. Alia. Magnetic resonance microscopy at cellular resolution and localised spectroscopy of medicago truncatula at 22.3 tesla. *Scientific Reports*, 10(1), 2020.

[64] Choong H. Lee, Niclas Bengtsson, Stephen M. Chrzanowski, Jeremy J. Flint, Glenn A. Walter, and Stephen J. Blackband. Magnetic resonance microscopy (mrm) of single mammalian myofibers and myonuclei. *Scientific Reports 2017 7:1*, 7(1):1–9, 1 2017.

[65] Peter Mansfield and Peter Morris. *NMR Imaging in Biomedicine*. Academic Press, 1982.

[66] Lord Rayleigh. XXXI. Investigations in optics, with special reference to the spectroscope. *The London, Edinburgh, and Dublin Philosophical Magazine and Journal of Science*, 8(49):261–274, oct 1879.

[67] P. T. Callaghan and C. D. Eccles. Sensitivity and resolution in nmr imaging. *Journal of Magnetic Resonance (1969)*, 71(3):426–445, 2 1987.

[68] J. Michael Tyszka, Scott E. Fraser, and Russell E. Jacobs. Magnetic resonance microscopy: recent advances and applications. *Current opinion in biotechnology*, 16(1):93–99, 2005.

[69] Z. H. Cho, C. B. Ahn, S. C. Juh, J. M. Jo, R. M. Friedenberg, R. E. Jacobs, and S.E. Fraser. Recent progress in nmr microscopy towards cellular imaging. *Philosophical Transactions of the Royal Society of London. Series A: Physical and Engineering Sciences*, 333(1632):469–475, 12 1990.

[70] C. B. Ahn and Z. H. Cho. A generalized formulation of diffusion effects in micron resolution nuclear magnetic resonance imaging. *Medical physics*, 16(1):22–28, 1989.

[71] A. G. Webb. Optimizing the point spread function in phase-encoded magnetic resonance microscopy. *Concepts in Magnetic Resonance Part A*, 22A(1):25–36, 5 2004.

[72] P. T. Callaghan and C. D. Eccles. Diffusion-limited resolution in nuclear magnetic resonance microscopy. *Journal of Magnetic Resonance (1969)*, 78(1):1–8, 6 1988.

[73] P. C. Lauterbur. Image Formation by Induced Local Interactions: Examples Employing Nuclear Magnetic Resonance. *Nature 1973 242:5394*, 242(5394):190–191, 1973.

[74] Choong H Lee, Stephen J Blackband, and Pedro Fernandez-Funez. Visualization of synaptic domains in the Drosophila brain by magnetic resonance microscopy at 10 micron isotropic resolution. *Scientific Reports*, 5(1):8920, aug 2015.

[75] Jeremy J. Flint, Choong H. Lee, Brian Hansen, Michael Fey, Daniel Schmidig, Jonathan D. Bui, Michael A. King, Peter Vestergaard-Poulsen, and Stephen J. Blackband. Magnetic resonance microscopy of mammalian neurons. *NeuroImage*, 46(4):1037–1040, jul 2009.

[76] J. S. Morrow. Nuclear magnetic resonance imaging: a tool for microscopists? *The journal of histochemistry and cytochemistry : official journal of the Histochemistry Society*, 34(1):75–81, 1986.

[77] Sungmin Choi, Xiao Wu Tang, and D G Cory. Constant time imaging approaches to NMR microscopy. *International Journal of Imaging Systems and Technology*, 8(3):263–276, 1997.

[78] Samuel Gravina and D. G. Cory. Sensitivity and Resolution of Constant-Time Imaging. *Journal of Magnetic Resonance, Series B*, 104(1):53–61, may 1994.

[79] S. Emid and J. H.N. Creyghton. High resolution NMR imaging in solids. *Physica B+C*, 128(1):81–83, 1985.

[80] O. Nalcioglu and Z. H. Cho. Limits to signal-to-noise improvement by FID averaging in NMR imaging. *Physics in Medicine and Biology*, 29(8):969–978, 1984.

[81] Paul T. Callaghan. *Principles of Nuclear Magnetic Resonance Microscopy*. Clarendon Press, 1991.

[82] Kevin M. Koch, Douglas L. Rothman, and Robin A. de Graaf. Optimization of static magnetic field homogeneity in the human and animal brain in vivo. *Progress in Nuclear Magnetic Resonance Spectroscopy*, 54(2):69–96, feb 2009.

[83] P. T. Callaghan, L. C. Forde, and C. J. Rofe. Correlated Susceptibility and Diffusion Effects in NMR Microscopy Using both Phase-Frequency Encoding and Phase-Phase Encoding. *Journal of Magnetic Resonance, Series B*, 104(1):34–52, may 1994.

[84] P. T. Callaghan, D. MacGowan, K. J. Packer, and F. O. Zelaya. High-resolution q-space imaging in porous structures. *Journal of Magnetic Resonance (1969)*, 90(1):177–182, oct 1990.

[85] Jürgen Link and Joachim Seelig. Comparison of deuterium NMR imaging methods and application to plants. *Journal of Magnetic Resonance (1969)*, 89(2):310–330, sep 1990.

[86] Edwin D. Becker, James A. Ferretti, and Prem N. Gambhir. Selection of Optimum Parameters for Pulse Fourier Transform Nuclear Magnetic Resonance. *Analytical Chemistry*, 51(9):1413–1420, 1979.

[87] Thomas L. James and Alexander R. Margulis. Biomedical magnetic resonance. 1984.

[88] H. Y. Carr and E. M. Purcell. Effects of diffusion on free precession in nuclear magnetic resonance experiments. *Physical Review*, 94(3):630, 5 1954.

[89] H. C. Torrey. Bloch Equations with Diffusion Terms. *Physical Review*, 104(3):563, nov 1956.

[90] Dan Xiao and Bruce J. Balcom. BLIPPED (BLIpped Pure Phase EncoDing) high resolution MRI with low amplitude gradients. *Journal of Magnetic Resonance*, 285:61–67, dec 2017.

[91] Eric Moore and Robert Tycko. Micron-scale magnetic resonance imaging of both liquids and solids. *Journal of Magnetic Resonance*, 260:1–9, nov 2015.

[92] Matthew D. Robson, John C. Gore, and R. Todd Constable. Measurement of the point spread function in MRI using constant time imaging. *Magnetic Resonance in Medicine*, 38(5):733–740, nov 1997.

[93] Huairen Zeng and R. Todd Constable. Image distortion correction in EPI: comparison of field mapping with point spread function mapping. *Magnetic resonance in medicine*, 48(1):137–146, 2002.

[94] R. Mark Henkelman. Measurement of signal intensities in the presence of noise in mr images. *Medical Physics*, 12(2):232–233, 3 1985.

[95] R. Mark Henkelman. Erratum: Measurement of signal intensities in the presence of noise in MR images [Med. Phys. 12, 232 (1985)]. *Medical Physics*, 13(4):544–544, jul 1986.

[96] Timothy M. Shepherd, Peter E. Thelwall, Greg J. Stanisz, and Stephen J. Blackband. Aldehyde Fixative Solutions Alter the Water Relaxation and Diffusion Properties of Nervous Tissue. *Magnetic resonance in medicine : official journal of the Society of Magnetic Resonance in Medicine / Society of Magnetic Resonance in Medicine*, 62(1):26, 2009.

[97] Yasuhiro Hasegawa, Lawrence L. Latour, Christopher H. Sotak, Bernard J. Dardzinski, and Marc Fisher. Temperature Dependent Change of Apparent Diffusion Coefficient of Water in Normal and Ischemic Brain of Rats. *Journal of Cerebral Blood Flow & Metabolism*, 14(3):383–390, may 1994.

[98] Albert Macovski. Noise in mri. *Magnetic Resonance in Medicine*, 36(3):494–497, 9 1996.

[99] W. Brian Hyslop and Paul C. Lauterbur. Effects of restricted diffusion on microscopic NMR imaging. *Journal of Magnetic Resonance (1969)*, 94(3):501–510, oct 1991.

[100] Paul T. Callaghan, Andrew Coy, Lucy C. Forde, and Craig J. Rofe. Diffusive relaxation and edge enhancement in NMR mxicroscopy. *Journal of Magnetic Resonance - Series A*, 101(3):347–350, 1993.

[101] Colleen E. Muir and Bruce J. Balcom. Pure Phase Encode Magnetic Resonance Imaging of Fluids in Porous Media. *Annual Reports on NMR Spectroscopy*, 77:81–113, jan 2012.

[102] Igor V. Mastikhin, Bruce J. Balcom, Pablo J. Prado, and Christopher B. Kennedy. SPRITE MRI with Prepared Magnetization and Centrick-Space Sampling. *Journal of Magnetic Resonance*, 136(2):159–168, feb 1999.

[103] Linqing Li, Florin Marica, Quan Chen, Bryce MacMillan, and Bruce J. Balcom. Quantitative discrimination of water and hydrocarbons in porous media by magnetization prepared centric-scan SPRITE. *Journal of Magnetic Resonance*, 186(2):282–292, jun 2007.

[104] Alexandre A. Khrapitchev, Benedict Newling, and Bruce J. Balcom. Centric-scan SPRITE magnetic resonance imaging with prepared magnetisation. *Journal of Magnetic Resonance*, 181(2):271–279, aug 2006.

[105] Marine A C Moussu, Luisa Ciobanu, Sergej Kurdjumov, Elizaveta Nenasheva, Boucif Djemai, Marc Dubois, Andrew G Webb, Stefan Enoch, Pavel Belov, Redha Abdeddaim, Stanislav Glybovski, M A C Moussu, M Dubois, S Enoch, R Abdeddaim, L Ciobanu, B Djemai, S Kurdjumov, P Belov, S Glybovski, E Nenasheva, and A G Webb. Systematic Analysis of the Improvements in Magnetic Resonance Microscopy with Ferroelectric Composite Ceramics. *Advanced Materials*, 31(30):1900912, jul 2019.

[106] Maria Angelica Schmidt. *Diffusion and and susceptibility effects in NMR microscopy*. PhD thesis, University of Aberdeen, 1993.

[107] John C. Ford, David B. Hackney, David C. Alsop, Hernan Jara, Peter M. Joseph, Christopher M. Hand, and Perry Black. MRI characterization of diffusion coefficients in a rat spinal cord injury model. *Magnetic resonance in medicine*, 31(5):488–494, 1994.

[108] Govind Nair, Stephen Dodd, Seung Kwon Ha, Alan P. Koretsky, and Daniel S. Reich. Ex vivo MR microscopy of a human brain with multiple sclerosis: Visualizing individual cells in tissue using intrinsic iron. *NeuroImage*, 223:117285, dec 2020.

[109] Hyunki Kim, Yolanda E. Hartman, Guihua Zhai, Thomas K. Chung, Melissa L. Korb, Timothy M. Beasley, Tong Zhou, and Eben L. Rosenthal. Dynamic Contrast Enhanced Magnetic Resonance Imaging Evaluates the Early Response of Human Head and Neck Tumor Xenografts following Anti-EMMPRIN therapy with Cisplatin or Irradiation. *Journal of magnetic resonance imaging : JMRI*, 42(4):936, oct 2015.

[110] T. H.R. Farmer, G. A. Johnson, G. P. Cofer, R. R. Maronpot, D. Dixon, and L. W. Hedlund. Implanted coil MR microscopy of renal pathology. *Magnetic Resonance in Medicine*, 10(3):310–323, jun 1989.

[111] Benjamin M. Hardy, Yue Zhu, Kevin D. Harkins, Bibek Dhakal, Jonathan B Martin, Jingping Xie, Junzhong Xu, Mark D. Does, Adam W. Anderson, and John C. Gore. Experimental demonstration of diffusion limitations on resolution and snr in mr microscopy. *Journal of Magnetic Resonance*, page 107479, 5 2023.

[112] Michael Bedford Taylor. Bitcoin and the age of Bespoke Silicon. *2013 International Conference on Compilers, Architecture and Synthesis for Embedded Systems, CASES 2013*, 2013.

[113] Robert E. Simons. The Evolution of IBM High Performance Cooling Technology. *IEEE Transactions on Components Packaging and Manufacturing Technology Part A*, 18(4):805–811, 1995.

[114] P. Styles, N. F. Soffe, C. A. Scott, D. A. Crag, F. Row, D. J. White, and P. C.J. White. A high-resolution NMR probe in which the coil and preamplifier are cooled with liquid helium. 60(3):397–404, dec 1984.

[115] David Ratering, Christof Baltes, Jurek Nordmeyer-Massner, Daniel Marek, and Markus Rudin. Performance of a 200-mhz cryogenic rf probe designed for mri and mrs of the murine brain. *Magnetic resonance in medicine*, 59(6):1440–1447, 2008.

[116] Juan Diego Sánchez-Heredia, Rafael Baron, Esben Søvsø Szocska Hansen, Christoffer Laustsen, Vitaliy Zhurbenko, and Jan Henrik Ardenkjær-Larsen. Autonomous cryogenic RF receive coil for 13 C imaging of rodents at 3 T. *Magnetic resonance in medicine*, 84(1):497–508, jul 2020.

[117] Wenjun Wang, Juan Diego Sánchez-Heredia, Rie Beck Olin, Esben Søvsø Szocska Hansen, Christoffer Laustsen, Vitaliy Zhurbenko, and Jan Henrik Ardenkjaer-Larsen. A cryogenic 14-channel 13C receiver array for 3T human head imaging. *Magnetic Resonance in Medicine*, 35:e4786, nov 2022.

[118] Alexander C Wright, Hee Kwon Song, and Felix W Wehrli. In Vivo MR Micro Imaging With Conventional Radiofrequency Coils Cooled to 77°K. *Magn Reson Med*, 43:163–169, 2000.

[119] Mailadil T. Sebastian. *Measurement of microwave dielectric properties and factors affecting them*. 2008.

[120] Solomon Musikant. Glass. *Encyclopedia of Physical Science and Technology*, Encycloped:781–806, 2003.

[121] S Gabriel, R W Lau, and C Gabriel. The dielectric properties of biological tissues: III. Parametric models for the dielectric spectrum of tissues. *Physics in Medicine and Biology*, 41(11):2271–2293, nov 1996.

[122] Mark Ingalls and Gordon Kent. Measurement of the characteristics of high-q ceramic capacitors. *IEEE Transactions on Components, Hybrids, and Manufacturing Technology*, 10:487–495, 1987.

[123] David M. Pozar. *Microwave Engineering*. John Wiley & Sons, Inc., fourth edi edition, 2012.

[124] R. A. Matula. Electrical resistivity of copper, gold, palladium, and silver. *Journal of Physical and Chemical Reference Data*, 8(4):1147–1298, 1979.

[125] F. Pawlek and D. Rogalla. The electrical resistivity of silver, copper, aluminium, and zinc as a function of purity in the range 4-298° K. *Cryogenics*, 6(1):14–20, feb 1966.

[126] S. Butterworth. Effective resistance of inductance coils at radio frequencies. *Experimental Wireless and the Wireless Engineer*, 3:203, 267, 417 and 483, 1926.

[127] B. H. Suits, A. N. Garroway, and J. B. Miller. Surface and gradiometer coils near a conducting body: The lift-off effect. *Journal of Magnetic Resonance*, 135:373–379, 12 1998.

[128] Deniss Stepins, Gundars Asmanis, and Aivis Asmanis. Measuring capacitor parameters using vector network analyzers. *ELECTRONICS*, 18:29–38, 6 2014.

[129] G. R. M. Garratt. *The Early History of Radio: from Faraday to Marconi*. 1994.

[130] G. Solomakha, J. T. Svejda, C. van Leeuwen, A. Rennings, A. J. Raaijmakers, S. Glybovski, and D. Erni. A self-matched leaky-wave antenna for ultrahigh-field magnetic resonance imaging with low specific absorption rate. *Nature Communications*, 12(1):455, dec 2021.

[131] Stéphane Serfaty, Nathalie Haziza, Luc Darrasse, and Siew Kan. Multi-turn split-conductor transmission-line resonators. *Magnetic resonance in medicine*, 38:687–689, 1997.

[132] Daniel H. Johansen, Juan D. Sanchez-Heredia, Jan R. Petersen, Tom K. Johansen, Vitaliy Zhurbenko, and Jan H. Ardenkjaer-Larsen. Cryogenic Preamplifiers for Magnetic Resonance Imaging. *IEEE transactions on biomedical circuits and systems*, 12(1):202–210, feb 2018.

[133] K. Godley, Steven M Wright, Jim X Ji, and Gregory H Huff. *Investigation of cryo-cooled microcoils* . PhD thesis, 2011.

[134] Jing Fang, M. S. Chow, K. C. Chan, K. K. Wong, G. X. Shen, E. Gao, E. S. Yang, and Q. Y. Ma. Design of superconducting mri surface coil by using method of moment. *IEEE Transactions on Applied Superconductivity*, 12:1823–1827, 2002.

[135] Aimé Labbé, Gilles Authelet, Bertrand Baudouy, Cornelis J. van der Beek, Javier Briatico, Luc Darrasse, and Marie Poirier-Quinot. Recent Advances and Challenges in the Development of Radiofrequency HTS Coil for MRI. *Frontiers in Physics*, 9:386, jul 2021.

[136] Nathan Dasenbrock-Gammon, Elliot Snider, Raymond McBride, Hiranya Pasan, Dylan Durkee, Nugzari Khalvashi-Sutter, Sasanka Munasinghe, Sachith E. Dissanayake, Keith V. Lawler, Ashkan Salamat, and Ranga P. Dias. Evidence of near-ambient superconductivity in a n-doped lutetium hydride. *Nature 2023 615:7951*, 615:244–250, 3 2023.

[137] R. S. Withers, G. C. Liang, B. F. Cole, and M. Johansson. Thin-film hts probe coils for magnetic-resonance imaging. *IEEE Transactions on Applied Superconductivity*, 3:2450–2453, 1993.

[138] Elmar Laistler, Marie Poirier-Quinot, Simon A. Lambert, Rose Marie Dubuisson, Olivier M. Girard, Ewald Moser, Luc Darrasse, and Jean Christophe Ginefri. In vivo mr imaging of the human skin at subnanoliter resolution using a superconducting surface coil at 1.5 tesla. *Journal of Magnetic Resonance Imaging*, 41:496–504, 2 2015.

[139] Richard G. Geyer and Jerzy Krupka. Dielectric properties of materials at cryogenic temperatures and microwave frequencies. *CPEM Digest (Conference on Precision Electromagnetic Measurements)*, pages 350–351, 1994.

[140] Lauren J. O'Donnell and Carl Fredrik Westin. An introduction to diffusion tensor image analysis. *Neurosurgery clinics of North America*, 22:185, 4 2011.

[141] Peter B. Kingsley. Introduction to diffusion tensor imaging mathematics: Part i. tensors, rotations, and eigenvectors. *Concepts in Magnetic Resonance Part A*, 28A:101–122, 3 2006.

[142] Kyoko Yoshida, Charles Jayyosi, Nicole Lee, Mala Mahendroo, and Kristin M. Myers. Mechanics of cervical remodelling: insights from rodent models of pregnancy. *Interface Focus*, 9(5), oct 2019.

[143] Brenda Timmons, Meredith Akins, and Mala Mahendroo. Cervical remodeling during pregnancy and parturition. *Trends in endocrinology and metabolism: TEM*, 21:353, 6 2010.

[144] J. P. Nott, E. Pervolaraki, A. P. Benson, E. A. Bonney, J. D. Pickering, N. Wilkinson, and N. A.B. Simpson. Diffusion tensor imaging determines three-dimensional architecture of human cervix: a cross-sectional study. *BJOG: An International Journal of Obstetrics & Gynaecology*, 125:812–818, 6 2018.

[145] Antara Chatterjee, Rojan Saghian, Anna Dorogin, Lindsay S. Cahill, John G. Sled, Stephen Lye, and Oksana Shynlova. Combination of histochemical analyses and micro-mri reveals regional changes of the murine cervix in preparation for labor. *Scientific Reports 2021 11:1*, 11:1–18, 3 2021.

[146] Sara Panizo, Laura Martínez-Arias, Cristina Alonso-Montes, Pablo Cannata, Beatriz Martín-Carro, José L. Fernández-Martín, Manuel Naves-Díaz, Natalia Carrillo-López, and Jorge B. Cannata-Andía. Fibrosis in chronic kidney disease: Pathogenesis and consequences. *International Journal of Molecular Sciences*, 22:1–19, 1 2021.

[147] Digsu N. Koye, Dianna J. Magliano, Robert G. Nelson, and Meda E. Pavkov. The global epidemiology of diabetes and kidney disease. *Advances in chronic kidney disease*, 25:121–132, 3 2018.

[148] Teresa K. Chen, Daphne H. Knicely, and Morgan E. Grams. Chronic kidney disease diagnosis and management: A review. *JAMA*, 322:1294, 10 2019.

[149] Frank C. Brosius and Rajiv Saran. Do we now have a prognostic biomarker for progressive diabetic nephropathy? *Journal of the American Society of Nephrology*, 23:376–377, 3 2012.

[150] Lin Wang, Jing Yuan, Shi Jun Zhang, Min Gao, Yuan Cheng Wang, Yi Xiang Wang, and Shenghong Ju. Myocardial t1 rho mapping of patients with end-stage renal disease and its comparison with t1 mapping and t2 mapping: A feasibility and reproducibility study. *Journal of magnetic resonance imaging : JMRI*, 44:723–731, 9 2016.

[151] Rongshuang Huang, Ping Fu, and Liang Ma. Kidney fibrosis: from mechanisms to therapeutic medicines. *Signal Transduction and Targeted Therapy 2023 8:1*, 8:1–20, 3 2023.

[152] Jinhua Tang, Na Liu, and Shougang Zhuang. Role of epidermal growth factor receptor in acute and chronic kidney injury. *Kidney International*, 83:804–810, 5 2013.

[153] Takamune Takahashi, Feng Wang, and Christopher C. Quarles. Current mri techniques for the assessment of renal disease. *Current opinion in nephrology and hypertension*, 24:217, 5 2015.

[154] Sang Youn Kim, Hyeonjin Kim, Joongyub Lee, Sung Il Jung, Min Hoan Moon, Kwon Wook Joo, and Jeong Yeon Cho. Quantitative magnetic resonance imaging of chronic kidney disease: an experimental in vivo study using rat chronic kidney disease models. *Acta radiologica (Stockholm, Sweden : 1987)*, 64:404–414, 1 2023.

[155] Stefanie J. Hectors, Octavia Bane, Paul Kennedy, Fadi El Salem, Madhav Menon, Maxwell Segall, Rafael Khaim, Veronica Delaney, Sara Lewis, and Bachir Taouli. T1rho mapping for assessment of renal allograft fibrosis. *Journal of magnetic resonance imaging : JMRI*, 50:1085–1091, 10 2019.

[156] Jared Guthrie Cobb, J. Herman Kan, and John C. Gore. T1rho mapping of pediatric epiphyseal and articular cartilage in the knee. *Journal of magnetic resonance imaging : JMRI*, 38:299–305, 8 2013.

[157] Swati Rane, John T. Spear, Zhongliang Zu, Manus J. Donahue, and John C. Gore. Functional mri using spin lock editing preparation pulses. *Magnetic resonance imaging*, 32:813–818, 2014.

[158] Zhongliang Zu, Xiaoyu Jiang, Junzhong Xu, and John C. Gore. Spin-lock imaging of 3-o-methyl-d glucose (3omg) in brain tumors. *Magnetic resonance in medicine*, 80:1110–1117, 9 2018.

[159] Ping Wang, He Zhu, Hakmook Kang, and John C. Gore. R1rho dispersion and sodium imaging in human calf muscle. *Magnetic resonance imaging*, 42:139–143, 10 2017.

[160] Yi Wang, Chaoyi Deng, Keni Cota-Ruiz, Jose R. Peralta-Videa, Youping Sun, Swati Rawat, Wenjuan Tan, Andres Reyes, Jose A. Hernandez-Viezcas, Genhua Niu, Chunqiang Li, and Jorge L. Gardea-Torresdey. Improvement of nutrient elements and allicin content in green onion (Allium fistulosum) plants exposed to CuO nanoparticles. *Science of The Total Environment*, 725:138387, jul 2020.

[161] Alfred G. Redfield. Nuclear magnetic resonance saturation and rotary saturation in solids. *Physical Review*, 98:1787, 6 1955.

[162] Seppo K. Koskinen, Anette M. Virta, Pekka T. Niemi, Sami A. Kajander, and Markku E.S. Komu. T1rho dispersion of rat tissues in vitro. *Magnetic resonance imaging*, 17:1043–1047, 9 1999.

[163] Fatemeh Adelnia, Zhongliang Zu, John T. Spear, Feng Wang, Kevin D. Harkins, and John C. Gore. Tissue characterization using r1rho dispersion imaging at low locking fields. *Magnetic Resonance Imaging*, 84:1–11, 12 2021.

[164] John T. Spear and John C. Gore. New insights into rotating frame relaxation at high field. *NMR in Biomedicine*, 29:1258–1273, 9 2016.

[165] Walter R.T. Witschey, Arijitt Borthakur, Mark A. Elliott, Eric Mellon, Sampreet Niyogi, Daniel J. Wallman, Chenyang Wang, and Ravinder Reddy. Artifacts in t1rho-weighted imaging: Compensation for b1 and b0 field imperfections. *Journal of magnetic resonance (San Diego, Calif. : 1997)*, 186:75, 5 2007.

[166] Maximilian Gram, Michael Seethaler, Daniel Gensler, Johannes Oberberger, Peter M. Jakob, and Peter Nordbeck. Balanced spin-lock preparation for b1-insensitive and b0-insensitive quantification of the rotating frame relaxation time t1rho. *Magnetic Resonance in Medicine*, 85:2771–2780, 5 2021.

[167] S. Chopra, R. E.D. McClung, and R. B. Jordan. Rotating-frame relaxation rates of solvent molecules in solutions of paramagnetic ions undergoing solvent exchange. *Journal of Magnetic Resonance (1969)*, 59:361–372, 10 1984.

[168] Jared G. Cobb, Jingping Xie, and John C. Gore. Contributions of chemical exchange to t1rho dispersion in a tissue model. *Magnetic Resonance in Medicine*, 66:1563–1571, 2011.

[169] Yì-Xiáng J. Wáng, Qinwei Zhang, Xiaojuan Li, Weitian Chen, Anil Ahuja, and Jing Yuan. T1rho magnetic resonance: basic physics principles and applications in knee and intervertebral disc imaging. *Quantitative Imaging in Medicine and Surgery*, 5:858, 12 2015.

[170] Jessica M. Overstreet, Yinqiu Wang, Xin Wang, Aolei Niu, Leslie S. Gewin, Bing Yao, Raymond C. Harris, and Ming Zhi Zhang. Selective activation of epidermal growth factor receptor in renal proximal tubule induces tubulointerstitial fibrosis. *FASEB journal : official publication of the Federation of American Societies for Experimental Biology*, 31:4407–4421, 10 2017.

[171] Courtney C. Hatcher, Amber T. Collins, Sophia Y. Kim, Lindsey C. Michel, William C. Mostertz, Sophia N. Ziemian, Charles E. Spritzer, Farshid Guilak, Louis E. DeFrate, and Amy L. McNulty. Relationship between t1rho magnetic resonance imaging, synovial fluid biomarkers, and the biochemical and biomechanical properties of cartilage. *Journal of Biomechanics*, 55:18–26, 4 2017.

[172] Yuxi Pang. An order parameter without magic angle effect (optima) derived from dispersion in ordered tissue. *Magnetic Resonance in Medicine*, 83:1783–1795, 5 2020.

[173] Bae Hoon Lee, Nathaniel Lum, Li Yuan Seow, Pei Qi Lim, and Lay Poh Tan. Synthesis and characterization of types a and b gelatin methacryloyl for bioink applications. *Materials 2016, Vol. 9, Page 797*, 9:797, 9 2016.

[174] Arely León-López, Alejandro Morales-Peñaloza, Víctor Manuel Martínez-Juárez, Apolonio Vargas-Torres, Dimitrios I. Zeugolis, and Gabriel Aguirre-Álvarez. Hydrolyzed collagen—sources and applications. *Molecules 2019, Vol. 24, Page 4031*, 24:4031, 11 2019.

[175] Luisa Ciobanu, Andrew G. Webb, and Charles H. Pennington. Signal enhancement by diffusion: experimental observation of the "DESIRE" effect. *Journal of magnetic resonance (San Diego, Calif. : 1997)*, 170(2):252–256, oct 2004.

[176] Ileana O. Jelescu, Nicolas Boulant, Denis Le Bihan, and Luisa Ciobanu. Experimental demonstration of diffusion signal enhancement in 2D DESIRE images. *Journal of magnetic resonance (San Diego, Calif. : 1997)*, 218:44–48, may 2012.

[177] Jeroen Van Gemert, Wyger Brink, Andrew Webb, and Rob Remis. High-permittivity pad design tool for 7T neuroimaging and 3T body imaging. *Magn Reson Med*, 81:3370–3378, 2019.

[178] Xinqiang Yan, John C. Gore, and William A. Grissom. Self-decoupled radiofrequency coils for magnetic resonance imaging. *Nature Communications*, 9(1):1–3, 2018.

[179] K. J. Suetterlin, R. Männikkö, E. Matthews, L. Greensmith, M. G. Hanna, H. Bostock, and S. V. Tan. Excitability properties of mouse and human skeletal muscle fibres compared by muscle velocity recovery cycles. *Neuromuscular Disorders*, 32:347–357, 4 2022.

[180] Fang-Cheng Yeh. Shape analysis of the human association pathways. *NeuroImage*, 223:117329, 2020.

[181] Fang-Cheng Yeh, Li Liu, T. Kevin Hitchens, and Yijen L. Wu. Mapping immune cell infiltration using restricted diffusion mri. *Magnetic Resonance in Medicine*, 77(2):603–612, 2017.

[182] Fang-Cheng Yeh, Van Jay Wedeen, and Wen-Yih Isaac Tseng. Generalized q-sampling imaging. *IEEE Transactions on Medical Imaging*, 29(9):1626–1635, 2010.

[183] Dung Minh Hoang, Evelyn B. Voura, Chao Zhang, Latifa Fakri-Bouchet, and Youssef Zaim Wadghiri. Evaluation of coils for imaging histological slides: Signal-to-noise ratio and filling factor. *Magnetic Resonance in Medicine*, 71(5):1932–1943, may 2014.

[184] Nian Wang, Leonard E. White, Yi Qi, Gary Cofer, and G. Allan Johnson. Cytoarchitecture of the mouse brain by high resolution diffusion magnetic resonance imaging. *NeuroImage*, 216:116876, 8 2020.

[185] Armin M. Nagel, Moritz Zaiss, Sina Straub, Oliver Speck, Mark E. Ladd, Ewald Moser, Martin Meyerspeer, David G. Norris, Peter Bachert, and Sebastian Schmitter. Pros and cons of ultra-high-field MRI/MRS for human application. *Progress in Nuclear Magnetic Resonance Spectroscopy*, 109:1–50, 2018.

[186] Thomas M. Fiedler, Mark E. Ladd, and Andreas K. Bitz. SAR Simulations & Safety. *NeuroImage*, 168(March 2017):33–58, 2018.

[187] Weihua Mao, Michael B. Smith, and Christopher M. Collins. Exploring the limits of RF shimming for high-field MRI of the human head. *Magnetic Resonance in Medicine*, 56(4):918–922, 2006.

[188] Vincent Gras, Alexandre Vignaud, Alexis Amadon, Denis Le Bihan, and Nicolas Boulant. Universal pulses: A new concept for calibration-free parallel transmission. *Magnetic Resonance in Medicine*, 77(2):635–643, 2017.

[189] Gregor Adriany, Jerahmie Radder, Nader Tavaf, Russell Lagore, Steve Jungst, Myung Kyun Woo, Andrea Grant, Yigitcan Eryaman, Bei Zhang, Shajan Gundamony, Riccardo Lattanzi, Kamil Ugurbil, and Pierre Francois Van De Moortele. Evaluation of a 16-channel transmitter for head imaging at 10.5T. In *Proceedings of the 2019 21st International Conference on Electromagnetics in Advanced Applications, (ICEAA) 2019*, pages 1171–1174. Institute of Electrical and Electronics Engineers Inc., sep 2019.

[190] Matthijs H.S. de Buck, Peter Jezzard, Hongbae Jeong, and Aaron T. Hess. An investigation into the minimum number of tissue groups required for 7T in-silico parallel transmit electromagnetic safety simulations in the human head. *Magnetic Resonance in Medicine*, 85(2):1114–1122, 2021.

[191] Morgane Le Garrec, Vincent Gras, Marie France Hang, Guillaume Ferrand, Michel Luong, and Nicolas Boulant. Probabilistic analysis of the specific absorption rate intersubject variability safety factor in parallel transmission MRI. *Magnetic Resonance in Medicine*, 78(3):1217–1223, 2017.

[192] E. F. Meliadò, A. J.E. Raaijmakers, A. Sbrizzi, B. R. Steensma, M. Maspero, M. H.F. Savenije, P. R. Luijten, and C. A.T. van den Berg. A deep learning method for image-based subject-specific local SAR assessment. *Magnetic Resonance in Medicine*, 83(2):695–711, 2020.

[193] Emre Kopanoglu, Cem M. Deniz, M. Arcan Erturk, and Richard G. Wise. Specific absorption rate implications of within-scan patient head motion for ultra-high field MRI. *Magnetic Resonance in Medicine*, 84(5):2724–2738, nov 2020.

[194] Ingmar Graesslin, Peter Vernickel, Peter Börnert, Kay Nehrke, Giel Mens, Paul Harvey, and Ulrich Katscher. Comprehensive RF safety concept for parallel transmission MR. *Magnetic Resonance in Medicine*, 74(2):589–598, 2015.

[195] Jin Jin, Feng Liu, Ewald Weber, and Stuart Crozier. Improving SAR estimations in MRI using subject-specific models. *Physics in Medicine & Biology*, 57(24):8153–71, nov 2012.

[196] Eugene Milshteyn, Georgy Guryev, Angel Torrado-Carvajal, Jacob White, Lawrence Wald, and Bastien Guerin. Approaching Real-Time Patient-Specific SAR Calculation for Parallel Transmission at 7 Tesla. *Proceedings of the International Society of Magnetic Resonance in Medicine 29*, 0619, 2021.

[197] Eugene Milshteyn, Georgy Guryev, Angel Torrado-Carvajal, Elfar Adalsteinsson, Jacob K. White, Lawrence L. Wald, and Bastien Guerin. Individualized SAR calculations using computer vision-based MR segmentation and a fast electromagnetic solver. *Magnetic Resonance in Medicine*, 85(1):429–443, jan 2021.

[198] Gabriele Eichfelder and Matthias Gebhardt. Local specific absorption rate control for parallel transmission by virtual observation points. *Magnetic Resonance in Medicine*, 66(5):1468–1476, 2011.

[199] Riccardo Lattanzi and Daniel K. Sodickson. Ideal current patterns yielding optimal signal-to-noise ratio and specific absorption rate in magnetic resonance imaging: computational methods and physical insights. *Magnetic resonance in medicine*, 68(1):286–304, 2012.

[200] Cem M. Deniz, Manushka V. Vaidya, Daniel K. Sodickson, and Riccardo Lattanzi. Radiofrequency energy deposition and radiofrequency power requirements in parallel transmission with increasing distance from the coil to the sample. *Magnetic Resonance in Medicine*, 75(1):423–432, 2016.

[201] Riccardo Lattanzi, Graham C. Wiggins, Bei Zhang, Qi Duan, Ryan Brown, and Daniel K. Sodickson. Approaching ultimate intrinsic signal-to-noise ratio with loop and dipole antennas. *Magnetic resonance in medicine*, 79(3):1789–1803, mar 2018.

[202] Mikhail Kozlov and Robert Turner. Fast MRI coil analysis based on 3-D electromagnetic and RF circuit co-simulation. *Journal of magnetic resonance (San Diego, Calif. : 1997)*, 200(1):147–152, sep 2009.

[203] Matthew Restivo, Alexander Raaijmakers, Cornelis van den Berg, Peter Luijten, and Hans Hoogduin. Improving peak local SAR prediction in parallel transmit using in situ S-matrix measurements. *Magnetic Resonance in Medicine*, 77(5):2040–2047, may 2017.

[204] Alireza Sadeghi-Tarakameh, Ehsan Kazemivalipour, Umut Gundogdu, Serhat Erdogan, and Ergin Atalar. Accelerating the co-simulation method for the design of transmit array coils for MRI. *Magma (New York, N.Y.)*, 34(1):165–178, feb 2021.

[205] Umberto Zanovello, Frank Seifert, Oriano Bottauscio, Lukas Winter, Luca Zilberti, and Bernd Ittermann. CoSimPy: An open-source python library for MRI radiofrequency Coil EM/Circuit Cosimulation. *Computer Methods and Programs in Biomedicine*, 216:106684, apr 2022.

[206] Arian Beqiri, Jeffrey W. Hand, Joseph V. Hajnal, and Shaihan J. Malik. Comparison between simulated decoupling regimes for specific absorption rate prediction in parallel transmit MRI. *Magnetic Resonance in Medicine*, 74(5):1423–1434, nov 2015.

[207] Emre Kopanoglu. Patient specific parallel transmit pulses are patient position dependent while safety models are fixed : safety implications. *Proceedings of the International Society of Magnetic Resonance in Medicine 29*, 2299, 2021.

[208] Graeme A. Keith, Christopher T. Rodgers, Aaron T. Hess, Carl J. Snyder, J. Thomas Vaughan, and Matthew D. Robson. Automated tuning of an eight-channel cardiac transceive array at 7 tesla using piezoelectric actuators. *Magnetic resonance in medicine*, 73(6):2390–2397, jun 2015.

[209] Ross D. Venook, Brian A. Hargreaves, Garry E. Gold, Steven M. Conolly, and Greig C. Scott. Automatic tuning of flexible interventional RF receiver coils. *Magnetic resonance in medicine*, 54(4):983–993, 2005.

[210] Christopher M. Collins and Michael B. Smith. Spatial resolution of numerical models of man and calculated specific absorption rate using the FDTD method: A study at 64 MHz in a magnetic resonance imaging coil. *Journal of Magnetic Resonance Imaging*, 18(3):383–388, 2003.

[211] Andreas Christ, Wolfgang Kainz, Eckhart G. Hahn, Katharina Honegger, Marcel Zefferer, Esra Neufeld, Wolfgang Rascher, Rolf Janka, Werner Bautz, Ji Chen, Berthold Kiefer, Peter Schmitt, Hans Peter Hollenbach, Jianxiang Shen, Michael Oberle, Dominik Szczerba, Anthony Kam, Joshua W. Guag, and Niels Kuster. The Virtual Family - Development of surface-based anatomical models of two adults and two children for dosimetric simulations. *Physics in Medicine and Biology*, 55(2):N23–38, 2010.

[212] Martijn de Greef, Ozlem Ipek, Alexander J. E. Raaijmakers, Johannes Crezee, and Cornelis A. T. van den Berg. Specific absorption rate intersubject variability in 7T parallel transmit MRI of the head. *Magnetic Resonance in Medicine*, 69(5):1476–1485, may 2013.

[213] Marie Christine Gosselin, Esra Neufeld, Heidi Moser, Eveline Huber, Silvia Farcito, Livia Gerber, Maria Jedensjo, Isabel Hilber, Fabienne Di Gennaro, Bryn Lloyd,

Emilio Cherubini, Dominik Szczerba, Wolfgang Kainz, and Niels Kuster. Development of a new generation of high-resolution anatomical models for medical device evaluation: the Virtual Population 3.0. *Physics in medicine and biology*, 59(18):5287–5303, sep 2014.

[214] P. J. Cassidy, K. Clarke, and D. J. Edwards. Determining the tuning and matching requirements of RF coils using electromagnetic simulation and electric circuit analysis. *Concepts in Magnetic Resonance Part B: Magnetic Resonance Engineering*, 25B(1):27–41, apr 2005.

[215] Xinqiang Yan, Xiaoliang Zhang, Baotong Feng, Chuangxin Ma, Long Wei, and Rong Xue. 7T transmit/receive arrays using ICE decoupling for human head MR imaging. *IEEE Transactions on Medical Imaging*, 2014.

[216] S. Wolf, D. Diehl, M. Gebhardt, J. Mallow, and O. Speck. SAR simulations for high-field MRI: How much detail, effort, and accuracy is needed? *Magnetic Resonance in Medicine*, 69(4):1157–1168, apr 2013.

[217] H. Homann, P. Börnert, H. Eggers, K. Nehrke, O. Dössel, and I. Graesslin. Toward individualized SAR models and in vivo validation. *Magnetic Resonance in Medicine*, 66(6):1767–76, 2011.

[218] Cem Murat Deniz, Ryan Brown, Riccardo Lattanzi, Leeor Alon, Daniel K. Sodickson, and Yudong Zhu. Maximum efficiency radiofrequency shimming: Theory and initial application for hip imaging at 7 tesla. *Magnetic Resonance in Medicine*, 69(5):1379–1388, may 2013.

[219] Giuseppe Carluccio, Danilo Erricolo, Sukhoon Oh, and Christopher M. Collins. An approach to rapid calculation of temperature change in tissue using spatial filters to approximate effects of thermal conduction. *IEEE Transactions on Biomedical Engineering*, 60(6):1735–1741, 2013.

[220] Christopher M. Collins, Shizhe Li, and Michael B. Smith. SAR and B1 field distributions in a heterogeneous human head model within a birdcage coil. *Magnetic Resonance in Medicine*, 40(6):847–856, 1998.

[221] IEC 60601-2-33. *IEC*, 3.2(06):Medical electrical equipment – Part 2–33, 2015.

[222] Aurélien Massire, Martjin A. Cloos, Michel Luong, Alexis Amadon, Alexandre Vignaud, Christopher J. Wiggins, and Nicolas Boulant. Thermal simulations in the human head for high field MRI using parallel transmission. *Journal of Magnetic Resonance Imaging*, 35(6):1312–1321, jun 2012.

[223] Frank Seifert, Gerd Wübbeler, Sven Junge, Bernd Ittermann, and Herbert Rinneberg. Patient safety concept for multichannel transmit coils. *Journal of Magnetic Resonance Imaging*, 26(5):1315–1321, nov 2007.

[224] Zhangwei Wang, James C. Lin, Weihua Mao, Wanzhan Liu, Michael B. Smith, and Christopher M. Collins. SAR and temperature: Simulations and comparison to regulatory limits for MRI. *Journal of Magnetic Resonance Imaging*, 26(2):437–441, aug 2007.

[225] Simone A. Winkler, Franz Schmitt, Hermann Landes, Joshua de Bever, Trevor Wade, Andrew Alejski, and Brian K. Rutt. Gradient and shim technologies for ultra high field MRI. *NeuroImage*, 168:59–70, mar 2018.

[226] Xin Li, Jullie W. Pan, Nikolai I. Avdievich, Hoby P. Hetherington, and Joseph V. Rispoli. Electromagnetic simulation of a 16-channel head transceiver at 7 T using circuit-spatial optimization. *Magnetic Resonance in Medicine*, 85(6):3463–3478, jun 2021.

[227] Karthik Lakshmanan, Martijn Cloos, Ryan Brown, Riccardo Lattanzi, Daniel K. Sodickson, and Graham C. Wiggins. The "Loopole" Antenna: A Hybrid Coil Combining Loop and Electric Dipole Properties for Ultra-High-Field MRI. *Concepts in Magnetic Resonance Part B, Magnetic Resonance Engineering*, 2020:1–9, sep 2020.

[228] Nikolai I. Avdievich, Georgiy Solomakha, Loreen Ruhm, Anton V. Nikulin, Arthur W. Magill, and Klaus Scheffler. Folded-end dipole transceiver array for human whole-brain imaging at 7 T. *NMR in biomedicine*, 34(8), aug 2021.

[229] Alireza Sadeghi-Tarakameh, Lance DelaBarre, Russell L. Lagore, Angel Torrado-Carvajal, Xiaoping Wu, Andrea Grant, Gregor Adriany, Gregory J. Metzger, Pierre Francois Van de Moortele, Kamil Ugurbil, Ergin Atalar, and Yigitcan Eryaman. In vivo human head MRI at 10.5T: A radiofrequency safety study and preliminary imaging results. *Magnetic Resonance in Medicine*, 84(1):484–496, jul 2020.

[230] Bei Zhang, Gregor Adriany, Lance Delabarre, Jerahmie Radder, Russell Lagore, Brian Rutt, Qing X. Yang, Kamil Ugurbil, and Riccardo Lattanzi. Effect of radiofrequency shield diameter on signal-to-noise ratio at ultra-high field MRI. *Magnetic resonance in medicine*, 85(6):3522–3530, jun 2021.

[231] A. Hoyos-Idrobo, P. Weiss, A. Massire, A. Amadon, and N. Boulant. On variant strategies to solve the magnitude least squares optimization problem in parallel transmission pulse design and under strict sar and power constraints. *IEEE Transactions on Medical Imaging*, 33(3):739–748, 2014.

[232] Di Qian, AbdEl-Monem M. El-Sharkawy, Paul A. Bottomley, and William A. Edelstein. An RF dosimeter for independent SAR measurement in MRI scanners. *Medical Physics*, 40(12):122303, 2013.

[233] Weiman Jiang, Fan Yang, and Kun Wang. Individualized and accurate SAR characterization method based on an equivalent circuit model in MRI system. *Proceedings of the International Society of Magnetic Resonance in Medicine 29*, 2302, 2021.

[234] Zhiyue J. Wang. Towards a complete coil array. *Magnetic Resonance Imaging*, 26(9):1310–1315, 2008.

[235] Xinqiang Yan, Zhipeng Cao, and William A. Grissom. Ratio-adjustable power splitters for array-compressed parallel transmission. *Magnetic Resonance in Medicine*, 2018.

[236] Khan Nouman, Zaman Asim, and Khan Qasim. Comprehensive study on performance of pid controller and its applications. *Proceedings of 2018 2nd IEEE Advanced Information Management, Communicates, Electronic and Automation Control Conference, IMCEC 2018*, pages 1574–1579, 9 2018.

[237] Muhidin Lellić and Zoran Gajić. A reference guide to pid controllers in the nineties. *IFAC Proceedings Volumes*, 33:69–78, 4 2000.